Crystalline Barium Strontium Titanate thin films on Amorphous Fused Silica Substrates for Frequency Agile Microwave Devices

A thesis submitted for the degree of

DOCTOR OF PHILOSOPHY

by

VENKATA SARAVANAN K

SCHOOL OF PHYSICS
UNIVERSITY OF HYDERABAD
HYDERABAD – 500046
INDIA

JULY 2009

DECLARATION

I hereby declare that the content embodied in this thesis entitled ***"Crystalline Barium Strontium Titanate thin films on Amorphous Fused Silica Substrates for Frequency Agile Microwave Devices"*** submitted to University of Hyderabad for the award of Doctor of **Philosophy** in **Physics** is a record of original research work carried out by me under the supervision of Dr. K. C. James Raju, School of Physics, University of Hyderabad, Hyderabad. This work has not been submitted partially or fully for any degree in any other university.

Date:
Place:

Venkata Saravanan. K

CERTIFICATE

This is to certify that the research work presented in this thesis entitled ***"Crystalline Barium Strontium Titanate thin films on Amorphous Fused Silica Substrates for Frequency Agile Microwave Devices"*** for the award of **DOCTOR OF PHILOSOPHY** is an original work carried out by **Mr. Venkatesh Saravanan. K** under my supervision at School of physics, University of Hyderabad, Hyderabad. This thesis work has not been submitted to this or any other university partially or fully for the award of any degree or diploma.

Date:
Place: Hyderabad

Dr. K. C. James Raju
(Supervisor)

Dean
School of Physics

Acknowledgements

It's my pleasure to write this part of my thesis and express my gratitude to one and all for helping me in a long run. It's time to bring them to stage since, most of them were behind the screens. I thank all of them involved directly or indirectly for the successful completion of this thesis.

I'm deeply indebted to Dr. K. C. James Raju, for his guidance and support though out my research. The way he inspired, advised and helped for both academic and personal life is unforgettable. He was always there to listen, advice, encourage and rectify the problems. The freedom he has given me is ultimate and unlimited and I hope that it was utilized in a proper way.

I would like to express my heartfelt note of deep gratitude to Dr. M. Ghanashyam Krishna for his valuable discussions and advice throughout my research (M.Phil and PhD) at University of Hyderabad. It is from him I learnt to be patient in research and in personal life.

My bountiful and sincere thanks to Prof. Anil K Bhatnagar. It's my privilege to have worked with him.

I'm deeply indebted to Prof. S.P. Tewari, Director, ACRHEM for his valuable discussions, support and encouragement.

I take this opportunity to thank Dr. G. Raghavan and Mrs. Tripura Sundari, IGCAR, Kalpakkam for their inspirational guidance during my M.Sc project at IGCAR.

I am thankful to my M.phil course faculties, Prof. M. Sivakumar, Prof. A. P. Pathak, Prof. C. S. Sunandana, Prof. Anil K Bharnagar, Dr. P. Ananta Lakshmi and Dr. P. K. Suresh, for their constant encouragement and inspiring lectures.

I am very grateful to Prof. R. Singh for extending the sputtering facility for the device metallization work.

Dr. B. Sridharan's (IICT, Hyderabad) timely help in XRD & XPS measurements and valuable discussions is gratefully acknowledged.

I thank Dr. S. Dhamodaran, IIT, Kanpur for his help in RBS measurements.

I thank Dr. V. Sivasubraminayam, IGCAR, Kalpakkam and Prof. Ram S. Katiyar and Dr. Manoj K. Singh, University of Puerto Rico for their help in RAMAN measurements.

I would like to thank all the faculty members of ACRHEM especially Dr. Soma Venugopal Rao and Dr. Anil Kumar Chaudhary for their valuable discussions and help in non linear optical experiments carried out at ACRHEM.

I thank the Dean, School of Physics Prof. C. Bansal and the former Deans, Prof. Vipin Srivastava, Prof. S. N. Kaul and Prof. V. S. S. Sastry, for providing me the facilities for the successful completion of my work. I also thank my doctoral committee member Prof. V. Seshubai for her valuable suggestions on my work. Also I would like to thank all the faculty members who have helped me throughout my stay here at the University of Hyderabad. I gratefully remember all my other teachers who taught me in school as well as the faculty members at Department of Physics, Pondicherry University.

My sincere thanks to the staff of the CIL, Mr. C. S. Murthy, Mr. Suresh, Dr. S. Manjunath, Mr. Nageshwar Rao, Mr. Sudhakar, Mr. Illayaa, Mr. Kishta Reddy and Mr. Rajkumar for the technical support they provided

I am thankful to Mr. Abraham, Office Assistant, School of Physics for his timely help. Mr. Anantha Rao, Mrs. Saramma, Mr. Purnachandra Rao of School of Physics, Mr. Rajeshwar and Mr. Nagaraj of ACRHEM are also acknowledged for their help.

I would like to thank my labmates Sudhi, GLN, Rajeeb, Vasu, Sachin, Pamu, Prashant, Kiran, Rambo, Anil and lakshun for helping me in various ways both academically and personally.

I thank all the scholars in School of Physics for helping me directly or indirectly. Abhilash and Joji need a special mention here for their timely help and support that they have provided me throughout my research. I don't have enough words to express my gratitude to them. I also thank Manimaran, Bharathi, Ajith, Ghanavel and Sai Preethi, who made my stay here pleasant and provided friendly atmosphere. Very special thanks to Sathish for being so helpful, supportive and understanding since my M.Sc days.

It's my pleasure to acknowledge the encouragement and support from my M.Sc classmates Ramnath, Prasanna, Ramki, goutham, Anand, Malli, Manu and Harhsan and my M.Phil classmates Rajinikanth and Jubi.

I would like to thank Lily, Vitso, Daniel, Tiger, Theurei, Asim, Imli, Abhijith, Chaya, Rankul, Ram Kumar (RK), Sudharshan and Prabuddha who made my stay at UoH memorable for life. Also it's my pleasure to thank the members of DSPs, Uncle Kill Me Quick and Misfits for providing lively atmosphere during my stay in UoH.

I thank ACRHEM, UoH for providing Senior Research Fellowship and also for the travel support to attend IMF-ISAF-2009 at China. I thank University of Hyderabad for providing financial support under UPE grant for attending AMF-5 at Tokyo, Japan. I also acknowledge the financial support from NPSM.

Above all it is the endless sacrifice, support and motivation from my Father and Mother which has brought me to the position where I am. I thank my Brother, Sister and all my relatives for their moral support.

Contents

Chapter I

Introduction, motivation and thesis overview

1.1 Introduction:

Linear and non-linear dielectric materials have received increasing attention in recent years, both from a fundamental perspective and from novel applications point of view. This chapter gives an introduction to dielectrics and ferroelectricity along with need for tunable devices for microwave applications. Various enabling technologies such as mechanical varactors, MEMS, semiconductor varactors and ferroelectric varactors are described and compared. The importance of the Barium Strontium Titanate (BST) thin films for optical and microwave tunable applications have been discussed. This chapter also introduces various preparation techniques for deposition of BST thin films. An overview on BST based devices has been given leading to the issues related to BST device fabrication and importance of fused silica as a suitable substrate material for optical and microwave applications. Based on these, the major objectives of the present study are identified and formulated.

1.2 Introduction to dielectrics:

A material is termed as "dielectric" if it has the ability to store electrical energy[1]. Dielectric materials commonly referred to as insulators, resist the flow of current in a circuit and can store electric charge. The dielectric response arises from the short-range motion of charge carriers under the influence of an externally applied electric field while capacitance is a measure of the ability of any two conducting plates in proximity to store a charge Q, when a potential difference V is applied across them[2]. The capacitance C is given as,

$$C=Q/V \text{ (in Farad, F)} \qquad (1.1)$$

The capacitance of a parallel plate capacitor without any dielectric in between them is known as the vacuum capacitor[3], whose capacitance is determined purely by the geometry. From elementary electrostatics it is known that the charge density on the plates, Q is proportional to the area A (in m^2) and the external electric field E = V/d, where d is the distance between the plates (in m). The proportionality constant is defined as ε_0, the permittivity of free space (8.854×10^{-12} F/m). Thus the capacitance of a vacuum capacitor shown in figure 1.1a will be,

$$Q= \varepsilon_0 (V/d)A \text{ and } C= \varepsilon_0 A/d \qquad (1.2)$$

The value of capacitance increases when a dielectric is introduced in between the plates as shown in figure 1.1b. The dielectric constant *k*, of the material introduced is given as the ratio of the capacitance of a capacitor with a dielectric between the plates to that with vacuum between them.

$$k = \frac{C}{C_0} = \frac{\varepsilon\ A/d}{\varepsilon_0 A/d} = \frac{\varepsilon}{\varepsilon_0} \qquad (1.3)$$

where ε is the permittivity of the dielectric material (in C^2/m^2 or F/m)

From the above we define the dielectric constant of a material as the ratio of the permittivity of the material to the permittivity of free space and hence it is also known as the relative permittivity, ε_r[4].

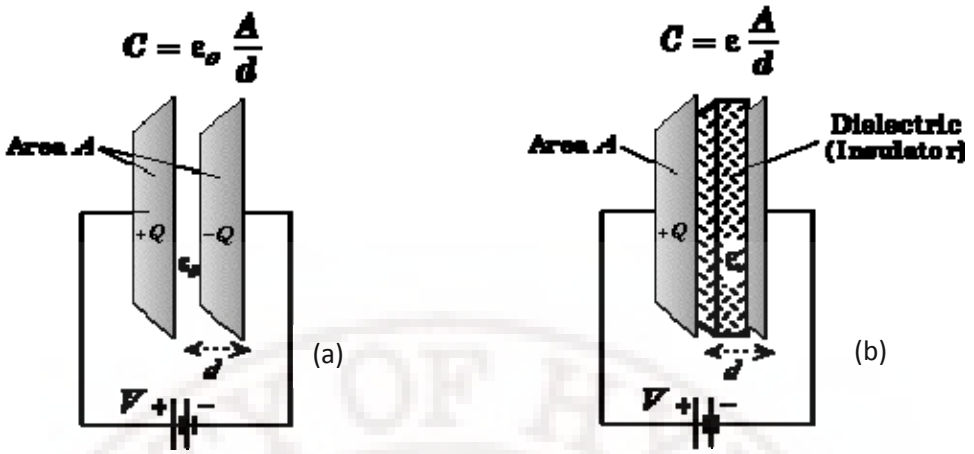

Figure 1.1: Capacitance of a parallel plate capacitor with (a) vacuum as dielectric and (b) dielectric material between them.

Now, if an AC sinusoidal potential V= V_0 exp iωt is applied across the dielectric then the charge varies with time as shown below and the resulting current will be made up of a charging current I_c and a loss current I_l that is related to the dielectric constant.

$$I_c \equiv \frac{dQ}{dt} = \frac{CdV}{dt} = i\omega CV = \omega CV_0 \exp\left[i\left(\omega t + \frac{\pi}{2}\right)\right] \qquad (1.4)$$

The loss current I_l arises from (1) the long-range migration of charges, e.g., dc ohmic conduction and (2) the dissipation of energy associated with the rotation or oscillation of dipoles.

An alternative way of expressing the concept of a real dielectric possessing both charging and loss processes is to use a complex dielectric constant to describe the material. The complex dielectric constant k consists of a real part k' which represents the storage and an imaginary part k'' which represents the loss. The following notations are used for the complex dielectric constant interchangeably,

$$k = k^* = \varepsilon_r = \varepsilon^*_r \qquad (1.5)$$

where, $\varepsilon_r^* \equiv \varepsilon_r' - j\varepsilon_r''$ and $k^* \equiv \frac{\varepsilon_r^*}{\varepsilon_0} = k' - ik''$

The real part of permittivity (ε_r') is a measure of how much energy is stored in a material from an externally applied electric field. The imaginary part of permittivity (ε_r'') is called the loss factor and is a measure of how dissipative or lossy is the material to an

external electric field. $\varepsilon_r^{''}$ is always greater than zero and is usually much smaller than $\varepsilon_r^{'}$. The loss factor includes the effects of both dielectric loss and conductivity.

When complex permittivity is drawn as a simple vector diagram as shown in figure 1.2 below, the real and imaginary components are 90° out of phase. The vector sum forms an angle "δ" with the real axis ($\varepsilon_r^{'}$). The relative "lossiness" of a material is the ratio of the energy lost to the energy stored.

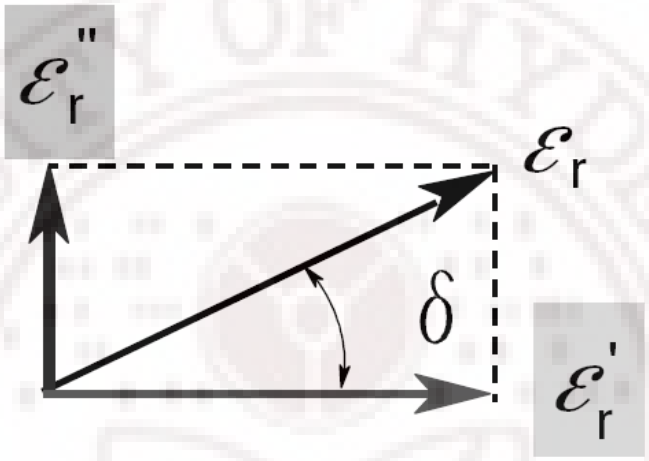

Figure 1.2: Loss tangent *tan (δ)* vector diagram.

The dissipation factor (D), loss tangent, loss angle, or tan δ is defined as the ratio of the imaginary part of the dielectric constant to the real part[5],

$$\tan\delta = \frac{\varepsilon_r^{''}}{\varepsilon_r^{'}} = \frac{k^{''}}{k^{'}} \qquad (1.6)$$

The reciprocal of dissipation factor i.e., $(\tan\delta)^{-1}$ termed as the quality factor (Q factor) of the material is commonly utilized in evaluating the figure of merit (FOM) in high frequency applications.

1.2.1 Frequency dispersion in dielectrics:

According to equation 1.3, introduction of a dielectric material in the parallel plate capacitor increases the ability of the plates to store charge. This is because the dielectric material has an arrangement of charged species that can be displaced in response to an electric field applied across the material[6]. The charges become polarized to compensate for the electric field such that the positive and negative charges move in opposite directions. The overall permittivity of a dielectric material may have a variety of

contribution from several dielectric mechanisms or polarization effects as shown in figure 1.3.

Atomic and electronic mechanisms are relatively weak and usually constant over the microwave region and the variation of permittivity in microwave range is mainly due to dipolar relaxation. The absorption peaks in the infrared region and above is mainly due to atomic and electronic polarizations and in the low frequency range, ε" is dominated by the influence of ion conductivity. Each dielectric mechanism has a characteristic "cutoff frequency". As frequency increases, the slow mechanisms drop out, leaving the faster ones to contribute to ε '. The loss factor (ε ") will correspondingly peak at each critical frequency. The magnitude and "cutoff frequency" of each mechanism is unique for different materials. The frequency dependence of different polarization mechanism in dielectrics is depicted in figure 1.3.

Electronic polarization:

Electronic polarization occurs in neutral atoms due to the displacement of the electron density/ cloud relative to the nucleus in the presence of an electric field. This induced dipole effect occurs in all materials, including air, but is usually very small compared to other polarization mechanisms. This mechanism of polarization is a resonant process which gives rise to a resonance absorption peak in the UV-optical range (10^{15}Hz). The index of refraction of the material depends on this polarization mechanism.

Atomic polarization:

Atomic or ionic polarization occurs at frequencies in the infrared range i.e., about 10^{12}-10^{13} Hz as shown in figure 1.3. Atomic polarization occurs when adjacent positive and negative ions stretch under an applied electric field. Ionic polarization is similar to atomic polarization but involves the shifting of ionic species under the influence of the field. This shift can be considerable and can lead to high values of dielectric constant, up to several thousand. A resonance absorption occurs at a frequency characteristic of the bond strength between the ions. The infrared absorption will be quite broad in the material with several types of ions or if the material has a distribution in bond strengths.

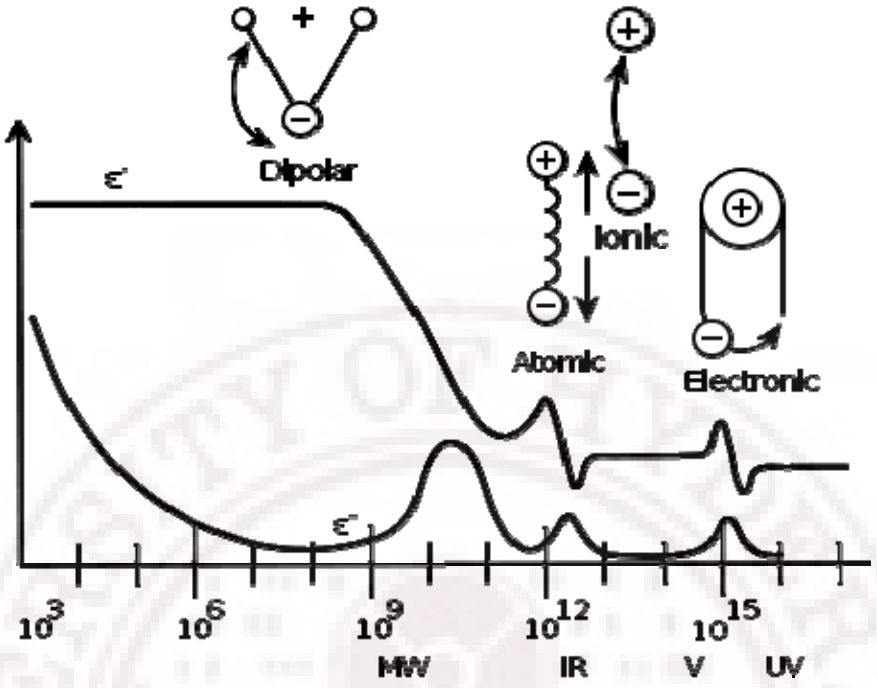

Figure 1.3: Frequency dependence of different polarization mechanisms in dielectrics.

Dipolar polarization:

This polarization mechanism contributes to the dielectric properties of the material in the sub-infrared range. It is also referred to as orientational polarization which involves the perturbation of the thermal motion of ionic or molecular dipoles, producing a net dipolar orientation in the direction of the field applied. This polarization mechanism can be divided into two categories. First, molecules containing a permanent dipole moment may be rotated against an elastic restoring force about an equilibrium position. The second mechanism is an especially important contribution to the room temperature dielectric behavior. It involves the rotation of dipoles between two equivalent equilibrium positions. It is the spontaneous alignment of dipoles in one of the equilibrium positions which gives rise to the nonlinear polarization behavior of ferroelectric materials. It is responsible for dielectric constant values of the order of 10^3 or more in such materials.

1.2.2 Relation between dielectric constant and polarization:

It is important to establish a relationship between the polarization, **P**, in the material and its complex dielectric constant k* in order to obtain a quantitative understanding of its dielectric properties. The total electric displacement field **D**, in a

dielectric caused by some external field **E** is the displacement $\mathbf{D_0}$ in vacuum plus the polarization **P** of the material as given below[7],

$$D = D_0 + P = \varepsilon_o E + P = \varepsilon^* E \qquad (1.7)$$

thus, $$P = E(\varepsilon^* - \varepsilon_0) \qquad (1.8)$$

Since $k^*=\varepsilon^*/\varepsilon_0$, we get,

$$k^* = 1 + \frac{P}{\varepsilon_0 E} \qquad (1.9)$$

and defining the electric susceptibility $\chi \equiv P/\varepsilon_0 E$,

we obtain, $$k^* = 1 + \chi \qquad (1.10)$$

The above two equations provide the relationship between k* and **P**.

In order to obtain a relation between k* and the fundamental polarizability of various charge displacement mechanisms contributing to the total polarization **P**,[8] we have,

$$\mathbf{P} = N_i \alpha_i \mathbf{E}' \qquad (1.11)$$

where, α_i is the polarizability of average dipole moment per unit local field strength $\mathbf{E}'$ and N_i is the number of dipoles of type *i*.

For simple dielectrics such as gases with little molecular interaction, the local field $\mathbf{E}'$ will be same as the external applied field **E**. But, for dielectric solids, the polarization is substantially affected by the surrounding medium. The first to derive the local field contribution by integrating the normal component of the polarized vector over the surface of a spherical cavity in a material was Mossotti and it is given as,

$$E' = E + \frac{P}{3\varepsilon_0} \qquad (1.12)$$

Since, $\mathbf{E}' = \mathbf{P}/N_i\alpha_i$, we have

$$N_i \alpha_i = \frac{P}{E_a + \frac{P}{3\varepsilon_0}} \qquad (1.13)$$

Now substituting equation 1.8 and k* in the above term and on rearranging we get,

$$N_i\alpha_i = \frac{3\varepsilon_0^2(k^*-1)}{\varepsilon_0(k^*-2)} \qquad (1.14)$$

so,

$$\frac{k^*-1}{k^*-2} = \frac{1}{3\varepsilon_0} N_i\alpha_i \qquad (1.15)$$

The above is the classic Clausius-Mossotti equation which gives the relation between k*, N_i and the polaizability α_i.[9] The dielectric constant of a material under atomic and electronic polarization is given as,

$$\frac{k^*-1}{k^*-2} = \frac{1}{3\varepsilon_0}(N_e\alpha_e + N_a\alpha_a) \qquad (1.16)$$

In the optical range where the atomic/ ionic polarization relaxes, the contribution to k* is governed by electronic polarization only and hence the Clausius-Mosotti equation is given as,

$$\frac{k^*-1}{k^*-2} = \frac{1}{3\varepsilon_0}(N_e\alpha_e) \qquad (1.17)$$

1.2.3 Classification of dielectrics:

Based on the Polarization-Electric field (P-E) characteristics, the dielectric materials can be broadly classified in to two classes, they are (i) linear dielectrics and (ii) non-linear dielectrics.

Linear dielectrics:

These are the class of materials whose polarization increases linearly with increase in the external electric filed and decreases to zero when the applied filed is zero (shown in figure 1.4a). These materials neither have a saturation polarization (P_{sat}) nor coercive field (E_c).

Non-linear dielectrics:

Nonlinear dielectrics are essentially crystalline materials which can exhibit very large value of dielectric constant of the order 10^3 or more. Unlike ferroelectric materials non-linear dielectric materials do not have domains, hence do not exhibit hysteresis

characteristic in polarization as shown in figure 1.4b. In ferroelectric materials the electric dipoles are ordered parallel to each other in regions called domains. In the presence of an external electric field these domains can switch from one direction of spontaneous alignment to another giving rise to a very large change in polarization and dielectric constant.

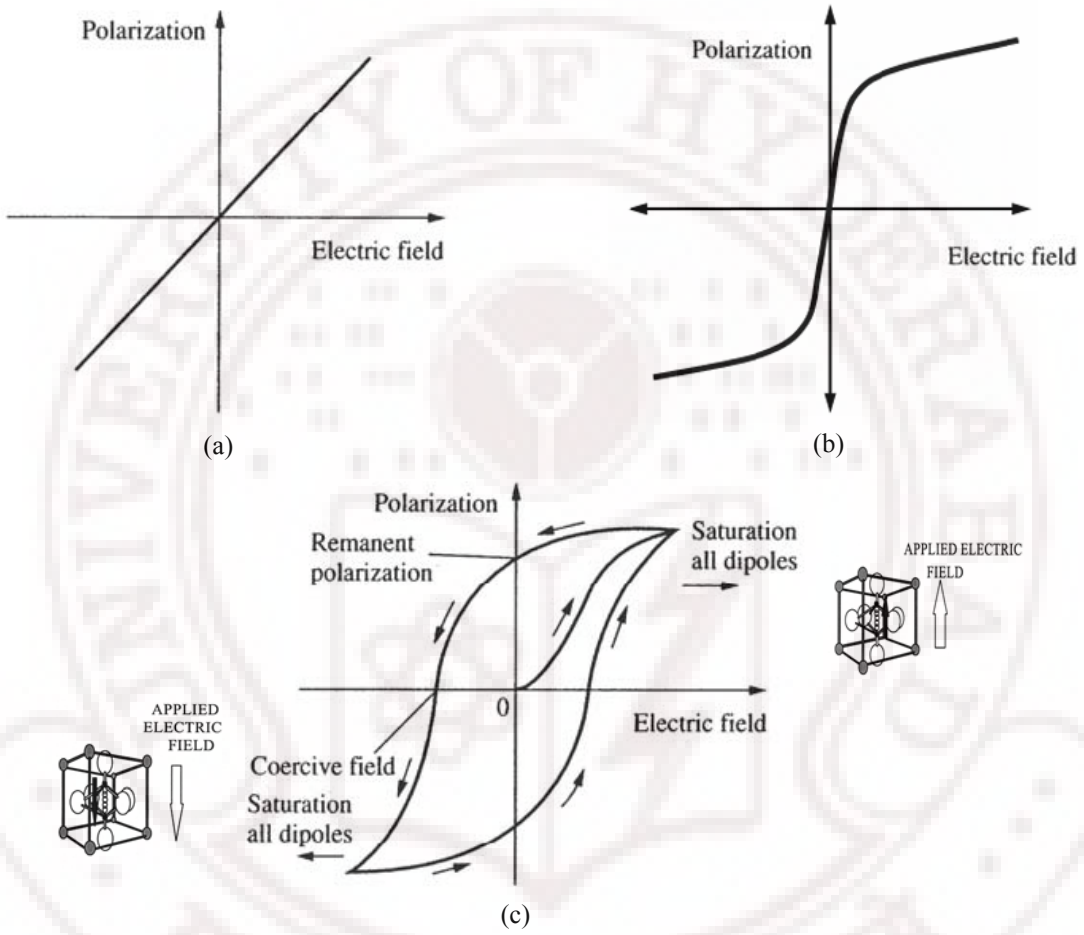

Figure 1.4: Electrical polarization of (a) Linear dielectric, (b) Nonlinear dielectric and (c) Hysteresis loop of ferroelectric material.

The nonlinear electric polarization is analogous to the nonlinear magnetic behavior of ferromagnetic materials[10,11]. The polarization increases as the external electric field is initially increased from zero, as more of the dipoles are lined up in the direction of the field. When the field is strong enough, all dipoles are lined up along the field direction, so the material is said to be in a saturation state giving rise to a saturation polarization (P_{sat}). Until this stage non-linear dielectrics and ferroelectrics behave similarly. Then, when the applied electric field decreases from the saturation point, the

polarization also decreases. However, when the external electric field reaches zero, the polarization in ferroelectrics does not reach zero as shown in figure 1.4c. Ferroelectric material remains to be electrically polarized in the absence of external electric field. The polarization of the material at zero field is called the remnant polarization (P_r). When the direction of the electric field is reversed, the polarization decreases further and when it reaches a certain value, called the coercive field (E_c), the polarization becomes zero. In other words, coercive field is defined as the minimum field requites to reduce the polarization of the material to zero after it has been driven to saturation. The non-linear dielectric behavior is observed in ferroelectric materials above the transition temperature, where the material is in paraelectric state. This phase is characterized by zero values of coercive field, no spontaneous polarization, and the absence of hysteresis. In the paraelectric state the material is centrosymmetric and therefore non-polar yet the non-linear dielectric behavior is still maintained. Since spontaneous polarization and hence domains do not exist in the paraelectric phase, the dielectric losses are reduced. This combination of a high non-linear dielectric response, lack of hysteresis, and low losses make compositions displaying paraelectric behavior at operational temperatures quite attractive for various applications, compared to the pure ferroelectric phase.

1.2.4 Crystallographic considerations of polar effects in crystalline solids:

It is well known that there are 32 point groups or in other words crystal classes. Out of the 32 crystal classes, 11 have center of symmetry and hence cannot possess polar or spontaneous polarization. One of the remaining 21 crystal classes which lack a center of symmetry has a symmetry element (cubic 432) which prevents polar characteristics. One or more polar axes are present in the remaining 20 point groups and hence these exhibit various polar effects such as ***piezoelectricity***, ***pyroelectricity*** and ***ferroelectricity***.

Piezoelectricity is the property of a crystalline material to exhibit electric polarity when brought under a stress, i.e., when a compressive stress is applied, a charge flows in a direction in the measuring circuit. A tensile stress causes charge to flow in the opposite direction. On the other hand, if an electric field is applied, a piezoelectric crystal will stretch or compress depending on the orientation of the field with polarization in the crystal[12]. All of the 20 crystal classes which lack center of symmetry are piezoelectric. However, spontaneous polarization is not guaranteed in a material just because of its

piezoelectric response. For example, in some cases as in quartz, which is a piezoelectric material, the polar directions are arranged in such a way that they self-compensate and cancel out spontaneous polarization and only exhibit a piezoelectric response. Of the 20 piezoelectric crystal classes, 10 posses a unique polar axis i.e., the properties measured one axis is different from the other. As these types of crystals are spontaneously polarized they are termed as polar crystals. The magnitude of polarization depends upon temperature and hence, if there is a change in temperature it imposes an electric charge on the faces perpendicular to the polar axis of the crystal. This is called the pyroelectric effect and each of the 10 classes of the polar crystals are pyroelectric.[13]

All ferroelectric crystals are pyroelectric in nature and have the additional property that an external field can reverse their spontaneous polarization. Hence, ferroelectric is a spontaneously polarized material with reversible polarization. This reversible polarization response manifests itself as a hysteresis loop in the presence of an external electric field which is similar to the hysteresis loop[14] generally observed for ferromagnetic materials.

1.3 Ferroelectricity: An Introduction

Sodium Potassium Tartrate Tetrahydrate ($NaKC_4H_4O_6.4H_2O$) was the first solid, which was recognized to exhibit ferroelectric behavior was observed by Joseph Valasek[15] in 1923. This crystal was discovered in La Rochelle, France in 1655 by Elie Seignette who was an apothecary. Joseph Valasek was the first to establish the analogy between the magnetic properties of ferromagnetism and the dielectric properties of Rochelle salt and hence the name *ferroelectrics*. He also demonstrated the hysteretic nature of the polarization and its marked dependence on temperature.

Ferroelectricity has also been called Seignette electricity, as Seignette or Rochelle Salt (RS) was the first material found to show ferroelectric properties such as a spontaneous polarization on cooling below the Curie point, ferroelectric domains and a ferroelectric hysteresis loop.

In 1935 ferroelectricity in Potassium dihydrogen Phosphate (KH_2PO_4) (KHP) and its sister crystal (KD_2PO_4)(KDP), was observed by Busch and Scherrer[16]. A huge leap in the research on ferroelectric materials came in the 1950's after Wul and Goldman[17] discovered many anomalous dielectric properties in $BaTiO_3$, leading to the widespread

use of barium titanate ($BaTiO_3$) based ceramics in capacitor applications and piezoelectric transducer devices. $BaTiO_3$ belongs to the family of materials called perovskite. $BaTiO_3$ is the prototype of many oxide based ferroelectric perovskites which are characterized by the chemical formula ABO_3. Since the discovery of ferroelectricity in $BaTiO_3$ ceramic, many other ferroelectric ceramics including lead titanate ($PbTiO_3$), lead zirconate titanate (PZT), lead lanthanum zirconate titanate (PLZT), and relaxor ferroelectrics like lead magnesium niobate (PMN) have been developed and utilized for a variety of applications.[11] The biggest use of ferroelectric ceramics have been in the areas such as dielectric ceramics for capacitor applications, ferroelectric thin films for non volatile memories, piezoelectric materials for medical ultrasound imaging and actuators, and electro-optic materials for data storage and displays. In the past few decades, many books and reviews have been written explaining the concepts of ferroelectricity in these materials[18-26].

1.3.1 General properties of ABO_3 type ferroelectric materials:

ABO_3 type ferroelectric materials are non-centrosymmetric, have a unique polar axis and therefore contain electric dipoles that are spontaneously polarized, which can be reversed by application of an electric field in the opposite direction.

In these materials, there exists a particular temperature called the Curie temperature (T_c) where the material undergo a transformation from a higher crystal symmetric paraelectric phase to a lower crystal symmetric ferroelectric phase. The ferroelectric phase shows hysteresis in polarization and is more useful in memory application whereas, the paraelectric phase shows no hysteresis and the polarization changes with the applied field making it useful in DRAM applications. This nature has been summarized in figure 1.5. Dielectric permittivity drastically increases in the vicinity of Curie temperature and above that it decreases according to the well- established Curie-Weiss law as given below[27],

$$\varepsilon = \varepsilon_0\left(1+\frac{C}{T-T_0}\right) \qquad (1.18)$$

where, C is the curie constant.

T_0 is the Curie-Weiss temperature ($T_0 \leq T_c$)

In the ferroelectric state i.e., below T_c, spontaneous polarization occurs. The structural transformation from a higher to lower symmetry causes a change in the cell volume leading to a strain in the system and hence the system exhibits domain structure in order to minimize this strain. Existence of domain structure is a hallmark of ferroelectric materials.

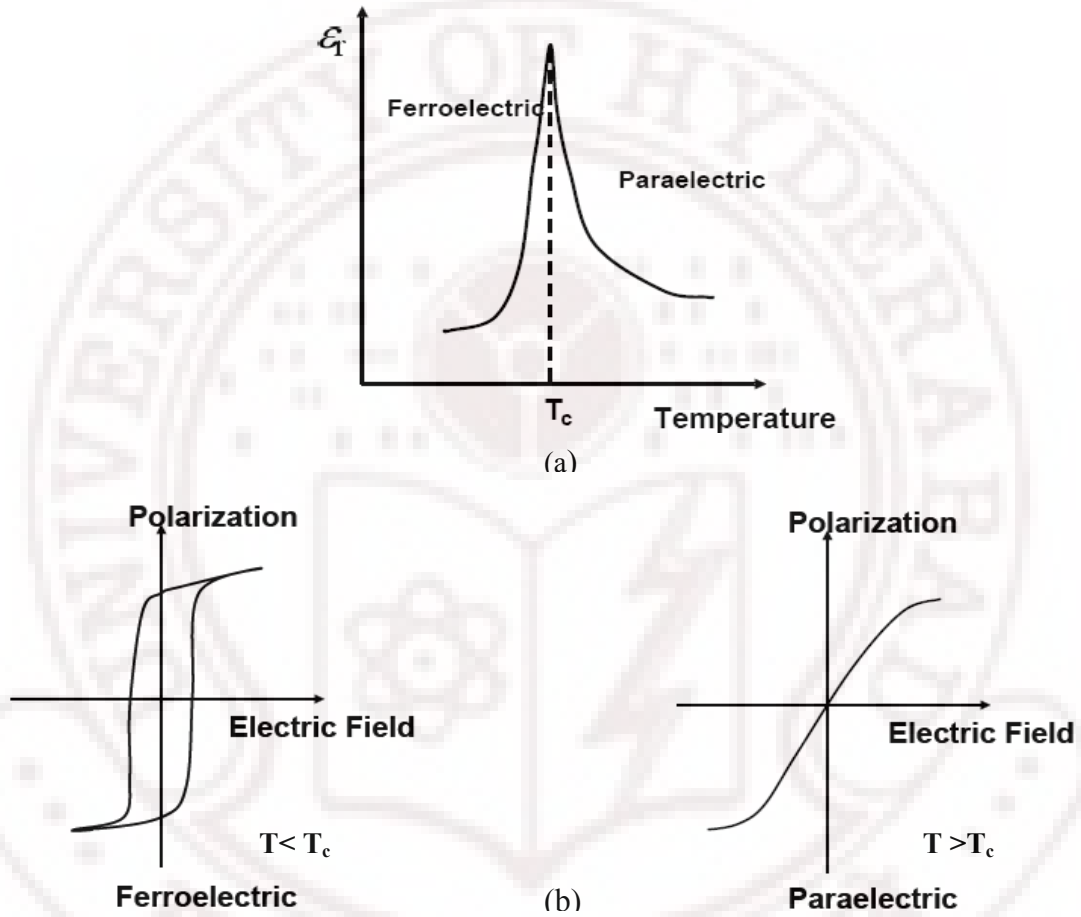

Figure 1.5: (a) Permittivity versus temperature and (b) the corresponding polarization characteristics of phase transition.

Domains contain uniformly aligned electric dipoles and are separated by domain walls across which the spontaneous polarization is discontinuous. The thickness of the domain wall ranges typically from 1-10 lattice parameters across. The 180^o domains are considered to have an abrupt change in the polarization direction and the 90^o domain walls are thicker than that of the 180^o domain walls. The angle between the directions of polarization on either side of the wall is the characteristic of domain walls. A schematic of unpoled ferroelectric material at different length scales is shown in figure 1.6. These

domain walls are generally formed to reduce the energy of the system. The grain size, crystal symmetry, magnitude of spontaneous polarization, defect structure, as well as the sample geometry and the method of preparation contribute to the size and structure of these domains[28,29].

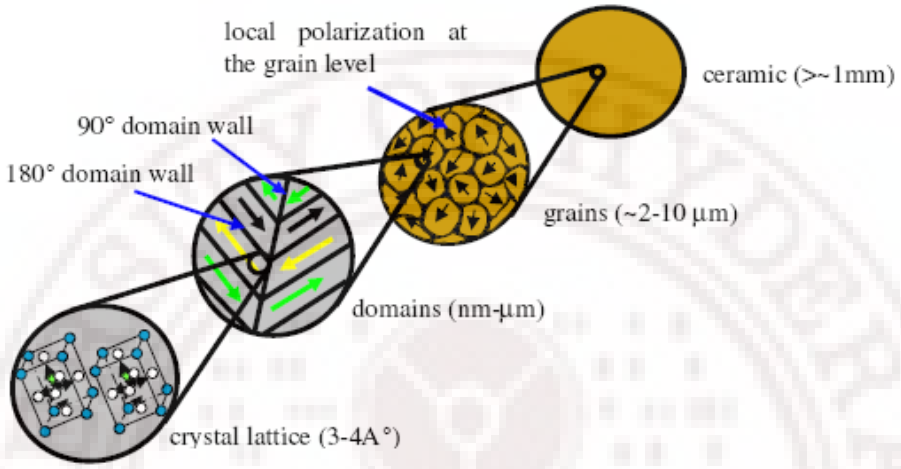

Figure 1.6: Schematic of an unpoled ferroelectric material at different length scales.[30]

1.3.2 Structure of perovskite-Barium Titanate ($BaTiO_3$):

Barium Titanate ($BaTiO_3$) is a ternary compound with the formula ABO_3. The unit cell of $BaTiO_3$ is illustrated in figure 1.7, where Barium (Ba), Titanium (Ti) and oxygen (O) atoms occupy the corner site, body-centered site, and face-centered site, respectively.

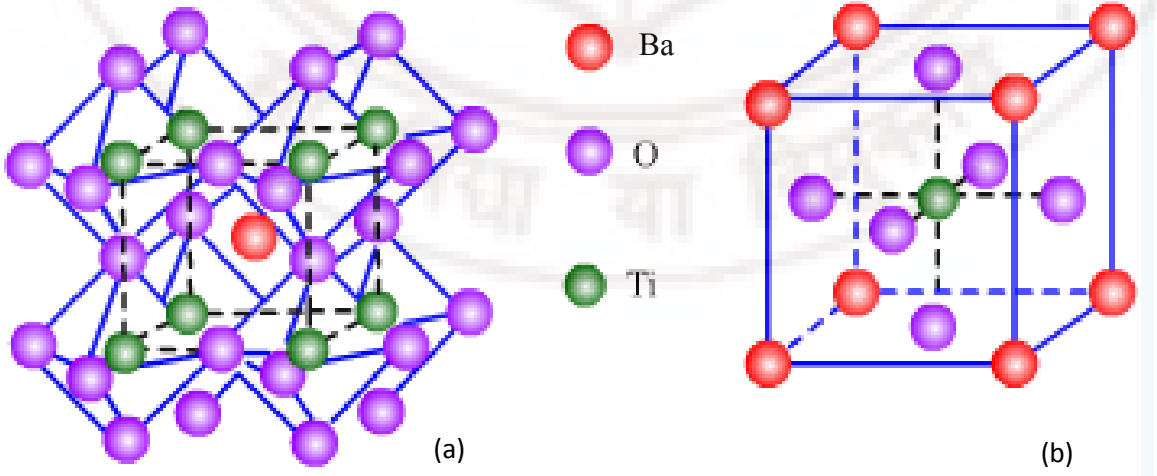

Figure 1.7: a) Three dimensional network of corner sharing octahedra of O^{2-} ions and (b) A cubic ABO_3 ($BaTiO_3$) perovskite-type unit cell.

The Titanium ion of $BaTiO_3$ is surrounded by six oxygen ions in an octahedral configuration. Since a regular TiO_6 octahedron has a center of symmetry, the six Ti-O dipole moments cancel each other in anti-parallel pairs. A net permanent moment of the octahedron can only result by a unilateral displacement of the positively charged Ti^{4+} ion against its surrounding of negatively charged O^{2-} ions. Ferroelectricity requires the coupling of such displacements and the dipole moments associated with the displacement. In the case of $BaTiO_3$, each of the oxygen has to be coupled to only two Ti ions. Consequently, the TiO_6 octahedra in BaTiO3 can be placed in identical orientation, joined at their corners, and fixed in position by Ba ions. This paves the way for an effective additive coupling of net dipole moment of each unit cell. Thus, this is considered as an FCC- derivative structure in which the larger, Ba cation and oxygen together form an FCC lattice while the smaller Ti cation occupies the octahedral interstitial sites in the FCC array. The large size of the Ba ion increases the size of the unit cell of the FCC BaO. Consequently, there are minimum energy positions for Ti atom which are off-centered and can therefore give rise to permanent electric dipoles.

In the ferroelectric phase i.e., $T<T_c$, the position of the Ti ion and the octahedral structure changes from cubic to tetragonal symmetry with Ti ion in an off-centered position corresponding to a permanent dipole moment. These dipoles are ordered leading to a domain structure with a net spontaneous polarization with these domains. As the temperature rises above T_c i.e., $T>T_c$ the thermal energy is sufficient enough to allow the Ti ion to move randomly from one position to another, so there is no fixed asymmetry. The open octahedral site allows the Ti atom to develop a large dipole moment in an applied electric field, but there is no spontaneous alignment of dipoles. In this symmetric configuration the material is said to be paraelectric.

Barium Titanate was extensively employed as a piezoelectric material for microphones and other transducers when in 1945 the first working transducer using $BaTiO_3$ was successfully demonstrated by R. B. Gary[31]. As a piezoelectric material, it was largely replaced by lead zirconate titanate (PZT) since 1950s. The pyroelectric properties of barium titanate are used in some types of un-cooled sensors for thermal cameras and detectors, the ferroelectric properties are used for non-volatile ferroelectric random-access memories (FRAM), the large value of static dielectric constant is used for dynamic random access memories (DRAM) and MOSFETS. $BaTiO_3$ (BTO) has been

widely used as the dielectric material for high density, multi-layer ceramic capacitors (MLCC) and in the past decade, these materials have generated renewed interest for tunable microwave and frequency agile devices.

Rearrangement of the microscopic dipoles in a ferroelectric material on application of an external bias causes a change in the value of their dielectric constant, which is termed as "tunability".

Apart from high value of dielectric tunability, the device utilizing this material also requires low value of loss tangent (tanδ). Hence, most of these ferroelectrics are used in their paraelectric phase, i.e above the Curie temperature (T_c) because it has been well established that the absence of domains in the paraelectric phase results in lower loss tangent when compared to that in the ferroelectric phase. Therefore, exploring the material in the paraelectric phase is more suitable for tunable microwave applications[32]. For practical room temperature device applications it is essential to maneuver the T_c of $BaTiO_3$. It has been well documented that, by partially replacing Barium with Strontium (Sr) atoms the T_c can be modulated[33-35].

1.3.3 Introduction to Barium Strontium Titanate:

Barium Strontium Titanate (BST) with the general formula $(Ba_{1-x}, Sr_x)TiO_3$ $[0 \leq x \leq 1]$ is a solid solution of $BaTiO_3$(BTO) and $SrTiO_3$ (STO). It is well known that $BaTiO_3$ is ferroelectric at room temperature where as $SrTiO_3$ is an incipient ferroelectric or quantum paraelectric[36].

BST belong to the perovskite family of materials with the general formula ABO_3. The structure of BST is similar to that of $BaTiO_3$. In BST, the A site occupied by Ba atoms and Sr atoms. The Ba^{2+} and Sr^{2+} ions occupy the angular point seats of the unit cell corners while Ti^{4+} occupies the center of the unit cell. The O^{2-} ions occupy the face centers of the unit cell.

BST can either be in tetragonal or cubic symmetry, depending upon the Ba: Sr ratio and temperature. At temperatures above the phase transition temperature, T_c, the material is in cubic paraelectric state while below T_c the material exhibit tetragonal ferroelectric state. The lattice parameter and the T_c depend on the Ba:Sr ratio. Sr can replace Ba over the entire range of composition to form a continuous solid solution,

leading to a smoothly varying T_c and lattice parameter. For room temperature applications BST with Ba:Sr ratio of 50:50 [$(Ba_{0.5},Sr_{0.5})TiO_3$, BST5] has been studied extensively and is the composition of interest in the present study. As the T_c of this composition is just below room temperature, the material remains in the paraelectric state. However, the properties of thin-films compared to their bulk counterpart are invariably different. In particular, shifted phase transition temperatures and lowering of dielectric constant have been reported[37].

In bulk BST ceramic, the relation between the barium content and T_c is given as $T_c = 371x - 241$, x is the Ba content. It has been suggested that the T_c drops by 3.4^o for every mole % addition of Sr in the $BaTiO_3$ matrix[38]. According to Tahan et, al.[39] this relation in BST in thin film form is given as $T_c = 185.23x - 176.04$. "Clamping effect" of the substrate on the thin film has been believed to cause the difference in T_c between bulk ceramic and thin films of BST.

The large interest in BST thin films is due to their field dependent dielectric permittivity. The variation in capacitance with an applied bias is not a property exclusive to thin film BST, but an intrinsic property of the material's low frequency optical phonons[40]. Typically, materials with large static dielectric constant (of the order of 10^3) have a low frequency transverse optical (TO) phonon or soft mode. Recently far infrared (FIR) ellipsometry and low-frequency dielectric measurements in strontium titanate thin films revealed that the dramatic reduction of the dielectric constant is a consequence of the soft-mode hardening[41]. It should be noted that the soft-mode temperature dependence in these thin films usually deviates from the values known for bulk materials.[42,43] From this point of view, it has been widely accepted that the lattice dynamical properties in particular, the soft mode behavior is of great importance in understanding the characteristics of these thin films[44]. Lattice dynamics is of central importance for the mechanism of ferroelectricity[45].

1.3.4 The concept of Soft Mode:

The classic and the most studied ferroelectric material, both from the theoretical and experimental point of view is barium titanate (BTO) and strontium titanate (STO).[23] The crystal structure of STO and BTO in the paraelectric cubic phase is similar. Explicit first-principles calculations by Weyrich et. al.[46] illustrates that the differences between

BTO and STO are to some extent volume effects, which are shown by a dilatation of STO unit cell to the volume of BTO or the compression of BTO unit cell to the volume of STO. As explained earlier, in the case of BST the Ba^{2+} and Sr^{2+} ion occupy the angular point sites of the unit cell corners while O^{2-} occupies the face centers of the unit cell. The Ti^{4+} occupying the center of the unit cell is surrounded by six oxygen ions and thus, Ti^{4+} forms a TiO_6 octahedral configuration with the surrounding O^{2-} ions. The characteristic facet of ferroelectrics, i.e. the spontaneous polarization, arises from a displacement of the center of positive charge with respect to the center of negative charge. This displacement, such as that of the Ti^{4+} ion with respect to the oxygen cage in the TiO_6 octahedra in perovskite structure, involves the same ionic movement as a zone-center transverse optical (TO) phonon mode, or the so called "soft mode".

Due to the interplay between the local restoring force and the long range dipole interaction, the soft mode has a low frequency. At 24^{o}C, BTO and STO have a TO mode of 1.2 THz and 2.7 THz respectively. The vibrational frequency of the lowest optical mode (the soft mode) approaches zero[47,48] as the temperature approaches the Curie temperature T_c ($\omega_{TO} \rightarrow 0$ as $T \rightarrow T_c$). The soft mode is frozen in the material, which leads to a ferroelectric phase transition [45].

The soft-mode theory, due to Cochran[45] and Anderson[49], has been proven by many lattice dynamics studies. The high value of dielectric constant in the paraelectric phase of ferroelectric material can also be explained using the soft-mode behavior.[50]

The Lyddane-Sachs-Teller (LST) relation connecting the macroscopic static $\varepsilon(0)$ and high frequency $\varepsilon(\infty)$ dielectric constants ε_∞ to the microscopic parameter i.e. the eigen-frequencies, ω_{LOj} and ω_{TOj}, of the longitudinal (LO) and transverse (TO) optical phonon modes for a crystal with N infrared-active optical modes is given as,

$$\frac{\varepsilon_0}{\varepsilon_\infty} = \prod_j^N \frac{\omega_{LOj}^2}{\omega_{TOj}^2} \qquad (1.19)$$

It is generally found that the eigen-frequencies of the higher optical modes exhibit no sizeable variation with temperature. In bulk materials, the LST relation has been proven experimentally, where the decrease in the soft-mode frequency as the temperature approaches T_c will cause a dramatic increase in $\varepsilon(0)$.

The zone-center frequency of the soft mode falls to zero when a ferroelectric material is cooled towards its T_c, given as,

$$\omega_{TO\,1}(T) = Const \times |T - T_c|^{\frac{1}{2}} \qquad (1.20)$$

As, we have seen earlier, the eigen-frequencies of other phonons are almost constant. According to the LST relation, the temperature dependence of the soft-mode frequency and the static dielectric constant are connected by,

$$\varepsilon_0(T) \propto \omega_{TO\,1}^{-2}(T) \qquad (1.21)$$

The above equation is consistent with the Curie-Weiss law for the temperature dependence of the static dielectric constant which is shown below:

$$\varepsilon_0(T) = const \times |T - T_c|^{-1} \qquad (1.22)$$

The dielectric nonlinearity i.e. the electric field dependence of dielectric constant is also based on the soft-mode behavior. The dielectric nonlinearity in these materials is due to the field-induced hardening of the soft mode frequency[51], which arises from the anharmonic restoring forces on the Ti ion when it is displaced from its equilibrium position[52]. According to the LST relation, a higher or in other words the field induced increase in the soft-mode frequency will lead to a decrease in the static dielectric constant. This is termed as "Tunability".

1.3.5 Tunability:

Tunability is defined as the relative change in permittivity at zero bias to the permittivity at some non-zero bias value.[53]

$$Tunability \quad (\%) = \frac{\varepsilon(0) - \varepsilon(E)}{\varepsilon(0)} \times 100 \qquad (1.23)$$

where ε(0) and ε(E) are the dielectric permittivity values at zero and non-zero electric\ bias field respectively.

Tunable dielectric materials are those which have a voltage-dependent dielectric permittivity. Majority of the applications based on tunable dielectrics falls in the Radio Frequency (RF, ranging from 20 kHz to 300 MHz) and microwave (MW, ranging from 300MHz to 300GHz) circuits.

The dielectric loss tangent (tan δ) or the quality factor (*Q* factor, defined as 1/ tanδ) of these materials is also dependent on the applied dc electric field. A major class of materials that are being considered for tunable applications is ferroelectric materials. Experiments show that a ferroelectric material with larger tunability usually has higher loss tangent. The loss tangent of the material is an important factor affecting the performances of electric circuit, in the development of electrically tunable devices. Usually there is a tradeoff between tunability and loss tangent.[54] For practical device application, one has to carefully choose the material with optimal tradeoff between these two parameters. This can be found by using the stricture known as figure of merit (FOM), which is given as,

$$\text{FOM}=\text{Tunability}/\text{ Loss Tangent} \qquad (1.24)$$

Usually for higher values of FOM, the ferroelectric materials are used in the paraelectric state i.e. very close to T_c, where the material has high dielectric permittivity and low loss tangent. A typical Capacitance – Voltage (C-V) plot of ferroelectric material is shown in figure 1.8a, where it displays the characteristic "butterfly loop". The maxima in the CV plot show two distinct peaks illustrating a hysteresis behavior.[31] On the other hand, above Curie temperature i.e., in paraelectric state, the material is non-polar and has higher crystal symmetry. In this phase due to the lack of hysteretic behavior, no "butterfly loop" is observed as shown in figure 1.8b.

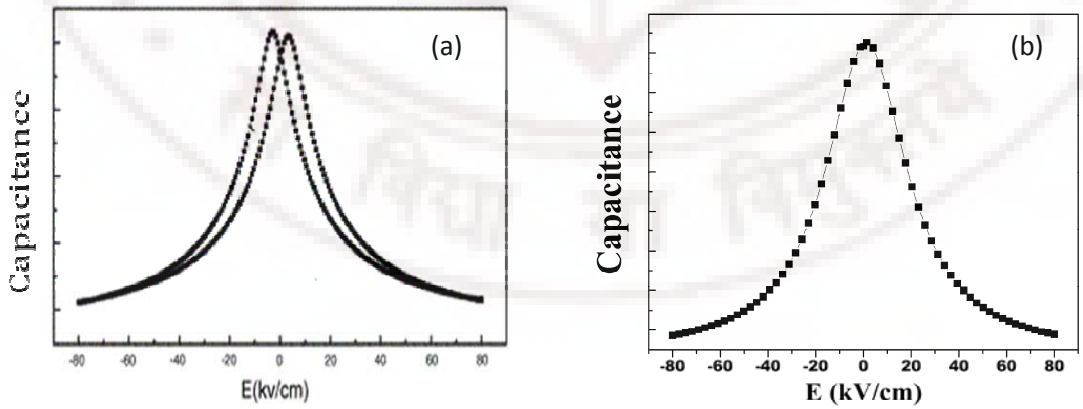

Figure 1.8: Typical C-V plot of (a) ferroelectric material and (b) paraelectric material.

1.4 Need for Tunable dielectrics:

Tunable devices are widely required in a range of applications from modern telecommunication systems to satellite services. Frequency agile application demands the use of low loss and highly tunable devices to allow multi-band and multi-mode communication system. These requirements impose significant challenges on the current tunable circuit technologies. Phase shifters, tunable resonators, filters and delay lines are some of the important tunable passive devices[55,56].

All frequency agile devices comprise of unit structures which are resonant systems and the resonant frequency (f_0) of any system can be reduced to an equivalent capacitance (C, units in F, Farad) and inductance (L, Unit in H, Henry). The resonant frequency (f_0) is inversely proportional to the square root of the product of LC, which is mathematically expressed as,

$$f_0 = \frac{1}{2\pi\sqrt{LC}} \qquad (1.25)$$

From a physical point of view, changing either the L or C will accomplish frequency agility. In general, methods of changing the capacitance are much more feasible than those for changing the inductance. Using tunable dielectric material will be sufficient in achieving variable capacitance.

The integration of ferroelectric materials (FE) into tunable microwave devices has been investigated since the early 1960s. [53,57] Due to difficulty in achieving low capacitance with desired tunability at moderate dc voltage levels, the original idea of utilizing bulk ferroelectric materials in tunable microwave devices was not very promising. As a result, extensive work was directed towards utilizing these materials in thin film form. Realization of FE thin films in tunable microwave devices will result in dramatic miniaturization and reduction in manufacturing cost. As a result of the recent advancement in thin film processing technology, the quality of the FE thin films has improved to a point where the properties can be fine tuned from the device perspective and the integration with the present semiconductor technology is realistic.

Tunable circuits such as phase shifters, filters, antennas, delay lines and matching networks based on thin films of FE are very attractive for wireless communication

systems as they offer the flexibility to adapt to changes in various operating conditions such as frequency, RF drive level or impedance environment. Implementing several separate transceiver circuits in a single hardware device increases the component count and hence the overall cost[58]. Therefore in terms of RF front end circuitry, significant cost saving can be achieved by using electronically tunable components. In this scenario, a single tunable component is employed to replace several fixed components. For example, a band pass filter (BPF) with a tunable pass band could replace several fixed filters or a tunable delay line could replace a set of fixed delay lines in the beam-forming network of a phased array antenna[59].

1.4.1 Enabling technologies for frequency- agility:

Various technologies including ferrites, mechanical varactors, semiconductor varactors, micro-electro-mechanical systems (MEMS) and ferroelectric (FE) varactors are being considered for frequency-agile devices. It is very important to understand these competing technologies to realize and appreciate the capabilities and potential of using FE varactors as frequency-agile devices. The choice of technology depends on the application, system specification, cost, integration with other technologies and reliability. Usually two or more of these technologies may be required to work in a complementary manner to achieve the required system performance.

Reggia and Spencer[60] were the first to report electronically variable ferrite phase shifter in 1957.

A ferrite based phase shifter has the advantages of low cost, and large power handling capability. However, they are slow (switching time, few μs ~ tens of μs) and consume high powers. In addition, ferrite based circuits have large size and mass which do not offer ease of monolithic integration with microstrip, stripline and finline circuits.

The mechanical varactors e.g., the rotary vane adjustable waveguide phase shifter based on mechanical tuning was the earliest form of tunable circuits. It was proposed by Fox in 1947[61]. It has been used since early days of radio for channel selection at the RF front-end. They offer high power handling capability, have extremely low insertion loss, are inexpensive and are easy to fabricate. However, their large size and weight prevents their use in all but very specialized applications. They also have rather low tuning speed.

Semiconductor varactors were introduced in tunable circuits for the first time in early 1960s and are the dominant devices for imparting frequency-agility[62,63]. The operation of semiconductor varactor is based on the principle of change in the depletion width when a reverse bias is applied to a p-n junction diode. The depletion width can be thought of as the distance between the two plates of an equivalent parallel plate capacitor. The depletion width increases with increasing reverse bias and hence the capacitance decreases with bias. They have high tuning ratio (as large as 15:1 for under 20 V bias), very fast tuning speed (<1μs) and small dimensions (typically in μms). They can be easily integrated with monolithic microwave integrated circuits (MMICs). Various frequency-agile devices such as tunable filters, matching networks, phase shifters, and antennas have been reported using semiconductor varactors. It is also the varactor of choice for most integrated and on-chip VCOs. In order to realize high tunability, the p-n junction should be lightly doped so that the depletion width is significantly changed with small change in the applied voltage. However, since the undepleted portion of the semiconductor layer also acts as one of the electrodes, lightly doped layers are resistive and contribute to high loss at microwave (MW) frequencies. Semiconductor varactors have *Q* factor in the range of 20–60 up to 10 GHz. Beyond that, the *Q* factor degrades dramatically. GaAs varactors offer higher *Q* factors than their silicon counterparts but they have a higher flicker noise due to increased mobility and have poor power handling capability. It is thus highly difficult to design semiconductor varactors which simultaneously meet the requirement of high Q and good power handling capabilities in the GHz frequency range.

Mircoelectromechanical systems or MEMS switch as a varactor at microwave frequencies was first demonstrated in early 1990s by Larson[64]. They are essentially miniature incarnations of mechanical switches fabricated at the micron scale using conventional photolithography techniques. In MEMS, the tunability is achieved by the physical movement of a component popularly known as the diaphragm which changes the capacitance of the device[65].

The movement of the diaphragm can be achieved by piezoelectric, electrostrictive, electrostatic or thermal effects[66]. MEMS- based varactors and switches are very small in size (typically in μms) and have been used to construct tunable filters, phase shifters and matching networks. MEMS switches have been used as low loss RF switches in multi-band communication devices to replace GaAs, MOS or PIN diode based switches. They

have low insertion loss at RF and MW frequencies and can handle high power levels. Despite all the advantages, the widespread use of MEMS has been impeded by their slow switching speed (2-100μs), high bias voltage (50-100V) and high cost of packaging. MEMS-based devices typically require stringent hermetically sealed packaging and this significantly increases the cost[67-69].

Ferroelectric varactors[70-77] utilizes the fact that the dielectric constant is a function of the applied electric field[78]. When a dc bias is applied to a FE film, the dielectric constant can be decreased by nearly an order of magnitude, thus changing the high-frequency wavelength in the microwave devices. FE varactor technology offers faster tuning speed, can handle more power when compared to the semiconductor varactors, have low loss at the RF and microwave frequencies and have low power consumption. Moreover, they are small sized and light-weighted. In this technology, the ferroelectric thin film can be either used in parallel plate or interdigitated configuration, both of which offer substantial integration capabilities in microelectronic circuits. These ferroelectric thin films are generally used in the paraelectric phase above the Curie temperature (T_c) where hysteresis is absent and losses are lower.

The most popular perovskite-type ferroelectric material which is used as dielectric for fabricating tunable capacitors is Barium Strontium Titanate (BST). BST, which offers high tunability, low loss and integration with other technologies, is highly promising. Both parallel plate and interdigitated configuration of BST varactors have been used to demonstrate tunable phase shifters, filters, matching networks and delay lines. When compared to a semiconductor varactor, ferroelectric varactor technology offer higher quality factor (*Q* factor) in the gigahertz range of frequencies[32].

1.5 BST device technology: An overview

Various device technologies have employed BST in either bulk, thick or thin film form. In the present context BST bulk, refers to the BST samples with thickness in the range of 500-2000μm, BST thick films are those with thickness > 1 μm, whereas BST thin films are those with thickness <1μm. BST in the bulk form can be used as lens antennas for beam steering applications but the biggest drawback of bulk BST is the requirement of very high tuning voltages (0.4–2 kV or more) that are typically required to

achieve a desired tuning range. This limits their use in all but very specialized applications where the availability of high voltages is not of primary concern.

BST thick films requiring substantially lower tuning voltages and are considerably more practical for device applications. These films can be prepared by screen-printing technology and it also affords integration with Low-Temperature Co-fired Ceramic (LTCC). The thickness usually ranges from 2–30 μm and tuning voltages required falls in a range between 100–500 V. Tunable filters, phase shifters and matching networks have been demonstrated using thick films of BST. Jackoby et al.[79] has reported the preparation of thick films of BST on low cost ceramic alumina substrates by screen printing technology. They reported the loss tangent and permittivity to be 0.01 and 450 respectively at zero bias. The tunability obtained was more than 60% for an applied field of 20 V/μm. A reflection type phase shifter at 2.2–2.6 GHz with an average differential phase shift of 48^o and insertion loss of 2.4 dB was demonstrated by Hu et al.[80] They used a 25 μm thick BST layer and 8 μm thick silver paste for the transmission line. The figure of merit (FOM) was 54 deg/dB at 2 GHz. The tuning voltage was 100 V.

Other researchers have also reported tunable filters and matching networks using BST thick-film where the material showed strong frequency dispersion. The results, though promising, are not as good as that obtained with thin-film BST. The most important difference is that thin-film BST has been shown to have non-dispersive behavior up to 40 GHz[81]. Furthermore, for thick films the tunability for an applied voltage is lower than that of thin-film. Even though the dielectric loss is one order of magnitude lower for bulk BST, BST thin-film have been very attractive for tunable microwave devices due to the low tuning voltages, typically between 2 and 100 V, depending on the thin-film composition, film thickness, and capacitor configuration.

There are basically two configurations of BST based capacitors; they are parallel plate (vertical) capacitor and interdigitated (planar) capacitor configuration.

In parallel plate capacitor (PPC), otherwise known as M-I-M (Metal- Insulator-Metal) structure the thin film is sandwiched between two metallic layers and in interdigitated capacitor (IDC) or otherwise known as interdigitated electrode (IDE) structure, the thin film is deposited directly on a substrate and the metal lines forming the

interdigitated structure is deposited over the surface of the film. The device schematics for both configurations are shown in figure 1.9.

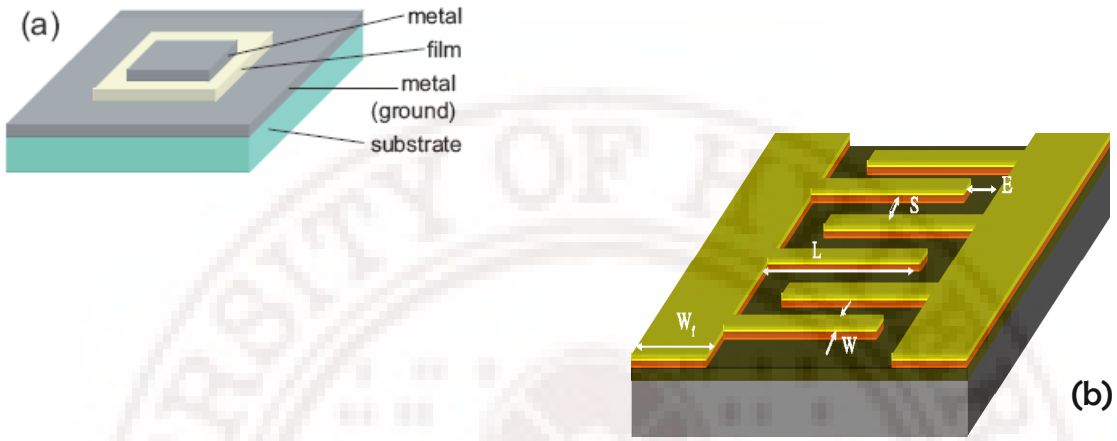

Figure 1.9: Representative 3D layout of BST based thin film (a) parallel plate and (b) interdigitated varactors.

Interdigitated devices requires only a single step metallization compared to their vertical MIM counterpart and hence are simpler to fabricate and integrate into circuits, but these IDE structures suffer from reduced tunability (due to large fringing electric field in the air) and higher control voltages. Having smaller spacing between the fingers can further increase available tunability at lower voltages. Typical operating voltages for interdigital capacitors are in the range of 100 V's with a typical tunability of 2:1. The parallel plate capacitors, on the other hand, can be operated with much lower bias voltages, (<20V) making them attractive for most of the microwave and millimeter-wave applications[82]. For parallel plate capacitors, BST films are deposited on a bottom electrode and then the top electrode is deposited on BST film creating metal-insulator-metal (MIM) structures. The distance between the electrodes is basically the BST film thickness which will be much smaller than the spacing in the interdigital structures. This is the reason why the control voltage typically scales with the film thickness. In vertical structures, the electric fields are better confined in the film and hence these structures offer a higher tunability when compared to interdigitated structures. The control voltage or power handling capacity is easily manipulated through control of the film thickness, but the integration of bottom electrodes and other structures require more meticulous

fabrication process. Parallel plate capacitors offer more flexibility in many circuit applications because large tunability can be realized at relatively lower bias voltages, which is one of the requirements of electronic systems which are very stringent in terms of voltage requirement. And thus tunable BST varactors remain the main candidate for the customer end applications such as wireless communication industry. Hence, many research groups have carried out extensive research in implementing BST thin films varactors in a number of tunable circuits and devices like voltage controlled oscillator (VCO), tunable filters, phase shifters, tunable matching networks etc. Victor et.al.[83,84] described the implementation of VCO using BST for the first time. This VCO demonstrated better noise performance than junction diode varactors with high power handling capability.

Variable phase shifters have been implemented in integrated form using MIM BST varactors[85]. The first phase shifter based on bulk BST used in the microstripline circuits was reported by Flaviis in 1997.[86] A phase sifter in the Ku/Ka band using both vertical (parallel plate) and planar (IDC) varactors on sapphire and glass substrates were reported by V. Acikel et al.[87] The phase shifter based on parallel plate varactors showed a phase shift of 180^o with 4 dB of insertion loss at 30 GHz. The tuning voltage was 30 V, while the phase shifter based on the IDC varactor showed a tuning of 460^o at 8 GHz with 8.8 dB of loss. Both circuits showed a promising FOM of 60 deg/dB at 10 GHz. Liu et al.[88] have demonstrated loaded-line phase shifters on sapphire substrates. Using a parallel plate capacitor configuration and less than 20 V tuning voltage they reported figures-of-merit of 93 deg/dB and 87 deg/dB at 6.3 and 8.5 GHz respectively. Kuylenstierna et al.[89,90] have reported true-time delay lines using laser ablated BST thin film parallel plate varactors on high resistivity silicon. They used gold metallization in a coplanar strip loaded line configuration for circuit fabrication. The absolute group delay was reported to be 70 ps at room temperature and tunable by up to 20% under 20 V bias voltage. The insertion loss was less than 3.5 dB at 20 GHz whereas, at 145 K the group delay increased to 100 ps and the tunability to 50% under similar bias conditions. At 7 GHz, the insertion loss was 3 dB.

Kim et al.[91] reported a silicon based phase shifter using high resistivity silicon substrates and TiO_2 as buffer layer for BST thin films deposited by PLD. Phase shift of 98^o at 17 GHz with an applied field of 50 V was reported. Though the FOM was quite

low it was reported to be a promising technology that will lead to monolithic integration with low cost. S. Lee et al.[92] demonstrated an X-band loaded transmission line type phase shifter by using BST thin films. The phase shifter consisted of coplanar waveguide (CPW) lines that are periodically loaded with voltage tunable BST varactors. The voltage tunable BST varactors showed a large dielectric tunability of 69% and a quality factor of 29.5 at a frequency of 10 GHz. Moon et al.[93] fabricated a phased array antenna using four element ferroelectric phase shifters with CPW transmission line structures based on BST thin films. This X-band phased array antenna system with the ferroelectric BST phase shifters was capable of having a beam steering of 15° in either direction.

Recently Sullivan et al.[94] reported BST phase shifter with over 20 dB improvement in isolation over a 2 MHz bandwidth. Nagra et al.[95] reported optimization techniques for loaded line phase shifters. They reported a 0–360 degree phase shift at 20 GHz with 4.2 dB of insertion loss.

Tunable matching networks are another area where BST has found good use. York et.al.[96] demonstrated the use of BST in integrated circuits on sapphire substrate to implement a tunable antenna in 450-500MHz. Katta et.al.[97] demonstrated the implementation of a tunable matching network for improving linearity performance of a power amplifier. Scheele et.al.[98] discussed the general behavior of BST varactor in tunable matching networks.

Chen et al.[99] reported a BST parallel plate varactor based tunable matching network at 900 and 450 MHz on sapphire substrates. The impedance transformer network was capable of transforming a 50 Ω impedance to a range of values between 13–29 Ω at 900 MHz. Using a slightly modified network, antenna matching was obtained over 425–490 MHz with approximately 1.5 dB of insertion loss.

BST parallel plate capacitors based tunable lowpass and bandpass filters in the VHF range was reported by Tombak et al.[100]. Nath et. al.[101] reported a tunable third order combline band pass filter using BST varactors fabricated on sapphire substrates. The application of a 0-200V DC bias varied the center frequency of the filter from 2.44 to 2.88 GHz (16% tuning) with 1 dB bandwidth of 400 MHz. The insertion loss varied from 5.1 dB at zero bias to 3.3 dB at full bias.

A 3-pole tunable combline bandpass filter using BST thin-film and LTCC technology was reported by Rahman et al.[102] The filter was targeted at the commercial cellphone market. The filter tuned from 1656 MHz to 1983 MHz with an average insertion loss of 4.3 dB. Noren et al.[103] reported a two-pole bandpass filter with 35% center frequency tuning from 910 to 1230 MHz for a 50% reduction in capacitance. The insertion loss was in the range of 6–7 dB over the tuning range.

Recently, Varanasi et al.[104] reported a tunability value of 76% at 20 GHz in parallel plate varactor shunt switches designed for microwave applications.

The two parameters that need to be optimized in BST thin films for microwave applications are the capacitance tunability and the *Q*-factor [the reciprocal of the loss tangent, $Q = (\tan\delta)^{-1}$], which should both be as high as possible. Many factors related to the device fabrication, including the thin film deposition process; processing and post-processing conditions choice of substrate material and metallization among many others affect the microwave properties of BST varactors. Therefore, it is very important to understand the relationship between the material and microwave properties of the devices, in order to optimize the performance of BST-based microwave components.

Thin film (Ba, Sr)TiO_3 (BST) has been studied extensively because of its high dielectric constant (>500) making them attractive materials for the fabrication of capacitors to be integrated in a range of electronic circuits. However, high permittivity can only be obtained in the crystalline phase, which usually requires high deposition or annealing temperatures (≥500^{o}C). The crystallinity and hence the dielectric constant of these films are widely dependant on the deposition/ annealing temperature. This is a serious limitation for the integration of these materials in packages that cannot sustain high temperatures (organic boards and other plastic packages). On the contrary, the amorphous state of BST can be readily obtained at low deposition temperatures (room temperature).

Crystallinity of BST thin films may impact their *I–V* characteristics significantly. Zhu et al.[105] demonstrated typical room temperature *I–V* characteristics of 125-nm-thick sol-gel derived BST thin films annealed at various temperatures. An excellent *I–V* characteristic of low leakage current for high applied field was achieved for amorphous BST thin films annealed at 475^{o}C, giving a typical electrical insulating behavior of

amorphous ferroelectric materials. Further increase in the annealing temperature to 600 and 650^{o}C causes polycrystalline grains and exhibit higher leakage currents for a much lower electric field.

Similar results were reported by Chen et al.[106,107] for BST films deposited by RF magnetron co-sputtering. A minimum leakage current was realized for the amorphous films deposited just below their crystallization temperature. Further increase in the deposition temperature resulted in polycrystalline films with higher leakage current and lower breakdown field. Zhu et al. studied the amorphous BST sensor for hydrogen gas detection. Kim et al.[108] investigated the dielectric properties of the amorphous BST. Melo et al.[109] demonstrated room temperature photoluminescence of amorphous BST doped with chromium.

Lyahovitskaya et al.[110] reported significant pyroelectric and piezoelectric effect (10 % of $BaTiO_3$ bulk) in RF sputtered $BaTiO_3$ thin films, which were annealed by pulling through a temperature gradient with peak temperature of 600°C. Though these films show that the structure is polar (through pyroelectric and piezoelectric effect), they were not in crystalline phase according to x-ray (XRD) and electron diffraction (ED) techniques. They found that this phase of the material is thermally stable up to 800°C.

Although the dielectric constant of amorphous films is much lower than their crystalline counterparts, it remains comparable to most other traditional oxides (such as HfO_2, ZrO_2, Ta_2O_5, Y_2O_3, Al_2O_3 etc. for instance) that are prepared at much higher temperatures. The dielectric constant of various traditional oxides is given in table 1.1.

Amorphous BST films also have excellent optical properties on par with most of the oxide thin films used in various optical applications. Amorphous BST thin films have reported to have high transmittance, band-gap and refractive index values as high as 92-94%, 4.2-4.6 eV and 2.1-2.4 respectively [111-113]. The optical band-gap and refractive index of various oxide materials is shown in table 1.1.

Name of the Material	ε_r	Eg (eV)	$n_{(\lambda=550\ nm)}$
Al_2O_3	10	8.7	1.7
Y_2O_3	16	5.6	1.9
HfO_2	18	5.7	1.9
ZrO_2	22	5.9	2.1
Ta_2O_5	25	4.5	2.2
La_2O_3	28	4.3	1.7
Pr_2O_3	30	3.5	1.7
TiO_2	100	3.4	2.2

Table 1.1: Dielectric constant, bandgap and refractive index values of various technologically important oxides.

1.6 Optical properties of BST thin films:

Barium strontium titanate (BST) thin films have been the focus of research in RF and microwave device applications due to their high dielectric constant, high electrical tunability and composition dependent Curie temperature (T_c) [114-116]. Because of the unique combination of large dielectric constant, large electro-optic (EO) coefficient[117-119] and low optical losses[120], BST thin films are considered for various EO and non-linear optical applications such as second harmonic generators (SHGs), infrared optical sensors, planar wave guides and electro-optic switches[121-124]. Therefore, for practical applications, knowledge of their optical response is highly essential. Optical properties such as refractive index (n_f), extinction coefficient (k) and optical band gap (E_g) are important parameters, which determine the overall optical behavior of these films.

The optical band gap in BST films is found to be sensitive to stoichiometry, grain size, lattice strain, defects/oxygen vacancies and crystallinity[125-127]. Kuo and Tseng[128] have observed a decrease in the band gap from 4.20 to 3.98 eV and have attributed it to the increase in the grain size from 8.8 to 10.8 nm in $Ba_{0.7}Sr_{0.3}TiO_3$ films, on annealing the films from 500 to 750◦C. Roy et al.[129] have reported a large blue shift in the optical band gap of sol–gel derived $Ba_{0.5}Sr_{0.5}TiO_3$ films due to defects in the form of oxygen vacancies. A shift in the band gap has also been observed due to a change in stoichiometry and lattice strain in BST thin films[130-132]. The same group reported a decrease in band-gap with increase in pH value of the parent sol in sol-gel derived $Ba_{0.5}Sr_{0.5}TiO_3$ thin films.[133] I. Suzuki et al.[134] carried out spectroscopic ellipsometry

characterization of BST thin films and determined the annealing temperature dependent refractive index and thickness of the films prepared by sol-gel method.

Aulika et al.[135] prepared thin films of BST on $Si/SrRuO_3$ (Si/SRO), Si and Pt coated substrates by PLD and reported a refractive index value of 1.77, 2.16, and 2.03 (@ λ= 633 nm) for BST thin films on Si/SRO, Si and Pt coated substrates respectively. They observed that the films with weakest XRD pattern had a lower value of refractive index than polycrystalline films. They also observed that the refractive index value of BST films were lower than those of bulk ceramics. The difference in the optical properties was attributed to the strain induced changes in the BST films and/or lower density of the BST thin films.

P. Pasierb et al.[136] reported the optical properties of RF sputtered $Ba_xSr_{1-x}TiO_3$ thin film with composition varied from $0 \leq x \geq 1$ and observed a decrease in refractive index with increase in Ba content which was attributed to the decrease in optical density of films with decrease in crystallinity.

B. Panda et al.[137] deposited BST films by RF sputtering and observed a decrease in optical band-gap with increase in Ba content. The dispersion data of the refractive index was found to follow the single electron oscillator model in the low absorption region.

S. Z. Li et al.[138] found that the substrate temperature, sputtering pressure, ratio of argon to oxygen and annealing temperature affects the refractive index of BST thin films deposited by RF magnetron sputtering. There was a 10% variation of refractive index for BST films deposited over a substrate temperature range of 560–650^oC without post deposition annealing. In the range of the sputtering pressure from 0.37 to 2.5 Pa, the refractive index of the as-deposited BST thin films increases with the pressure. However, when the pressure increases up to 3.9 Pa, the refractive index reduces to 1.86. The refractive index has been found to increase with the ratio of oxygen to argon. The main reason attributed to this is the improvement of the film stoichiometry and texture, which are affected by the ratio of oxygen to argon. The increase of the refractive index with annealing temperature is due to the increase in packing density of the films. Finally, the refractive index of BST thin films is also affected by the films' microstructure and texture.

In comparison to semiconductor alternatives thin-film BST devices promise to be extremely competitive in terms of cost without a significant sacrifice in performance for many applications. In order to fully exploit this advantage, careful attention must be paid to the choice of substrate and metallization, deposition methods, circuit design, and packaging. The BST thin-film technology is still relatively immature, with numerous problems to be solved. The growth optimization of the BST material, the electrodes and electrode-BST interfaces are sources of difficulty. The fabrication technology of BST varactors is equally important and must be addressed carefully by the researchers in the field.

1.7 BST thin film processing:

A significant amount of effort has been directed toward developing methods to grow high-quality BST thin films on different substrates. A survey reveals that a variety of methods can be used to deposit BST thin films, which can be broadly classified as,

(a) Physical Vapor Deposition (PVD)
(b) Chemical Vapor Deposition (CVD)
(c) Chemical solution deposition (CSD)

Chemical solution deposition (CSD) methods such as sol-gel, metal-organic decomposition etc. is being widely used for the deposition of high quality thin films including BST and other perovskite and oxide thin films. The development of CSD process for depositing perovskite thin films started in mid-1980s when Budd et. al. [139,140] demonstrated the process of sol-gel for the deposition of lead (Pb) based perovskite while Fukushima et al.[141] used metalorganic decomposition (MOD) technique. These methods are simple, rapid and do not require vacuum infrastructure and hence are cost effective. But scalability, reproducibility, morphological, phase and composition control are their setbacks.

Chemical vapor deposition (CVD) includes metalorganic chemical vapor deposition (MOCVD), Atmospheric Pressure Chemical Vapour Deposition (APCVD), atomic layer deposition (ALD) etc. The widely and most commonly used CVD process for depositing BST thin films is MOCVD. MOCVD method offers very high control over the growing thin film. Organic precursors, such as metal alkoxides and β-diketonates,

containing the required cation are vaporized and transported into the heated reactor chamber using a carrier gas. High temperature in the chamber and on the substrate surface decomposes the precursors and the liberated atoms recombine to form the desired compound. [142-145] Precise control of the precursor and gas flow rates into the reactor chamber results in strict control over film stoichiometry and growth. MOCVD offers many advantages including: large area growth, conformal deposition, excellent composition control, and uniformity. The downside to oxide MOCVD is the overall cost of the system and the difficulties presented by precursor chemistry. Tombak et al.[77] have reported deposition of BST parallel plate varactors on silicon using MOCVD.

Physical vapor deposition (PVD) includes sputtering (DC and RF), molecular beam epitaxy (MBE) and pulsed laser deposition (PLD). PLD and sputtering are the most commonly used technique in PVD process for depositing BST thin films[146].

In PLD, a pulsed laser beam is focused onto the target in a vacuum chamber. Lasers that are commonly used include ArF, KrF excimer lasers, and Nd:YAG laser. It is generally recognized[147] that the shorter the wavelength, the more effective the ablation. Accordingly, excimer lasers have become the standard ones. When the high-energy laser beam is focused on the target surface and when the laser energy density (energy per unit area at the target surface) is above a threshold value, the target gets ablated, forming a plasma plume of the material which subsequently gets deposited on the substrate. PLD method affords the ability to maintain target composition in the deposited thin films and fast rates of deposition. Other advantages are that PLD is clean, low cost and capable of producing multilayer samples simply by switching between several different targets. There are also a number of disadvantages in PLD. These include: The plume cross-section is generally small (in the order of cm^2) due to a limited laser spot size. This, in turn, limits the sample size that can be prepared by PLD. In addition, this also brings difficulty in controlling the film thickness and uniformity across the sample. Finally in PLD process, there is an intrinsic “splashing” associated with laser ablation itself, which produces droplets or big particles of the target material on the substrate surface. From an industrial perspective, this is particularly serious as it will result in device failure.

Sputtering is a versatile and promising vacuum based, physical process, in which the positive ions in a glow discharge strike a target surface and eject atoms from it by momentum transfer. These atoms travel and gets deposited on the substrate surface.

Sputtering occurs when the kinetic energy of the incoming ions exceeds the binding energy of the surface atoms of the target. The quality of the films deposited by sputtering depends on various processing and post processing parameters and hence these parameters such as substrate temperature, working pressure, sputter power, target-to-substrate distance, base pressure, etc have to be optimized in order to achieve high quality thin films. During oxide deposition, oxygen must be introduced into the chamber in order to assist the formation of the desired phase and film composition.

Padmini et al.[148] have investigated the effect of texturing on the tunability of BST films. They concluded that <100> textured BST thin-film shows good tunability under optimized conditions. They optimized the deposition conditions such that the film was predominantly <100>oriented. It was noted that a biaxial tension in the film results in the polar axis of the material to orient itself along the substrate surface and this results in increased tunability.

Liu et al.[149] reported that the crystallinity of RF sputtered BST films affects the temperature coefficient of dielectric constant (TCD) of thermal-sensitive BST thin film capacitors. The crystallinity of BST thin films is heavily affected by the sputtering conditions.

Xu et al.[150] studied the effect of substrate and post deposition anneal on the properties of sputtered BST film on MgO and $LaAlO_3$ substrates. They reported better tunability on MgO compared to $LaAlO_3$ due to tensile stress in the former. Tunability was also improved by post deposition anneal in air at 900^{o}C for 5 hours. The tunability obtained was 22% for 100 kV/cm (10 V/μm) and a loss tangent of 0.0023 at 1 MHz and room temperature.

1.8 Choice of substrate for BST thin-film deposition:

Depending up on the application, thin films of BST have been deposited on a variety of substrates including single crystal substrates, such as $LaAlO_3$ (LAO), MgO, Al_2O_3 (AlO, Sapphire), metal coated substrates such as Pt/ Si, polycrystalline substrates such as alumina and amorphous substrates such as fused silica (or amorphous quartz).

For planar geometry of tunable varactors, substrates such as LAO, MgO, AlO (Sapphire) and alumina are used. For tunable varactors with MIM structures Pt/ Si is

generally being employed. For optical applications, highly transparent substrates such as fused silica become the forerunner.

The choice of substrates for optical and microwave application depends upon its dielectric constant, loss, lattice match between the film and substrate, thermal expansion coefficient (TEC), size, cost and availability[151]. The properties of various substrates are tabulated in table 1.2. The lattice constant and TEC of $(Ba_{0.5}Sr_{0.5})TiO_3$ is 3.9471 Å and 7-8 x 10^{-6} ^{o}C respectively.

Most of the studies on BST5 films have been on single crystal substrates like $LaAlO_3$, sapphire and MgO[152-154]. These single crystal substrates are costly and have a higher value of microwave dielectric constant. Hence, designing microwave circuits on such substrates create a variety of impedance matching issues. On the other hand ceramic substrate such as alumina is cost effective. It should be noted that alumina, which is the polycrystalline form of Al_2O_3 and sapphire have similar properties in terms of TEC, permittivity and loss. The opaque nature of alumina substrates impedes the transmission characteristics of the deposited BST film in the optical range.

Substrate Material	Lattice constant (Å)	TEC (K^{-1})	Dielectric constant	Loss	Cost* (US $)
$LaAlO_3$	a=3.79 c= 13.11	10 *x* 10^{-6}	25	3 x 10^{-4}	24
MgO	4.216	12.8 *x* 10^{-6}	9.8	< 2 x 10^{-5}	25
Sapphire (Al_2O_3)	a =4.758 c= 12.992	7.5 *x* 10^{-6}	9.4 @ a axis 11.58@ c axis	< 2 x 10^{-5}	24
Alumina	a =4.758 c= 12.992	<7.7 *x* 10^{-6}	9.4	< 2 x 10^{-5}	10
Pt/Si	3.9231	9 *x* 10^{-6}	--	--	14
Fused Silica	Amorphous	0.55 *x* 10^{-6}	3.82	2 x 10^{-4}	2

* 2 side polished substrates of 1 cm x 1cm x 0.5 mm

Table 1.2: The typical physical properties of various technologically important substrates.[155]

When compared to the single crystal and ceramic substrates, fused silica substrates are not only cost effective but also have good microwave characteristics and are transparent (94% transmittance) in the visible region of the spectrum and have

minimal optical loss, which is important for optical characterization of thin films. As fused silica substrates are amorphous in nature, growth of device quality crystalline films on them becomes quite challenging and hence considerable work has been carried out as part of this thesis to deposit good quality BST thin films on fused silica substrates. The structural, micro-structural, optical and microwave characteristics of BST films deposited on fused silica substrates have been studied in detail.

1.9 Choice of electrode:

In the microwave range, losses in the capacitor's electrode metallization become significant, mitigating the advantages of low loss-tangent films. The conductivity of the metal, ease of patterning, cost and availability are to be considered while choosing the metal electrode for microwave applications. Ideally, one would like to have the metallization with highest conductivity and maximum possible thickness for patterning as permissible by the lithography process. The high conductivity is to be ensured since the metal (either top or buried electrode) must carry high frequency current with as minimum loss as possible. Since, in the present work commercially available (111) oriented Pt (150 nm)/ Ti (10 nm)/ SiO_2 (300 nm) / Si (100) (Pt/Si, Inostek, South Korea) substrates were used, not much attention has been given for issues concerning to the buried electrodes. Table 1.3 summarizes the electrical conductivity of technologically important metals that are considered for metallization.

Material	**Conductivity (10^7 S/m) @ 20^oC**
Silver (Ag)	6.173
Copper (Cu)	5.813
Gold (Au)	4.098
Chromium (Cr)	3.846
Aluminum (Al)	3.816
Tungsten (W)	1.825
Nickel (Ni)	1.449
Platinum (Pt)	0.952
Titanium (Ti)	0.175

Table 1.3: Conductivity data for common metals.[156]

1.10 Motivation and Research Objectives:

As discussed earlier in this Chapter, various studies on BST thin films for tunable device applications have been carried out on single crystal substrates such as MgO, $LaAlO_3$ and Sapphire (Al_2O_3)[157-164]. Another common approach has been to deposit BST thin films on Pt coated Si substrates[148,165,166]. However, for many non-military applications, the high cost of conventionally processed ferroelectric thin films and devices are a limiting factor. The high cost stem from the use of single crystal as substrate materials. Alternatively, BST films deposited directly on fused silica can prove to be cost effective. Despite its excellent microwave properties and low cost, there are no reports of BST films grown directly on fused silica (SiO_2) substrates for microwave applications.

Fused silica substrates have a low microwave dielectric constant of 3.8 and low loss factor of the order of 10^{-4}. Lower values of dielectric constant for substrate material are advantageous in designing microwave circuits.

Moreover, BST on above said single crystal substrates are considered ‘‘discrete devices’’ and require mounting in a ‘‘hybrid’’ microwave integrated circuit (MIC) type of construction. The fabrication and tuning of MIC’s (hybrid-mount construction) is labor intensive and expensive. Additionally, this configuration is not considered as a ‘‘direct’’ integration process and poses reliability issues via component mount-bond failure. Additional drawbacks originate from the fact that ceramic substrates such as MgO, LAO and AlO are only available in small size geometries (~1x1 in. pieces) which are not suitable for large-area film deposition. Since most electronic systems, both military and commercial, are built as integrated circuits (ICs), i.e., ensembles of both active and passive devices on Si substrates linked via metal interconnects, it is of significant interest to integrate these BST-based thin films with Si substrates. This interest is driven by the affordability and large size availability of Si wafers and the widespread industrial/commercial use of Si-based processing technology.

However, for microwave device applications, such integration precludes the use of bare Si substrates since Si is not a ‘‘microwave friendly’’ material, i.e., at microwave frequencies, Si becomes less resistive, and consequently is too lossy for use in microwave devices. Therefore, Si is not the substrate of choice for microwave components[167].

One possible solution for this problem is replacing the normal silicon wafer with a high resistive silicon wafer. [168,169] The high resistive silicon wafers used for microwave devices have a nominal resistivity of at least 5000Ωcm, but the resistivity gets reduced during the subsequent high temperature deposition/ annealing process of BST films. An alternative approach to integration is silicon on sapphire (SoS) technology. In the silicon on sapphire process, a thin (about 0.5μm) silicon film is deposited onto the r-plane sapphire substrate. The advantage of SoS in integrated circuits is the high isolation between devices, which allows higher operating speed, lower power dissipation and smaller parasitic effects[170, 171].

However if the films are grown on fused silica (amorphous SiO_2) substrates, it opens the possibility for integrating BST with the existing Si technology by using a thick insulating layer of SiO_2 with more than 2 μm thick. This can be achieved either by thermally oxidizing Si or by depositing SiO_2 layer on Si using techniques that are industrially compatible with Si-based technology. The thick insulating layer of SiO_2 is deposited for minimization of microwave insertion loss of normal Si having with low resistivity, which gives rise to high loss tangent due to eddy current induced in it. In this case, where BST is deposited on SiO_2/ Si substrates, there is negligible attenuation of the microwave energy by the substrate.

Hence a study on the growth of BST films on SiO_2 as the substrates (in this case fused silica) and the impact of thermal treatments on them is an important prelude to develop process technologies for BST thin films compatible with Si technology. Consequently in this study the effect of thermal treatment on the growth of BST5 thin films on fused silica substrates and their microwave response are key objectives. The only drawback of this substrate material is its amorphous nature. Hence, obtaining crystalline BST5 (c-BST5) thin films on amorphous fused silica substrates pose a great challenge. To achieve this objective, it is important to study the influence of processing and post processing conditions on the structural, microstructural, optical and dielectric (in low and high frequencies) properties for successful implementation of BST thin films on fused silica substrates for device application in the optical and microwave frequency range.

RF magnetron sputtering has been widely accepted as one of the versatile techniques for the deposition of high quality BST thin films by several research groups [148-150]. In sputtering process, the desired film property can be achieved by carefully

controlling the processing parameters, which include power density, working/sputtering gas pressure, sputter gas mixture i.e, the $Ar:O_2$ ratio (oxygen mixing percentage, OMP), substrate to target distance and deposition/ post-deposition annealing temperature.

Out of the above mentioned parameters, deposition/ post-deposition annealing temperature highly influences the crystalline property of BST thin films. Deposition / post-deposition annealing temperature greater than 500^oC are required for obtaining crystalline BST films even on single crystal substrates. The thermal energy required for crystallization can either be provided during deposition of BST thin film i.e., BST thin films can be deposited *in situ* at elevated temperatures (this process does not require breaking vacuum) or the room temperature deposited BST thin films can be *ex situ* annealed at high temperatures (after breaking vacuum). BST films deposited or post-deposition annealed at temperatures lower than 500^oC are found to be amorphous. Amorphous BST films have dielectric and optical properties comparable to most of the technologically important oxides that are prepared at much higher temperatures and hence BST films in the amorphous phase have the potential to be an interesting alternative material system where thermal budget is of concern.

The other parameter that plays a vital role in sputter deposition process is the Oxygen Mixing Percentage (OMP). The exact OMP i.e., $Ar:O_2$ ratio in sputter deposition of oxides is always the subject of detailed optimization in any oxide system. There is a tradeoff between the ideal level of energetic impingement in oxygen containing plasma and the risk of anion deficiency that can occur under low OMP.

The effects of OMP during sputtering appear to be complex; the oxygen partial pressure influences not only the oxygen incorporation into the films, but also the titanium non-stoichiometry and the A/B site ratio which are strongly linked to the zero-field dielectric permittivity and loss.

The important objectives of this study are:

i. Fabrication of 2" dia ceramic targets of $(Ba_{0.5},Sr_{0.5})TiO_3$, BST5 suitable for sputter deposition process.
ii. Crystallize BST5 thin films on amorphous fused silica substrates.
iii. Study the effect of deposition/ post deposition annealing temperature on the structural, microstructural, optical and dielectric properties of crystalline BST5 thin films.
iv. Deposition of amorphous BST5 thin films and determine its microstructural, optical and dielectric properties.
v. To study the amorphous to crystalline transition in BST5 thin film system.
vi. Establish the influence of OMP on the stoichiometry of the deposited films and therefore on other properties.
vii. Deposition of BST5 thin films on single crystal substrates and study the effect of substrate on the crystalline structure, microstructure and broadband tunable dielectric properties.
viii. Optimizing photolithography process for the fabrication of test structures and devices with feature size of about 3μm.
ix. Demonstrate tunable varactors both in the planar and parallel plate geometry.

In general, the present study describes the growth and characterization of BST5 thin films deposited by RF magnetron sputtering for application in frequency agile devices. Emphasis has been laid on the correlation between the processing and post processing conditions on the various properties of BST5 thin films.

1.11 Thesis overview:

In this chapter, an introduction to basic theory of dielectrics and ferroelectricity was given. The need for tunable devices for microwave applications was briefed. Various technologies for frequency-agile systems were discussed and compared. The importance of the Barium Strontium Titanate (BST) thin films for optical and microwave tunable applications have been discussed. A survey of frequency-agile devices using thick-film, thin-film and bulk BST was also presented. Most authors have used expensive single crystalline substrates for BST thin-film fabrication as it is usually believed that epitaxial growth of BST thin-film on such substrates results in improved electrical properties. There is need for a BST process that allows integration with the existing passive technologies on Si. This would result in lower cost and also promote increased usage. Various configurations of capacitors such as MIM and IDC were discussed. Each configuration has its own advantage depending on the particular application. Choice of substrates and metal electrodes for optimum BST varactor performance was discussed along with the motivation and other important objectives of the current study.

The methodology for the synthesis of $Ba_{0.5},Sr_{0.5}TiO_3$ (BST5) ceramic targets by solid-state reaction technique, deposition of BST5 thin films by RF magnetron sputtering and the composition of the BST5 films deposited as a function of oxygen mixing percentage (OMP) are discussed in ***Chapter2***.

Chapter 3 introduces different characterization techniques used in the present study. The measured parameters and their respective characterization techniques are: 1) Film thickness by surface profilometer. 2) Crystal structure and crystallite size by X-ray diffraction. 3) Optical constants using UV-Vis-NIR spectrophotometer. 4) Surface roughness, and surface topography by Atomic Force Microscope 5) Low-frequency dielectric properties up to 100 KHz using a LCZ meter and up to 1 MHz using an impedance analyzer and 6) High-frequency (microwave) dielectric properties using Vector Network Analyzer (VNA).

This chapter also gives an introduction to photolithography and lift-off process and the steps involved in realizing test structures and devices of feature size down to 3μm.

The room temperature deposition and characterization of amorphous BST5 (a-BST5) thin films deposited on fused silica substrates as a function of Oxygen Mixing Percentage (OMP) and the influence of *ex situ* annealing on the crystallization/ structural, microstructural, optical and electrical properties have been described in ***chapter4***.

Two different *ex situ* annealing treatments were followed for crystallizing a-BST5 thin films. They are: *Treatment 1*: Annealing a-BST5 thin films deposited at different OMP at 900^{o}C for 1 min and *Treatment 2*: Annealing a-BST5 thin films deposited at 50% OMP at different temperatures for 1 hr. In T*reatment 1*, all the annealed films crystallized to cubic perovskite phase. In the case of films annealed using *Treatment 2*, the onset of crystallization of a-BST5 was about 700^{o}C.

The next two chapters of the thesis deals with the growth and characterization of crystalline BST5 (c-BST5) thin films deposited *in situ* at elevated deposition temperatures.

Chapter 5 describes the *in situ* deposition as well as the structural, microstructural and optical characterization of c-BST5 thin films. Two series of films were deposited as part of this work. They were designated as (i) OMP series and (ii) temperature series. In the case of OMP series, BST5 thin films were deposited on fused silica substrates at a fixed deposition temperature of 800^{o}C while varying the OMP from 0% to 100% in steps of 25%. In the case of temperature series, the OMP was fixed at 50% and the films were deposited on fused silica, Pt/Si, MgO, LaO and Al_2O_3 substrates at different temperatures from 600^{o}C to 800^{o}C in steps of 100^{o}C.

Chapter 6 discusses the electrical properties of c-BST5 thin films deposited at elevated deposition temperatures. The low-frequency dielectric and tunable properties of c-BST5 thin films deposited on Pt/Si substrates were studied using Metal-Insulator-Metal (MIM) structure. The dielectric permittivity (@100kHz) values were 250, 496 and 583 for the films deposited at 600, 700 and 800^{o}C respectively. Though a higher value of dielectric permittivity was obtained for the films deposited at 800^{o}C, the associated loss was also high. These films deposited at 800^{o}C had a loss tangent (tanδ) value of 0.01, whereas the films deposited at 600 and 700^{o}C had tanδ values of 0.005 and 0.008 respectively. A maximum tunability of 62% for an applied field of 300kV/cm was observed for the films deposited on Pt/Si substrates at 800^{o}C.

The microwave dielectric constant and loss tangent of c-BST5 films deposited on fused silica substrates were measured at a spot frequency of 10 GHz using split post dielectric resonator (SPDR) technique. Broadband microwave dielectric properties of c-BST5 films deposited on single crystal and on fused silica substrates were measured using calibration comparison technique.

Tunability measurements in microwave frequencies were performed using coplanar wave guide (CPW) structure. In the CPW geometry, highest tunability of about 23% for an applied field of 10kV/cm was obtained for the BST5 films deposited on sapphire. In the case of BST5 films grown on fused silica substrates, the tunability was less (13% @ 10kV/cm). This could be attributed to a variety of factors like crystalline orientation, microstructure and lack of favorable stress states. However, it is shown that crystalline BST5 films can be realized on amorphous fused silica substrates and the films are tunable.

A detailed discussion on the process parameter-physical property correlation is presented in ***chapter 7***. It is shown that the physical properties such as crystallite size, spectral transmittance, refractive index, optical band gap, dielectric constant and loss tangent show a strong dependence on the processing parameters such as substrate temperature (during and after deposition). The effects of each of these parameters on the properties are isolated and it is demonstrated that device goals can be achieved by appropriately maneuvering the processing parameters during deposition. A comparison between *in situ* and *ex situ* annealing treatments and the effect of amorphous to crystalline transition on the properties of BST5 thin films is discussed.

One of the core components in RF and microwave devices is the voltage controlled capacitor known as tunable varactor where the value of dielectric capacitance varies according to the applied DC bias voltage. Varactors of interdigitated capacitor (IDC) structure were fabricated on BST5 films deposited on fused silica substrates and parallel plate varactors with CPC structures were fabricated on BST5 films deposited on Pt/Si substrates. A capacitance tunability of 10% and 30% (@ 5GHz) was realized with IDC and CPC varactors respectively.

Chapter 8 gives the overall conclusion of the thesis and the outlook for future works that can be carried out along similar lines.

References:

1. J. C. Anderson, *Dielectrics*, Chapman and Hall Ltd., London (1964).
2. W. D. Kingery, H. K. Bowen and D.R. Uhlmann, *Introduction to Ceramics*, 2nd ed., John Wiley & Sons, New York (1926).
3. Kwan Chi Kao, *Dielectric phenomenon in solids*, Academic press, New York (2004)
4. A. R. West, *Basic solid state chemistry*, John Weiley & Sons, Chichester (2001)
5. H. Frohlish, *The theory of dielectrics*, London, Oxford university press, 2nd edition.
6. C. P. Smyth, *Ann. Rev.Phys. Chem*., **17**, 433 (1966).
7. J. C. Maxwel, A. Treatise, *Electricity and magnetism*, Clarendon press, Oxford, (1892)
8. W. H. Rodebugh and C. R. Eddy, *J. Chem. Phys*., **8**, 424 (1940).
9. S. O. Kasap, *Principles of Electronic Materials and devices*, McGraw –Hill (2006)
10. G. H. Haertling, *J. Am. Ceram Soc*., **82**, 797 (1999).
11. A. J. Moulson and J. M. Herbert, "Electroceramics: Materials, properties, applications", chapman and hall, New Yok, USA (1997)
12. B. Jaffe, W. R. Cook and H. Jaffe, "Piezoelectric Ceramics", John Wiley and Sons, New York, USA (1960).
13. J. C. Burfoot and G. W. Taylor, "*Polar dielectrics and their applications",* University of California Press, Los Angeles, CA (1979).
14. C. B. Sawyer and C. H. Tower, *Phys. Rev*, **35**, 269 (1930).
15. J. Valasek, *Phys. Rev*., **15**, 537 (1920).
16. G. Busch and P. Scherrer, *Naturwissenschaften*, **23**, 737 (1935).
17. B. M. Wul, I. M. Goldman, *Dokl. Akad. Nauk SSSR*, **46**, 154 (1945).
18. H. D. Megaw, *Ferroelectricity in Crystals*, Methuen, London (1957).
19. W. G. Cady, *Piezoelectricity*, Dover Publications, New York (1962).
20. M. Deri, *Ferroelectric Ceramics*, Gordon and Breach, New York (1969).
21. J. C. Burfoot, *Ferroelectrics*, Van Nostrand, New York (1967).
22. T. Mitsui, I. Tatsuzaki and E. Nakamura, *An Introduction to the Physics of Ferroelectrics*, Gordon and Breach, London (1976).
23. M. E. Lines and A. M. Glass, *Principles and Applications of Ferroelectric and Related Materials*, Clarendon Press, Oxford (1977).
24. J. M. Herbert, *Ferroelectric Transducers and Sensors*, Gordon and Breach, London (1982).
25. R. C. Buchanan, *Ceramic Materials for Electronics - Processing, Properties and Applications*, Marcel Dekker, New York (1986).

[26] L. M. Levinson, *Electronic Ceramics - Properties, Devices and Applications*, Marcel Dekker, New York (1987).

[27] T. Mitsiu, I. Tatsuzaki and E. Nakamura, "An introduction to the physics of ferroelectrics", Gordon and Breach Science Publishers, Ltd., London (1976).

[28] D. Damjanovic, "Ferroelectric, dielectric and piezoelectric properties of ferroelectric thin films and ceramics", Rep. Prog. Phys., 61, pp 1267-1324 (1998).

[29] Y. Xu, "Ferroelectric materials and their applications", North-Holland, New York, USA (1991)

[30] Phd Thesis of William Sumner Oates titled "*Fracture of Ferroelectric Materials*", Georgia Institute of Technology, July 2004.

[31] L. E. Cross and R. E. Newnham, "*History of ferroelectrics*," in ceramic and civilization, Vol III, High-Technology Ceramics- Past, Present, and Future, pp 289-305, American Ceramic Society, Inc., 1987.

[32] A. K. Tagantsev, V. O. Sherman, K. F. Astafiev, J. Venkatesh and N. Setter, *J. Electroceramics*, **11**, 5 (2003).

[33] L. Zhou, P.M. Vilarinho and J.L. Baptista, *J. Eur. Ceram. Soc*., **19**, 2015 (1999).

[34] V.V. Lemanov, E.P. Smirnova, P.P. Syrnikov and E.A. Tarakanov, *Phys. Rev. B*, **54**, 3151 (1996).

[35] J. H. Jeon, *J. Eur. Ceram. Soc*., **24**, 1045 (2004).

[36] A. Tagantsev, *Appl. Phys. Lett.*, **76**, 1182 (2000).

[37] C. B. Parker, J.-P. Maria and A. I. Kingon, *Appl. Phys. Lett*., **81**, 341 (2002).

[38] K. Bethe and E. Welz, *Mater. Res. Bull*., **6**, 209 (1971).

[39] D. M.Tahan, A. Safari and L. C. Klein, ISAF'96, *Proc. 10th IEEE International Symposium on Application of Ferroelectrics*, East Brunswick, NJ, USA, 483 (1996).

[40] X. X. Xi, H-C. Li, W. Si, A. A. Sirenko, I. A. Akimov, J. R. Fox, A. M. Clark and J. Hao, *J. Electroceramics*, **4**, 393 (2000).

[41] A. A. Sirenko, C. Bernhard, A. Golnik, A.M. Clark, J. Hao, W Si and X.X. Xi, *Nature*, **404**, 373 (2000).

[42] Yu.I. Yuzyuk, R. Farhi, V.L. Lorman, L.M. Rabkin, L.A. Sapozhnikov, E.V. Sviridov, and I.N. Zakharchenko, *J. Appl. Phys*., **84**, 452 (1998).

[43] I. Fedorov, V. Železnỳ, J. Petzelt, V. Trepakov, M. Jelinek, V. Trtik, M. Čerňanskỳ, and V. Studnička, *Ferroelectrics*, **208-209**, 413 (1998).

[44] C. Zhou and D. M. Newns, *J. Appl. Phys.*, **82**, 3081 (1997).

[45] W. Cochran, *Adv. Phys.*, **9**, 387 (1960).

[46] K.-H. Weyrich and R. Siems, *J. Phys. B: Condens. Matter*, **61**, 63 (1985).

[47] J. L. Servoin, Y. Luspin and F. Gervis, *Phys. Rev. B*, **22**, 5501 (1980).

[48] G. Shirane and Y. Yamada, *Phys. Rev.*, **177**, 858 (1969).

49. P. W. Anderson, in Fizika Dielektrikov, ed. Skanavi, G. I., Moscow: Akademica Nauk S.S.S.R. Fizicheskii Inst. im P. N. Lebedea (1960).

50. H. Frölich, *Theory of Dielectrics*, Clarendon Press, Oxford (1949).

51. Worlock, and P. A. Fleury, *Phys. Rev. Lett.*, **19**, 1176 (1967).

52. G. Rupprecht, R. O. Bell, and B. D. Silverman, *Phys. Rev.*, **123**, 97 (1961).

53. M DiDomenico, D. A. Johnson and R. H. Pantell, *J. Appl. Phys.*, **33**, 1697 (1962).

54. Ki-Byoung Kim, Tae-Soon Yun, Ran-Young Kim, Hyun-Suk Kim, Ho-Gi Kim and Jong-Chul Lee, *Microw. Opt. Tech. Lett.*, **45**, 15 (2005).

55. P. M. Suherman, H. T. Su, T. J. Jackson, F. Huang and M. J. Lancaster, *Ferroelectrics*, **367**, 170 (2008).

56. Robert Schafranek, Andre Giere, Adam G. Balogh, Thorsten Enz, Yuliang Zheng, Patrick Scheele, Rolf Jakoby and Andreas Klein, *J. Euro. Ceram. Soc*., **29**, 1433 (2009)

57. G. Rupprecht and R. O. Bell, "Dielectric constant in paraelectric perovskites", *Phys. Rev.*, **135**, 748 (1964).

58. A. R. Rofougaran, M. Rofougaran and A. Behzad, *IEEE Microwave.*, **6**, 38 (2005).

59. F.W. Van Keuls, R. R. Romanofsky, D. Y. Bohmon, M. D. Winters, F. A. Miranda, C. H. Muller, R. E. Treece and D. Galt, *Appl.Phys.Lett*., **70**, 3075 (1997).

60. F. Reggia and E. G. Spencer, *Proc. IRE*, **45**, 1510 (1957).

61. A. G. Fox, *Proc. IRE*, **35**, 1489 (1947).

62. K .M. Johnson, *IEEE Trans. Microwave Theory Tech.*, **14**, 564 (1966).

63. J. F. White, *IEEE Trans. Microwave Theory Tech.*, **13**, 233 (1965).

64. L. E. Larson, R. H. Hackett, M. A. Melendes, and R. F. Lohr, *Microw. Millimeter-Wave Monolithic Circuits Symp. Dig.,* Boston, MA, 27 (1991).

65. L. Lin, C. Nguyen. R. T. Howe and A. P. Pisano, *Proceedings of IEEE micro Electro Mechanical Systems*, MEMS'92, 226 (1992).

66. H. D. Wu, K. F. Harsh, R. S. Irwing, Z. Wenge, A. R. Mickelson, Y. C. Lee and J. B. Dobsa, *IEEE MTT-S Int. Microwave Symp. Dig.*, **1**, 127 (1998).

67. C. L. Goldsmith, Z. Yao, S. Eshelman, and D. Denniston, *IEEE Microwave Wireless Compon. Lett.*, **8**, 269 (1998).

68. J. B. Hacker, R. E. Mihailovich, M. Kim, and J. F. DeNatale, *IEEE Trans. Microw. Theory Tech*., **51**, 305 (2003).

69. Yi Zhang, Kazumasa Onodera and Ryutaro Maeda, *Jpn. J. Appl. Phys*., **45**, 300 (2006).

70. A. T. Findikoglu, Q. X. Jia and D. W. Reagor, *IEEE Trans. Appl. Supercond.*, **7**, 2925 (1997).

71. D. Galt and J. C. Price, *IEEE Trans. Appl. Supercond.*, **5**, 2575 (1997).

72. I. Woodridge, C. W. Turner and P. A. Warburton, *IEEE Trans. Appl. Supercond*., **9**, 3220 (1999).

73. A. Tombak, F. T. Ayguavives, Jon-paul Maria, G. T. Stauf, A. I. Kingon and A. Mortazawi, *IEEE MTT-S Int. Microwave Symp. Dig*., **3**, 1345 (2000).

74. Jayesh Nath, Dipankar Gosh, Jon- Paul Maria, Michael B. Steer and Angus I. Kingon, *Proc. of the Asian Pacific Microwave Conference (APMC'04)*, Newdelhi, India, 939 (2004).

75. R. York, A. Nagra, E. Erker, T. Taylor, P. Periyasamy, J. Speck, S. Streiffer and O. Auciello, *Proc. of the IEEE Int. Symp. on Appl. on Ferroelectrics*, **1**, 195 (2000).

76. S. S. Gevorgian, E. F. Carlsson, R. Runder, U. Helmersson, E. L. Kollber, E. Wikborg and O. G. Vendik, *IEEE Trans. Appl. Supercond*., **7**, 2458 (1997).

77. A. Tombak, F. T. Ayguavives, Jon-Paul Maria, G. T. Stauf, A. I. Kingon and A. Mortazawi, *IEEE MTT-S Int. Microwave Symp. Dig*., **3**, 1453 (2001).

78. J. A. Gonzalo and B. Jimenez, *Ferroelectricity: The Fundamentals Collection*, Weinhein, Germany: Wiley-VCH Verlag GmbH & Co. (2005).

79. R. Jackoby, P. Scheele, S. Muller and C. Weil, *IEEE MTT-S Int. Microwave Symp. Dig.*, **5**, 369 (2005).

80. W. Hu, D. Zhang, M. J. Lancaster, S. K. Yeo, T. W. Button and B. Su, *IEEE MTT-S Int. Microwave Symp. Dig.,* **5**, 411 (2005).

81. Luciene S. Demenicis, Luiz Fernando M. Conrado, Walter Margulis, Maria Cristina R. Carvalho, *Microw. Opt. Tech. Lett.*, **47**, 290 (2006).

82. B. Acikel, T. R. Taylor, P. J. Hansen, J. S. Speck and R. A. York, *IEEE Microwave and Wireless Components Letters*, **12**, 237 (2002).

83. A.Victor, J. Nath, D. Ghosh, B.Boyette, J.P.Maria, M.B.Steer, A.I.Kingon and G.T. Stauf, In *IEE proceedings on Microwaves, Antenna propagation*, **153**, 96 (2006).

84. A.Victor, J. Nath, D. Ghosh, B.Boyette, J.P.Maria, M.B.Steer, A.I.Kingon and G.T. Stauf, *In IEEE Radio and Wireless Conference* (2004).

85. H. Katta, H. Kurioka and Y. Yashima, In *IEEE Ttransactions on Microwave Theory and Techniques*, **53**, 1 (2005).

86. F. D. Flaviis, N. G. Alexopouls, O. M. Stafsudd, *IEEE.Trans.Microwave Theory and Tech*., **45**, 963 (1997).

87. B. Acikel, Y. Liu, A. S. Nagra, T. R Taylor, P. J. Hansen, J. S. Speck and R. A. York, *IEEE MTT-S Int. Microwave Symp. Dig*., **2**, 1191 (2001).

88. Y. Liu, A. S. Nagra, E. G. Ecker, P. Periswamy, T. R Taylor, J. S. Speck, and R. A. York, *IEEE Microw. Guided Wave Lett.,* **10**, 448 (2000).

89. D. Kuylenstierna, A. Vorobiev, P. Linner, and S. Gevorgian, *Proc. 34th Eur. Microw. Conf.*, Amsterdam, Netherlands, 157 (2004).

90. D. Kuylenstierna, A. Vorobiev, P. Linner, and S. Gevorgian, *IEEE Trans. Microw. Theory Tech*., **53**, 2164 (2005).

91. K.-B. Kim, T.-S. Yun, H.-S. Kim, I.-D. Kim, H.-G. Kim and J.-C. Lee, *Proc. 35th Eur. Microw. Conf*., Paris, France, 649 (2005).

92. S. J. Lee, H. C. Ryu, S. E. Moon, M. H. Kwak, Y. T. Kim and K. Y. Kang, *J. Kor. Phy. Soc*., **48**, 1286 (2006).

93. S. E. Moon, H. C. Ryu, M. H. Kwak, Y. T. Kim, S. J. Lee and K. Y. Kang, *ETRI Journal*, **27**, 677 (2005).

94. T. O'Sullivan, R. A. York, B. Noren and P. M. Asbeck, *IEEE Trans. Microw. Theory Tech.,* **53**, 106 (2005).

95. A. Nagra and R. A. York, *IEEE Trans. Microw. Theory Tech.,* **47**, 1705 (1999).

96. L. Y. Vicki, Roger Forse, D. Chase and Robert York, *IEEE MTT-S Int.*, **1**, 261 (2004).

97. H. Katta, H. Kurioka and Y. Yashima, *IEEE MTT-S Int.,***2**,189 (2006).

98. P. Scheele, F. Goelden, A. Giere, S. Mueller and R. Jakoby, *In IEEE MTT-S Int. Microw. Symp.Did.*,**7**, 603 (2005).

99. L.-Y. V. Chen, R.Forse, D.Chase, and R. A. York, "*IEEE MTT-S Int. Microwave Symp. Dig.*, **6**, 261 (2004).

100. A. Tombak, J.-P. Maria, F. T. Ayguavives, G. T. Stauf, A. I. Kingon, and A. Mortazawi, *IEEE Trans. Microw. Theory Tech*., **51**, 462 (2003).

101. Jayesh Nath, Dipankar Ghosh,Jon Paul Maria, Angus.I.Kingon,Wael Fathelbab, Paul D. Fran Zon and Michael .B.Steer, *IEEE Trans.Microwave theory and technique*, **53**, 2707 (2005).

102. M. Rahman, and K. Shamsaifar, *IEEE MTT-S Int. Microwave. Symp. Dig*., **3**, 1767 (2003).

103. B. Noren, *Microwave J*., **47**, 210 (2004).

104. C.V. Varanasi, K.D. Leedy, D.H. Tomich and G. Subramanyam, *Thin Solid Films*, **517**, 2878 (2009).

105. W. G. Zhu, O. K. Tan, J. Deng and J. T. Oh, *J. Mater. Res.,* **15**, 1291 (2000).

106. X. F. Chen,W. G. Zhu, O. K. Tan and M. S. Tse, *Ferroelectrics*, **232**, 71 (1999).

107. X. F. Chen, W. G. Zhu and O. K. Tan, *Mater. Sci. Eng. B*, **77**, 177 (2000).

108. T. G. Kim, J. Oh, Y. Kim, T. Moon, K.S. Hong and B. Parky, *Jpn. J. Appl. Phys*., **42**, 1315 (2003).

109. D. M. A. Melo, A. Cesar, A. E. Martinelli, Z. R. Silva, E. R. Leite, E. Longo, P.S. Pizanni, *J. Solid State Chem*., **177**, 670 (2004).

110. V. Lyahovitskaya, I. Zon, Y. Feldman, S. R. Cohen, A. K. Tagantsev, and I. Lubomirsky, *Adv. Mater*., **15**, 1826 (2003).

111. Yuan-Chang Liang, *Electrochem. Solid-State Lett*., **12**, G54 (2009).

112. Lin-JungWu and Jenn-MingWu, *J. Phys. D: Appl. Phys*., **40**, 4948 (2007).

113. A. K. Bain, T. J. Jackson, Yiannis Koutsonas, M. Cryan, S. Yu, M. Hill, R. Varrazza, J. Rorison and M. J. Lancaster, *Ferroelectrics Lett. Sec*., **34**, 149 (2007).

[114.] L. Chen, J. Shen, S. Y. Chen, G. P. Luo, C. W. Chu, F. A. Miranda, F. W. Wan Keul, J. C. Jiang, E. I. Meletis and H. Y. Chang, *Appl. Phys. Lett.* **78**, 652 (2001).

[115.] F. M. Pontes, E. R. Leite, D. S. L. Pontes, E. Longo, E. M. S. Santos, S. Mergulhao, P. S. Pizani, F. Lanciotti Jr, T. M. Boschi and J. A. Varela, *J. Appl. Phys.*, **91**, 5972 (2002).

[116.] J. S. Lee, H. Wang, S. Y. Lee, S. R. Foltyn and Q. X. Jai *Appl.Phys. Lett.*, **83**, 5494 (2003).

[117.] J. Li, F. Duewer, C. Gao, H. Chang and X.-D. Xiang, *Appl. Phys. Lett.,* **76**, 769 (2000).

[118.] D. Y. Wang, C. L. Mak, K. H. Wong, H. L. W. Chan and C. L. Choy, *Ceram. Int*., **30**, 1745 (2004).

[119.] D.-Y. Kim, S. E. Moon, E.-K. Kim, S.-J. Lee, J.-J. Choi and H.-E. Kim, *Appl. Phys. Lett.*, **82**, 1455 (2003).

[120.] K. Takeda, T. Muraishi, T. Hoshina, H. Kakemoto and T. Tsurum, Mater. Sci. Engg (in press)

[121.] F. J. Walker, R. A. Mckee, H. W. Yen and D. E. Zelmon, *Appl. Phys. Lett.*, **65,** 1495 (1994).

[122.] J. Li, F. Duewaer, C. Gao, H.Chang, X. D. Xiang and Y. Lu, *Appl. Phys. Lett.*, **76**, 769 (2002).

[123.] D. Y. Kim, S. E. Moon, E. K. Kim, S. J. Lee, J. J. Choi and H. E. Kim, *Appl. Phys. Lett.*, **82**, 1455 (2003).

[124.] J. F. Scott, A. Q. Jiang, S. A. T. Redfern, M. Zhang and M. Dawber, *J. Appl. Phys.*, **94**, 3333 (2003).

[125.] K. Venkata Saravanan, K. Sudheendran, M. Ghanashyam Krishna, K. C. James Raju and A. K. Bhatnagar, *Vacuum*, **81**, 307 (2006).

[126.] S. Bobby Singh, H. B. Sharma, H. N. K. Sarma and S. Phanjoubam, *Ferroelectr. Lett. Sect.*, **33**, 83 (2006).

[127.] H. Y. Tian, J. Choi and K. No, *Mater. Chem. Phys.*, **78**, 138 (2003).

[128.] Y. F. Kuo and T. Y. Tseng, *Mater. Chem. Phys.*, **61**, 244 (1999).

[129.] S. C. Roy, G. L. Sharma and M. C. Bhatnagar, *Solid State Commun.*, **141**, 243 (2007).

[130.] R. Thielsch, K. Kaemmer, B. Holzapfel and L. Schultz, *Thin Solid Films*, **301**, 203 (1997).

[131.] R. Thomas, D. C. Dube, M. N. Kamalasanan and S. Chandra, *Thin Solid Films*, **346**, 212 (1999).

[132.] Y. Zheng, S. Wang and H. A. Huan, *Proc.—Mater. Res. Soc.*, **872,** J14.5 (2005).

[133.] Somnath C. Roy, G. L. Sharma, M. C. Bhatnagar, R. Machanda, V. R. Balakrishna and S. B. Samantta, ", *Appl. Surf. Sci*., **236**, 306 (2004).

[134.] Iwao Suzuki, Masahiro Ejima, Kenichi Watanabe, Yi- Ming Xiong and Tadashi Saitoh, *Thin Solid Films*, **313-314**, 214 (1998).

[135.] I. Aulika, J. Pokorny, V. Zauls, K. Kundzins, M. Rutkis and J. Petzelt, "*Opt. Mater.*, **30**, 1017 (2008).

[136.] P. Pasierb, S. Komornicki, M. Radecka, *Thin Solid Films*, **324**,134 (1998).

[137.] B. Panda, A. Dhar, G. D. Nigam, D. Bhattacharya and S. K. Ray, *Thin Solid Films*, **332**, 46 (1998).

[138.] S. Z. Li, Y. Q. Yang, L. Liu, W. C. Liu and S. B. Wang, "*Physica B*, **403**, 2618 (2008).

[139.] K. D. Budd, S. K. Dey and D. A. Panday, "The effect of hydrolysis conditions on the charactertistics of lead titanate gel and thin films", Mater. Res. Sco. Symp. Proc., 73, pp 711-716 (1986).

[140.] K. D. Budd, S. K. Dey and D. A. Panday, *Mater. Res. Sco. Symp. Proc.*, **73**, 711 (1986).

[141.] J. Fukushims, K. Kodaira and T. Matsushita, *J. Mater. Sci.*, **19**, 595 (1984).

[142.] A. C. Jones, *J. Mater. Chem.*, **12**, 2576 (2002).

[143.] L. A. Wills, W. A. Feil, B. W. Wessels, L. M. Tonge and T. J. Marks, *J. Cryst. Growth*, **107**, 712 (1991).

[144.] A. C. Jones, *J. Mater. Chem*, **12**, 2576 (2002).

[145.] T. Kawahara, M. Yamamuka, T. Makita, J. Naka, A. Yuuki, N. Mikami and K. Ono, *Jpn. J. Appl. Phys.*, **33**, 5129 (1994).

[146.] S. Saha and S. B. Krupanidhi, "*J. Appl. Phys.*, **86**, 3056 (2000).

[147.] T. J. Jackson and S. B. Palmer, *J. Phys. D: Appl. Phys.*, **27**, 1581 (1994).

[148.] P. Padmini, T. R. Taylor, M. J. Leferve, A. S. Nagra, R. A. York and J. S. Speck, *Appl. Phys. Lett.,* **75**, 3186 (1999).

[149.] Shi-Jian Liu, Xiang-Bin Zeng and Jun-Hao Chu, *Microelectronic J.*, **35**, 601 (2004).

[150.] J. Xu, W. Menesklou and E. I. Tiffee, *J. Eur. Ceram. Soc.,* **24**, 1735 (2004).

[151.] V. Borasee, *Microwaves* (1982).

[152.] E. J. Cukauskas, S. W. Kirchoefer and W. Chang, *J. Cryst. Growth*, **236**, 239 (2002).

[153.] I. B. Misirlioglu, A. L. Vasilier, M. Aindow, S. P. Alpay and R. Ramesh, *Appl. Phys Lett.*, **84**, 1742 (2004).

[154.] Z. Yuan, Y. Lin, J. Weaver, X. Chen, C. L. Chen, G. Subramanyan, J. C. Jiang and E. I. Meletis, *Appl. Phys. Lett.*, **87**, 152901 (2005).

[155.] MTI Corporation, USA, www.mtixtl.com

[156.] D. M. Pozar, *Microwave Engineering*, 2nd edition, John Wiley & Sons Inc., New York, USA (1998).

[157.] W. Chang, J. Horwitz, A. Carter, J. Pond, S. Kirchoefer, C. Gilmore and D. Chrisey, *Appl. Phys. Lett.*, **74**, 1033 (1999).

[158.] E. Cukauskas, S. Kirchoefer and J. Pond, in *Proc. IEEE Inter. Symp. Appl. Ferroelectrics*, **2**, 875 (2000).

[159.] D. Bubb, J. Horwitz, S. Qadri, S. Kirchoefer, C. Hubert and J. Levy, *Appl. Phys. A*, **79**, 99 (2004).

[160.] L. Knauss, J. Pond, J. Horwitz, D. Chrisey, C. Mueller and R. Treece, *Appl. Phys. Lett.*, **69**, 25 (1996).

[161.] J J. Bellotti, E. K. Akdogan, A. Safari, W. Chang and S. K. Kirchoefer, *Integ. Ferroelectrics*, **49**, 113 (2002).

[162.] C. Carlson, T. Rivkin, P. Parilla, J. Perkins, D. Ginley, A. Kozyrev, V. Oshadchy and A. Pavlov, *Appl. Phys. Lett.*, **76**, 1920 (1999).

[163.] S. Kirchoefer, J. Pond, A. Carter, W. Chang, K. Agarwal, J. Horwitz, and D. Chrisey, *Microwave and Optical Technology Letters*, **18**, 168 (1998).

[164.] S. -J. Lee, S. Moon, M. -H. Kwak, H. -C. Ryu, Y. -T. Kim and K. -Y. Kang, *Jap. J. Appl. Phys.*, **43**, 6750 (2004).

[165.] S. Gevorgian, A. Vorobiev, D. Kuylenstierna, A. Deleniv, S. Abadei, A. Eriksson and P. Rundqvist, *Integ. Ferroelectrics*, **66**, 125 (2004).

[166.] A. Vorobiev, P. Rundqvist, K. Khamachane and S. Gevorgian, *J. Appl. Phys.*, **96**, 4642 (2004).

[167.] R. E. Williams, *Gallium Arsenide Processing Techniques*, Artech House, Dedham, MA (1984)

[168.] S. Gevorgian, *Int. J. RF Microw. Comput.-Aided Eng.*, **8**, 433 (1998).

[169.] H. S. Gamble, B. M. Armstrong, S. Mitchell, Y. Wu, V. F. Fusco and J. A. Stewart, *IEEE Microw. Guid. Wave Lett.*, **9**, 395 (1999).

[170.] E. A. Fardin, A. S. Holland, K. Ghorbani, E. K. Akdogan, W. K. Simon, A. Safari and J. Y. Wang, *Appl. Phys. Lett.*, **89**, 182907 (2006).

[171.] H. Li, J. Finder, Y. Liang, Gregory and W. Qin, *Appl. Phys. Lett.*, **87**, 072905 (2005).

Chapter II

Target preparation, thin film deposition and compositional characterization

2.1 Introduction:

As discussed in chapter 1, tunable applications, which require high tunability and low loss, barium strontium titanate (BST) in the paraelectric phase is preferred to that in the ferroelectric phase. BST with Ba:Sr ratio of 50:50 [($Ba_{0.5}$, $Sr_{0.5}$)TiO_3, BST5] with its Curie temperature T_c, just below room temperature is found to be paraelectric and hence is the material of study in this work. This chapter describes the methodology for the synthesis of BST ceramic targets by solid-state reaction technique and deposition of BST thin films by RF magnetron sputtering. The phase purity, crystallinity and crystallite size of the target material were determined using X-ray diffraction (XRD) technique and the surface morphology of these targets was characterized by scanning electron microscopy (SEM). The target fabrication steps were optimized for obtaining BST5 targets of high density with good surface finish, suitable for sputtering. These targets were used for depositing thin films by RF magnetron sputtering. It is well known that the structural, microstructural, optical and electrical properties of BST thin films depend on the Ba/Sr, (Ba+Sr)/ Ti ratio and oxygen stoichiometry. Hence, it is essential to determine the composition of the deposited films. The composition of the films was analyzed by Rutherford Backscattering Spectrometry (RBS) and X-ray Photoelectron Spectroscopy (XPS). RBS allows precise determination of the thin film stoichiometry without calibration standards required in contrast to methods like wavelength dispersive and energy dispersive X-ray spectrometries (WDS and EDS).[1] For probing the surface composition of the BST5 thin films, X-ray Photoelectron Spectroscopy (XPS) measurements were performed.

2.2 Target fabrication:

Detailed optimization of conditions for the preparation of ceramic targets of BST5, which was used for deposition of BST thin films by RF magnetron sputtering, was carried out.

The main objectives of this part of the work were the following:

1. To synthesize Barium Strontium Titanate powder with Ba/Sr ratio 50/50 [$(Ba_{0.5}Sr_{0.5})TiO_3$, BST5)] without any secondary phases.
2. Optimize sintering conditions i.e., sintering time and temperature to obtain high density sputtering targets with good surface finish, suitable for sputtering.
3. To estimate the shrinkage and to obtain 2"diameter targets after sintering.

2.2.1 Powder preparation:

Several methods can be used for the preparation of ceramic powders. The methods can be divided into two categories: mechanical methods and chemical methods[2,3,4]. In the mechanical methods, small particles are produced from larger ones by mechanical forces, a process referred to as comminution. The process of comminution involves operations such as crushing, grinding and milling. In some cases, a mechanical milling step forms a part of the process. A wide range of chemical methods exist for the preparation of ceramic powders. The methods can be divided into three broad categories: (i) solid state reactions, (ii) precipitation from solution and (iii) vapor phase reactions. In our case the powders were prepared using the solid state reaction method.

Target preparation using the solid state reaction method (otherwise known as ceramic method) involves the following steps: (a) Stoichiometric weighing of the starting reagents, (b) Uniform mixing, (c) Calcination, (d) Particle size reduction, (e) Uni-axial pressing and (f) Sintering. Cost effectiveness, ease of processing and the abundant availability of starting reagents are the major advantages of this process. The main disadvantage for this method is the need of high processing temperatures in order to achieve best properties. In the present study, BST5 targets were prepared using carbonates of Barium and Strontium and Titanium dioxide as the starting materials. The simple reaction is given as,

$$M^{I}CO_3 + M^{II}O_2 \rightarrow M^{I}M^{II}O_3 + CO_2\uparrow$$

where, $M^{I} \rightarrow$Ba, Sr

$M^{II} \rightarrow$Ti

2.2.2 Stoichiometric weighing of reagents:

The chemical reaction considered for preparation of $(Ba_{0.5},Sr_{0.5})TiO_3$ powder is given in equation 2.1.

$$0.5\ (BaCO_3) + 0.5\ (SrCO_3) + TiO_2 \rightarrow (Ba_{0.5}, Sr_{0.5})TiO_3 + CO_2 \uparrow \qquad (2.1)$$

The molecular weights of $BaCO_3$, $SrCO_3$ and TiO_2 are 197.35, 147.6 and 79.9 gms respectively. On adding the molecular weights according to equation 2.1, we get the total weight of the sample as 252.375 gms.

Hence for the preparation of 1 gram of stoichiometric powder we take,

$$\text{Barium Carbonate } (BaCO_3) \rightarrow \frac{0.5 \times 197.35}{252.375} \rightarrow 0.3910 \text{ gms}$$

$$\text{Strontium Carbonate } (SrCO_3) \rightarrow \frac{0.5 \times 147.6}{252.375} \rightarrow 0.2924 \text{ gms}$$

$$\text{Titanium dioxide } (TiO_2) \rightarrow \frac{79.9}{252.375} \rightarrow 0.3166 \text{ gms}$$

The required amount of the starting reagents with purity >99.9%, (Aldrich Chemicals) were weighed using an electronic balance (A&D technologies, Model GR-120), with an accuracy of 0.1mg.

2.2.3 Uniform mixing of reagents:

In order to ensure a complete chemical reaction, the starting reagents have to be mixed uniformly to increase the point of contact between the reagents. Hence, the measured starting materials along with acetone as mixing medium and zirconia grinding balls were taken in zirconia jar (vial) and were thoroughly mixed for 1 hr at 150 rotations per minute (rpm) using a planetary Ball Mill (Retsch PM 100, Germany). After mixing, the slurry was transferred to an alumina crucible and was dried at 100^{o}C over night in an oven.

2.2.4 Calcination:

Calcination (also referred to as calcining) is a thermal treatment which brings about thermal decomposition or removal of a volatile fraction and phase transition. In the present case, chemical reaction takes between the initial reactants by chemical decomposition reactions in which the solid reactants such as $BaCO_3$ and $SrCO_3$ decompose to form a new solid phase such as BaO and SrO respectively. During this process CO_2, which is commonly associated with the metal carbonates are released. BaO and SrO which are not stable phases of Ba and Sr reacts with TiO_2 to form $(Ba,Sr)TiO_3$. A clear illustration is given below,

$$M^{I}CO_3 \xrightarrow[\Delta]{} M^{I}O + CO_2 \uparrow \qquad (2.2)$$

$$M^{I}O + TiO_2 \xrightarrow[\Delta]{} M^{I}TiO_3 \qquad (2.3)$$

where, M^{I} → Ba, Sr

The calcination process normally takes place well below the melting temperature of the product materials[5,6]. The parameters such as temperature and duration of calcinations are important factors influencing shrinkage of the material during sintering.

The uniformly mixed and dried powders were calcined in a furnace at different temperatures and duration. The important point in the calcination process is to prepare single phase powder with no secondary phases at the lowest possible temperature and duration. The completion of reaction, phase formation and the absence of secondary phases were confirmed using XRD. The XRD patterns of some of the calcined samples are shown in figure 2.1.

It can be seen from figure 2.1 that the powders calcined at 1100^{o}C for 5 hrs yielded single phase BST5 powder. In order to bring down the calcination temperature, the powders were calcined at 1000^{o}C and 900^{o}C, which did not yield single phase BST5 even after calcining to 10 hrs and 5 hrs respectively. On the other hand, calcining the starting materials at 1000^{o}C for 10 hrs yielded single phase BST5 powder with no secondary phases. This calcination condition was therefore chosen for further processing.

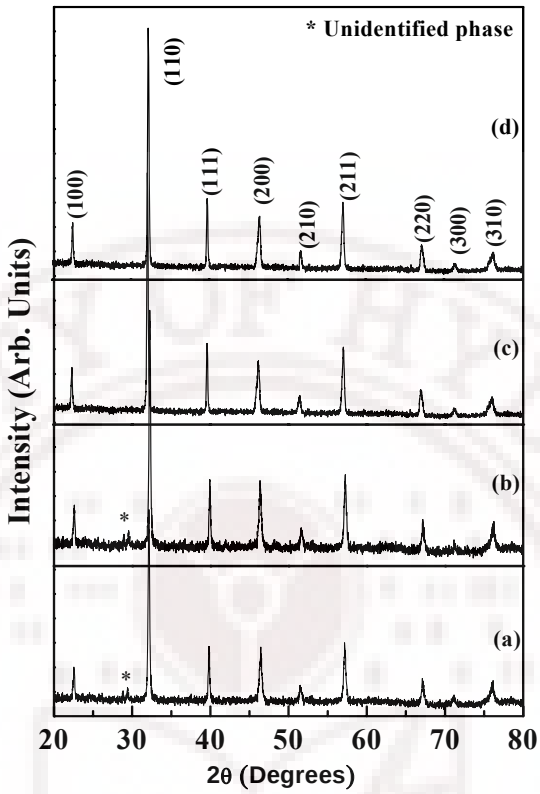

Figure 2.1: X-ray diffraction pattern of BST5 powder calcined at (a) 900^{o}C for 10 hrs, (b) 1000^{o}C for 5 hrs, (c) 1000^{o}C for 10 hrs and (d) 1100^{o}C for 5 hrs.

2.2.5 Particle size reduction:

The particle size reduction (also known as pulverization) of the complex oxides after the calcinations stage is important. It is well known that particles with small size can be compacted well, which in turn yields higher density at lower sintering temperatures. In our case a planetary ball mill (Retsch PM 100, Germany) was used for pulverization. There are several processing variables in pulverization that determine the final size of the particles of the product. The variables include milling speed, milling time, grinding ball: powder ratio etc.[7] In the present study, calcined powders were dry ground for different milling durations; The ball: powder ratio and the milling speed were fixed at 3:1 and 350 rpm respectively. The XRD pattern of pulverized BST5 powder as a function of milling time is shown in figure 2.2.

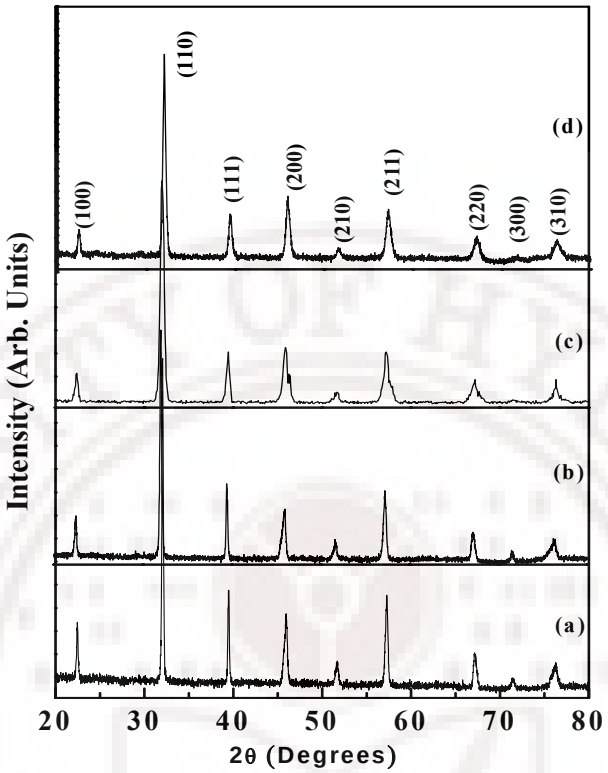

Figure 2.2: X-ray diffraction pattern of BST5 powder pulverized at 350 rpm for (a) 1hr (b) 2 hrs, (c) 3 hrs and (d) 4 hrs.

The variation in full width at half maxima (FWHM) and crystallite size as a function of milling time is shown in figure 2.3. It can be observed that the crystallite size decreases with increase in milling time till about 3 hrs. Further increase in the milling time causes the particles to agglomerate leading to an increase in crystallite size (decrease in FWHM). Hence, for a milling speed of 350 rpm, the optimum milling time for BST5 powder was found to be 3 hrs.

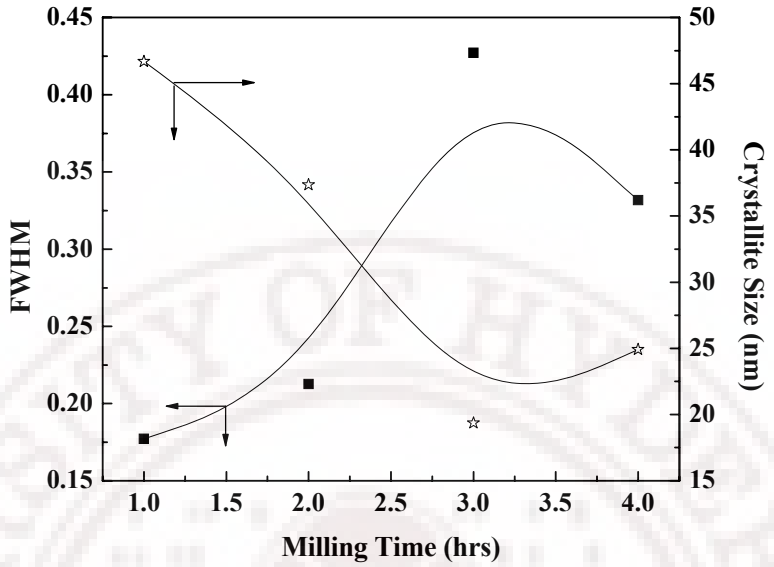

Figure 2.3: Variation in crystallite size and FWHM of BST5 powder as a function of milling time.

2.2.6 Uniaxial pressing:

The next step in the process is to compact the pulverized powders in to cylindrical discs (referred as green pellets) by uniaxial pressing. The compaction of the powder should be done slowly to facilitate the escape of the entrapped air. To make green pellets of the ceramic powder, a rigid die which is rust free is to be used. The die and plunger used in the present study is shown in figure 2.4a and the uniaxial press is shown in figure 2.4b. Prior to every pressing of the BST5 green pellet, dummy discs of stearic acid are made to ensure that the walls of the die and plunger are free of dust, rust and other contaminations. The inner diameter of the die used in the present study is 57 mm, which is also the diameter of the green pellets. The thickness of the green pellet is determined by the amount of material (BST5 powder) used and the force applied. Depending up on the amount of material used, the force was varied between 10 and 15 ton to make green pellets of BST5. At this stage (prior to the sintering process) the density of the green pellet would be between 50 and 55% of the theoretical density of bulk BST5 (ρ_o=5.58 g/cm^3). In order to increase the strength of the green pellets, binding agents such as polyvinyl alcohol (PVA) are generally used[8]. These binding agents are volatile and get removed during sintering process. Though it looks advantageous, it has its own short

comings, such as formation of pores, dents and crevice, which would lead to higher porosity, poor density and inferior quality of the end product. So, in the present study no such binding agents were used.

Figure 2.4a: Photograph of the die and plunger used in this study.

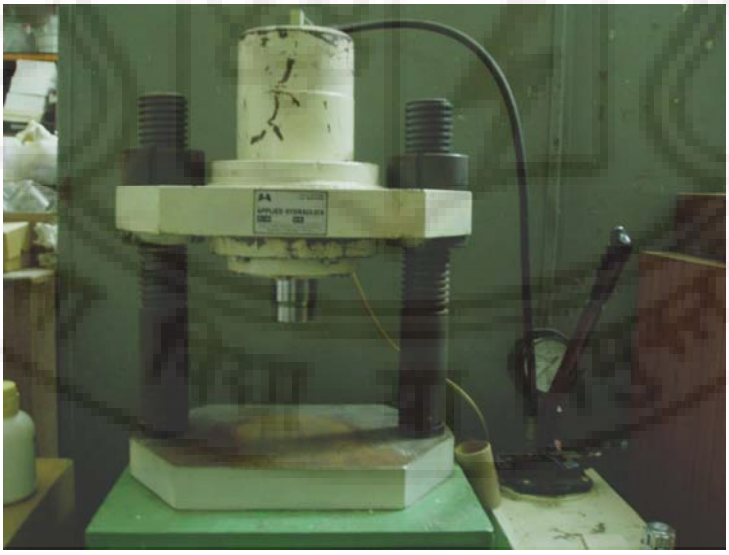

Figure 2.4b: Photograph of the uniaxial press used in this study.

2.2.7 Sintering:

Sintering is the final stage of the target preparation process[9]. The objective of sintering in the present study is to reduce porosity in the compact target material and also to realize targets of the required diameter and thickness. The elimination of porosity and densification of the target material in this stage is determined by the sintering temperature and duration.

In the present study, the green pellets were subjected to various sintering treatments as shown in table 2.1 below, (ρ/ρ_o x 100) is the percentage of the measured density relative to theoretical density (termed as "relative density" from here on).

Sample Code	Sintering Temperature (^oC)	Sintering Duration (hrs)	Volume Shrinkage (%)	ρ/ρ_0 (%)
Green pellet	none	none	-	55.15
BST1a	1100	1	5.89	70.37
BST1b	1100	2	5.97	70.43
BST1c	1100	3	6.21	70.61
BST1d	1100	4	6.32	70.7
BST2a	1200	1	11.59	74.91
BST2b	1200	2	14.85	77.77
BST2c	1200	3	17.14	79.92
BST2d	1200	4	18.24	81.00
BST3a	1300	1	17.24	80.00
BST3b	1300	2	20.18	82.97
BST3c	1300	3	22.04	84.94
BST3d	1300	4	22.53	85.78
BST4a	1400	1	30.27	94.98
BST4b	**1400**	**2**	**31.05**	**96.05**
BST5a	1350	1	22.04	85.01
BST5b	1350	2	26.39	89.96
BST5c	1350	3	27.96	91.93
BST5d	1350	4	28.80	93.01

Table 2.1: Sintering behavior for BST5 target material.

The plot in figure 2.5 shows the variation in shrinkage with sintering temperature of the BST5 green pellets.

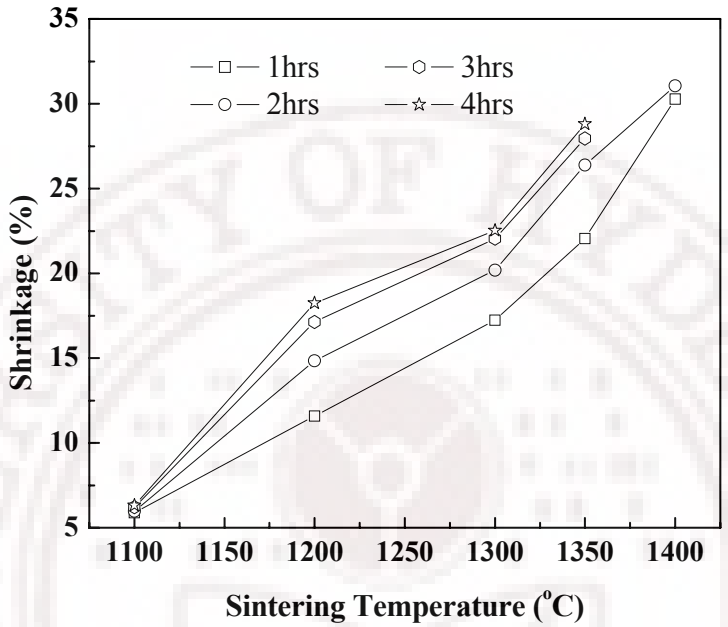

Figure 2.5: Percentage of shrinkage in BST5 ceramics sintered at various temperatures and durations.

It can be observed from the above plot that the shrinkage increases with increase in temperature and duration. The increase is attributed to the densification of the samples. Figure 2.6 confirms the increase in relative density of the samples with increase in sintering temperature and duration.

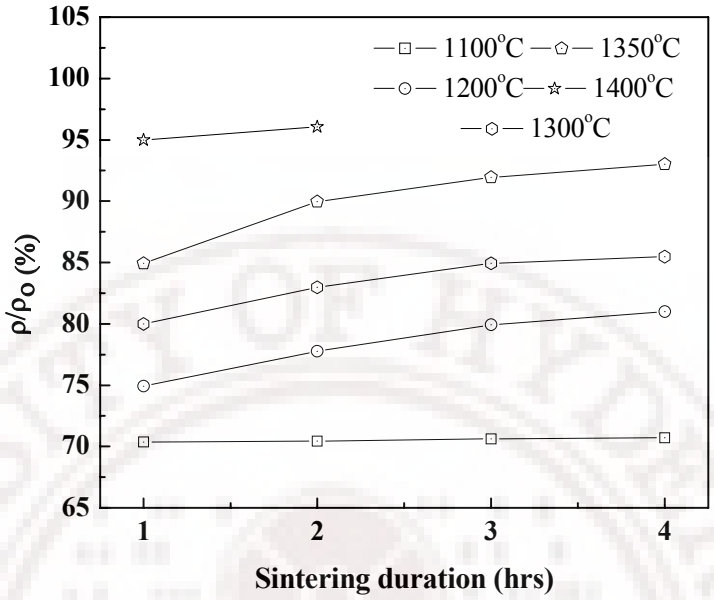

Figure 2.6: Relative density of BST5 ceramics subjected to various sintering durations and temperatures.

The optimized sintering condition for BST5 target preparation in the present study is 1400°C for 2hrs. This sintering condition yielded the maximum relative density of 96%. The SEM micrograph of the sintered target is shown in figure 2.7.

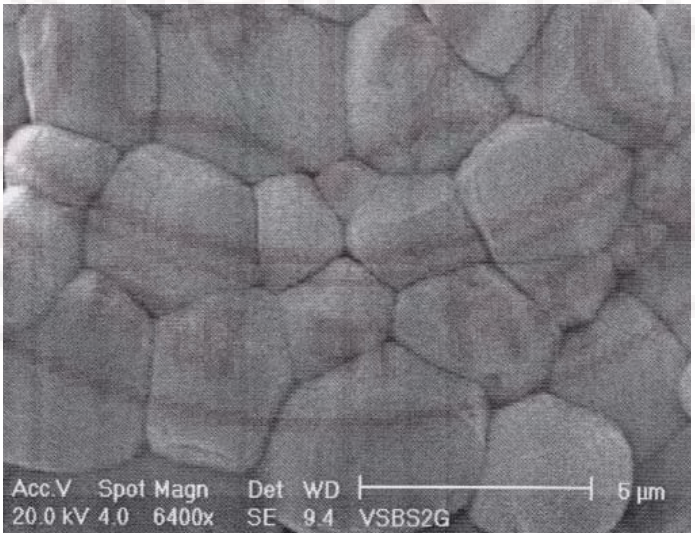

Figure 2.7: SEM micrograph of sintered BST5 target material.

The samples sintered between 1100°C and 1300°C did not yield the required density even after sintering for 4 hrs. A sintering condition of 1350°C for 2hrs and above

was required to achieve relative density of >90%. The green pellets which were subjected to a sintering condition of 1400^{o}C for 3 hrs and 4 hrs resulted in cracks propagating through the thickness of the material, reaction with the alumina supporting plate and black colored surface (indicating oxygen deficiency) and hence cannot be used as target material in sputtering process. The photographs of some of the targets prepared are shown in figure2.8.

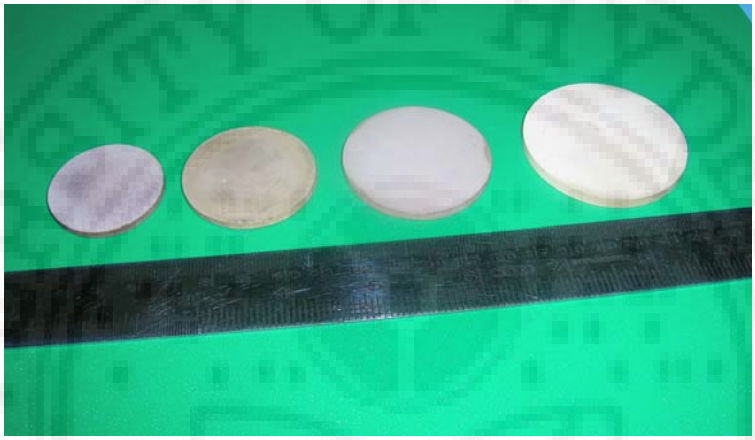

Figure 2.8: Photographs of the BST5 targets prepared.

2.3 Thin film deposition by RF magnetron sputtering:

RF magnetron sputtering has been widely accepted as one of the versatile techniques for the deposition of high quality BST thin films by several research groups[10,11,12,13,14]. It has been employed for the following reasons: any solid material (metals, insulators and semiconductors) can be sputtered, complex compounds can be sputtered stoichiometrically, use of low gas pressure for sputtering, appreciable rates of deposition and uniformity over large area is possible. The parameters such as the RF power density (in W/cm^2), substrate temperature, sputter gas mixture i.e, the Ar/O_2 ratio (from here on referred as oxygen mixing percentage, OMP), working/sputtering gas pressure and substrate to target distance can be controlled to influence the material properties of the sputtered films. It is important to note that the control over parameters that influence the physical properties is in general, greater during deposition (*in situ*) than it is after deposition (*ex situ*). Therefore, *in situ* treatment of thin films is always preferred over *ex situ* treatments. However, some of the thermal processes in the device fabrication procedure could amount to an *ex situ* annealing treatment as far as the film is concerned.

Hence, it is important to study the influence of each type of processing (*in situ* or *ex situ*) and optimize for ideal device behavior.

The schematic of the RF magnetron sputtering system used in this work is shown in figure 2.9. It consists of a 30 liter stainless steel vacuum chamber (VC) which houses 3 cathodes and a substrate holder. Out of the 3 cathodes, 2 are RF powered while the other one is dc powered. One of the RF powered cathodes was used for the deposition of BST5 thin films.

During deposition of thin films, the vacuum chamber is continuously cooled by flow of water through the water cooling jackets fitted on the exterior to the vacuum chamber. The vacuum chamber is evacuated through the electro-pneumatic roughing valve (RV) from atmospheric pressure to $\leq 2 \times 10^{-3}$ Torr using a rotary vane mechanical pump (RP, DS-102, Varian, Italy), with an approximate pumping speed of 6.84 m^3h^{-1}. The vacuum chamber is isolated from the turbo molecular pump (TMP, Turbo-V 301, Varian, Italy) through a mechanical screw driven gate valve (GV) which is attached to the VC by a 6" conflat flange with copper gasket. The pumping speed of the TMP is about 15 $m^3 h^{-1}$. Once the chamber pressure reaches $\leq 2 \times 10^{-3}$ Torr, the RV is closed and the TMP is evacuated through electro-pneumatic backing valve (BV). As the fore-line pressure reaches $\leq 2 \times 10^{-3}$ Torr, the TMP is switched on and the GV is opened. The pressure in the vacuum chamber can now be brought into the high vacuum regime. The pressure is monitored using a cold cathode gauge (Pfeiffer vacuum, Germany). A base pressure of 2 x 10^{-6} Torr can be achieved in about 2 hrs. Two mass flow controllers (MFC, Bronckhurst Hi-tech, Ruurlo-Holland) which can independently control flows of argon (Ar, 99.9% purity) and molecular oxygen (O_2, 99.999% purity) are connected to the VC through a solenoid valve. The use of a gas mixture of inert argon and reactive oxygen helps to achieve the same stoichiometry as that of the target in the film. The working pressure during sputtering is controlled partly by adjusting the total input gas flow and by reducing the throughput of the TMP by partially closing the manual gate valve. The working pressure is monitored by a capacitance manometer (CMM, Inficon, USA). Once the pre-determined working pressure and deposition temperature is achieved, the sputter deposition process is started by initiating the plasma using the RF power generator (RF-

VII Inc, USA) coupled with the matching network. The VC walls and substrate holding stage form the grounded electrode.

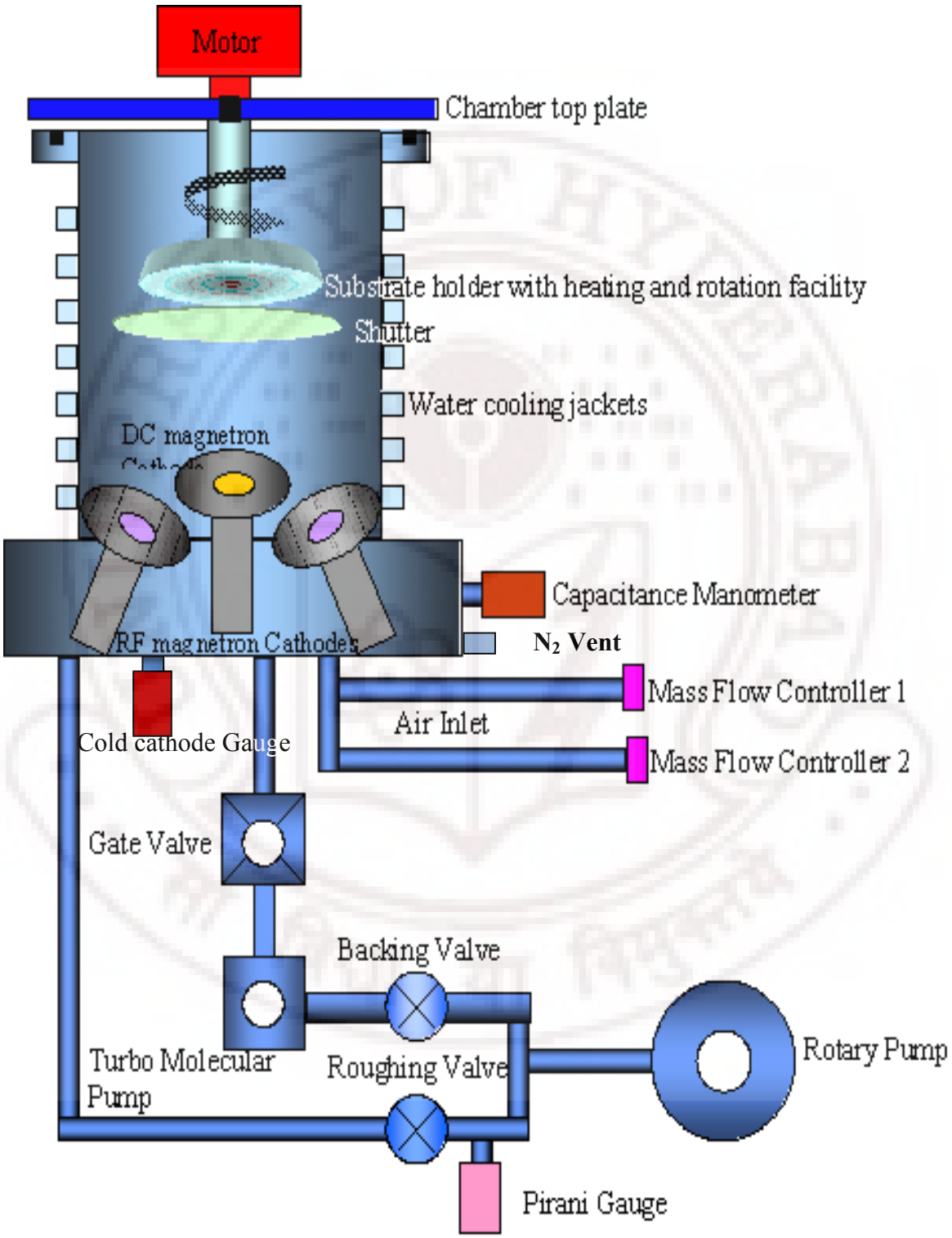

Figure 2.9: Schematic of the sputtering system used in this study.

The substrate holding stage (AJA International, USA) is placed on the top plate of the VC and is capable of rotating on its own axis and at the same time allows the deposition of oxide films at temperatures ranging from room temperature up to 800^{o}C. Prior to every sputter deposition, the target was conditioned by pre-sputtering[15] for an hour by closing the shutter. The system is vented to atmosphere after closing all valves to isolate the pumps from the VC. The photographs of the sputter deposition unit, inner view of the vacuum chamber and RF plasma generated during sputtering of BST5 are shown in figure 2.10.

Figure 2.10: Photograph of (a) the sputtering system, (b) inner view of the vacuum chamber and (c) RF plasma generated during BST5 deposition.

As mentioned earlier, parameters such as RF power density, substrate temperature, OMP, working gas pressure, substrate to target distance, type of substrate used and post-deposition annealing treatments influence the properties of the sputtered films. Optimization of all the sputtering conditions for the best material properties in the deposited film can be very cumbersome and time consuming. Initial studies indicated that

the power densities < 2.5 W/cm^2 resulted in very low rates of sputtering where as power densities > 3.5 W/cm^2 resulted in target damage. Hence, the power density was fixed at 3W/cm^2. The substrate to target distance was fixed at 5cms because higher distances led to lower deposition rates and lower distances led to damage of the vacuum seals near the cathode due to heat radiating from the substrate heater at higher temperatures. The working pressure was fixed at 20 mTorr. The different deposition parameters used in the current study are given in table 2.2.

Parameter	Value
Power density (W/cm^2)	3.0 W/cm^2
Substrate to target distance (cms)	5 cms
Working pressure (mTorr)	20 mTorr
Oxygen mixing percentage, OMP (%)	Varied from 0-100 in steps of 25%
Substrate Temperature (^{o}C)	RT and 400^{o}C to 800^{o}C
Substrate Type	Fused silica and Pt/Si as the primary substrates. Single crystal substrates: $LaAlO_3$, MgO, c- plane sapphire. Si for RBS and XPS analysis.
Post-deposition annealing treatment	900^{o}C for 1 min (Quasi rapid thermal annealing). 400^{o}C to 1000^{o}C for 1 hour

Table 2.2: Sputter deposition parameters used in the current study.

Out of the above mentioned parameters, substrate temperature and post-deposition annealing treatments highly influences the crystalline property of BST5 thin films where as the influence of OMP i.e., Ar:O_2 ratio, during sputtering appear to be complex; the ambient oxygen partial pressure not only influences the oxygen incorporation into the films, but also the titanium non-stoichiometry and the A/B site ratio which are strongly linked to the zero bias field dielectric permittivity and loss. The exact OMP in sputter deposition of oxides is always under considerable scrutiny in any oxide system[16,17,18]. There is a tradeoff between the ideal level of energetic impingement in an oxide containing plasma, and the risk of anion deficiency that can occur under low OMP. Hence, it is important to systematically vary OMP and study its impact on the cation and anion stoichiometry.

2.4 Compositional characterization:

For compositional analysis, BST5 thin films were deposited on RCA[19] cleaned Si substrates. The OMP was varied from 0-100% in steps of 25% while keeping the other

parameters fixed. Deposition and characterization of BST5 thin films deposited at 100% oxygen ambient has been carried out and reported for the first time by our group.

The composition and rate of deposition (derived from the thickness) of BST5 films deposited at 800^{o}C was determined using Rutherford backscattering spectroscopy (RBS). X-ray photoelectron spectroscopy (XPS) provided information about the chemical bonds present near the surface. The important objective of the RBS and XPS experiments was to establish the composition of the films sputtered from a stoichiometric target of $Ba_{0.5}Sr_{0.5}TiO_3$ and to establish the OMP that yields the composition of the sputtered film close to that of the target. The results of these analyses are provided below; in each case, a brief introduction to the technique is also given.

2.4.1 Rutherford Backscattering Spectroscopy:

The apparatus for Rutherford backscattering analysis of thin films consist of three major components:

1. A helium ion source.
2. An accelerator to deliver mono-energetic helium ions.
3. A solid state detector to measure the energy of scattered ions.

A schematic representation of the system is shown in figure 2.11.

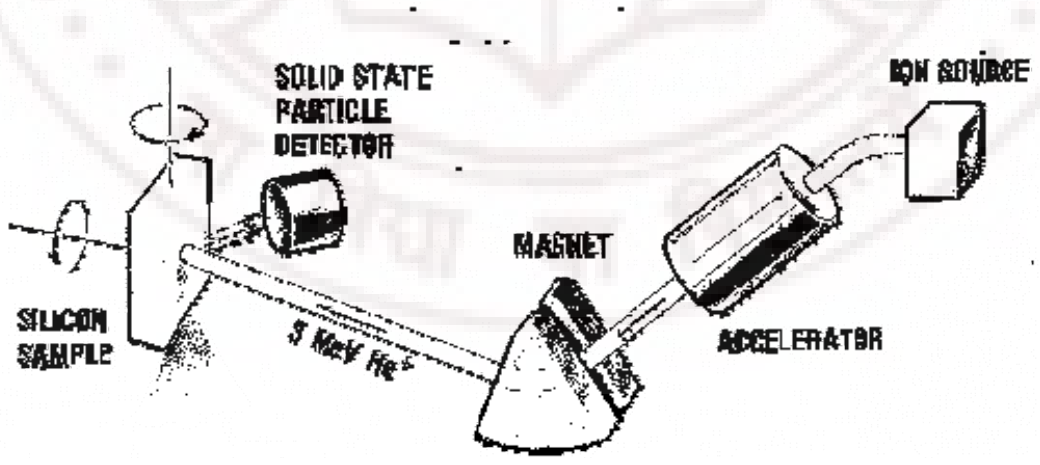

Figure 2.11: Schematic diagram of a Rutherford Backscattering Spectroscope.

In Rutherford backscattering, the sample under study is bombarded with mono-energetic beam of $^{4}He^{+}$ particles, which travel hundreds of nanometers or even microns

into the sample. The scattering processes which the ions undergo are influenced by the constituent atoms present in the sample. This allows determining the composition of the sample. The backscattered particles are detected by the solid-state detector system which measures the energies of the particles. During the collision, energy is transferred from the incident particle to the atoms of the target specimen. The change in energy of the scattered particle depends on the masses of incoming and target atoms. If, incident particle of mass M_1 and energy E_0 bombard on a target atom of mass M_2, the residual energy E of the particle scattered at angle θ after collision can be expressed as[20]:

$$E = k\,E_0 \qquad (2.4)$$

$$k = \left[\frac{\left(M_1 Cos\theta + \sqrt{M_2^2 - M_1^2 Sin^2\theta}\right)}{M_1 + M_2}\right]^{1/2} \qquad (2.5)$$

where, k is known as the kinematic scattering factor, which is actually the energy ratio of the particle before and after the collision.

Since $M_1 = 4$ for He, E_o is determined by the accelerator and E is measured by the detector, k is simply determined by the mass of the target atoms.

In the present study, the RBS experiments were carried out at IIT Kanpur, using 2MeV $^4He^+$ particles delivered from 1.7MV Tandetron accelerator. The scattered particles were detected at an angle of 155^0 with a surface barrier detector having resolution of 18keV.

The spectra were theoretically fitted using SIMNRA software[21]. The measured and fitted RBS spectra are shown in figure 2.12. The fit between the measured and calculated data is reasonably good for the Ba, Sr, Ti and O atoms in the films.

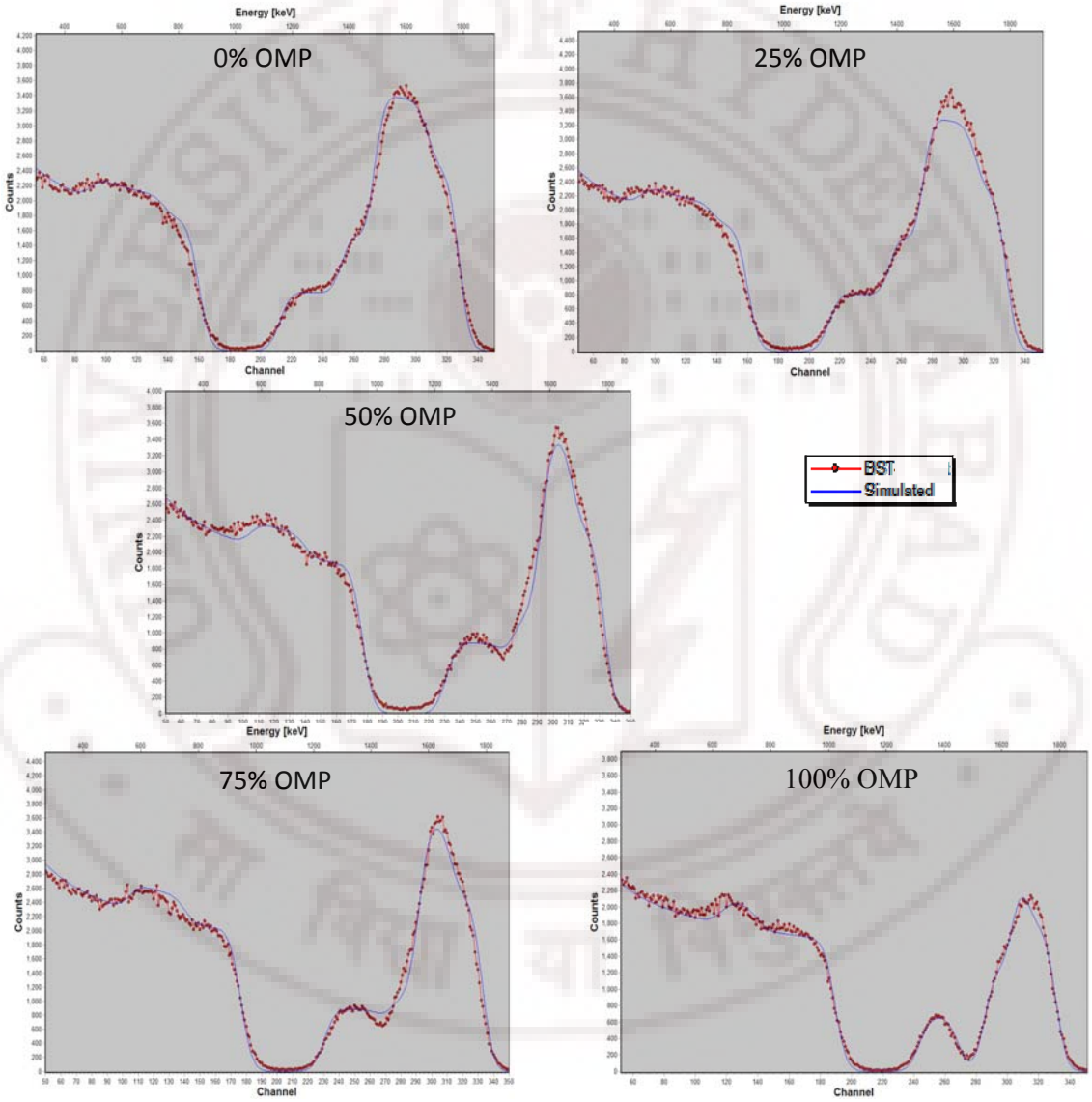

Figure 2.12: Measured and simulated RBS ($^4He^+$) data for BST5 films deposited from a $Ba_{0.5}Sr_{0.5}TiO_3$ target as a function of OMP.

Figure 2.13 provides the stoichiometry information and rate of deposition determined by SIMNRA.

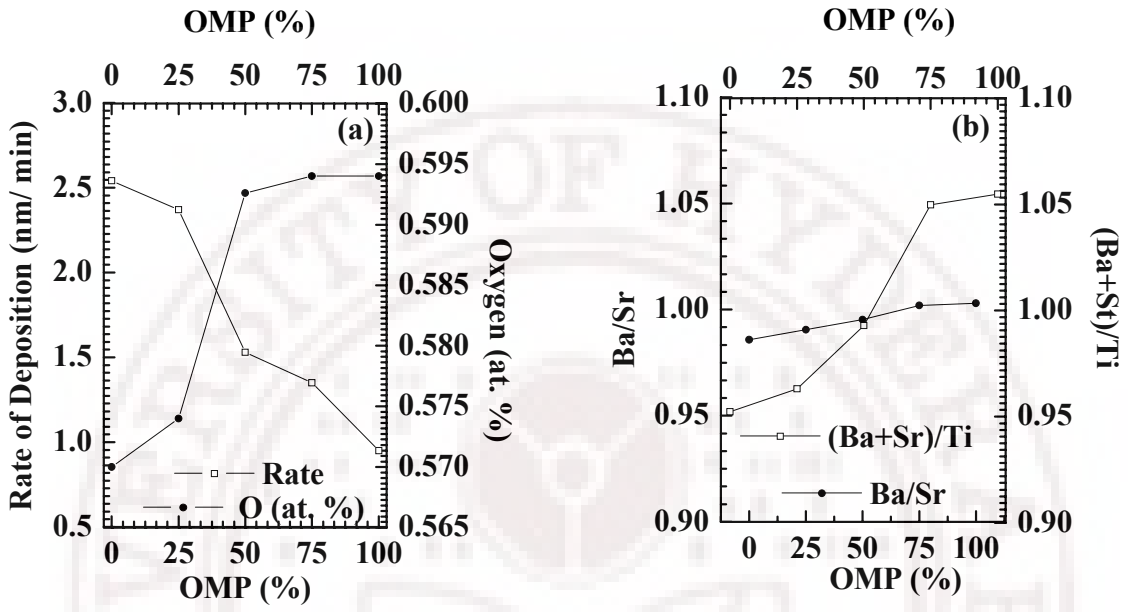

Figure 2.13: Compositional analysis of BST5 thin films as a function on OMP (a) Rate of deposition and oxygen incorporation as a function of OMP (b) Ba/Sr ratio and (Ba+Sr)/Ti ratio of BST5 films as a function of OMP.

From figure 2.13a, it can be observed that the rate of deposition decreased with increase in OMP. The decrease in deposition rate with increase in OMP is due to lower molecular weight of oxygen (O_2, 31.998) when compared to that of Ar (39.948). Figure 2.13 also shows the variation in film composition with OMP. Note that the ideal composition of $Ba_{0.5}Sr_{0.5}TiO_3$ is 10 at.% Ba, 10 at.% Sr, 20 at.% Ti and 60 at.% oxygen. It can be noted that the films deposited at 0 and 25 % OMP are found to be significantly oxygen deficient. Oxygen vacancies are undesirable, because they increase the optical and microwave loss of the BST thin films[22,23,24]. The films deposited at 50% OMP and above show improved oxygen stoichiometry.

As discussed earlier, the Ba/Sr ratio influences the Curie point of the film. In the present case, the Ba/Sr ratio remains rather constant at a value close to the nominal target composition. This indicates that for these set of conditions, OMP has low impact on the A-site stoichiometry.

On the other hand, it is found that Ti- stoichiometry in the films is highly influenced by OMP. The films deposited at 0 and 25 % OMP are Ti-rich, while BST5 films deposited at 75 and 100% OMP are Ti-deficient. In general, BST thin films with a (Ba+Sr)/Ti ratio close to 1 have shown the highest permittivity and tunability[25,26]. The excess Ti in the Ti-rich samples can be accommodated in the grains and/or grain boundaries depending up on their concentration. High concentration of Ti can lead to precipitations of amorphous TiO_{2-x} between the grains[27].

Close replication of the target stoichiometry was achieved for films sputter deposited at 800^{o}C with working pressure of 20 mTorr using 50% OMP.

The same set of samples, which were used for RBS analysis were used for X-ray Photoelectron Spectroscopy (XPS) also. XPS provides information about the chemical bonds present near the surface of films.

2.4.2 X-ray Photoelectron Spectroscopy:

X-ray Photoelectron Spectroscopy (XPS, also known as Electron Spectroscopy for Chemical Analysis, ESCA) is a surface analytical technique, which is based upon the photoelectric effect[28]. The core level shift provides information about the chemical bonding and valence states in a thin surface layer (~15Å) of the sample [20]. Each atom in the surface has core electrons with a characteristic binding energy that is conceptually, not strictly, equal to the ionization energy of that electron. When the sample surface is irradiated using a monochromatic x-ray beam, the energy of the x-ray photon is absorbed by the core electron of the atom. If the photon energy, hv, is large enough, the core electron will then escape at a takeoff angle, θ, from the surface plane of the sample. The emitted electron with kinetic energy of E_k is referred to as the photoelectron. The binding energy, E_b of the core electron is give by the relation[29],

$$E_b = hv - E_k^{-} \varphi \qquad (2.6)$$

where hv is the energy of the x-ray photon. E_k is measured by the energy analyzer of the instrument. As, the work function, φ, induced by the analyzer can be compensated artificially, the above equation can be given as,

$$E_b = hv - E_k \qquad (2.7)$$

The photoemission process is shown in figure 2.14. Unlike RBS, XPS does not provide accurate compositional information without the use of appropriate reference standards. The X-ray Photoelectron Spectroscopy (XPS) measurements described in this section were performed at Indian Institute of Chemical Technology (IICT), Hyderabad using a Kratos Axis 165 Spectrometer with Mg K_α radiation (1253.6 eV) and a takeoff angle of $\theta=45^o$. The X-ray power supply was run at 15 kV and 5 mA. The pressure in the analysis chamber during the scans was $\sim 10^{-9}$ Torr.

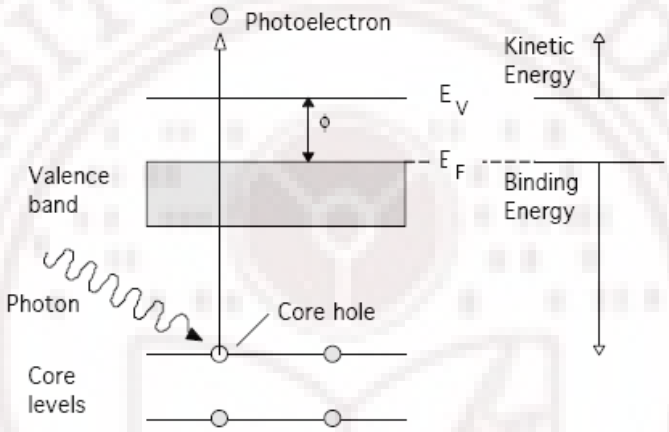

Figure 2.14: Photoemission process.

For samples such as BST which are highly insulating, a positive charge zone will be formed on the surface as the photoelectrons are emitted out of the sample surface. The positive potential can vary from few volts to tens of volts and this would result in a shift in the XPS peak position. In such a case, the binding energy of adventitious Carbon, C 1s peak with a characteristic binding energy of 284.8 eV is used as the reference for calibration. A low-energy electron flood gun is used to deliver the electrons to the sample surface, in order to neutralize the surface charge during data acquisition. The electron flood gun can be tuned to provide the right current to push the XPS peaks back to the real position.

The core electron of any element has a unique binding energy, which is like a "fingerprint" and is sensitive to the chemical environment of the element. The core electron of the same atom bonded to different chemical species can exhibit a change in the binding energy. This variation in the binding energy results in the shift of the corresponding XPS peak, which would range from 0.1 eV to 10eV. This effect is called

the "chemical shift", which is useful in identifying the chemical state of surface elements[30].

For the samples deposited as a function of OMP, a complete spectrum (survey scan) of data for ejected photoelectrons with energies in the range 0 to 1100 eV was gathered, with a 2 eV step size. A typical survey spectrum on BST5 is shown in figure 2.15.

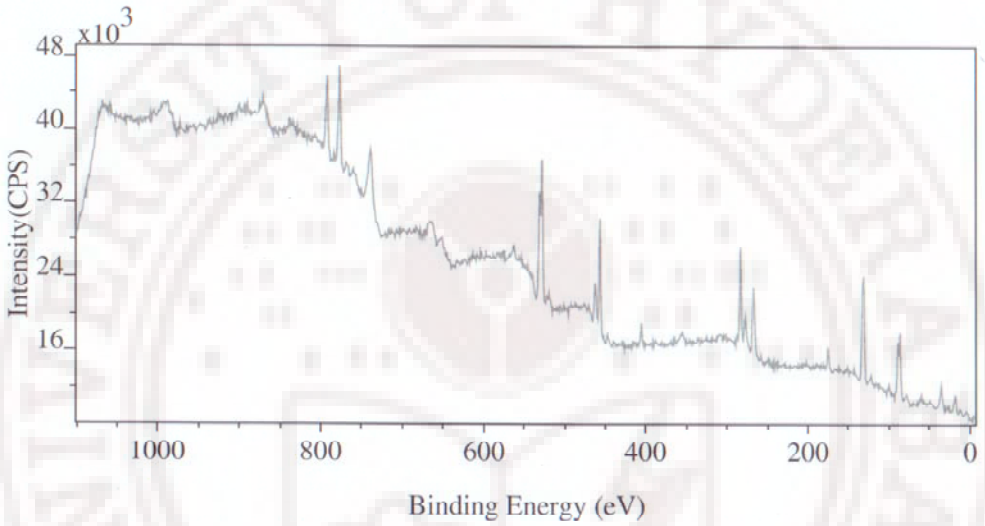

Figure2.15: XPS survey spectrum of BST5 thin film deposited at 50% OMP.

Refined spectra with a 100 meV step size were also gathered and fitted with a Lorentzian function for the constituent elements in BST5. The Ba 3*d*, Sr 3*d*, Ti 2*p* and O1*s* spectrum were recorded in the binding energies ranging from ~775 to 800 eV, ~129 to 139 eV, ~440 to 480 eV and ~524 to 540 eV, respectively.

Traces of carbon were detected at 284.6 eV in all the BST5 films deposited at different OMP as shown in figure 2.16 Compensation for sample charging was performed by comparison of the C 1*s* peak in each of the wide spectra with the known value (284.6 eV) of the C 1*s* peak.

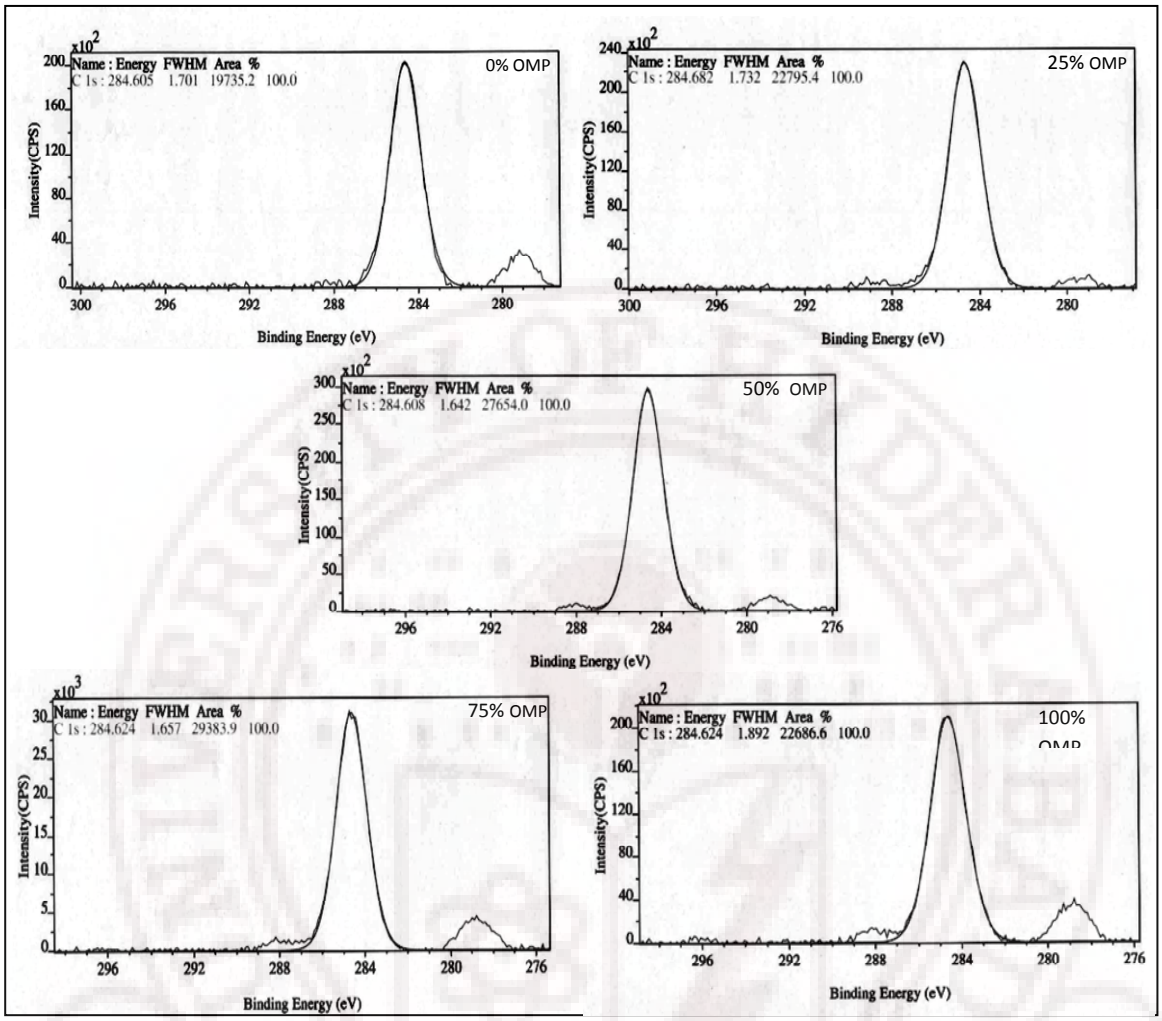

Figure 2.16: C 1s photoemission spectra of BST5 films deposited at different OMP.

The above photoelectron spectra show a prominent peak at 284.6 eV. This peak is attributed to the adsorbed hydrocarbon (adventitious carbon) having a general formula C_xH_x.[31] Apart from the adventitious hydrocarbon no other signal pertaining to any other additional component is observed. It is noted that the binding energy of C (1s) electron in metallic carbonates is between 289.6 -290.5eV. Since none of the above spectra show any components in this energy range, it can be concluded that all the samples are devoid of contaminations in the form of metallic carbonates on the surface.

The Ti (2p) photoelectron spectra of BST5 films deposited at different OMP is shown in figure 2.17. It can be seen that the spectra are identical in shape and the binding

energy of $2p_{1/2}$ and $2p_{3/2}$ in all the samples are centered around 463.5±0.2 and 458±0.2 eV respectively.

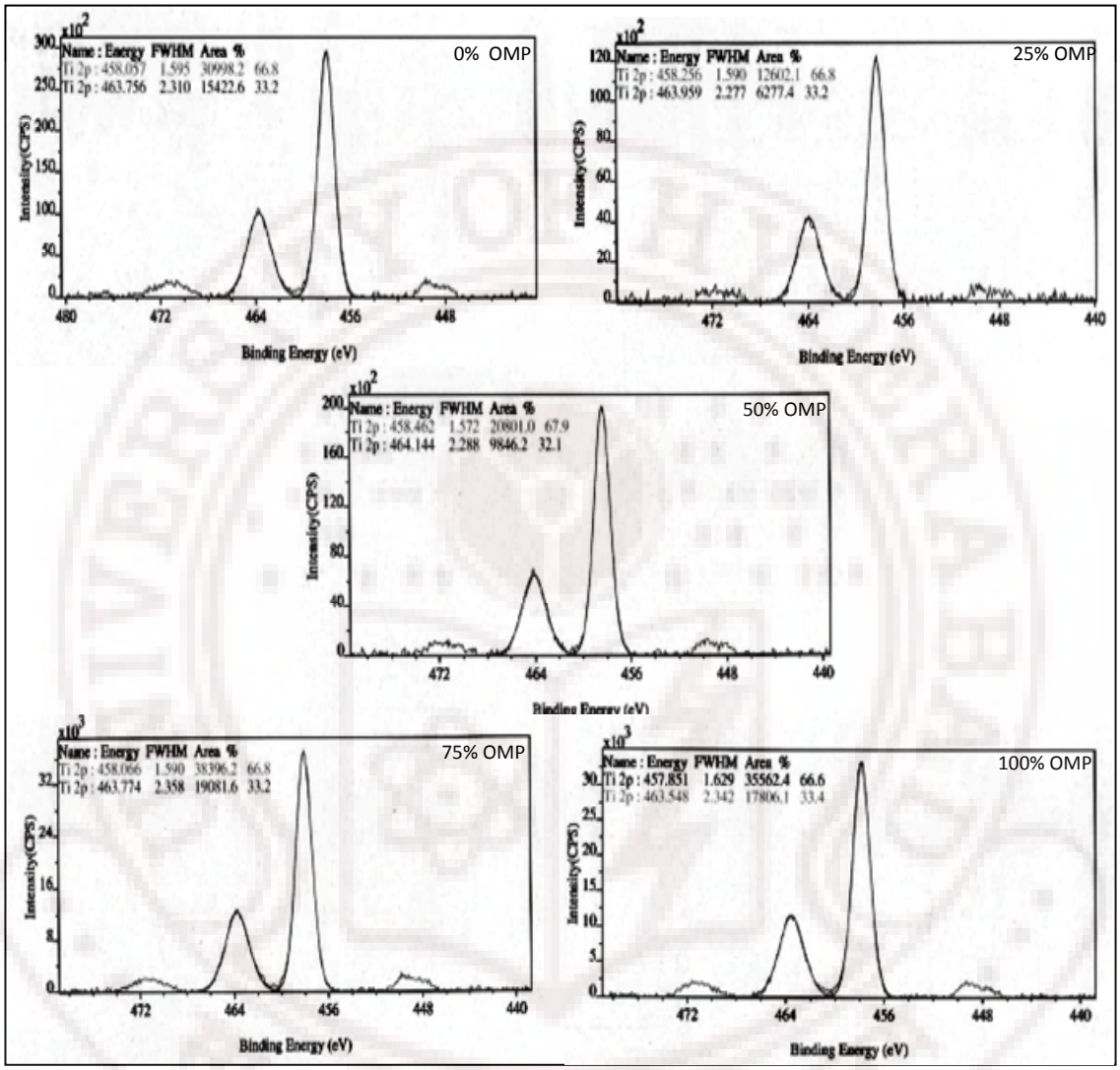

Figure 2.17: Ti 2p photoemission spectra of BST5 films deposited at different OMP.

The valance state of Ti in all the films were confirmed to be Ti^{4+}, because it is known that the binding energy of Ti $2p_{3/2}$ electrons in 3+ and 2+ states shifts to lower binding energies by 2.0 and 3.6 eV respectively. The difference in binding energies of the two peaks is about 5.7eV, which is very close to the reported value of 5.8 eV for Ti-O in the perovskite lattice[32]. The difference in $2p_{1/2}$ and $2p_{3/2}$ in metallic Ti is about 6.7eV. So, it could be concluded that the Ti in the present case corresponds to Ti in the oxide

perovskite lattice and does not have any metallic chemical state even for films deposited at 0 and 25% OMP.

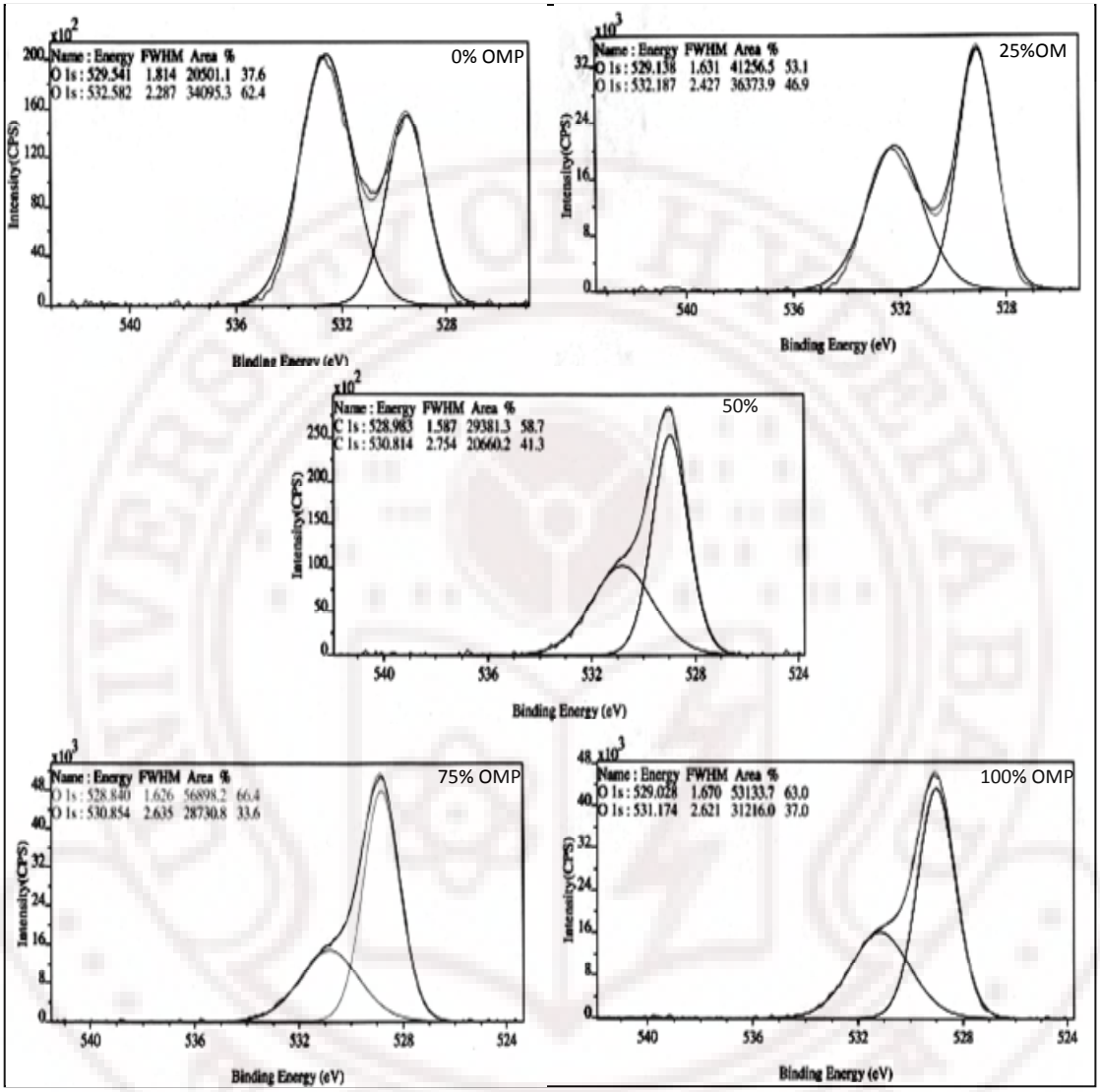

Figure 2.18: O1s photoemission spectra of BST5 films deposited at different OMP.

The O (1s) spectra in figure 2.18 show two components; the peak at 529 eV correspond to the binding energy of the O in the BST lattice while the other centered about 531.5 eV is indicative of defects. These defects can arise due to strongly chemisorbed moisture, metallic hydroxides or carbonates (CO_3^{2-})[33]. The existence of metallic carbonates can be completely neglected as the C (1s) spectra do not show any signal pertaining to metallic carbonates in the energy range of 289.6 -290.5eV. Hence, the defect peak might arise due to formation of metallic hydroxides on the surface.

The other observation which could be made from the above spectra is that the intensity of the higher binding energy component of O 1s decreases with increase in OMP. This shows that the BST5 films deposited at 0 and 25% OMP have oxygen vacancies which were confirmed by RBS analysis also. As the oxygen percentage (OMP) during sputtering is increased, the density of oxygen vacancies decrease and thus the intensity of the higher binding energy component of the O 1s decreases.

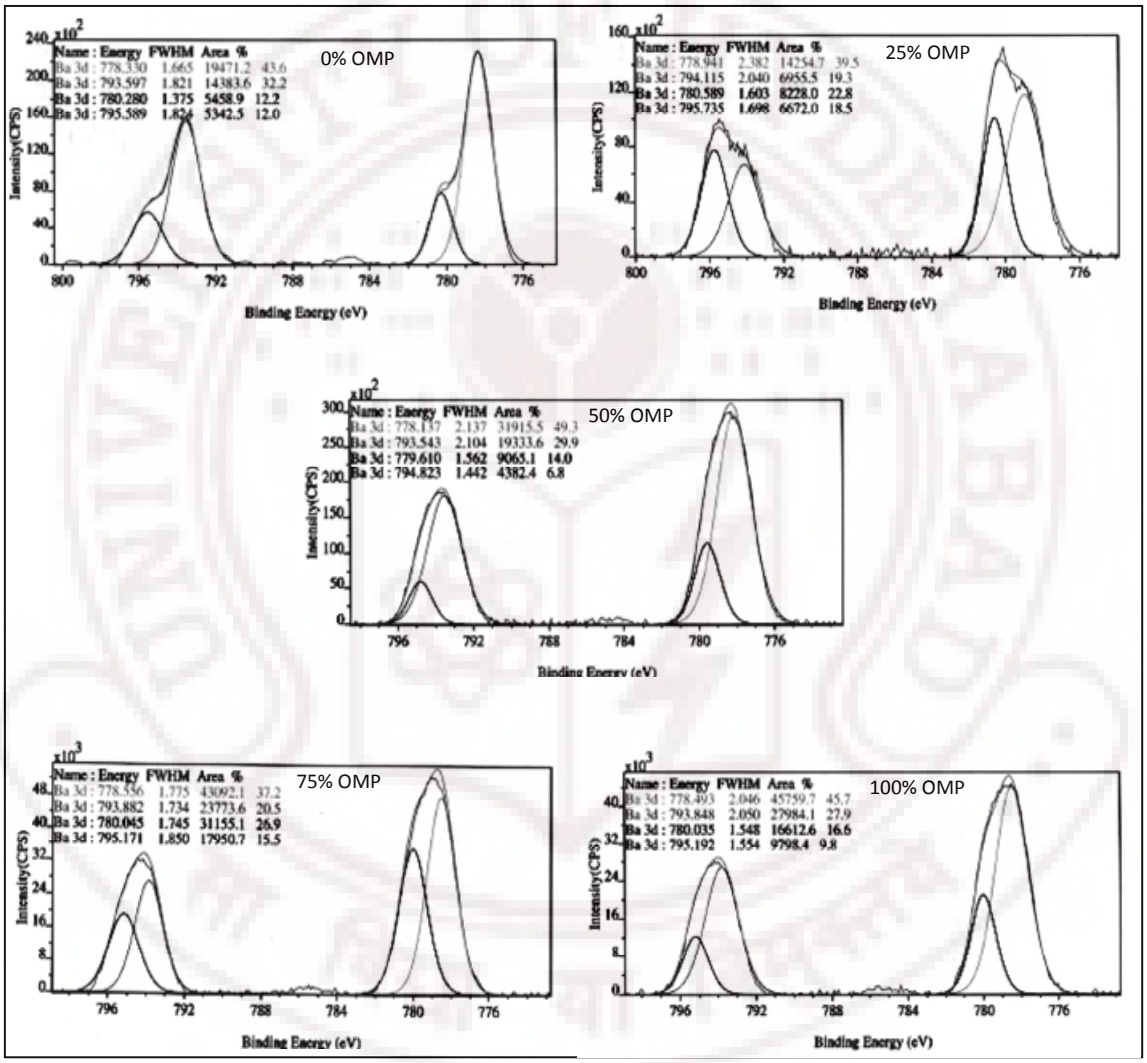

Figure 2.19: Ba 3d photoemission spectra of BST5 films deposited at different OMP.

XPS spectra of the Ba (3d) of BST5 films deposited at different OMP are shown in figure 2.19. Each of the Ba $3d_{3/2}$ and Ba $3d_{5/2}$ peaks can be fitted with two peaks separated by around 1.5±0.1 eV. The lower binding-energy peaks, i.e., 795.3 and 778.5 eV can be assigned to Ba atoms in the BST perovskite lattice[34] where as the high binding

energy peaks at 795.7 and 780.5 eV are assigned to defects[35]. Since the formation of a carbonate on the surface is neglected, the most probable reason for this high energy component would be the formation of hyderoxides[36].

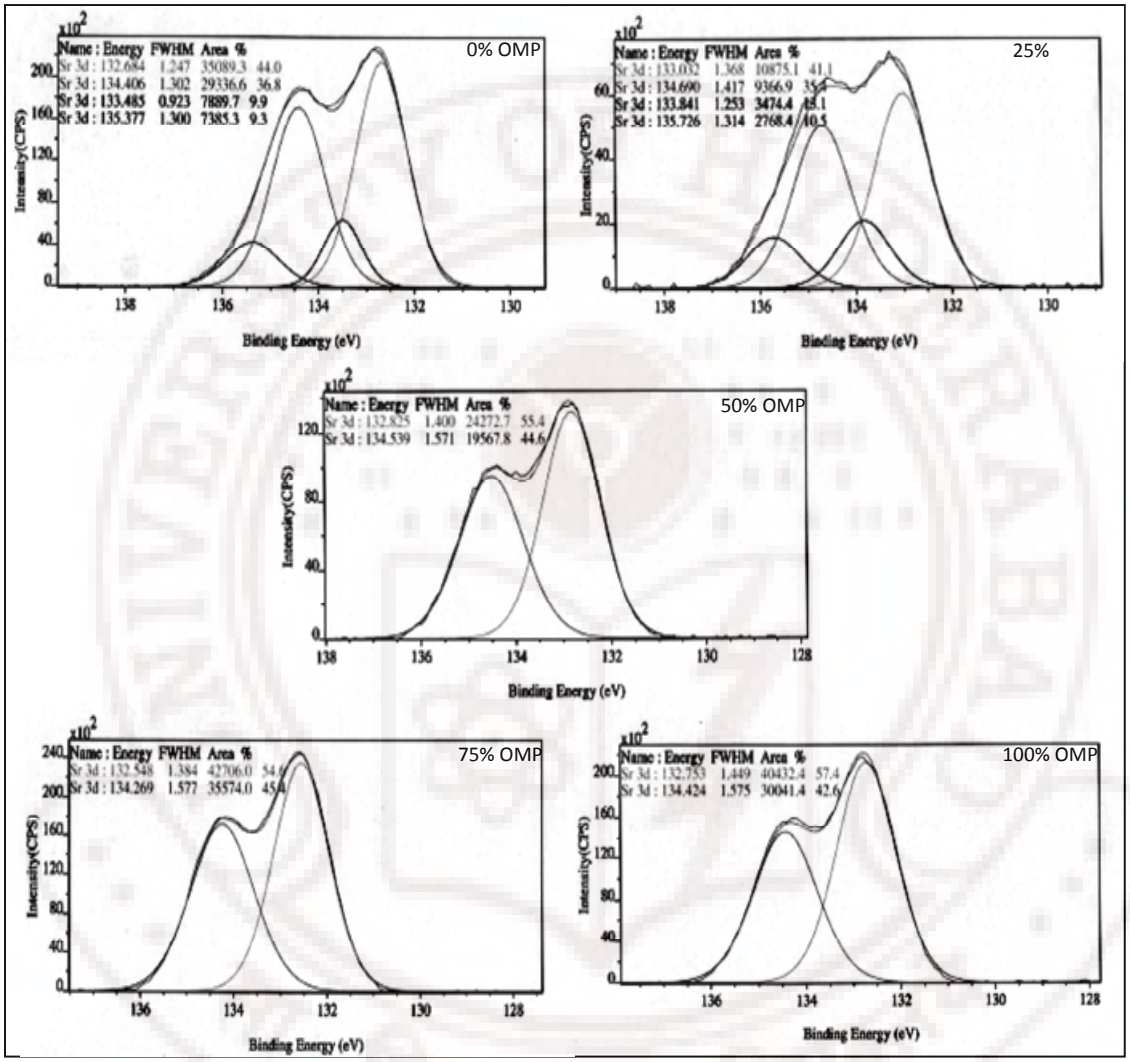

Figure 2.20: Sr 3d photoemission spectra of BST5 films deposited at different OMP.

It could also be seen that the BST5 films deposited at 0% and 25% OMP has two distinct high binging energy components each in Ba $3d_{3/2}$ and Ba $3d_{5/2}$. But as the OMP increases the high energy components merges with that of the low energy peak, indicating the reduction in the defect density of Ba on the film surface. This can be observed even more clearly in Sr (3d) spectra shown in figure 2.20, where the high energy components of Sr $3d_{3/2}$ and Sr $3d_{5/2}$ vanished completely for the films deposited at higher OMP.

2.5 Summary:

In summary, this chapter has presented a study on the fabrication of ceramic targets of $Ba_{0.5}Sr_{0.5}TiO_3$ (BST5) by solid-state reaction method. First, the calcination process was optimized to obtain single phase BST5 powders at 1000^oC. The calcined powder was then pulverized in a planetary ball mill for 3 hrs. The pulverized powder was then pressed in to cylindrical discs and sintered at different conditions. The sintering conditions i.e., sintering time and temperature were optimized to obtain high density sputtering targets with good surface finish, suitable for sputtering. The percentage of volume shrinkage and the relative density of the material after sintering were estimated. A sintering condition of 1400^oC for 2 hrs yielded high quality target material with 96% relative density. The crystallite size and phase purity was confirmed by X-ray diffraction technique. The surface morphology was studied using scanning electron microscopy.

Thin films of BST5 were deposited by RF magnetron sputtering technique from a single stoichiometric target of BST5. RF magnetron sputtering has been widely accepted as one of the versatile techniques for the deposition of high quality BST thin films.

The influence of oxygen mixing percentage (OMP) on the composition of BST5 film was estimated by RBS and XPS techniques. The total working pressure was fixed at 20 mTorr. The results obtained from RBS analysis indicate that OMP not only influences the oxygen incorporation into the films, but also the (Ba+Sr)/ Ti ratio. The effect of OMP on Ba/Sr ratio was found to be marginal. The films deposited at 0 and 25% OMP were oxygen deficient and had excess Ti. A close replication of the target stoichiometry was achieved for films sputter deposited at 50% OMP.

The XPS results clearly indicated the presence of oxygen vacancies in the films deposited at 0 and 25% OMP, complementing the RBS results. The oxygen vacancy chemisorbs moisture, forming metal hydroxides on the surface of the film. An increase in OMP shows decrease in oxygen defect density.

An introduction to other characterization techniques used in this study to determine the structural, microstructural, optical and electrical properties have been discussed in the next Chapter.

References:

[1] W-K. Chu, J. W. Mayer and M. A. Nicolet, *Backscattering Spectrometry*, 1st ed., Academic Press, New York (1978).

[2] M. N. Rahaman, *Ceramic processing and sintering*, Marcel Dekker Inc., New York (2003).

[3] D. Seagal, *Chemical synthesis of advanced ceramic materials*, Cambridge University Press, Cambridge (1991).

[4] R. E. Carter, *J. Chem. Phys*., **34**, 2010 (1961).

[5] Kumaravinothan Sarma, Rehan Farooq, Katy Jarman, Robert C. Pullar, Peter K. Petrov, and Neil Mc N. Alford, *Integ. Ferroelectr*., **62**, 249 (2004).

[6] Yi-Cheng Liou, Jen-Hsien Chen and Chi-Ting Wu, *Mater. Res. Soc. Symp. Proc*., **848**, FF.3.3.1 (2005).

[7] C. Suryanarayana, *J. Prog. Mater. Sci*., **46**, 1 (2001).

[8] F. Ya. Kharitonov, S. S. Vishnevskaya and G. I. Barashenkov, *Refract. Indus. Ceram*., **27**, 208 (1986).

[9] S-J. Kang, *Sintering, densification, grain growth and microstructure*, Elsevier, Amesterdam (2002).

[10] P. Padmini, T.R. Taylor, M.J. Lefevre, A.S. Nagra, R.A. York and J.S. Speck, *Appl. Phys. Lett*., **75**, 3186 (1999).

[11] J. Im, O. Auciello and S. K. Streiffer, *Thin Solid Films*, **413**, 243 (2002).

[12] J. H. Won, S. H. Paek, Y. S. Hwang, K. K. Kim and Y. S. Cho, *J. Mate. Sci*., **6**, 616 (1995).

[13] C. B. Samantaray, A. Dhar, M. L. Mukherjee, D. Bhattacharya and S. K. Ray, *Mater. Sci. Engg. B*, **88**, 14 (2002).

[14] Brian Laughlin, Jon Ihlefeld, and Jon-Paul Maria, *Mat. Res. Soc. Symp. Proc*., **784**, C 5.3.1 (2004).

[15] J. Hanisch, E. Ahlswede and M. Powalla, *Thin Solid Films*, **516**, 7241 (2008).

[16] M. S. Tsai and T. Y. Tseng, *J. Phys. D: Appl. Phys*., **32**, 2141 (1999).

[17] K. Venkata Saravanan, K. Sudheendran, M. Ghanashyam Krishna, K. C. James Raju, *Ferroelectr*., **356**, 158 (2007).

[18] S. Ezhilvalavan and Tseung-Yuen Tseng, *Mater. Chem.Phys*., **65**, 227 (2000).

[19] K. Choi, H. Harris, S. Gangopadhyay and H. Temkin, *J. Vac. Sci. Technol. A*, **21**, 718 (2003).

[20] M. Ohring, *The Materials Science of Thin Films*, Academic Press, New Jersey (1992).

[21]M. Mayer, *SIMNRA User's Guide*, Max-Planck-Institut fÄur Plasmaphysik, Boltzmannstr. 2, D-85748 Garching, Germany, 2004. Available online: www.rzg.mpg.de/»mam

[22] A. Vorobiev, P. Rundqvist, K. Khamachane, and S. Gevorgian, *J. Appl. Phys*., **96**, 4642 (2004).

[23] Taeho Moon, Byungjoo Lee, Tae-Gon Kim, Jeongmin Oh, Young Woo Noh, Sangwook Nam and Byungwoo Park, *Appl. Phys. Lett*., **86**, 182904 (2005).

[24] M.W. Cole and R.G. Geyer, *Revista Mexicana De Fisica*, **50**, 232 (2004).

[25] J. Im, O. Auciello, P. K. Baumann, S. K. Streirer, D. Y. Kaufman and A. R. Krauss, *Appl. Phys. Lett*., **76**, 625 (2000).

[26] N. Pervez, P. Hansen and R. York, *Appl. Phys. Lett*., **85**, 4451 (2004).

[27] S. Stemmer, S.K. Streiffer, N.D. Browning and A.I. Kingon, *Appl. Phys. Lett*., **74**, 2432 (1999).

[28] J. A. Gardella Jr., *Anal. Chem*., **61**, 589A (1989).

[29] C. Kittel, *Introduction to Solid State Physics*, 7th ed. New York: John Wiley (1996).

[30] Friedrich Reinert and Stefan Hüfner, *New J. Phys*., **7**, 1 (2005).

[31] Sandip Halder, Ulrich Boettger, Theodor Schneller, Rainer Waser, Oliver Baldus, Philipp Jacobs and Martin Wehner, *Mater. Sci. Engg. B*, **133**, 235 (2006).

[32] N. V. Giridharan, R. Jatavel and P. Ramasamy, *Cryst. Res. Technol*., **36**, 65 **(**2001).

[33] M.E. Pilleux and V.M. Fuenzalida, *J. Appl. Phys*., **74**, 4664 (1993).

[34] J.T. Verhoven and H. Van Doveren, *Appl. Surf. Sci*., **5**, 361 (1980).

[35] C. Miot, E. Husson, C. Proust, R. Perre, J.P. Coutures, *J. Mater. Res*., **12**, 2388 (1997).

[36] Sanjiv Kumar, V. S. Raju and T. R. N. Kutty, *App. Surf. Sci*., **206**, 250 (2003).

Chapter III

Characterization techniques

3.1 Introduction:

In this chapter, we discuss the details of various analytical techniques used in the present study for thin film characterization. The techniques involve stylus profilometry for thickness measurements and X-ray diffraction for examining crystallinity, crystallite size and orientation. Dynamic Force Microscope (DFM) and Atomic Force Microscope (AFM) were used for surface topography and surface roughness determination. UV-Vis-NIR spectrophotometer was used to obtain spectral transmission curves from which the optical constants such as refractive index and optical band gap were extracted. The low frequency dielectric characteristics and tunable properties of BST5 were carried out using a LCZ meter and an impedance analyzer using Metal-Insulator-Metal (MIM) structures. The microwave dielectric characteristics of BST5 thin films were determined using a vector network analyzer (VNA). A brief introduction to photolithography and lift-off process is also given.

3.2 Material characterization:

3.2.1Thickness measurement:

The thickness of all the samples were measured using stylus profiler (also known as profilometer) (Model XP-1, Ambios Technology, USA). Surface profilometry[1] is a direct, simple and fast measurement technique for determining the physical thickness of thin films. The only requirement is the existence of a step as shown in figure 3.1. In this study, the step was made by covering a part of the substrate using a thin stainless steel shadow mask during deposition. This method involves loading a stylus (generally a diamond stylus) slightly in contact with the film surface and gently dragging it across the step as shown in figure 3.1. The vertical deflection measures the change in step height (film thickness) and the trace is recorded with high accuracy. Film thickness was also estimated from the spectral transmittance curves as described later.

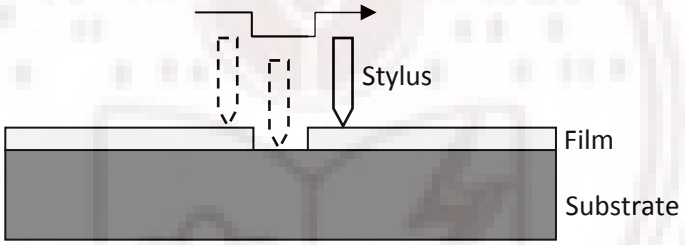

Figure 3.1: Illustration of stylus profillometry to measure film thickness.

3.2.2 X-Ray Diffraction:

X-ray diffraction is a well-known technique for characterizing the crystal structure of materials. X-rays have a wavelength of the order of Angstroms (10^{-10} m), which is comparable to the inter-atomic spacing in crystalline solids. Therefore, a diffraction pattern can be observed when a beam of x-ray is directed on a crystalline material (where the atoms are arranged periodically). This diffraction pattern is directly related to the crystal structure of the material under observation. The diffraction of x-rays by a crystalline material is illustrated in figure 3.2.

In the present work, two types of X-ray diffractometers with different x-ray source were used to characterize the samples. One was equipped with Co Kα (λ=1.7889Å) radiation in a wide angled powder X-ray diffractometer (INEL Model CPS120) and a position sensitive detector while the other one was a conventional X-ray diffractometer operating in the Bragg-Brentano geometry with Cu K_α (λ=1.54056 Å) radiation (Philips

PW 1830 diffractometer). Calibration using a Si standard was done to account for the instrumental line broadening and the value was approximately 0.05^{o} for the former and 0.10 for the later. The patterns were compared with standard patterns (JCPDS) and the phases and degree of crystallinity was determined. A slow scanning rate of 0.5°/min was used to extract data for the measurement of crystallite size. These results gave important information regarding the variation in the films' orientation, lattice constants, crystallite size, strain etc. as a function of processing conditions.

3.2.2.1 *Calculation of crystallite sizes from x-ray diffraction patterns:*

***Bragg's Law*:**

In figure 3.2 below, consider rays 1 and 1a in the incident beam. They strike atoms K and P in the first plane of atoms and are scattered in all directions. Only in the directions 1' and 1a', the scattered beams are completely in phase (because QK – PR = PK Cos θ - PK Cos θ = 0) and so capable of reinforcing one another.

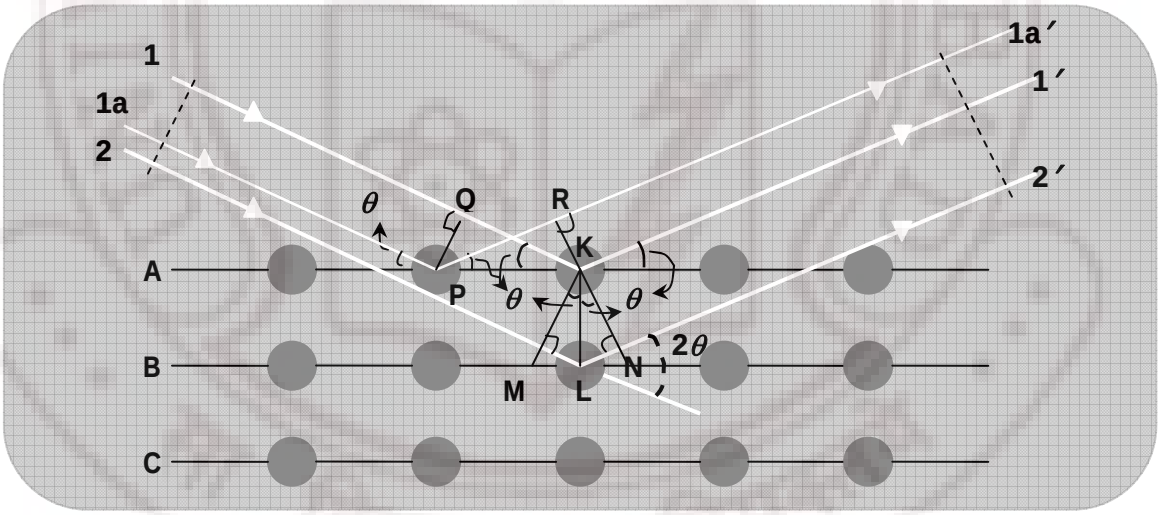

Figure 3.2: Diffraction of X -rays by periodically arranged atoms in a crystalline material.

This relationship is true of all the planes separately, and we have to find the condition for reinforcement of rays scattered by atoms in different planes.

Let us take rays 1 and 2 scattered by atoms K and L, and the path difference for rays 1K1' and 2L2' is

$$ML + LN = d \sin\theta + d \sin\theta \qquad (3.1)$$

If this path difference is equal to a whole number n of wavelengths,

$$n\lambda = 2d \sin\theta \qquad (3.2)$$

where, θ is the diffraction angle, λ is wavelength of the X-ray and n is the order of reflection, which may take any integral value consistent with sinθ but not exceeding unity.

This relation was first formulated by W. L. Bragg and is known as the Bragg law[2].

$$\frac{n\lambda}{2d} = \sin\theta < 1 \qquad (3.3)$$

i.e., nλ must be less than 2d. For n =1 the condition for diffraction at any observable angle 2θ is λ < 2d.

For most sets of crystal planes d is of the order of 3 Å or less, which means that λ cannot exceed about 6 Å.

Scherrer's formula is used to estimate the crystallite size, *t* given by,

$$t = \frac{0.93\lambda}{\beta \cos\theta_\beta} \qquad (3.4)$$

where, β is angular width, in terms of 2θ and is measured in radian at an intensity equal to half the maximum intensity and is called full width at half maximum (FWHM) (shown in figure 3.3 below)

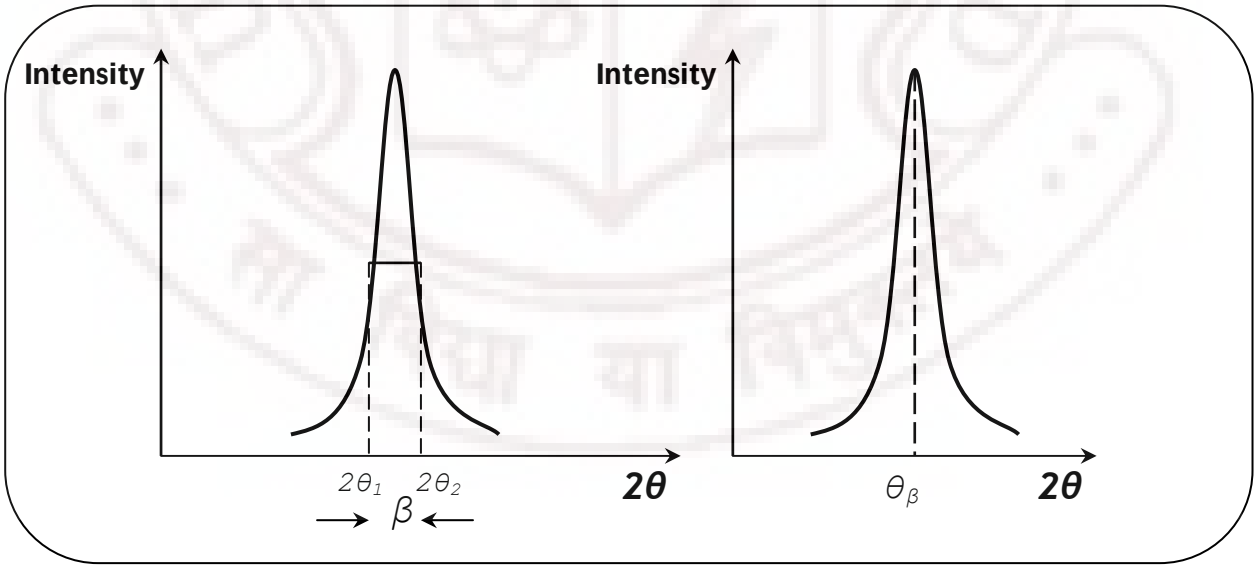

$$\beta = \frac{1}{2}(2\theta_1 - 2\theta_2) \qquad (3.5)$$

Figure 3.3: Graphs show the FWHM.

3.2.2.2 *Calculation of misfit strain:*

The misfit strain u_m, can be calculated using the formula,[3,4]

$$u_m = \frac{a_s - a_f}{a_s} \qquad (3.6)$$

where, a_s is the substrate lattice parameter or that of the lower lying layer and a_f is the lattice parameter of the deposited film.

3.2.2.3 *Calculation of residual strain:*

The residual strain, can be calculated using the formula,[5]

$$u_b = \frac{d_b - d_f}{d_b} \qquad (3.7)$$

where, d_b is the inter-planar spacing of the bulk BST5 and d_f is that in the film.

3.2.3 Scanning Probe Microscopy:

Scanning probe microscopy (SPM) covers several related technologies for imaging and measuring surfaces on a fine scale, down to the level of molecules and groups of atoms. SPM technologies share the concept of scanning an extremely sharp tip (3-50 nm radius of curvature) across the sample surface. The tip is mounted on a flexible cantilever, allowing the tip to follow the surface profile.

When the tip moves in proximity to the investigated object, forces of interaction between the tip and the surface influence the movement of the cantilever[6]. These movements are detected by selective sensors. Various interactions can be studied depending on the mechanics of the probe. Our interest is in the atomic force microscope (AFM). The atomic force microscope (AFM) probes the surface of a sample with a sharp tip (often less than 100A^o in diameter). The tip is located at the free end of a cantilever that is 100 to 200μm long. Forces between the tip and the sample surface cause the cantilever to bend, or deflect. A detector measures cantilever deflections as the tip is scanned over the sample, or the sample is scanned under the tip. The measured cantilever deflection is mapped as the surface topography[7]. AFM can be used for insulator and semiconductor as well as electrical conductors[8]. The schematic diagram of AFM is shown in figure 3.4.

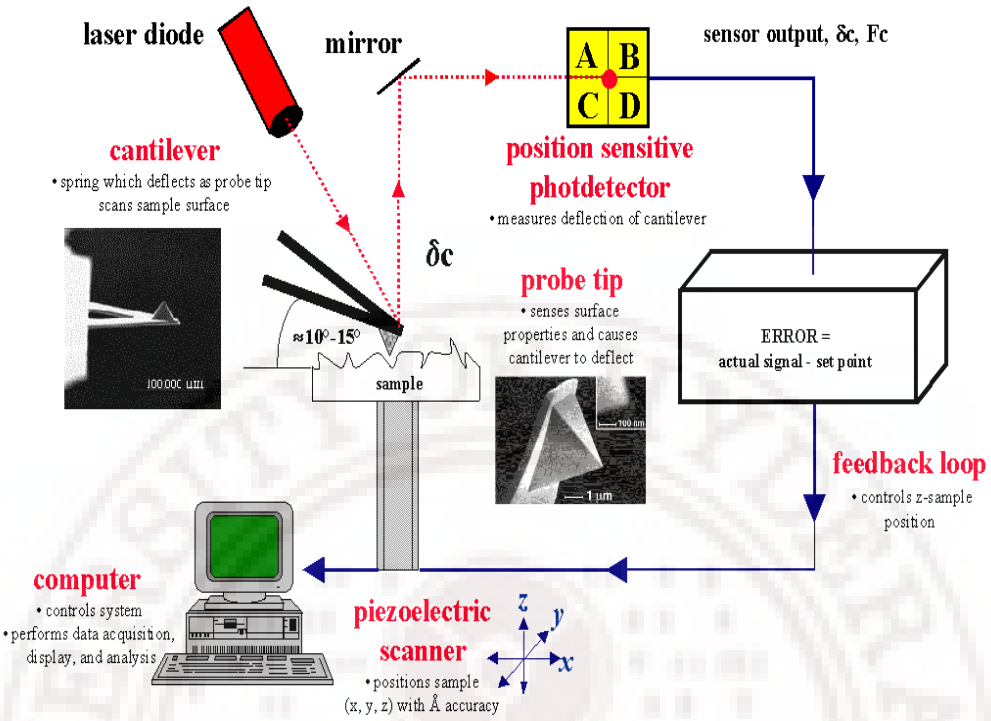

Figure 3.4: Schematic diagram of atomic force microscopy (AFM)[9].

Several forces contribute to the deflection of an AFM cantilever. The force most commonly associated with atomic force microscopy is an inter-atomic force called the Van der Waals force depending upon the distance between tip and sample as shown in figure 3.5.

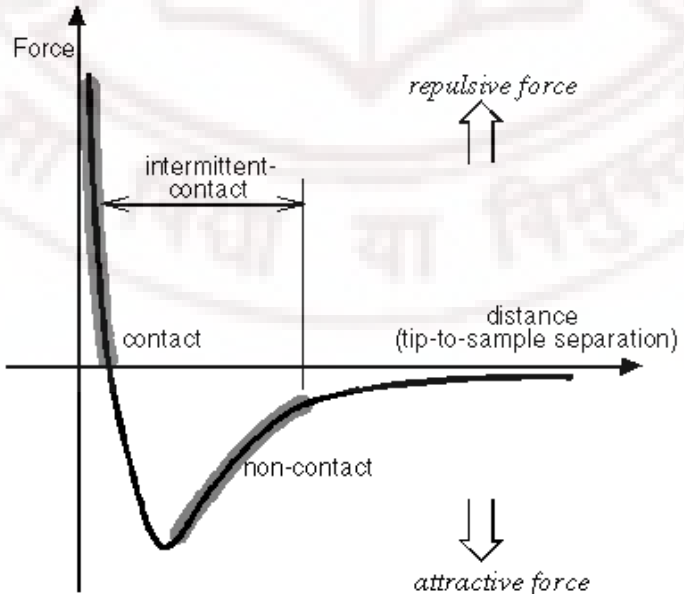

Figure 3.5: Nature of forces in the Contact and Non-contact mode of AFM operation.

Two distance regimes are labeled in figure 3.5 the contact regime and the non-contact regime. In the contact regime, the cantilever is held less than a few angstroms above the sample surface and the interatomic force between the cantilever and sample is repulsive[10]. In the non-contact regime, the cantilever is held about tens to hundreds of angstroms away from its attractive regime (largely a result of the long-range Van der Waals interactions).

3.2.3.1 *Non-contact AFM:*

Non-contact AFM (NC-AFM, otherwise known as dynamic force microscope, DFM) is one of the modes of operation in AFM, where the cantilever is vibrated near the surface of the sample. The spacing between the tip and sample for DFM is of the order of tens to hundreds of angstroms. This spacing is indicated in the Van der Waal force curve in figure 3.5 as the non-contact regime.

DFM is desirable because it provides a means for measuring sample topography with little or no contact between the tip and sample. Similar to contact-AFM, DFM can also be used to measure the topography of the insulator and semiconductors as well as electrical conductors. The total force between the tip and sample is very low, generally 10^{-12}N.

Since the force between tip and sample in the non-contact regime is low, it is more difficult to measure this region than in the contact regime. In addition, the cantilever used in DFM is stiffer than those used for contact AFM because soft cantilevers can be pulled easily onto the sample surface. Hence, both these factors make the DFM signal difficult to measure. Thus, a sensitive, AC detection scheme is used in this operation.

In the non-contact mode, the system vibrates a stiff cantilever near its resonant frequency (typically from 100 to 400 kHz). Then, it detects the changes in the resonant frequency or vibration amplitude as the tip comes near the sample surface. The sensitivity of this detection scheme provides sub-angstrom vertical resolution in the image, as with contact AFM.

The relationship between the resonant frequency of the cantilever and variations in sample topography can be explained as follows. The resonant frequency of a cantilever varies as the square root of its spring constant. In addition, the spring constant of the

cantilever varies with the force gradient experienced by the cantilever. Finally, the force gradient, which is the derivative of the force Vs distance curve changes with the tip-to-sample separation. Thus, change in the resonant frequency of the cantilever can be used as a measure of change in the force gradient, which changes with the tip-to-sample spacing, or sample topography.

DFM does not suffer from the tip or sample degradation effects that are sometimes observed after taking numerous scans with contact AFM. As mentioned above, DFM is preferable to contact AFM for measuring soft samples. In the case of rigid samples, contact and non-contact AFM for images may look the same. In the present study Seiko SPA-400 scanning probe microscope was used in the DFM mode to obtain the surface morphology of BST5 thin film samples.

3.3 Optical Characterization:

Optical properties of the BST5 films were studied using a JASCO V-570 UV-VIS-NIR double beam Spectrophotometer. The optical studies of thin films are mainly concerned with physical phenomena like transmission, reflection, absorption and also the interaction of photon energy with matter and consequent changes in electronic states[11]. The important parameters that can be obtained from the measured spectral transmittance data include optical band gap, refractive index and the thickness. In the present study the data were collected in the range of 190 to 2500 nm, with air as reference.

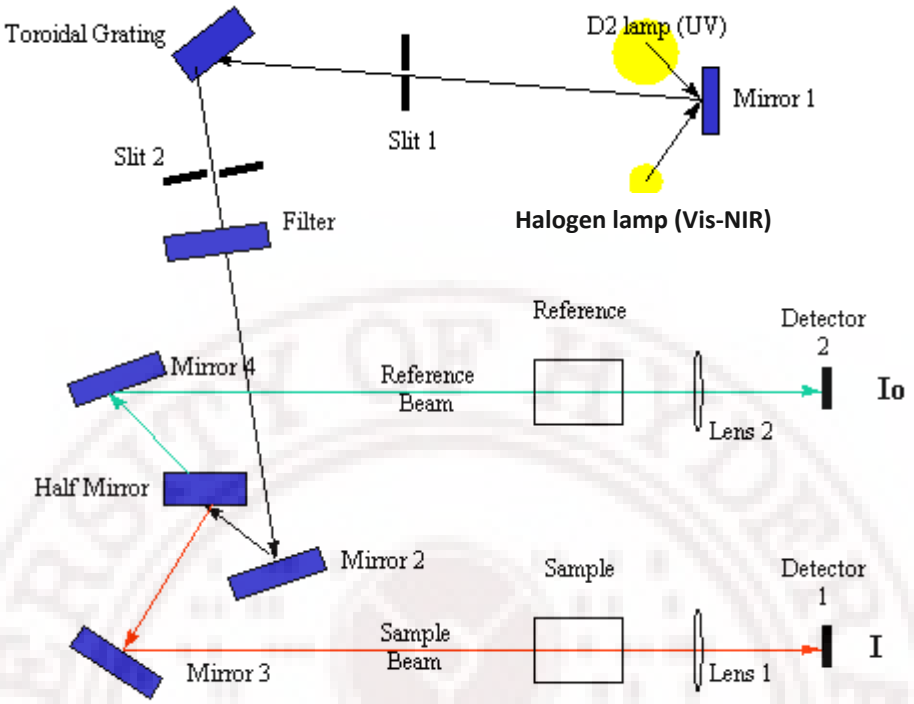

Figure 3.6: Schematic diagram of UV-VIS-NIR spectrophotometer.

The Ultra Violet -Visible-Near Infrared (UV-VIS-NIR) spectrophotometer uses two light sources, a deuterium (D_2) lamp for ultraviolet region and a halogen lamp for visible and NIR region. The light from the source lamp gets reflected from mirror 1 and beam passes through slit 1 and hits a diffraction grating. The grating can be rotated allowing for a specific wavelength to be selected. At any specific orientation of the grating, only monochromatic (single wavelength) beam successfully passes through slit 2. A filter is used to remove unwanted higher order diffracted beam. The light beam hits a second mirror before it gets split by a half mirror (half of the light is reflected, the other half gets transmitted). One of the beams is allowed to pass through a reference sample (air in the present case), the other passes through the film coated substrate. The intensities of the light beams are then measured at the end as shown in figure 3.6. The photometer (not shown) computes the ratio of the sample signal to reference signal (I/I_0) to obtain the transmittance.

If light is incident on a film of refractive index, n, coated onto a substrate of refractive index s, then at the air-film, the film-substrate and substrate-air interfaces, part of the incident intensity is reflected and part of it is transmitted. From fundamental considerations of optics it follows that since the reflected and transmitted beams originate

from a single coherent source, the beams will exhibit interference effects[12]. The schematic diagram of the optics is shown in figure 3.7 and the typical interference spectrum of the transmitted beams is shown in figure 3.8.

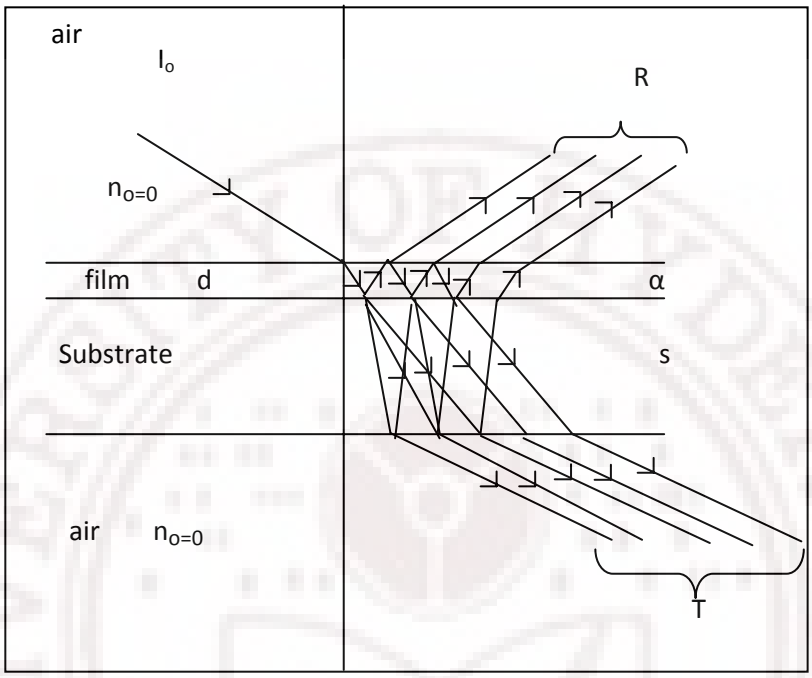

Figure 3.7: Interference from a thin film on a thick transparent substrate, s>>d.

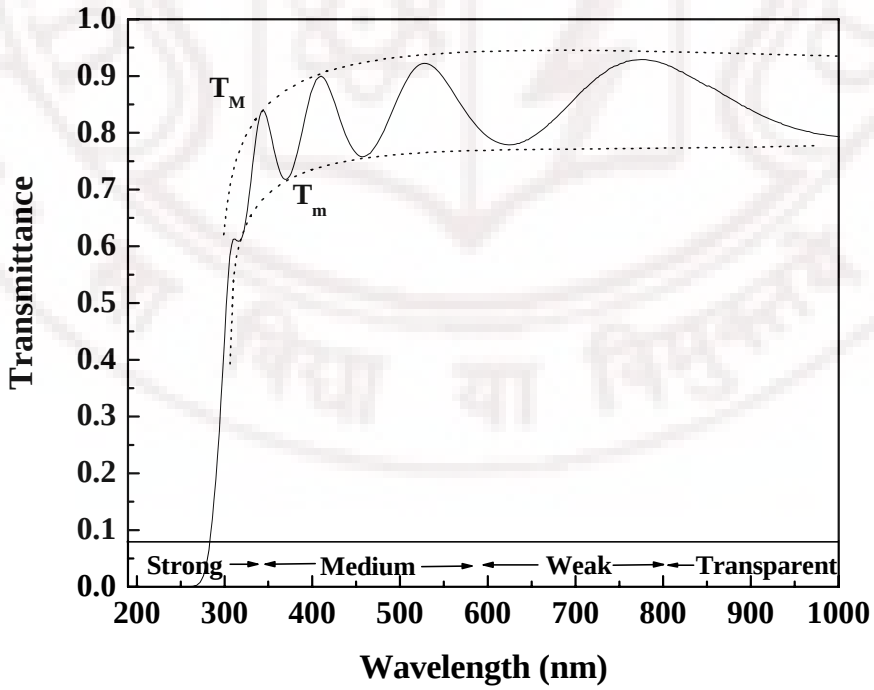

Figure 3.8: A typical spectral transmittance curve drawn with the envelope for the calculation of optical constants.

The condition for constructive interference in such a case is given by,

$$2nd = m\lambda \qquad (3.8)$$

where n is the refractive index of the film at a wavelength λ and m is the order of interference. d is the thickness of the film that can be calculated from the derived values of refractive indices.

In general the transmission T, is given by the expression[13],

$$T = \frac{Ax}{B - Cx\cos\varphi + Dx^2} \qquad (3.9)$$

where,

$A=16n^2s$

$B=(n+1)^3(n+s^2)$

$C=2(n^2-1)(n^2-s^2)$

$D=(n-1)^3(n-s^2)$

$\varphi = 4\pi nd/\lambda$

$x=\exp(-\alpha d)$

For such a system at the points of constructive and destructive interference, the transmittance T_M and T_m, respectively are given by

$$T_M = \frac{Ax}{B - Cx + Dx^2} \qquad (3.10)$$

and

$$T_m = \frac{Ax}{B + Cx + Dx^2} \qquad (3.11)$$

For simplicity it can be assumed that the transmission is a continuously varying function of wavelength which can be approximated by drawing an envelope across the spectrum, connecting all the maximas and all the minimas.

From this it can be shown in the region of weak absorption that

$$n = [N + (N^2 - n_s^2)^{\frac{1}{2}}]^{\frac{1}{2}} \qquad (3.12)$$

where,

$$N = 2n_s \frac{T_M - T_m}{T_M T_m} + \frac{n_s^{\ 2} + 1}{2}$$

On adding the reciprocals of the equations 3.10 and 3.11 yields,

$$\frac{2T_M T_m}{T_M + T_m} = \frac{Ax}{B + Dx^{\ 2}} \qquad (3.13)$$

and solving for x we get,

$$x = \frac{F - F[F^2 - (n^2 - 1)(n^2 - s^4)]^{\frac{1}{2}}}{(n-1)^3 (n - s^2)} \qquad (3.14)$$

where

$$F = \frac{8n^2 s}{T_i}$$

and

$$T_i = \frac{2T_M T_m}{T_M + T_m}$$

T_M is the maximum of transmission on the envelope at a wavelength λ, and T_m is the minimum in transmission on the envelope at the same wavelength. The T_M and T_m at each wavelength can therefore be read off from the envelope and the refractive index, consequentially can be derived at each wavelength.

From the condition for constructive interference it can be seen that for two successive maxima occurring at wavelengths λ_1 and λ_2, the equation becomes,

$$2n_1 d = m_1 \lambda_1 \qquad (3.15)$$

and

$$2n_2 d = m_2 \lambda_2 \qquad (3.16)$$

Also $$|m_1 - m_2| = 1 \qquad (3.17)$$

So,

$$d = \frac{\lambda_1 \lambda_2}{2(n_1 \lambda_2 - n_2 \lambda_1)} \qquad (3.18)$$

In the region of strong absorption, from Beer-Lambert's law given by,

$$I = I_o \exp(-\alpha d) \qquad (3.19)$$

where,

I_o= incident intensity =1

I= intensity at a given wavelength, λ

d is the thickness of the film and α the absorption coefficient in cm^{-1}.

Since d is known from previous calculations and I is a measured quantity (i.e. the transmission at a wavelength λ) the absorption coefficient α can be calculated. Knowing α, from the expression for the so-called "Tauc gap" the fundamental absorption edge of the material can be determined.

The expression for the Tauc gap is given by[14],

$$\alpha h\upsilon = \text{constant} \times (h\upsilon - E_g)^2 \qquad (3.20)$$

x-intercept of the extrapolation of the linear region in a plot of $(\alpha h\nu)^{1/2}$ vs hν will give the value of the band gap E_g. The error associated with the measurement of k, n and d is ±0.005, ±0.02 and ±10nm respectively.

The thickness measured using this technique was comparable with the thickness measured using the stylus profiler.

3.4 Electrical Characterization:

None of the material analysis techniques discussed above require specific sample preparation or any complex test structures. However, electrical characterization of the BST5 thin films requires special test structures and sample preparation. The electrical characterization includes measurement of dielectric constant, dielectric loss and tunability at low frequency (40Hz to 1MHz) and at microwave frequencies (2 GHz to10 GHz). The test structures used for electric characterization are M-I-M capacitor structure and Co-planar wave guide (CPW) lines. In the present study, these structures were fabricated using a single step photolithography and lift-off process. The top silver (Ag)/ gold (Au) multilayer metallization was done using a dual cathode RF magnetron sputtering system (MAGSPUT-1G2-RF-HOT-UPG, Torr, USA). Silver was chosen because of its high conductivity and the thin layer of gold acts as a capping layer because of its oxidation resistance.

3.4.1 Photolithography and lift-off process:

Photolithography is a process of transferring patterns of geometric shapes on a mask to a thin layer of photosensitive material covering the surface of a substrate (wafer) or a film coated substrate. The photosensitive material is known as "photoresist". The resist pattern defined by the lithographic process is not a permanent element of the final device, but only a replica of device features[15]. There are two types of photoresists, they are positive photoresist and negative photoresist[16]. In the present work, an "i" line (λ=365nm) positive photoresist (OIR620-10M, Fuji films) was used. The steps involved in the photolithographic process are wafer cleaning; dehydration bake, photoresist spin coating; soft baking; mask alignment and exposure and development.

***Cleaning*:** In order to remove the traces of dust, organic and ionic contamination from the surface, the thin film coated substrates were ultrasonically cleaned for 5 minutes each in acetone, isopropyl alcohol and de-ionized (DI) water. The substrates were then rinsed under free flowing DI water for 30 seconds and desiccated using dry N_2.

***Dehydration bake*:** The cleaned substrates were baked at 110^{o}C for 15 minutes to dry off moisture that may be present on the wafer surface.

***Photoresist spin coating*:** The photoresist is coated on the surface of thin film deposited substrate using a spin-coating machine (WS-400B-6NPP, Laurell). The substrate is placed on a vacuum chuck which can rotate along its own axis while holding the substrate. A small quantity of the photoresist is dispensed in the centre of the spinning substrate and the rotation causes the resist to be spread across the surface of the wafer with excess being thrown off. The uniformity and thickness of the photoresist depends on the spinning process. Initial spinning speed of 5rpm (rotations per minute) and then at 2500 rpm for 30 seconds guaranteed uniform spreading and thickness of 1.2 ± 0.05 μm. The spin coating process is shown in figure 3.9.

Soft bake: The photoresist coated substrates were gently heated at 105^{o}C for 15 min in a hotplate to evaporate the resist solvent and to partially solidify the resist. Soft bake time and temperature also influence resist thickness, adhesion, exposure and development rate. The thickness of the soft baked resist was about 1.0 ± 0.05 μm after soft bake process.

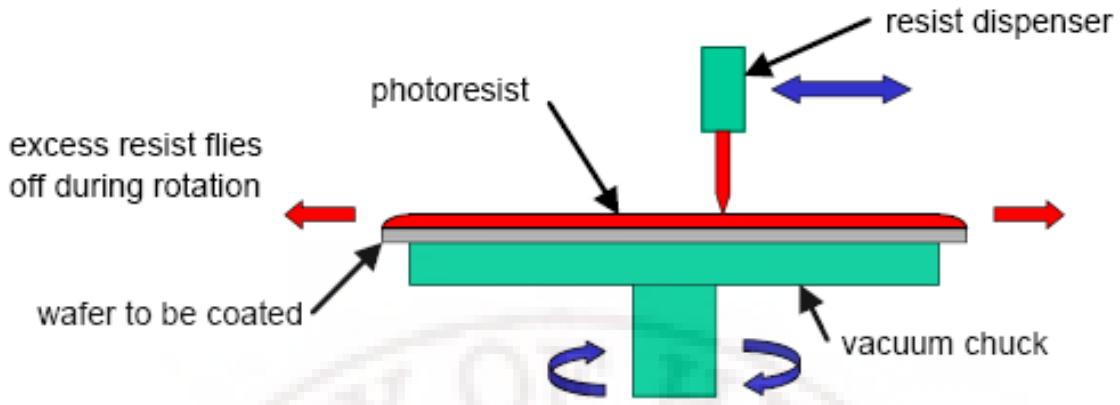

Figure 3.9: Spin coating process.

***Exposure*:** The soft baked photoresist is exposed to UV light through a photomask containing the geometric patterns. The photomask is created by a photographic process and developed onto a glass substrate. Alignment of the mask is critical and is achieved by adjusting x-y positions as well as by rotation (θ) as shown in figure 3.10.

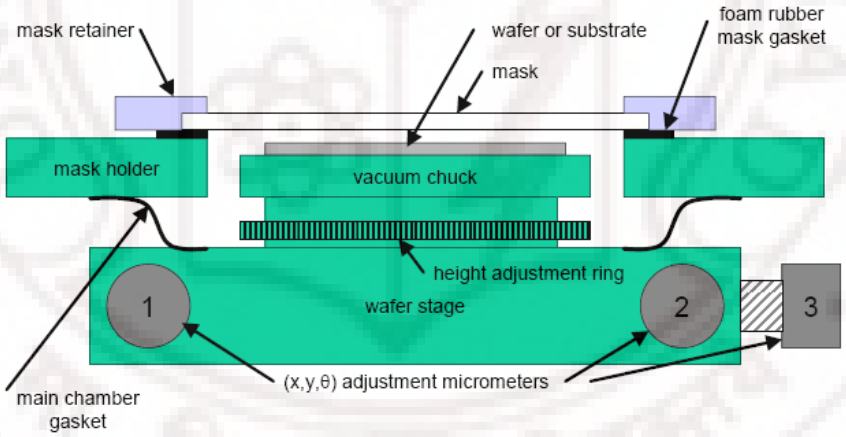

Figure 3.10: Alignment fixture.

Once the mask is accurately aligned with the pattern on the substrate's surface, the photoresist is exposed through the pattern on the mask with a high intensity ultraviolet light. The alignment and UV light exposure for 10 seconds was done using a contact aligner (MJB4 mask aligner, Suss). The photograph of the aligner is shown in figure 3.11.

Figure 3.11: Photograph of the Suss MJB4 contact aligner.

Developing: During the exposure process, the resist undergoes a chemical reaction, depending on the chemical composition of resist. The action of light on a positive resist as in our case causes it to polymerize in places where it has been exposed to UV light. Thus the polymerized part can be removed during developing, which is the last steps in the photolithographic process. In our case the exposed resist was developed in a water based developer solution for 60 seconds, thoroughly rinsed in running DI water and dried in a hot plate.

The top electrode consisting of multilayer of silver (Ag, 400nm) and gold (Au, 100nm) was deposited on the substrate such that both the exposed and un-exposed regions are covered completely.

In the lift-off process, the metalized substrates were put in an ultrasonic acetone bath for about 10 minutes to remove the unwanted photoresist and the metal layer.

Various electrical measurements were carried out using these top electrode patterned BST5 thin films.

3.4.2 Low frequency dielectric measurements:

The frequency and voltage dependent dielectric properties of BST5 films grown on Pt/Si substrates were characterized at low frequencies (≤ 1MHz) using the MIM

structures. The top electrode of 300μm^2 area of the MIM structure was fabricated using the photolithographic process as described in the previous section. The measurements were carried out from 40 Hz to 1 MHz using an Agilent 4294A impedance analyzer (shown in figure 3.12).

Figure 3.12: Photograph of the Agilent 4294A impedance analyzer.

The schematic cross section and top view of the M-I-M structure fabricated is shown in figure 3.13.

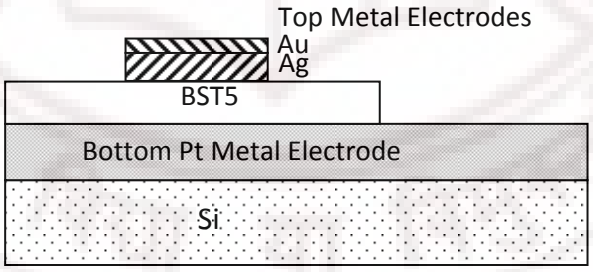

Figure 3.13: Cross-sectional view of the MIM structure.

The top and bottom electrodes of the MIM (Au/Ag/BST5/Pt) structures were connected to the impedance analyzer through two tungsten probes connected to their respective micropositioners in the probe station (LMS 2709, J microtechnology), which in turn is connected with the impedance analyzer allowing a straight forward calculation of dielectric permittivity by the parallel plate capacitor equations.

An impedance analyzer measures the current response of the circuit by applying a sinusoidal voltage signal and calculates the impedance and phase angle. The impedance is converted to capacitance while the phase angle to tan δ assuming an equivalent circuit of ideal capacitors and resistors to mimic a real capacitor that allows the flow of alternating current. Capacitance and tan δ can be measured over a range of DC bias superimposed on the sinusoidal voltage signal. The collected *C-V* data allows calculation of the permittivity, dielectric loss, and tunability of the BST film at discrete DC bias voltages. The tunability measurements using impedance analyzer in the present study was carried out at 100 kHz and 1 MHz.

Dielectric frequency dispersion was measured using the same set-up that is used for C-V characterization. The Agilent 4294A impedance analyzer can operate between 40 Hz and 110 MHz but the MIM capacitors are only impedance matched to the measurement circuit over a range of 40 Hz to 1 MHz of frequency. Thus for frequency higher than 1 MHz the calculated capacitance and tan δ values were dominated by measurement artifacts.

This set of electrical characterization experiments allows a comprehensive understanding of the dielectric properties of BST5 thin films as they relate to tunable varactors in frequency-agile circuits. Capacitance versus DC bias yields a quantitative estimate of tunability, loss tangent and the ability to tolerate high fields while measurement of the frequency dispersion gives a qualitative assessment of the mobility and concentration of excess charges.

The dielectric properties were calculated using the following equations[17].

Relative permittivity,
$$\varepsilon_r = \frac{C \cdot d}{A \cdot \varepsilon_0} \qquad (3.21)$$

Quality Factor,
$$Q = \frac{1}{\tan \delta}. \qquad (3.22)$$

$$\text{Relative tunability}\,(\%) = \frac{\varepsilon_{\max} - \varepsilon_{\min}}{\varepsilon_{\max}} x100 \qquad (3.23)$$

and Figure of merit,

$$FOM = \text{Re}\,lative \quad tunability \times Q \qquad (3.24)$$

Here, ε_0 is the permittivity of free space, A and d are the capacitor area and film thickness respectively and Q is the measured quality factor of the capacitor under test.

3.4.3 Microwave characterization:

3.4.3.1 Modified cavity perturbation technique

Microwave dielectric measurement of permittivity and loss tangent of the BST5 thin films deposited on fused silica substrates were carried out at an X band spot frequency of 12.15 GHz using the modified cavity perturbation technique[18,19]. The experimental measurements were performed using a TE_{10n} mode WR-90 rectangular cavity of length 11.6cm, width 2.3 cm and height 1.07 cm connected through a coaxial to wave-guide adapter to Port 1 of the Agilent 8722ES Vector Network Analyzer (VNA) after performing the one port calibration at the adapter surface. The photograph of the VNA connected to the rectangular cavity is shown in figure 3.14.

Figure 3.14: Photograph of the rectangular cavity connected to the VNA.

A 1 mm thick bare fused silica substrate with 25mm length and 5mm width was thoroughly cleaned and placed inside the cavity through a slot drilled at the center of the cavity. The position of the slot is taken such that the sample surface would be tangential to the maximum electric field (E_{max}) position always. First the resonance frequency and quality factor of the empty cavity with the bare substrate is recorded. The bare substrate is then coated with BST5 thin film and this coated substrate is again inserted in to the cavity and the corresponding resonance frequency and quality factor are determined. The

superimposed response of the empty cavity, cavity with bare substrate and cavity with film coated substrate are given in figure 3.15.

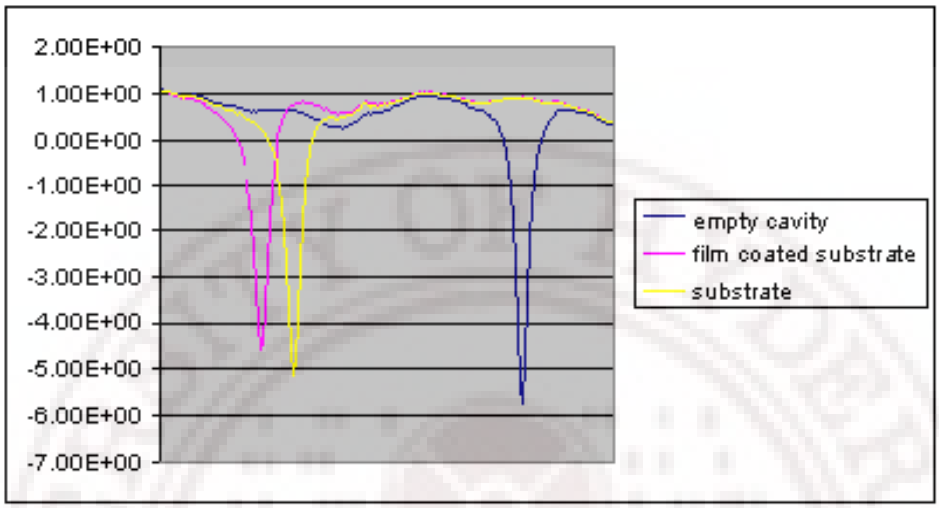

Figure 3.15: The response of the empty cavity, cavity with bare substrate and cavity with -film coated substrate superimposed in the same scale.

The main assumption of this method is that the dimensions of the sample are small compared to the wavelength, which is always true in the case of thin films. If the sample surface lies across the cavity and tangential to the electric field then the dielectric constant is given by[20],

$$\varepsilon' = K\frac{L}{\tau}\frac{\Delta f}{f_{0s}} + 1 \qquad (3.25)$$

where L is the cavity length, τ is the film thickness, Δf is the frequency shift, f_{0s} and f_0 are the resonance frequencies of the cavity with bare substrate and film coated substrate respectively. The coefficient, K, is a measure of the area of the sample with respect to the cross sectional area of the cavity. It is equal to unity when the whole cross section is covered by the film and is less than unity when the cross section is partially filled with the film. Similarly dielectric loss is given by[20],

$$\varepsilon'' = K\frac{L}{2\tau}\left[\frac{1}{Q_{L_s}} - \frac{1}{Q_{L_0}}\right] \qquad (3.26)$$

where Q_{Ls} and Q_{L0} denote the unloaded Q factor of the cavity with and without the film coated substrate. The uncoated substrate, in this method therefore, is considered as part of the cavity giving a net resonant frequency, f_0, provided the substrate is of a low dielectric

constant material. The cavity with the film-coated substrate inside is taken as the perturbed cavity with a resonance frequency f_{0s}. Q_{L0} and Q_{Ls} are the corresponding unloaded quality factors of the cavity. It was assumed that the shift in resonance frequency and quality factor from ($f_{0,}$ Q_{L0}) to ($f_{Ls,}$ Q_{Ls}) is only due to the properties of the film since the substrate is considered as part of the cavity[18,19]. It is a reasonable assumption when dielectric constant of the substrate is low as for fused silica (έ= 3.8) in the present case. Hence, the above equations can be applied directly to find out the dielectric constant and loss tangent of the thin film deposited on low dielectric constant substrates. The dielectric constant of BST5 films deposited on single crystal substrates cannot be measured using any of the resonant perturbation techniques because of their high value of dielectric constant.

3.4.3.2 Split post dielectric resonator technique:

This is a non-destructive and accurate technique for measuring the complex permittivity of dielectric substrates and thin films deposited on them at a spot frequency[21]. It is another resonant structure but without a metallic cavity. It consists of two sapphire dielectric post resonators separated by a distance in which the electric field is uniform [22]. The gap between the resonators can be used for inserting low dielectric constant substrates of 1 inch square area before and after coating the films. The rest of the principle remains the same as that of the modified cavity perturbation technique. The geometry of split post dielectric resonator used in our measurements is shown in figure 3.16.

The SPDR typically operates in the TE_{01n} mode that has only an azimuthal electric field component, so that the electric field remains continuous on the dielectric interfaces[23]. This makes the system insensitive to the presence of air gaps perpendicular to the z-axis of the fixture. The real part of permittivity ε_r of the sample is found on the basis of the measurements of the resonant frequencies and thickness of the sample as an iterative solution.

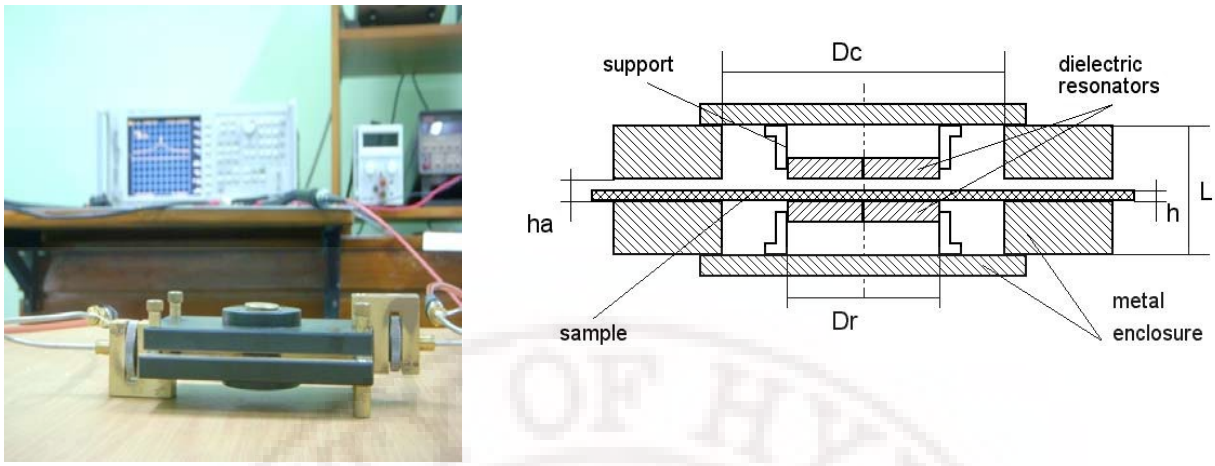

Figure 3.16: A picture of the split dielectric resonator measurement set up with its schematic diagram.[21]

$$\varepsilon' = \frac{1+(f_0 - f_s)}{hf_0 K_s(\varepsilon', h)} \qquad (3.27)$$

Here, h is the sample thickness, f_0 and f_s are the resonance frequency of the SPDR with the substrate and the film coated substrate respectively. K_s is a function of the sample's dielectric constant ε_r and thickness h. Since K_s is a slowly varying function of ε_r and h, the iterations using the equation 3.27 converges rapidly.

The loss tangent is computed using the equation,

$$\tan\delta = \frac{Q^{-1} - Q_{DR}^{-1} - Q_c^{-1}}{p_{es}} \qquad (3.28)$$

where, Q is the unloaded Q factor of the SPDR containing the dielectric sample and p_{es} is the electrical energy-filling factor of the sample. Q_c is the Q factor depending on the metal losses of the SPDR containing the dielectric sample and Q_{DR} is the Q-factor depending on the dielectric losses in the dielectric resonators.

3.4.3.3 On-wafer test and analysis:

For the measurement of the scattering parameter of any test device, the device has to be connected to a vector network analyzer. Before the advent of coplanar probes, finding the RF behavior of a device was a complicated process. The wafer had to be diced and an individual die had to be mounted onto a test fixture[24]. Only then could the device performance be known. Fixturing involved attaching the die to a PCB, wire bonding to

the bond pads, connecting RF cables to the fixture, and measuring. Discriminating between the device and the fixture response had become central problem for high volume screening. One of the obvious advantages of the on-wafer prober at microwave frequencies is that one can get instant measurements on wafers. Thus on-wafer characterization became inevitable in microwave measurements of unpackaged devices. A typical on-wafer microwave measurement setup is shown in figure 3.17 and it consists of a Vector Network Analyzer (VNA), a probe station, on-wafer probes, RF cables and a calibration substrate. The quality of RF measurements depends on the VNA, the reliability of the RF cable and fixture, connectors and the calibration quality. A brief description of the measurement setup is given below.

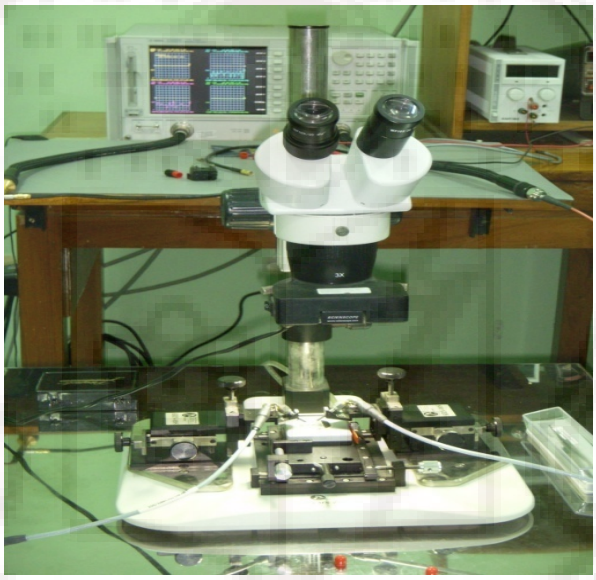

Figure 3.17: Photograph of the on-wafer measurement setup.

Network Analyzer: Network analyzers are widely used to measure the four elements in a 2 port scattering matrix (S_{11}, S_{12}, S_{21}, and S_{22}). Basically, a network analyzer can separate and measure the four waves independently; two forward waves, a_1 and a_2 and two reverse traveling waves, $b_1$and b_2. The scattering parameters can then be obtained by a combination of these four waves. In our experiments, Agilent Technologies 8722ES VNA was used for the S parameter measurements. It can operate over a frequency range of 50 MHz to 40 GHz.

***Probe station**:* In a probe station, the wafer is held on to a vacuum chuck. The probes are fixed to micro-positioners (KRN-09S) magnetically attached to the probe station. The micro-positioners, enable fine movement up to 0.5" in the x, y plane and up to 0.5" lift in the z direction with 40 turns per inch (tpi) precision movement. RF probes with 250 μm pitch with Ground- Signal- Ground (GSG) configuration (GGB Industries, USA) were used for the measurements.

***Calibration substrate**:* An accurate and easily usable calibration substrate with a well defined calibration coefficient and a detailed instruction set to allow accurate calibration of the measurement system (VNA+cabling+probes) is essential for the on-wafer measurements. Typical elements for calibrating a microwave measurement system consist of open, short, matched loads and a thru. These four elements have electrical characteristics that are very different from one another so that each element contributes an important part to the overall calibration process. In the present study, the calibration substrate (model no. Cs-5, GGB industries, USA) that contains high precision elements for calibrating out the errors and losses in an on wafer probing arrangement involving a microwave network analyzer, its associated cabling, and the probes are used.

3.4.3.4 Coplanar wave guide:

The Co-Planar Waveguide (CPW) is a type of planar transmission line used in microwave integrated circuits (MIC) as well as in monolithic microwave integrated circuits (MMIC). The unique feature of this transmission line is that it is uniplanar in construction i.e., all the conductors are on the same side of the substrates[25] which, simplifies the manufacturing and allows fast and inexpensive characterization using on-wafer techniques. The basic structure of the CPW is illustrated in figure 3.18.

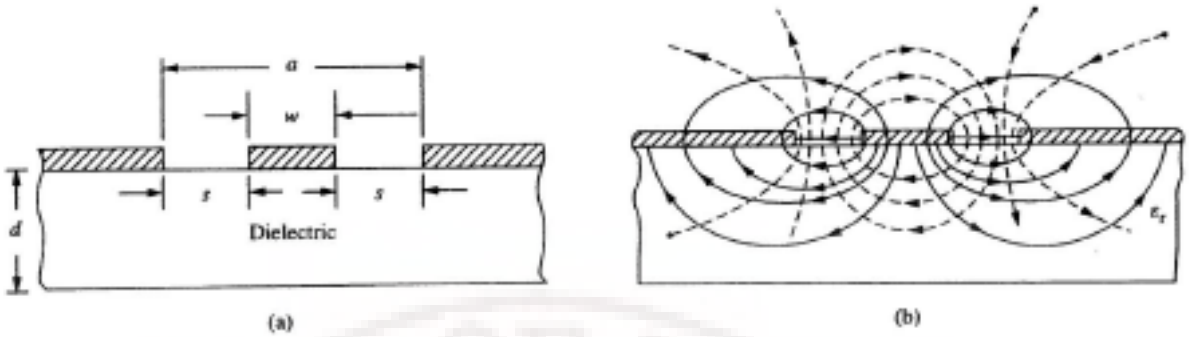

Figure 3.18: A typical coplanar waveguide (a) cross-sectional view of the structural dimensions, (b) electromagnetic field distribution. The solid lines represent electric fields and the dashed lines represent the magnetic field lines.

This arrangement is assumed to be symmetrical with the strip width, w, and the longitudinal gap, s. The side conductors are ultimately grounded theoretically at infinity. The CPW has some advantages compared to the other transmission lines such as microstriplines. They are simple to fabricate and have reduced dispersion (for small dimensions) as well as radiation losses. They have a reduced cross talk between the lines with higher directivity and a low dependence on substrate thickness. However, the current density on the CPW signal line is not uniform across its surface. The current is concentrated more on the edges of the CPW signal line when compared to that of a microstripline of the same dimensions, which leads to a higher insertion loss in CPW geometry. The biggest advantage of the CPW over microstripline is that the CPW line width is independent of its line impedance. Therefore, one can use wider line which in turn helps in reducing the high frequency conductor loss. It is also possible to achieve a wider range of impedance values in a CPW line when compared to that of other transmission lines like microstriplines.

3.4.3.5 Calibration comparison techniques:

This is a broad band technique that can be used for the extraction of dielectric properties of thin films on a substrate. This technique can also be employed to extract the voltage dependent dielectric properties. The calibration comparison technique makes use of two identical coplanar waveguides (CPW) patterned on the surface of the film[26] and the bare substrate. Two CPW test structures of a 100-micron gap and a 200 micron width were patterned simultaneously, one on the test film and the other on the bare substrate by

a lift–off process as shown in figure 3.19. The scattering parameters of these CPW transmission lines were measured using a VNA and a probe station (LMS-2709) mounted with the GSG probes of 250-micron pitch.

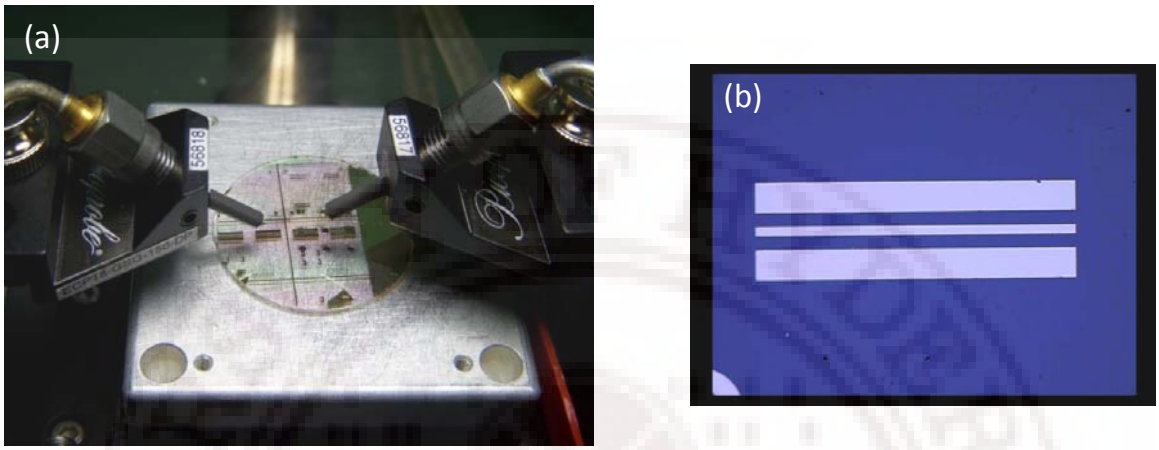

Figure 3.19: (a) A picture of the CPW transmission lines fabricated for on-wafer measurement, mounted on the probe station and (b) CPW lines on BST5 thin film deposited on fused silica.

The method used in this study compares the propagation characteristics of the transmission lines fabricated on the bare substrate (reference sample) and the substrate coated with the thin film of BST (test sample). This technique has been successfully used in the past for the characterization of low k as well as high k dielectric thin films[27]. The resistance and inductance of the reference and test CPW lines are assumed to be same. Also the loss tangent of the low–loss microwave substrate is assumed to be negligible. The ratio of the propagation constants of the CPW lines in both the cases is given as:

$$\frac{\gamma_{test}}{\gamma_{ref}} = \frac{\sqrt{\left[\left(R_{test} + j\omega L_{test}\right)\cdot\left(G_{test} + j\omega C_{test}\right)\right]}}{\sqrt{\left[\left(R_{ref} + j\omega L_{ref}\right)\cdot\left(G_{ref} + j\omega C_{ref}\right)\right]}} \qquad (3.29)$$

This can also be written as:

$$\frac{\left(\alpha_{test} + j\beta_{test}\right)}{\left(\alpha_{ref} + j\beta_{ref}\right)} = \frac{\sqrt{\left[G_{test} + j\omega C_{test}\right]}}{\sqrt{\left(j\omega C_{ref}\right)}} \qquad (3.30)$$

where, α and β are the frequency dependent attenuation and the phase constant respectively. The R, L, C, and G are the resistance, inductance, capacitance and conductance per unit length of the CPW transmission line and they all are frequency

dependent parameters. The conductance per unit length of the test sample can be expressed as:

$$G_{test} = \omega\left(C_{test} \tan \delta_{eff}\right) \qquad (3.31)$$

where, tan δ_{eff} is the effective loss tangent of the CPW structure. Substituting G_{test} from equation 3.29, and $C_{test} = C_{film} + C_{ref}$ in equation 3.28, and comparing the real and imaginary parts of the left and right hand sides and solving them, we get the capacitance of the film (C_{film}). The dielectric constant of the film ε_{film} is determined from C_{film} using the conformal mapping technique[28]. In the limit of the dielectric film thickness t<<s, where s is the spacing between the centre conductor and the ground line,

$$\varepsilon_{film} = \left(s \cdot C_{film} / \left(2\varepsilon_0 t\right)\right) - \varepsilon_{substrate} \qquad (3.32)$$

and the loss tangent of the film is given as:

$$\tan \delta_{film} \approx \tan \delta_{eff} \cdot \left(1 + C_{ref} / C_{film}\right) \qquad (3.33)$$

The frequency dependent attenuation, α and phase constant, β for the test and reference lines are calculated from the measured magnitude and phase of the S_{21}.

3.4.3.6 Tunability measurements- using CPW structures:

The calibration comparison method can also be extended to measure the dielectric properties of the films under an applied electric field (tunability measurements)[29]. For the microwave tunability measurements, a DC bias voltage was applied to the CPW lines through the high voltage bias tees connected to the VNA. DC blocking capacitors were used at both the ports of the VNA to give additional protection to it during these measurements. The magnitude and phase of the S_{21} of the CPW lines patterned on the BST5 thin films are measured under a bias voltage of 100 V. This voltage was able to produce a field of around 10 KV/cm only in the test structures employed. Higher fields were not achieved in this geometry due to the limitation in the bias tees employed.

3.5 Summary:

In summary, an introduction to various characterization techniques such as surface profilometer, X-ray diffraction, UV-Vis-NIR spectrophotometer, Atomic Force microscope used in the present were discussed. The test structures used for measuring the low-frequency dielectric properties using LCZ meter and impedance analyzer and high-frequency (microwave) dielectric properties using Vector Network Analyzer (VNA) were also discussed. An introduction to photolithography and lift-off process and the steps involved in realizing test structures and devices were given.

The next chapter deals with the deposition of amorphous BST5 thin films and the effect of *ex situ* annealing on the structural, microstructural, optical and dielectric properties.

References:

[1] K Creath and A Morales, *Contact and noncontact profilers in optical shop testing*, 2nd ed. Wiley, NewYork (1992)

[2] B. D. Cullity, *X-ray Diffraction*, Addison-Wesley, Reading, MA (1956).

[3] Z.-G. Ban and S. P. Alpay, *J. Appl. Phys*., **91**, 9288 (2002).

[4] Z.-G. Ban and S. P. Alpay, *J. Appl. Phys*., **93**, 504 (2003).

[5] B. E. Warren, *X-ray Diffraction*, Dover, New York (1990).

[6] J. Giessibl Franz, *Reviews of Mod. Phys.* **75**, 949 (2003).

[7] P. West, *Introduction to Atomic Force Microscopy: Theory, Practice and Applications* www.AFMUniversity.org.

[8] Q. Zhong, *Surf. Sci. Lett*., **290**, L688 (1993).

[9] http://pscl.me.ntu.edu.tw

[10] J. B. Hudson, *Surface Science-An Introduction*, John Wiley & Sons, New York (1998).

[11] Olaf Stenzel, *The Physics of Thin Film Optical Spectra: an Introduction*, Springer, Germany (1996).

[12] J. C. Manifacer, J. Gasiot and J. P. Fillard. *J. Phys. E*, **9**, 1002 (1976).

[13] R Swanepoel, *J. Phys. E: Sci. Instrum.,* **16**, 1214 (1983).

[14] J.C. Tauc, *Amorphous and Liquid Semiconductor*, Plenum Press, New York (1974).

[15] C. Richard Jaeger, *Introduction to Microelectronic Fabrication,* Upper Saddle River: Prentice Hall (2002).

[16] Omkaram Nalamasu, May Cheng, Allen G. Timko, Victor Pol, Elsa Reichmabis and Larry F. Thompson, *J. Photopoly. Sci. Technol.,* **4**, 299 (1991).

[17] Hari Singh Nalwa, *Handbook of Thin Film Materials*, Academic Press (2002).

[18] R. G. Geyer, M. W. Cole, P. C. Joshi, E. Ngo, C. Hubbard and W. Nothwang, *Mat. Res. Soc. Symp. Proc.*, **720**, H.4.3.1 (2002).

[19] K.Sudheendran, K. Venkata Saravanan, M Ghanashyam Krishna, and Anil K Bhatnagar, *Proc. Intern. Conf. Smart Mater. Struct. Syst*., **2**, SC-85 (2005).

[20] Maria A. Rzepecka, and M.A.K. Hamid, *IEEE Trans. Microwave Theory and Techniques*, **MTT-20**, 30 (1972).

[21] J. Krupka, A. P. Gregory, O. C. Rochard, R. N. Clarke, B. Riddle and J. Baker-Jarvis, *J. Eur. Ceram. Soc.*, **21**, 2673 (2001).

[22] J. Dela Balle, P. Guillon and Y. Garault, *AEU Electron. Commun.*, **35**, 80 (1981).

[23] J. Krupka, S.A. Gabelich, K. Derzakowski and B.M. Pierce, *Meas. Sci. Technol*., **10**, 1004 (1999).

[24] S.Wartenberg, *Microwave J.*, **46**, 3 (2003).

[25] C. P. Wen, *IEEE Trans. Microwave Theory and Tech.*, **17**, 1087 (1969).

[26] Guru Subramanyam, Emily Heckman, James Grote, Frank Hopkins, Robert Neidhard and Edward Nykiel, *Microwave and Opt. Tech. Lett.,* **46**, 278 (2005).

[27] K. Venkata Saravanan, K. Sudheendran, M. Ghanashyam Krishna and K. C. James Raju *Ferroelectrics*, **35**, 181 (2007).

[28] E. Carlsson and S. Gevorgian, *IEEE Trans. Microwave Theory and Tech*., **47**, 1544 (1999).

[29] G. Subramanyam, C. Chen and S. Day, *Integrated Ferroelectrics*,**77**, 189 (2005).

Chapter IV

Deposition of a-BST thin films and influence of *ex situ* annealing

4.1 Introduction:

Barium Strontium Titanate (BST) thin films have received great attention in the research community for more than a couple of decades for their potential applications in various electronic and optoelectronic. Crystalline BST (c-BST) thin films possess high value of dielectric constant, low loss, high tunability and excellent optical properties. Even though BST thin films exhibit a number of important properties for device applications, their full potential needs to be further studied.

On comparing the dielectric and optical properties of amorphous BST (a-BST) with the properties of various other technologically important oxides it could be inferred that a-BST can prove to be an interesting alternative material system where thermal budget is of concern. An interesting study therefore would be to explore the properties of BST films in the amorphous phase (a-BST).

The c-BST films can only be obtained at deposition/annealing temperatures greater than $500^{o}C$. In contrast, a-BST films can be obtained by depositing at room temperature. Most of the applications exploit the crystalline nature of these films, but their amorphous counterpart has seldom been studied. In order to use a-BST films in practical device applications, it is necessary to study the relationship between the film quality and the deposition conditions.

This chapter deals with the preparation and characterization of a-BST5 thin films as a function of Oxygen Mixing Percentage (OMP). The influence of ex situ annealing on the crystallization/structural, microstructural, optical and electrical properties have been studied and discussed.

4.2 Deposition of a-BST5:

The a-BST5 thin films were deposited on fused silica substrates by RF magnetron sputtering as a function of OMP. The substrate holder was water cooled to maintain the substrate temperature between 23-25^{o}C in order to prevent the rise in temperature of the substrates due to ion bombardment during sputter deposition process. The temperature of the un cooled substrates rose up to 120-140^{o}C during sputtering. The power density and working pressure was maintained at a constant value 3W/cm^2 and 20 mTorr respectively. The OMP was varied from 25 to 100 % in steps of 25%.

***Ex-situ* annealing of a-BST5 thin films:**

In order to crystallize a-BST5 films, two *ex situ* annealing treatments were adopted, they are:

a) Annealing at high temperatures for a short period of time.

and

b) Annealing at low temperatures for a long period of time.

In the former case, a-BST5 films deposited as a function of OMP was cold inserted in a pre-heated furnace at 900^{o}C for one minute. This annealing treatment gives a quasi-rapid thermal annealing approach. While, in the later case the a-BST5 films deposited at fixed OMP of 50% was annealed at different temperatures from 400^{o}C to 1000^{o}C for 1 h at intervals of 100^{o}C in a horizontal box furnace and quenched to ambient temperature.

4.3 Characterization of a-BST5 thin films:

4.3.1 Structural properties:

The structural characterization of the deposited films was carried out using X-ray diffraction (XRD) technique using Co Kα radiation. The XRD pattern of a-BST films deposited on fused silica as a function of OMP is shown in figure 4.1. None of the films show any evidence for long range order in the diffraction pattern indicating that all the films are x-ray amorphous in nature.

The term “x-ray amorphous” essentially means the absence of long range order within the limits of detection of x-ray diffractometer.

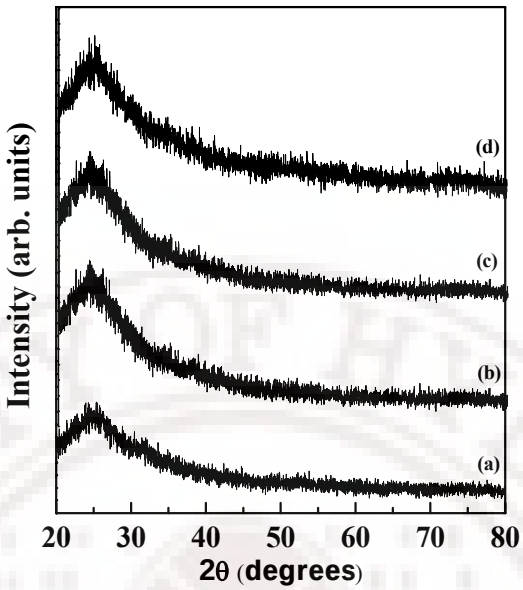

Figure 4.1: XRD pattern of a-BST films deposited at various OMP (a) 25%, (b) 50 %, (c) 75% and (d) 100%.

4.3.2 Surface morphology:

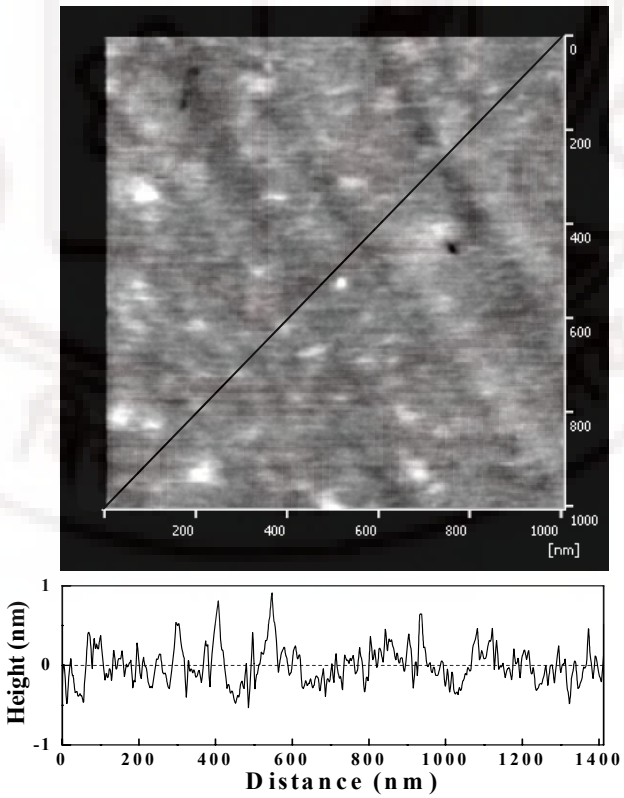

Figure 4.2: 1μm x 1μm AFM image and the corresponding line profile along the diagonal of a-BST5 film deposited at 50% OMP.

The surface morphology and root mean square roughness (rms roughness) of the a-BST5 films deposited as a function of OMP was studied using the Atomic Force Microscope (AFM). The results indicated no marked grains or grain boundaries. Hence, the rms roughness was very low (1.9 nm) and no noticeable deviation was observed in the roughness value as a function of OMP. A typical AFM image and the corresponding line profile of a-BST5 film are shown in figure 4.2.

4.3.3 Spectral Transmission:

The optical properties such as optical band-gap (E_g) and refractive index (n) along with the film thickness (d) was derived from the measured transmittance curves using the formulae discussed in section 3.3. The transmittance was recorded in a UV-Vis-NIR spectrophotometer in the wavelength range of 200–1500nm.

The dispersion in refractive index**,** as a function of wavelength for the a-BST5 films deposited at different OMP is shown in figure 4.3.

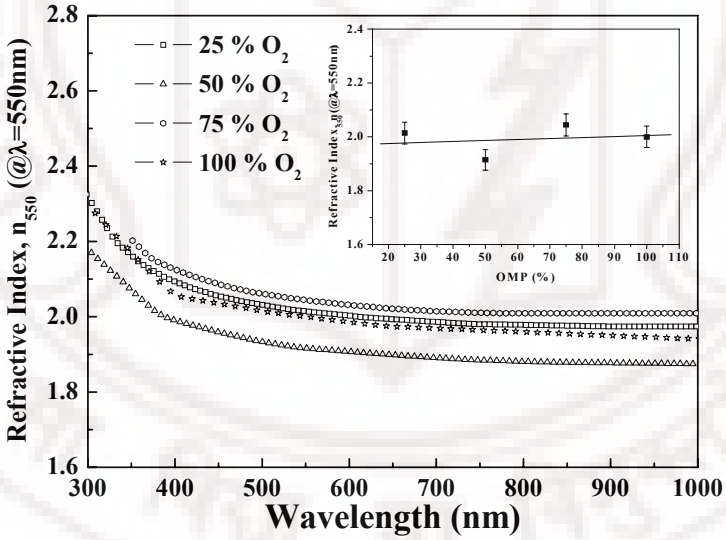

Figure 4.3: (a) Variation in refractive index as a function of wavelength for a-BST5 deposited at different OMP and the inset shows the variation in refractive index (λ=550nm) as a function of OMP.

It is observed that the dispersion curve rises rapidly toward the shorter wavelengths, showing the typical shape of a dispersion curve near an electronic interband transition. The strong increase in refractive index at shorter wavelengths is associated with the fundamental band gap absorption. The refractive index value at λ=550nm is shown in the inset of figure 4.3. At 550 nm the refractive indices were 2.01, 1.91, 2.04

and 2.00 for the films deposited at 25, 50, 75 and 100% OMP, respectively. The graph shows that the variation in refractive index is ~5-6%. The optical band gap E_g for a-BST5 films was calculated using the Tauc relation[1], which is given by,

$$(\alpha h\nu) = C.(h\nu - E_g)^r \qquad (4.1)$$

where C is a constant, α is the absorption coefficient, *hν* is the incident photon energy and r =0.5, 1.5, 2 or 3 for allowed direct, forbidden direct, allowed indirect, and forbidden indirect electronic transitions, respectively. In the present case the band gap energy (E_g) has been estimated by assuming an allowed direct transition (r = 0.5) between the highest occupied state of the valence band and the lowest unoccupied state of the conduction band. In the high-energy region the factor $(\alpha h\nu)^2$ varies linearly with hν whereas in the low-energy region, the absorption spectrum deviates from a straight line, as shown in figure 4.4a. The band gap energy, E_g of the film was obtained by extrapolating the linear portion of the plot of $(\alpha h\nu)^2$ against hν to $(\alpha h\nu)^2 = 0$. The inset in figure 4.4a illustrates the optical band gap variation of a-BST5 deposited at different OMP. The variation in the value of E_g was only between 4.1 and 4.2 eV with OMP. The corresponding transmission edge can be clearly observed in figure 4.4b shown in the region of strong absorption between 250 and 375 nm.

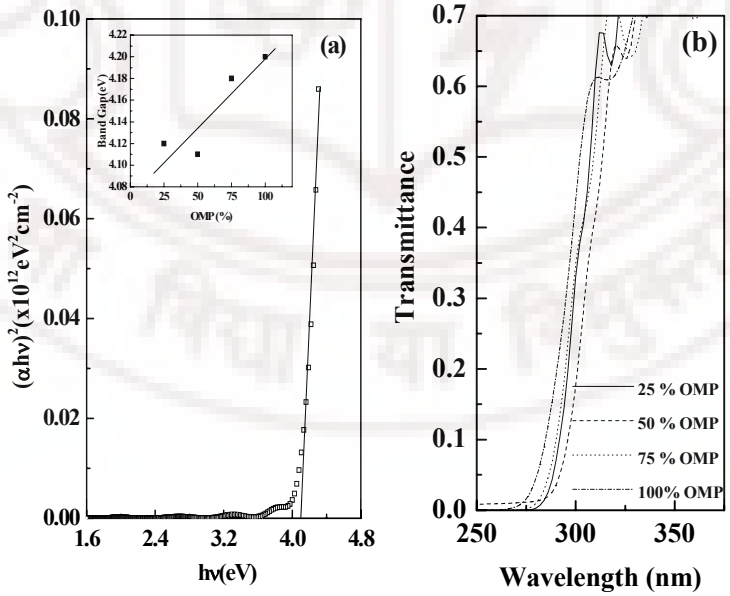

Figure 4.4: (a) Plot of $(\alpha h\upsilon)^2$ versus hυ for the a-BST5 film deposited at 50% OMP, the variation in band-gap as a function of OMP is shown in the inset and (b) optical transmittance in the region of strong absorption.

4.3.4 Electrical characterization:

4.3.4.1 Low frequency characterization:

The dielectric constant and loss tangent of a-BST5 films deposited on Pt/Si substrates were measured from 40 Hz to 1 MHz using an impedance analyzer. MIM structure with a 300μm^2 top electrode of Ag/Au was patterned using a single step photolithographic process.

The dielectric constant (ε') and loss tangent (tanδ) of the a-BST5 films measured at 1 MHz do not show much variation with OMP. The data is tabulated in table 4.1. The frequency dependent dielectric constant and loss tangent of a-BST5 film deposited at 50% OMP is shown in figure 4.5.

OMP (%)	Dielectric constant (ε')	tanδ
25	24.5	0.0014
50	24.3	0.0015
75	24.4	0.0015
100	24.4	0.0016

Table 4.1: Dielectric constant and loss tangent of a-BST5 film deposited at different OMP.

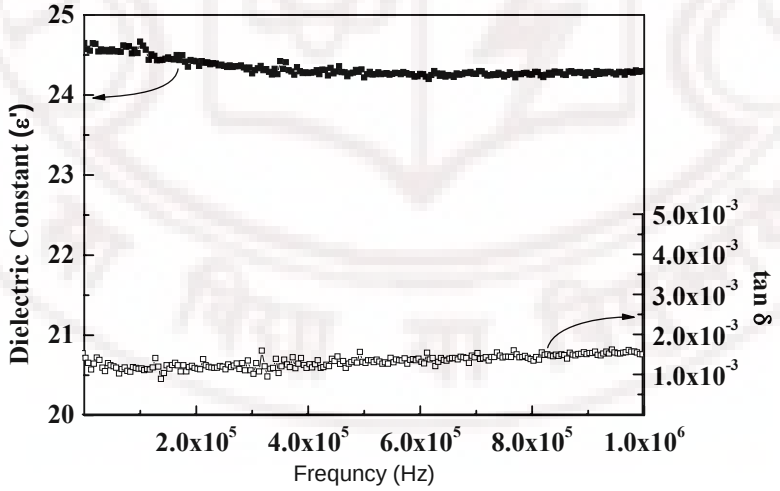

Figure 4.5: Frequency dependant dielectric constant and the corresponding loss tangent of a-BST5 film deposited on Pt/Si substrates at 50% OMP.

At low frequencies the a-BST5 films showed dispersion free characteristic in their dielectric response in the measured frequency range. All the a-BST films had a lower

value of dielectric constant (~24) and the corresponding loss tangent was also low (~$1.5x10^{-3}$). This low value is attributed to absence of long range ordering in the material in their amorphous state.

4.3.4.2 High frequency characterization:

The microwave dielectric permittivity and loss tangent of the a-BST5 thin films were carried out at an X band spot frequency of 12.15GHz using the modified cavity perturbation technique. The details of the technique are discussed in section 3.4.3.1.

The main assumption of this method is that the dimensions of the sample are small compared to the wavelength, which is always true in the case of thin films. This technique can only be used for films deposited on insulating substrates with low value of dielectric constant e.g. SiO_2. Hence a-BST5 films deposited on fused silica (ε'=3.8) substrates were used for determining the microwave dielectric properties.

The variation in dielectric constant and loss tangent of the a-BST5 thin films deposited at different OMP is shown in figure 4.6.

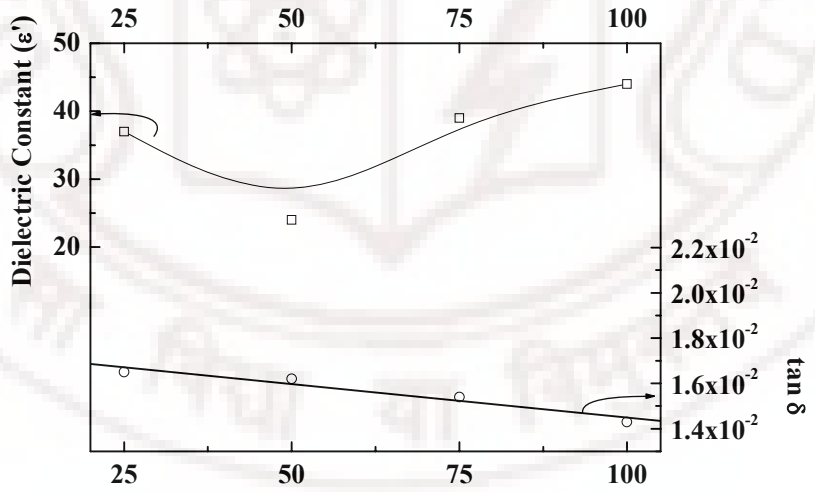

Figure 4.6: Variation in microwave dielectric constant (ε') and loss tangent (tan δ) at 12.15 GHz of a-BST5 films deposited on fused silica substrates at different OMP.

The dielectric constant of a-BST measured at a microwave frequency showed that except for films deposited at 50% OMP, the values are about 40 and that is almost twice as that in the previous case of low frequency data on film grown on Pt/Si. However, here

also at 50% OMP, the dielectric constant is lower as in the case of observed refractive index values for the films grown on fused silica substrates. This reduction however could be attributed to the lowering of packing density noticed for samples prepared at 50% OMP.

4.3.4.3 Voltage dependent dielectric properties:

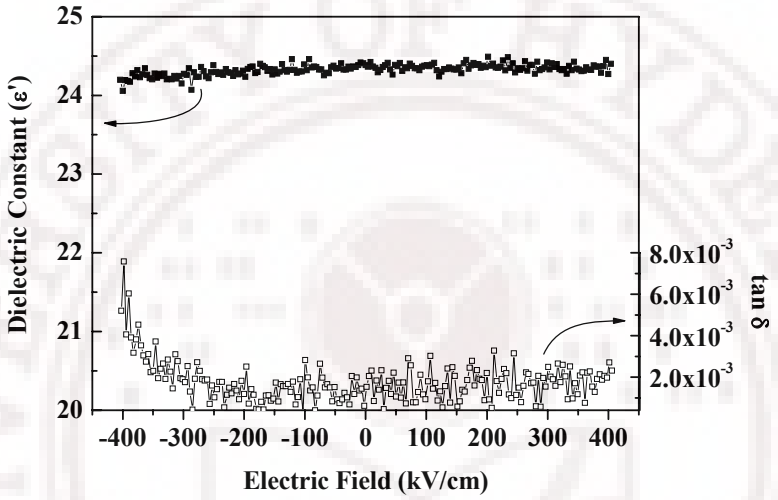

Figure 4.7: Variation in dielectric constant and loss tangent of a-BST5 films deposited on Pt/Si substrates at 50 % OMP as a function of applied electric filed and measured at 1MHz.

The MIM structure on Pt/Si substrates was used for establishing the dependence of dielectric constant on applied electric field (Voltage). No variation in dielectric constant was observed with applied electric field as seen in figure 4.7. Hence, these films will not be relevant in tunable device applications. On the other hand, a-BST5 films could withstand high electric fields of about 400 kV/cm (the limit to which they were observed in this study) and has a dielectric constant of ~24 which is comparable with most of the high-k dielectric oxides. Hence, these films could be considered for applications which require low dielectric constant with high power handing capabilities. The low loss tangent in a-BST is an additional advantage.

4.4 *Ex situ* annealing at high temperature for a short period of time:

4.4.1 Structural properties:

The x-ray diffraction patterns of the BST5 films are shown in figure 4.8. The as-deposited BST5 films were x-ray amorphous, which crystallized to cubic perovskite phase on cold insertion at 900°C for 1min in air. The inset in figure 4.8 shows the increase in full-width at half maxima (FWHM) of the (111) plane as a function of OMP. The FWHM is higher for the BST5 films deposited at higher OMP. The average crystallite size of the films was estimated from the FWHM values using Scherrer's equation. The results indicated a decrease in average crystallite size from 33 nm to 24 nm with increase in OMP from 25% to 100%. Figure 4.9 displays the variation in average crystallite size with OMP.

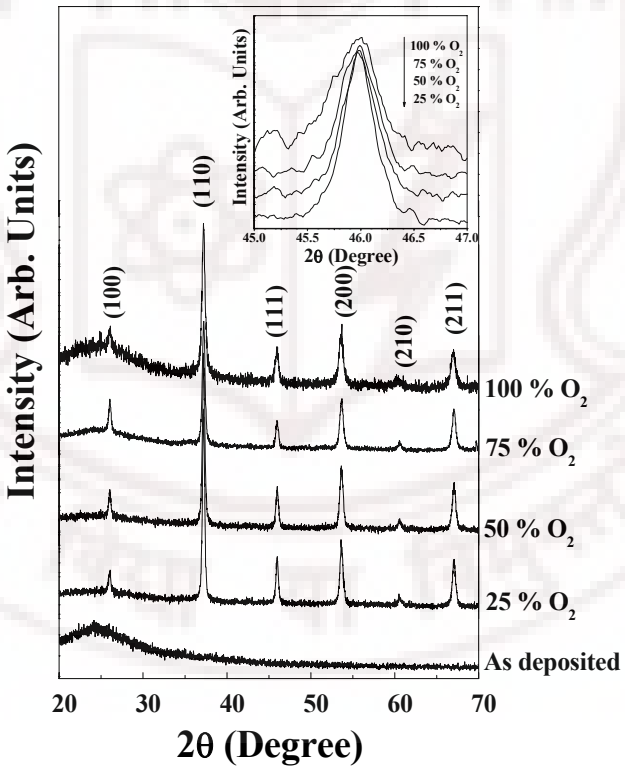

Figure 4.8: XRD θ-2θ scan of $(Ba_{0.5},Sr_{0.5})TiO_3$ films on fused silica substrate deposited at different OMP and annealed at 900°C. Inset shows the increase in full width at half maximum (FWHM) of the (111) plane with increase on OMP.

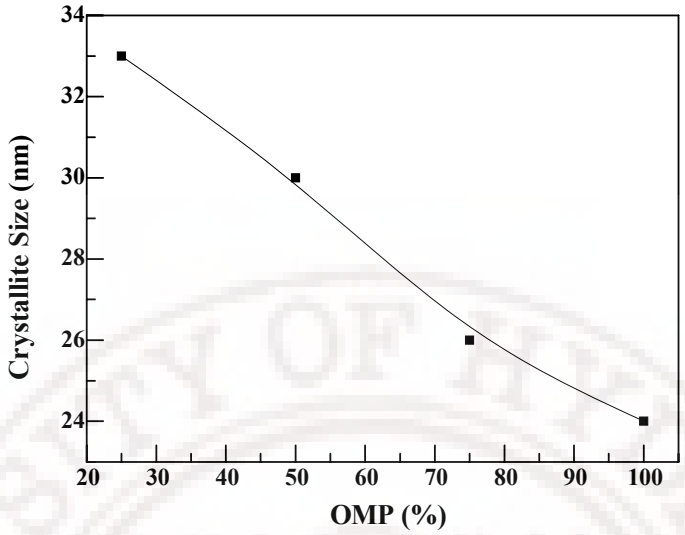

Figure 4.9: Variation in crystallite size as a function of OMP for the films annealed at 900°C for 1 minute.

4.4.2 Surface morphology:

The surfaces of the a-BST5 films were smooth with fine grains as seen in figure 4.2. On annealing, as the films crystallize there is an enhancement in the grain growth and hence the annealed films show coarse grain morphology, as shown in figure 4.10. The surface roughness was about 2.96 nm for a-BST5 films deposited at 50% OMP, which increased to about 6.28 nm on annealing. The high value of surface roughness might also be due to the annealing process.

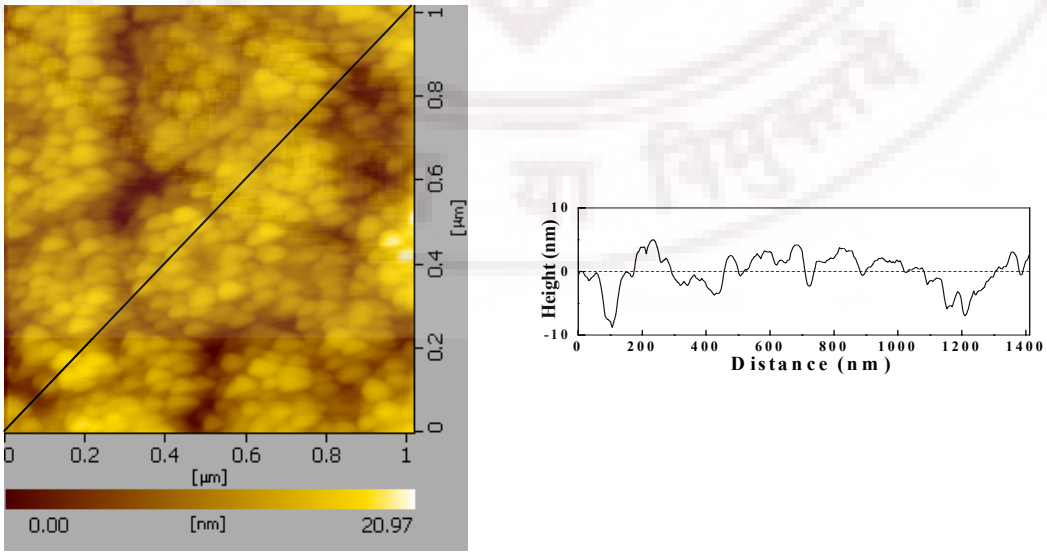

Figure 4.10: AFM image (1µm x 1µm) and the corresponding line profile along the diagonal of the annealed BST5 films.

On the other hand, The BST5 films deposited on Pt/Si substrates developed visible cracks and crevice, which propagate through the thickness of the films, leading to a rough surface of the BST5 film. This might be due to the thermal shock received by the film and the Pt layer on cold insertion at 900°C. Due to the thermal mismatch between platinum and silicon, hillock formation[2] on Pt was also observed. In some cases complete peeling-off of the films were observed during wafer-cleaning in the photolithography process. The surface morphology of the c-BST5 films deposited on Pt/Si and the surface morphology of the bare Pt/Si substrate (after the annealing treatment) are shown in figure 4.11.

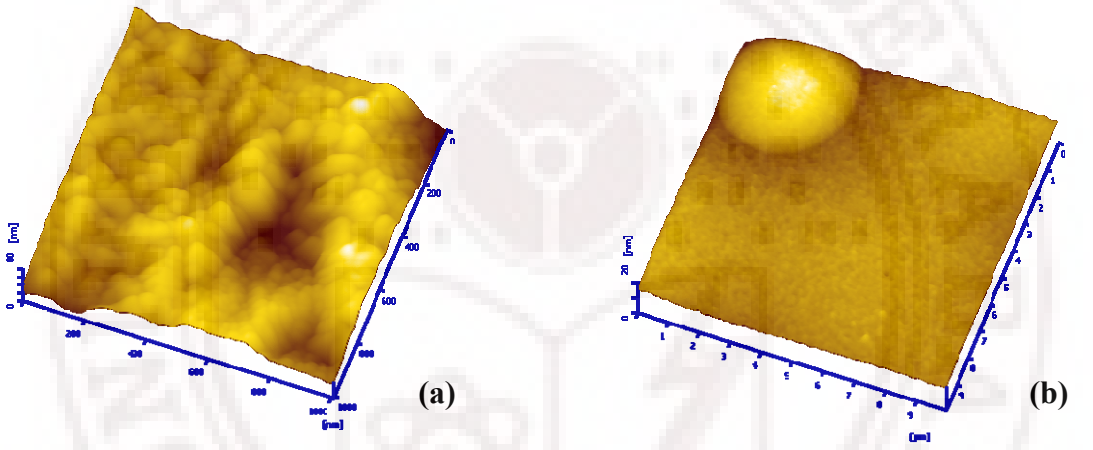

Figure 4.11: AFM image of (a) c-BST5 film on Pt/Si substrate (b) hillock formation on Pt layer.

4.4.3 Optical characterization:

Figure 4.12 shows the typical spectral transmission recorded in the wavelength range 190-1000 nm for a weakly absorbing a-BST5 and c-BST5 film deposited on fused silica substrates. The top dashed line represents the transmittance of the uncoated fused silica substrates.

It could be observed that the absorption edge of a-BST5 films is high but decreased sharply on annealing at 900°C for 1 min.

On the other hand, c-BST5 films show higher values of refractive index when compared to that of the a-BST5 films. For example, for the a-BST5 films deposited at 75% OMP, the refractive index was 2.04 (at λ=550 nm) which increased to 2.26 at the

same wavelength on annealing. The dispersion in refractive index as a function of wavelength for the c-BST5 deposited at different OMP is shown in figure 4.13.

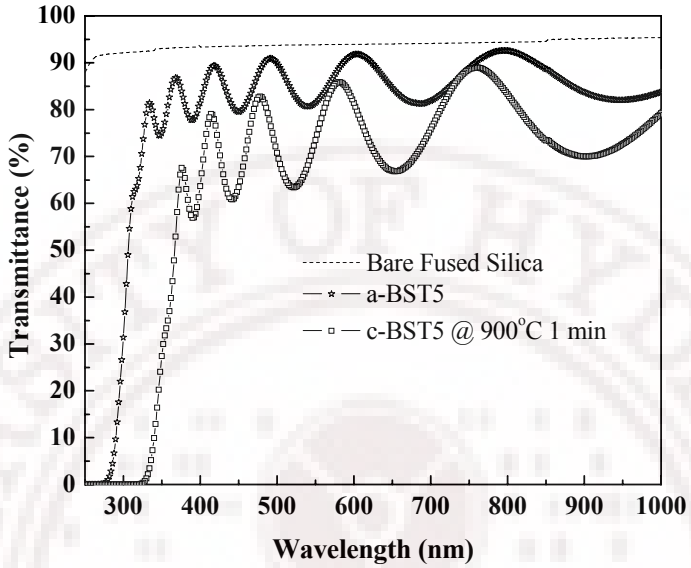

Figure 4.12: Optical transmittance spectra of a-BST5 film deposited on fused silica substrate compared with that of q-BST5 films and the uncoated substrate.

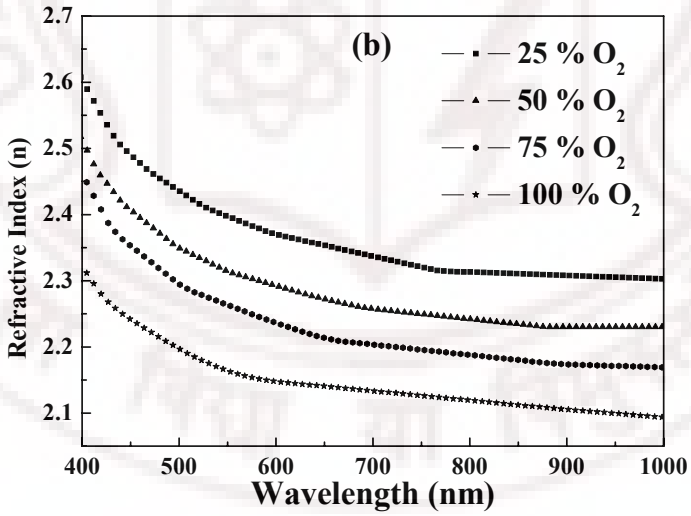

Figure 4.13: Variation in refractive index as a function of wavelength for c-BST5 deposited at different OMP.

The refractive index of a transparent thin film is directly proportional to its electronic polarization and the electronic polarization is in turn inversely proportional to the inter-atomic separation[3]. It can also be directly correlated to the film packing density,

microstructure and crystallinity. It should be noted that in the present case, the as-deposited films being amorphous shows lower film density, which in turn causes the lowering of the refractive index. On annealing, there is a reduction in the inter-atomic spacing due to crystallization that leads to higher densification and hence an increase in the refractive index. The relation between the refractive index of the film (n_f) and the packing density (P_d) can be expressed as,[4,5]

$$P_d = \frac{n_f^2 - 1}{n_f^2 + 2} \times \frac{n_b^2 + 2}{n_b^2 - 1} \qquad (4.2)$$

where n_b is the bulk refractive index.

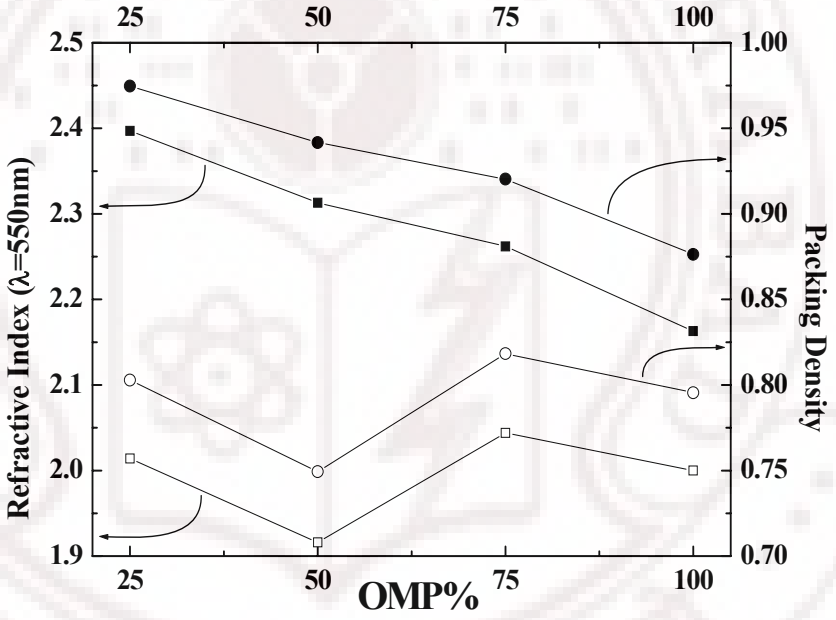

Figure 4.14: Variation of refractive index (@λ=550nm) and packing density, P_d, as a function of OMP. The open and closed symbols represent the a-BST5 and c-BST5 films respectively.

Figure 4.14, displays the variation of packing density (P_d) and refractive index (n_{550}, λ= 550nm) with OMP for both a-BST5 and annealed c-BST5 films. In the case of c-BST5 films the refractive index decreased with increase in OMP. This decrease in refractive index with high OMP could be attributed to lower packing density as is evident from the same graph.

In order to calculate the packing density of the film and the bulk material, from the refractive index data, the effective medium model of Bragg and Pippard, which takes the growth morphology[6,7] of the film into account, was used. For close-packed columnar grain morphology, the relation is given by,

$$n_f^2 = \frac{n_b^4 . P_d + (2 - P_d) . n_b^2 . n_p^2}{(2 - P_d) . n_b^2 + P_d . n_p^2} \qquad (4.3)$$

while that for a columnar structure of reduced density it is given by

$$n_f^2 = \frac{(1 - P_d) . n_p^4 + (1 + P_d) . n_p^2 . n_b^2}{(1 + P_d) . n_p^2 + (1 - P_d) . n_b^2} \qquad (4.4)$$

where n_p denotes the refractive index of the voids, which is taken as 1 for empty voids or 1.33 in the case of moisture filled voids.

Figure 4.15(a) depicts the calculated dependence of refractive index n_f (λ=550 nm) on the packing density, P_d, for a close-packed columnar structure and a columnar structure of reduced density, both with empty and moisture filled voids and figure 4.15(b) shows the refractive index versus the packing density for the present BST5 films.

A comparison of figures 4.15(a) and 4.15(b) reveals that a close fit could be achieved in the packing density by assuming the mode of closed packed columnar growth with empty voids and columnar growth with voids filled with moisture. The reduced packing density might cause the decrease in refractive index of the a-BST5 films. This assumption is further justified by the fact that oxide films deposited by RF-magnetron sputtering generally have a columnar growth structure with voids[8,9]. Furthermore, since the as-deposited films were deposited at room temperature, the possibility that the voids could be filled with moisture is high. However, in the case of annealed films, the presence of moisture in the films cannot be taken in to account due to the high temperatures (900^{o}C) of annealing. In this case, the mode of closed packed columnar growth with empty voids is, therefore, a good fit.

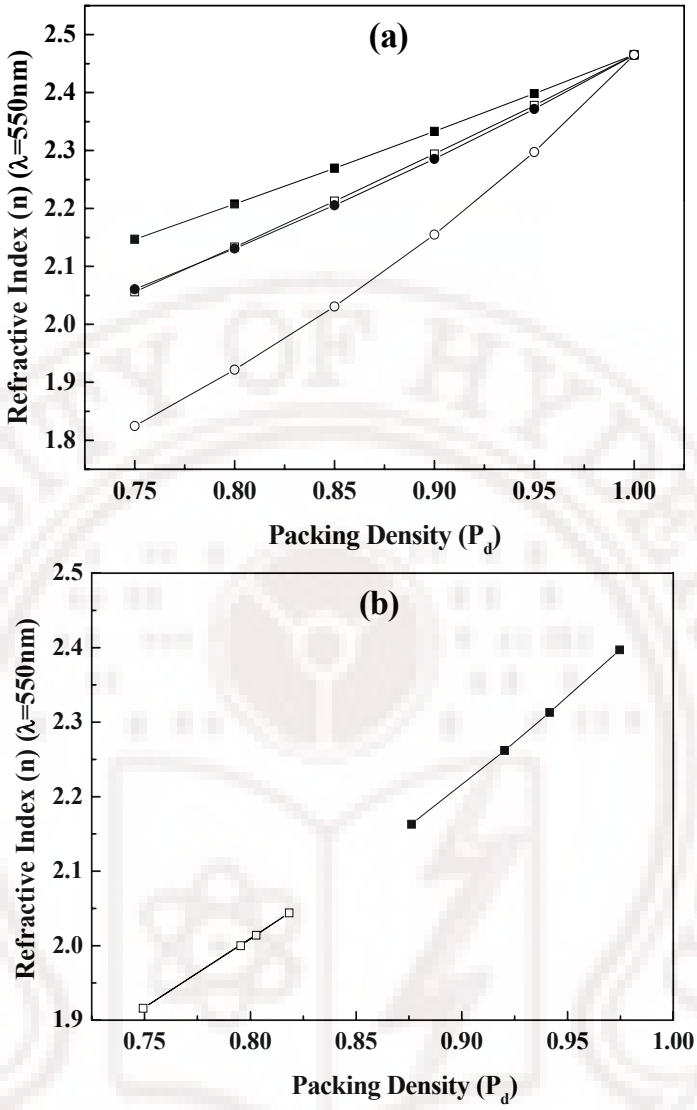

Figure 4.15: (a) Refractive index (λ=550nm) as a function of packing density, P_d, for two microstructures calculated according to Bragg- Pippard model: (■) close-packed columns with moisture filled voids; (□) close-packed columns with empty voids; (●) columnar growth with moisture filled voids; (○) columnar growth with empty voids. (b) Refractive index n (λ=550nm) versus the packing density, P_d of (■) a-BST5 and (□) c-BST5 thin films.

The optical band gap E_g for all the films was calculated using the Tauc relation. Figure 4.16 illustrates the optical band gap of c-BST5 films as a function of OMP.

The absorption edge of a-BST5 films varied between 4.1 and 4.2 eV with OMP (as in figure 4.4), which decreased sharply to about 3.5-3.66 eV on annealing at 900^{o}C, as observed in figure 4.16. The decrease in band-gap represents the transition from an amorphous phase to crystalline phase.

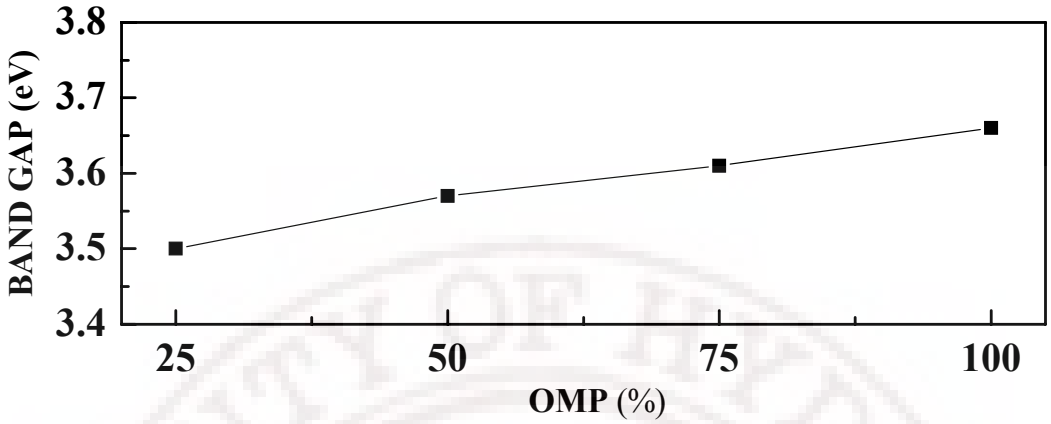

Figure 4.16: Variation in band-gap as a function of OMP for c-BST5 films.

The calculated band gap for the c-BST5 films is in good agreement with the reported bulk values of $BaTiO_3$ and $SrTiO_3$ (E_g= 3.2 and 3.6, respectively)[10]. The possible reason for higher value of band gap in the a-BST5 is the existence of density of states within the gap, as explained by Davis and Mott[11], causing the formation of a fundamental absorption edge due to the band tailing rather than an optical band gap. In the crystalline state the states within the gap disappear and the optical band gap then becomes equal to that of the single crystal value which is the difference between the top of the valence band and the bottom of the conduction band.

Although the band gap energy is a constant for a material in the bulk form it is known to vary in thin films with crystallite size[12]. The dependence of optical band gap on crystallite size of c-BST5 is shown in figure 4.17. It can be observed that the films with smaller crystallite sizes exhibit larger band gap energy than those with larger crystallite size. Similar investigations on the dependence of crystallite size on the optical band gap of $BaTiO_3$[13] and BST[14,15] thin films have been reported previously.

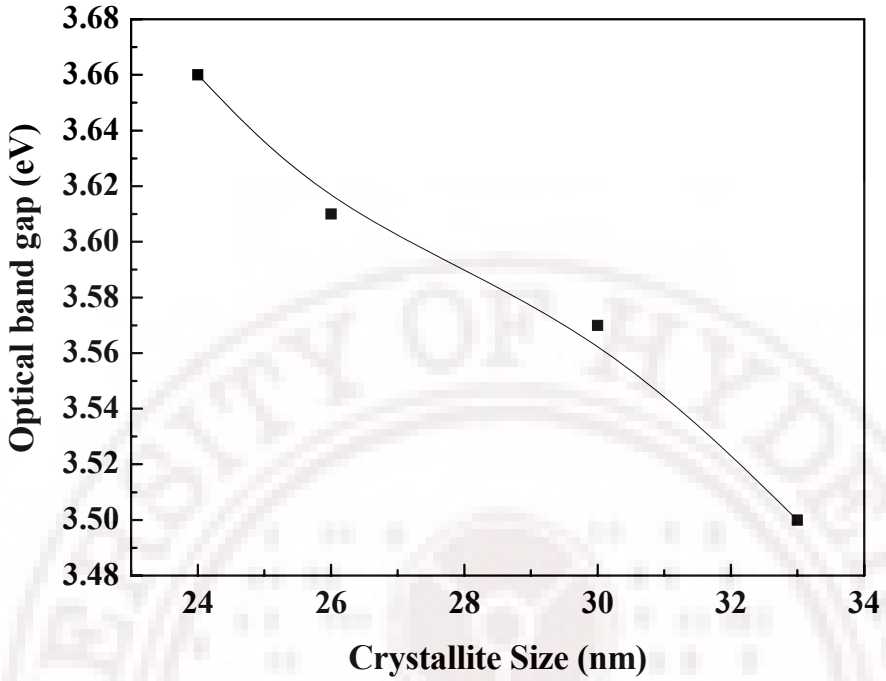

Figure 4.17: Variation in optical band gap as a function of crystallite size for c-BST5 films.

4.4.4 Microwave dielectric properties:

Microwave range measurement of permittivity and loss tangent of c-BST5 thin films on fused silica substrates were carried out at an X band spot frequency of 12.15 GHz using the modified cavity perturbation technique.

The variation in dielectric permittivity and loss tangent of the a-BST5 and c-BST5 thin films are shown in figure 4.18. It could be observed that the a-BST5 films show low values of dielectric permittivity and loss tangent when compared to that of the c-BST5 films. The high dielectric permittivity in perovskite thin films in the paraelectric state is mainly due to the large ionic polarization that is facilitated by the B-site ion *vs* Oxygen octahedra lattice mode vibrations. In the amorphous state where there is absence of long range ordering, this mechanism fails and hence the low value of dielectric permittivity. The phenomenon of enhanced dielectric permittivity with crystallization can be attributed to the highly polarizable ions that oscillate in a perovskite structure that inherently favour ionic polarization.

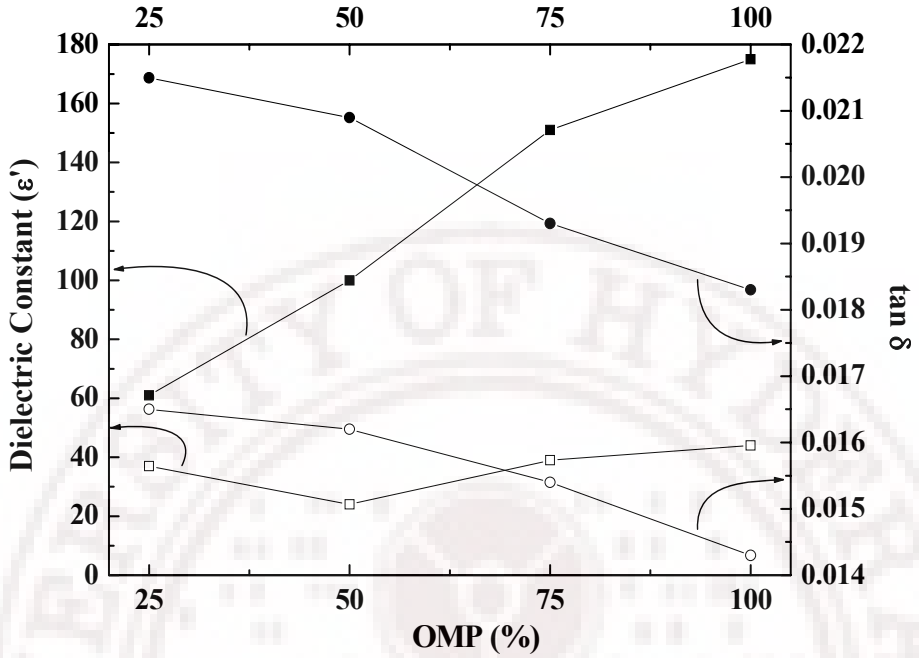

Figure 4.18: Variation in microwave dielectric constant (ε') and loss tangent (tan δ) at 12.15 GHz for $(Ba_{0.5},Sr_{0.5})TiO_3$ films deposited at different OMP. The open and closed circles represent the a-BST5 and c-BST5 films respectively.

Presence of defects in the form of oxygen vacancy can distort the lattice modes pertaining to the BO_6 octaheda, substantially affecting the polarization, which results in lower value of dielectric constant. When the films are deposited at higher OMP, the oxygen defect density reduces and hence a higher value of dielectric constant is observed.

4.4.4.1 Broadband microwave properties:

The broadband (10-14 GHz) dielectric properties of c-BST5 thin films were determined using a calibration comparison technique that makes use of two identical coplanar waveguides (CPW) patterned on the surface of the film[16] and the bare substrate using 500nm thick Ag/Au electrode. CPW test structures of 100 micron gap and 200 micron width were patterned simultaneously, one on the test film and the other on the bare substrate (fused silica) by lift – off process (figure 4.19).

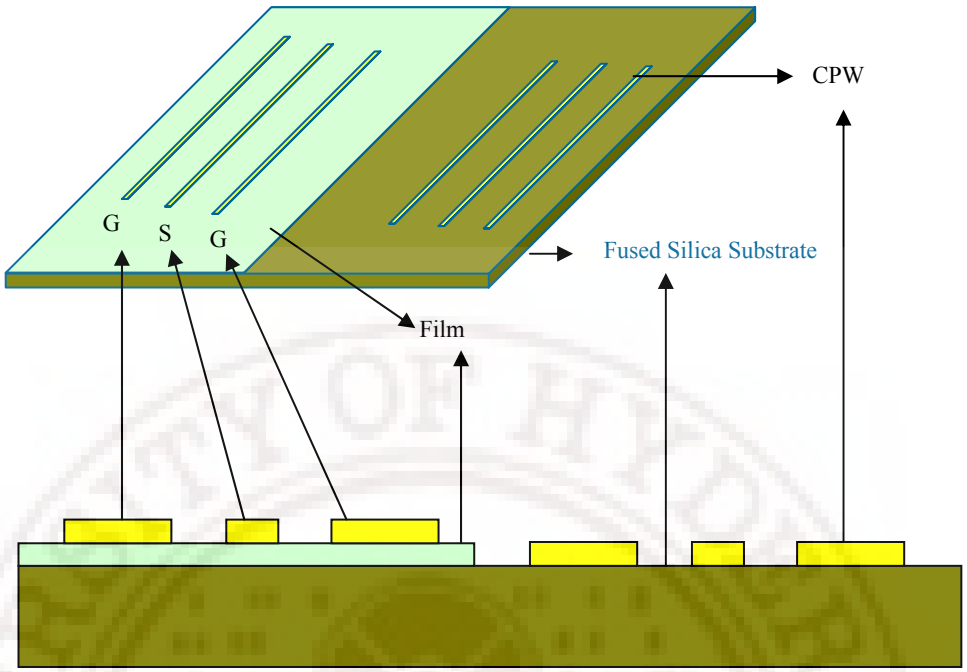

Figure 4.19: Top and cross-sectional view of the CPW transmission lines on test (film) and reference substrates with the G, S and G lines indicating the ground, signal and ground.

The microwave dielectric constant and loss tangent of c-BST5 films deposited at 25%OMP and 100%OMP are shown in figure 4.20 over a range of (10-14 GHz).

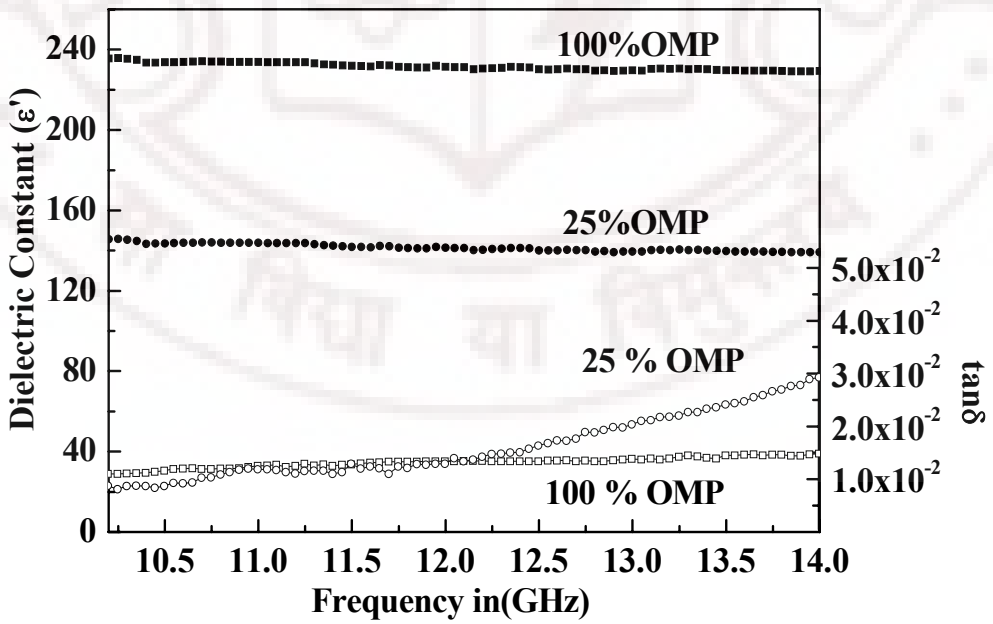

Figure 4.20: Variation of the microwave dielectric constant (closed symbols) and loss tangent (open symbols) of c-BST5 thin films deposited on fused silica substrates.

4.5 *Ex situ* annealing at low temperatures for a long period of time:

In the previous section, it was shown that there are significant changes in the optical and microwave properties of c-BST5 films as a function of OMP after an *ex situ* annealing treatment of 900°C for 1 minute. In the present section, the effect of post-deposition annealing is presented by annealing the films deposited on fused silica substrates at temperatures in the range of 400 to 1000°C. The OMP in the present study was fixed at 50%.

4.5.1 Structural characterization:

In order to crystallize a- BST5, *ex situ* annealing was carried out at different temperatures for 1hour. The XRD patterns of the BST5 thin films *ex situ* annealed at different temperatures in figure 4.21 shows that the films remain X-ray amorphous up to temperatures of 600°C.

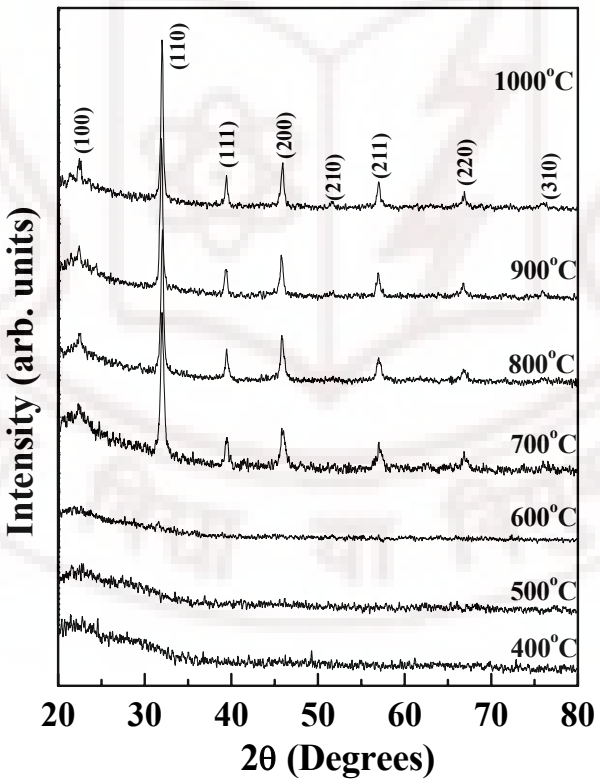

Figure 4.21: XRD θ-2θ scan of BST5 thin films annealed at different temperatures for 1h.

The films annealed at temperatures of 700°C and above crystallize into a polycrystalline cubic perovskite phase with no preferred orientation. Though there was no evidence of any secondary phase formation, the diffraction angle of the films annealed at 900°C and above showed a shift towards lower angle, indicating an increase in the lattice parameters. The peak position of the prominent (110) peak in figure 4.22 shows that, apart from the shift in the peak position, there is a decrease in the full width at half maximum (FWHM) value with the increase in the annealing temperature indicating an increase in the crystallite size. The increase in the lattice parameter could be a result of lattice strain due to defects in the form of oxygen vacancies[17].

Oxygen vacancies tend to form in oxide films at high temperatures[18,19] and are one of the most dominant defect centres in perovskite materials, especially titanates[20,21]. Removal of an oxygen atom from its normal site, O_O, is associated with the generation of free charge carriers according to the following equation:

$$O_O \rightarrow V_o^{++} + 2e- + {}^1\!/_2 O_2, \qquad (4.5)$$

where, V_o^{++} represents the doubly charged oxygen vacancy and e− the free electronic charge generated through the vacancy formation.

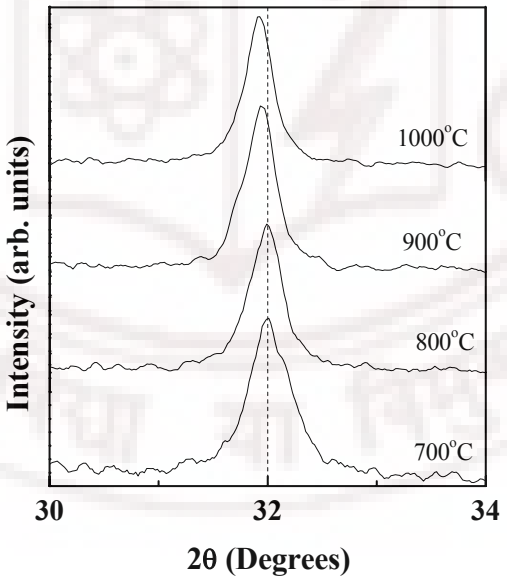

Figure 4.22: XRD pattern of BST5 thin films showing a low-angle shift when annealed at higher temperatures.

The average crystallite size of the films was estimated from the FWHM values using Scherrer's formula. The results indicated an increase in the crystallite size from

about 19 to 29 nm with an increase in the annealing temperature from 700 to 1000◦C. The variation in the lattice constant and the crystallite size with the annealing temperature is plotted in figure 4.23 and it shows an increase in the crystallite size due to enhancement in grain growth at high temperatures.

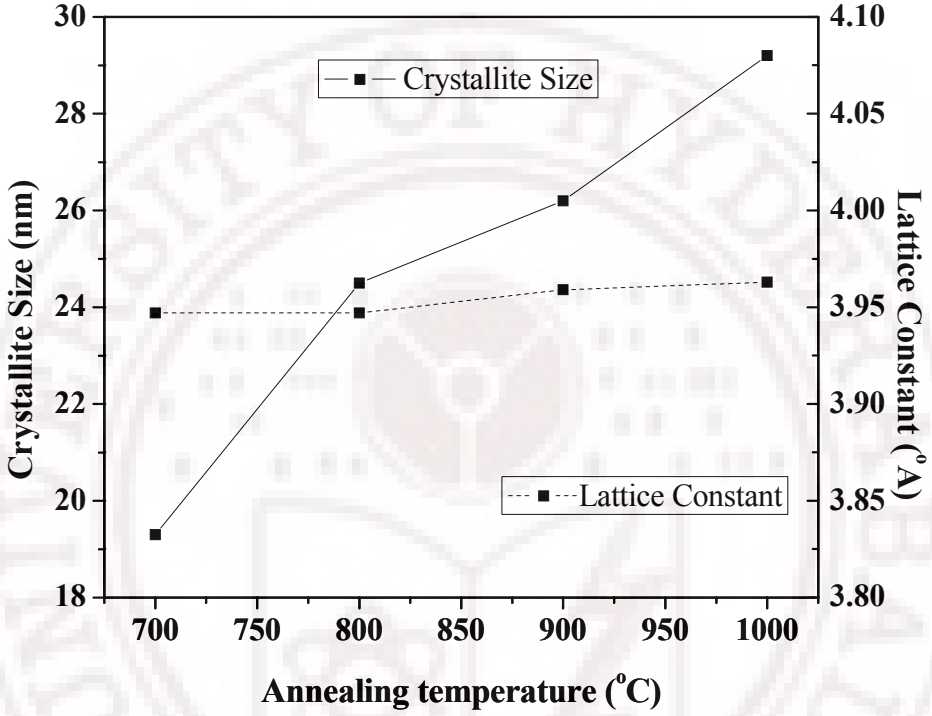

Figure 4.23: Graph showing the variation in lattice constant and crystallite size with annealing temperature.

4.5.2 Surface morphology:

The surface morphology of the BST5 films annealed at different temperatures is shown in figure 4.24. It is evident that there was no apparent grain structure for the film deposited at room temperature. On annealing, the evolution of grains is evident with pronounced grain boundaries. Though the films annealed at 600°C were x-ray amorphous, the AFM image reveals that the films exhibit nano-size grain morphology with an average grain size of about 60 nm. The films annealed at temperatures greater than 700°C show enhanced grain growth with the grain size between 150 and 250 nm.

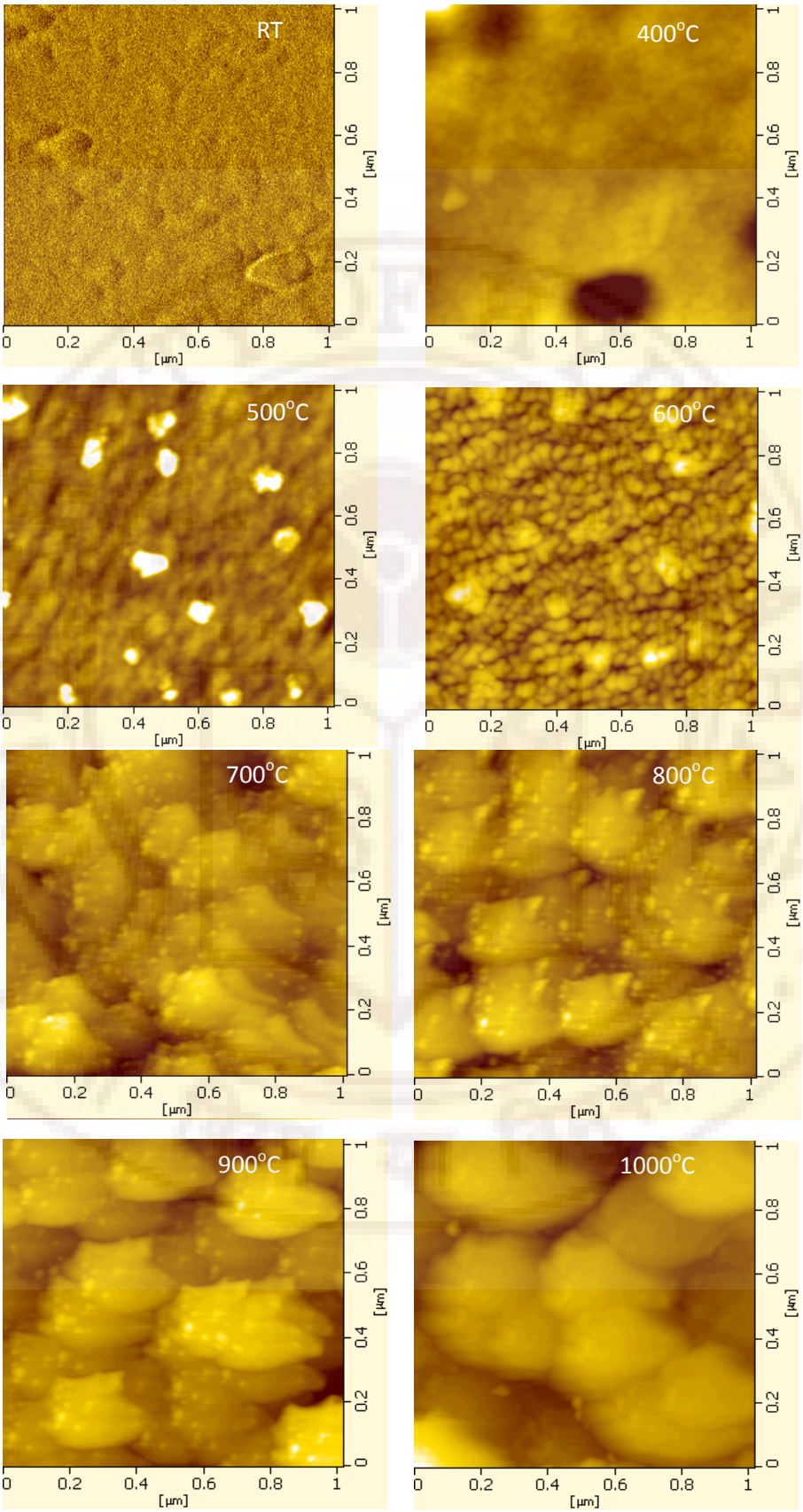

Figure 4.24: AFM image of BST5 films annealed at different annealing temperature.

4.5.3 Optical characterization:

The optical properties of the BST5 films *ex situ* annealed at different temperatures were investigated from the spectral transmittance spectra obtained from a JASCO V-570 spectrophotometer. As seen in figure 4.25, the room temperature deposited a-BST5 films are more transparent when compared with the annealed films due to the absence of scattering at grain boundaries.

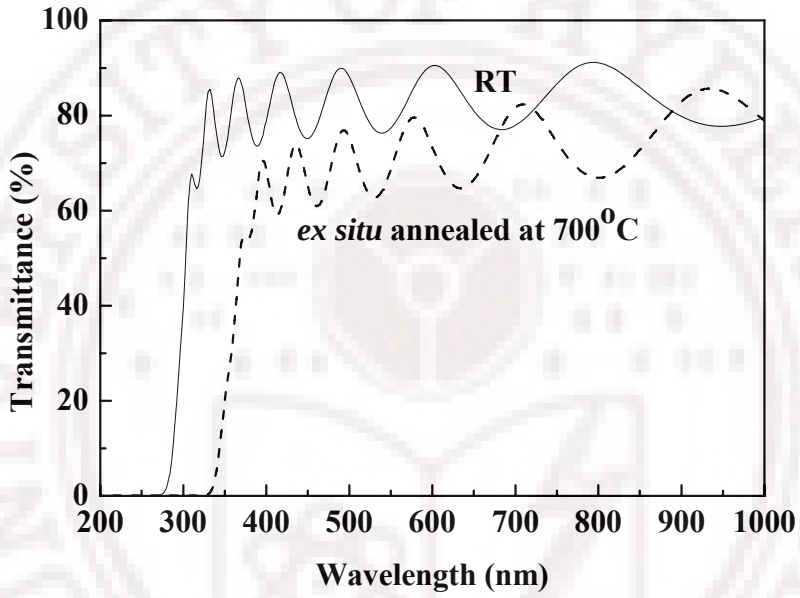

Figure 4.25: Optical transmittance spectra of room temperature deposited BST5 thin films compared with BST5 films *ex situ* annealed at 700°C for 1h.

The transmission edge in the region of strong absorption between 250 and 500 nm is shown in figure 4.26. A decrease in the absorption edge with increase in annealing temperature is observed for the films annealed up to 800°C. Such observations have been reported previously on $BaTiO_3$ and BST5 films[22,23,24,25].

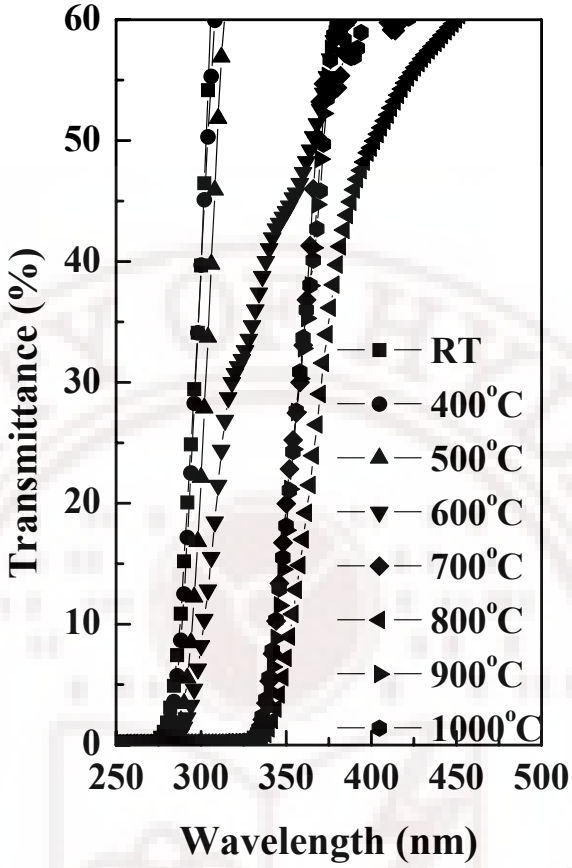

Figure 4.26: Graph showing the optical absorption edge of the BST films annealed at different annealing temperatures.

The optical band gap, E_g, for the films was calculated using the Tauc relation as discussed in chapter 3. In the present case, the band-gap energy (E_g) has been estimated by assuming an allowed direct transition between the highest occupied state of the valence band and the lowest unoccupied state of the conduction band. The variation of the band gap (Eg) with the annealing temperature is shown in figure 4.27.

The E_g of the as-deposited films was 4.37 eV which decreases slightly with the increase in annealing temperature till 600°C. On annealing the films at temperatures greater than 600°C, there is a sharp decrease in E_g which correlates with the onset of crystallinity as observed in XRD pattern shown in figure 4.21. On further annealing the films at temperatures greater than 800°C, E_g increases though the films remain crystalline. The increase in E_g of the films indicates that the films lose oxygen.

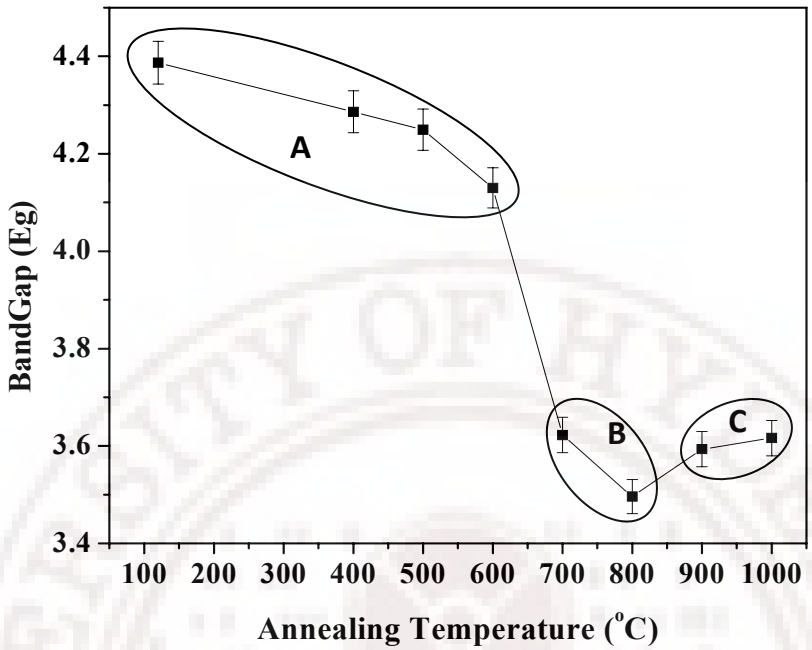

Figure 4.27: Graph showing the variation in band gap of the BST5 films annealed at different annealing temperatures

The variation in E_g with the annealing temperature presented in figure 4.27 can be divided into three regions: A, B and C. Region A represents the temperature range in which the E_g decreases slightly with the increase in temperature. Films in this region are X-ray amorphous and exhibit smooth grain morphology. Region B represents the temperature range in which the films crystallize and has the required oxygen stoichiometry. The transition from region A to B represents the amorphous-to-crystalline transition. Region C represents the temperature range in which the films remain crystalline but show an increase in E_g. The increase in E_g can be explained by the Burstein–Moss effect[26,27].

The removal of an oxygen atom from its normal site results in the generation of free charge carriers especially electrons, as seen from equation (4.5). The presence of a large number of free electrons in the film instigates an effect similar to heavy n-type doping. The Burstein–Moss effect suggests that heavy n-type doping in a material blocks the lower lying states in the conduction band, thus increasing the effective band gap of the material by ΔE_g. For an ideal crystalline material with no defects, the energy–momentum (E–k) diagram is as shown in figure 4.28*a*, which indicates that the band gap, E_g, is given

by the difference between the lowest state in the conduction band and the highest state in the valence band. The parabolic band approximation is valid only when there is a periodic potential and therefore cannot be applied for amorphous materials.

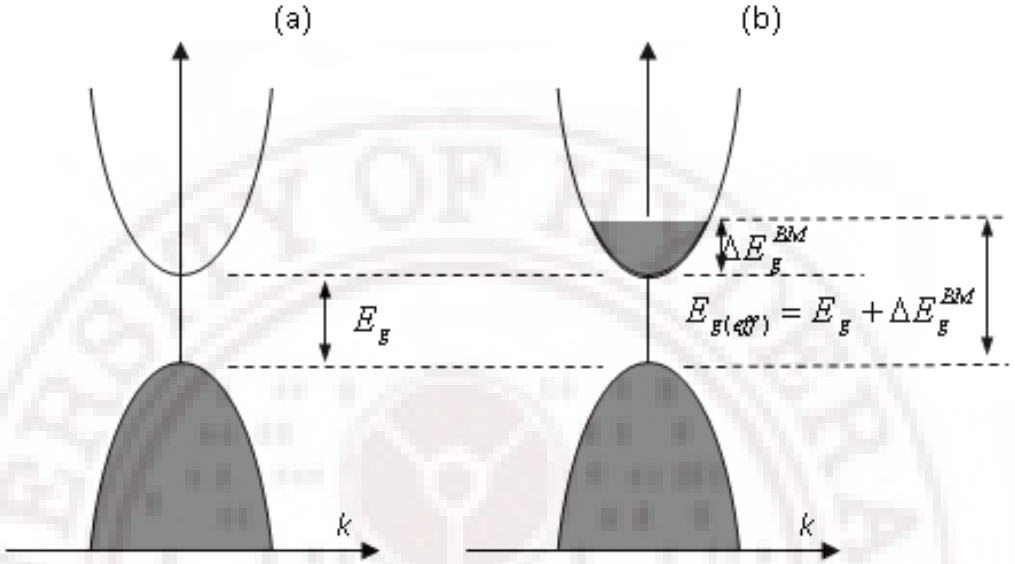

Figure 4.28: Band diagrams of normal and defect-doped BST thin films (a) depicts the situation in the case of normal film and (b) represents the band diagram of films with a large oxygen vacancies.[26]

In the present case, this approximation is valid for films annealed at temperatures ≥ 700°C but not for films annealed at temperatures ≤ 600°C because these films are amorphous in nature. The band gap in BST thin films is believed to be due to the separation between the 2p levels of the oxygen ions and 3d levels of titanium ions. When the films are annealed, the band gap decreases, indicating that the separation between the levels is influenced by long-range ordering. When the films have a large number of oxygen vacancies, then according to the Burstein–Moss effect the lower lying state in the conduction band gets blocked and hence the effective band gap $E_{g(eff)}$ increases by ΔE_g^{BM} as shown in figure 4.28 (*b*).

The effect of annealing on the refractive index (λ = 550 nm) and packing density of the films is shown in figure 4.29. The refractive index shows a transition on crystallization as is the case with band-gap behaviour. The variation in the refractive index is microstructural in origin, in contrast to the reasons for the variations in the optical band gap. The films densify on annealing resulting in an increase in the refractive index.

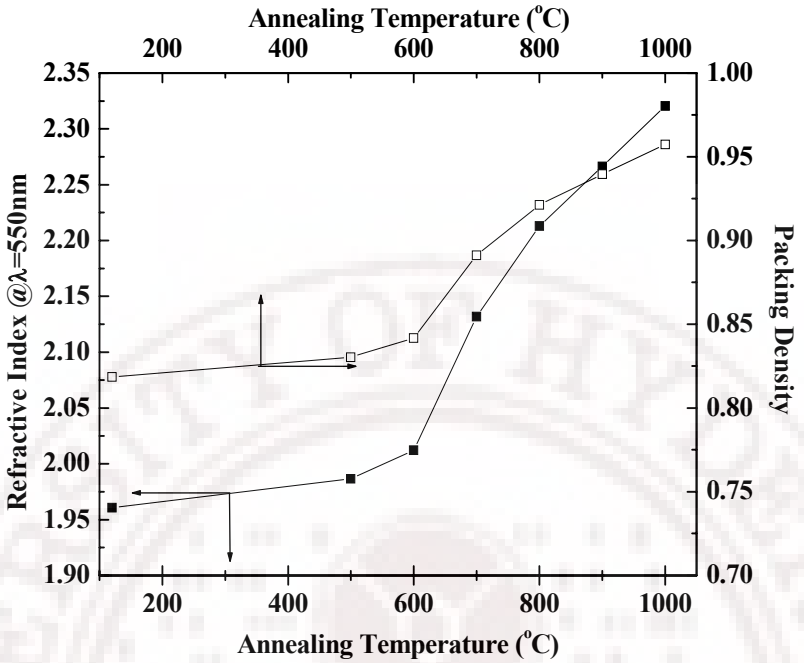

Figure 4.29: Variation in refractive index (@ λ=550nm) and packing density of BST5 thin films as a function of annealing temperature.

The packing density of films was estimated using equation 4.2. This relationship between the refractive index and the packing density or densification of the films has been well studied and it is known that films with a denser microstructure show a higher refractive index than those with porous microstructures. Figure 4.30 displays the variation in the value of refractive index with packing density in this study. It thus appears that there are two consequences for the annealing process apart from crystallization, namely the creation of oxygen vacancies and the densification of the films. While the former leads to nonstoichiometry in the films affecting the band structure, the latter leads to changes in the refractive index.

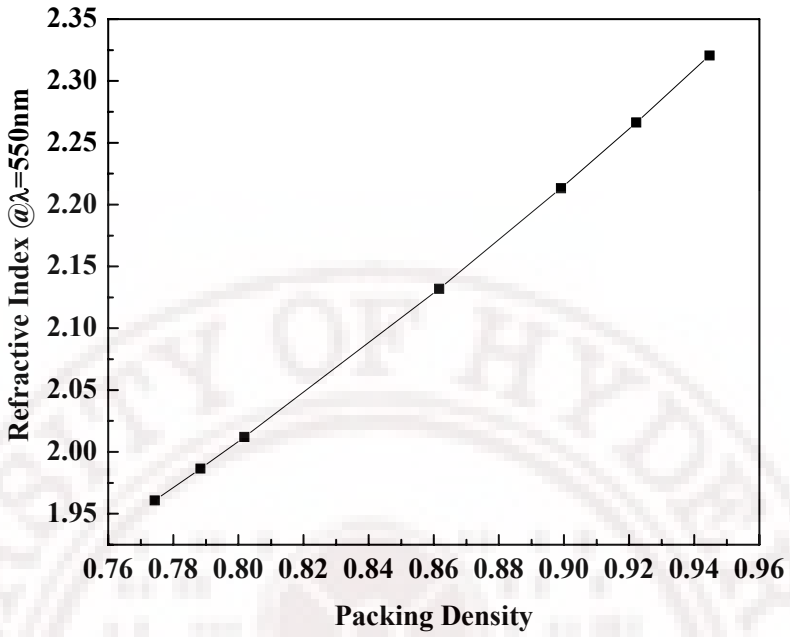

Figure 4.30: Variation in refractive index, n (@ λ= 550nm) with packing density, P of BST5 thin films.

4.5.4 Microwave dielectric properties:

Measurement of permittivity and loss tangent of the as-deposited and annealed BST5 thin films was carried out at an X-band spot frequency of 12.15 GHz using the extended cavity perturbation technique. The details of the technique have been discussed in detail in chapter 3.

The variation in the dielectric permittivity and loss tangent of the a-BST5 and *ex situ* annealed BST5 thin films is shown in figure 4.31. It can be observed that the a-BST5 films and the films annealed at 500^{o}C show low values of dielectric permittivity (between 40 and 56) and a loss tangent of 0.01. The films annealed at 600^{o}C, which were x-ray amorphous and had nano-crystalline surface morphology, showed a dielectric constant of about 106. A twofold increase in the dielectric constant could be observed for the films annealed at 700 and 800^{o}C. These films were crystalline with pronounced grain growth. Annealing the films to temperatures higher than 800^{o}C resulted in a decrease in the dielectric constant.

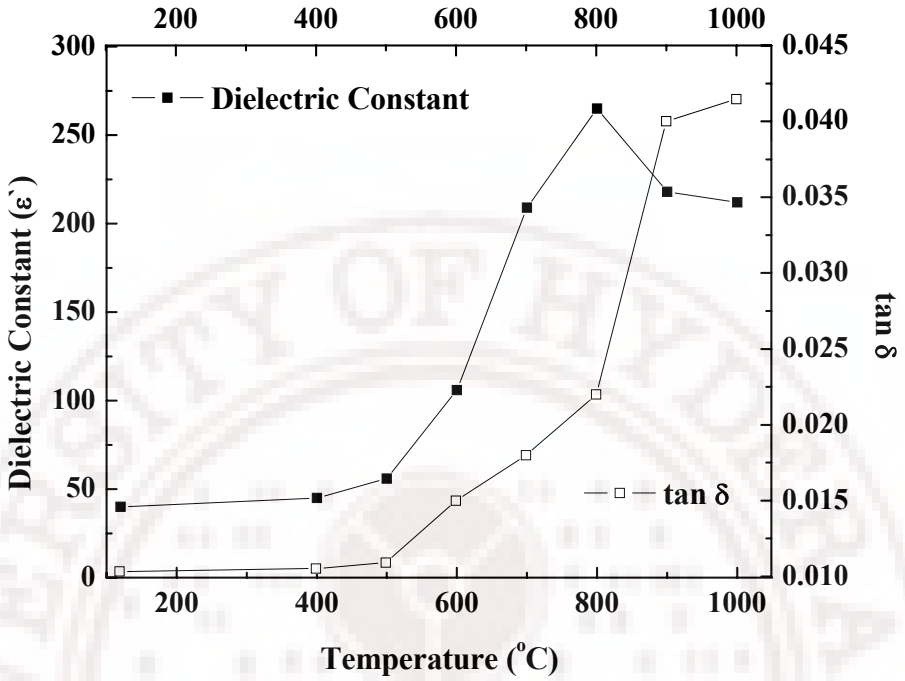

Figure 4.31: Graph showing the variation in microwave dielectric constant (ε') and loss tangent (tan δ) at 12.15 GHz for BST5 films annealed at different annealing temperatures.

A maximum value of $\varepsilon = 265$ is obtained for the films annealed at 800°C. It can be noted that with a further increase in the annealing temperature, the dielectric constant decreases, possibly due to the lattice strain owing to defects in the form of oxygen vacancies.

Oxygen vacancies are one of the most dominant defect centres[20] in oxide materials. These defects absorb microwave photons by the generation of an acoustic phonon which increases the dielectric loss.[28] Hence, the dielectric loss tangent of the films annealed at 900 and 1000°C are higher.

4.6 Summary:

In summary, structural, microstructural, optical and electric properties of amorphous BST5 (a-BST5) thin films have been studied. The a-BST5 films were deposited on water cooled substrates at different OMP. The a-BST5 films have band-gap, refractive index and dielectric constant values comparable to most of the technologically important oxides. These films show zero tunability, but have excellent dielectric strength. Hence a-BST5 films can be considered for applications which require moderate dielectric constant (about 30) with high power handing capabilities. The low loss tangent in a-BST is an additional advantage. No significant differences in the properties of a-BST5 thin films were observed as a function of OMP.

In order to crystallize a-BST5 films, they were *ex situ* annealed using two different annealing profiles. In the first approach, all the BST5 films deposited as a function of OMP at RT were crystallized by cold inserting a-BST5 films at 900^{o}C for 1 min. This annealing approach yielded crystalline BST5 (c-BST5) films with good structural, optical and microwave dielectric properties on fused silica substrates.

In the second approach, the a-BST5 films deposited at 50% OMP were *ex situ* annealed from 400^{o}C to 800^{o}C in intervals of 100^{o}C. The onset of crystallinity was found to be 700^{o}C and films annealed above 800^{o}C loose oxygen. The effects of this *ex situ* annealing approach on crystallinity and oxygen stoichiometry on the structural, microstructural, optical and microwave dielectric properties have been addressed. Though both the annealing approaches gave crystalline BST5 films, no good MIM structures were realized on Pt/Si substrates, due to high thermal shock received from the *ex situ* annealing process. The difference in thermal expansion coefficient of Pt and Si resulted in hillock formation on Pt layer, which in turn significantly deteriorated the surface morphology of the c-BST5 layer. These lead to electrically shorted MIM structure. This necessitated crystallizing BST5 thin film during the growth process. Hence, the films were crystallized *in situ* by depositing BST5 films at elevated deposition temperatures (T_d).

The next chapter deals with the structural, microstructural and optical properties of c-BST5 films deposited *in situ* at elevated temperatures.

References:

[1] K. Venkata Saravanana, K. Sudheendrana, M. Ghanashyam Krishnaa, K.C. James Raju and Anil K. Bhatnagar, *Vacuum* **81**, 307 (2006).

[2] S.R. Summerfelt, D. Kotecki, A. Kingon and H.N. Al-Shareef, *Mat. Res. Soc. Symp. Proc.,* **361**, 257 (1994).

[3] P. Li, J. F. McDonald and T. M. Lu, *J. Appl. Phys.*, **71**, 5596 (1992).

[4] G. Bauer, *Ann. Phys.*, **19**, 434 **(**1934).

[5] R. Jacobson, *Phys. Thin Films*, **8**, 51 (1975).

[6] W. L. Bragg, and A. B. Pippard, *Acta Crystallogr*., **6**, 865 (1953).

[7] H. A. McLeod, *J. Vac. Sci. Technol*., **4**, 418 **(**1986).

[8] R Thielsch, K. Kaemmer, B. Holzapfel and L. Schultz, *Thin Solid Films*, **301**, 203 (1997).

[9] J. A. Thornton, *J. Vac. Sci. Technol*., **11**, 666 (1974).

[10] S. H. Wemple, and M. Didomenico Jr., *Phys. Rev. B*., **3**, 1338 (1971).

[11] E. A. Davis, and N. F. Mott, *Phil. Mag*., **22**, 903 (1970).

[12] D. Pamu, M. Ghanashyam Krishna, K. C. James Raju and Anil K. Bhatnagar, *Solid State Commun*., **7**, 135 (2005).

[13] X. M. Lu, J. S. Zhu, W. Y. Zhang, G. Q. Ma, and Y. N. Wang, *Thin Solid Films*, **274**, 165 (1996).

[14] Somnath C. Roy, G. L. Sharma, M. C. Bhatnagar, R. Manchanda, V. R. Balakrishnan, and S. B. Samanta, *Appl. Surf. Sci*., **236**, 306 (2004).

[15] Yu- Fu Kuo, and Tseung-Yuen Tseng, *Mater. Chem. Phys*., **61**, 244 (1999).

[16] Guru Subramanyam, Emily Heckman ,James Grote, Frank Hopkins, Robert Neidhard and Edward Nykiel, *Microwave and optical Technol. Lett*., **46**, 278 (2005).

[17] L A Knauss, J M Pond, J S Horwitz, D B Chrisey, C H Mueller and R Treece, *Appl. Phys. Lett.,* **69**, 25 (1996).

[18] B H Park, Y Gim, Y Fan, Q X Jia and P Lu, *Appl. Phys. Lett.,* **77**, 2587 (2000).

[19] S-T Zhang, G-L Yuan, J Wang, Y-F Chen, G-X Cheng and Z-G Liu 2004 *Solid State Commun.* **132**, 3156 (2006).

[20] A A Sirenko, I A Akimov, J R Fox, A M Clark, H-C Li, W Si and X X Xi , *Phys. Rev. Lett.,* **82**, 4500 (1999).

[21] R Waser and D M Smyth, *Ferroelectric Thin Films: Synthesis and Basic Propertie,* Gorden and Breach, Amsterdam (1996).

[22] W T Liu, S T Lakshmikumar, D B Knorr, T M Lu and I G A Vander Leeden, *Appl. Phys. Lett.,* **63**, 574 (1993).

[23] N F Mott, and E A Davis, *Electronic Processes in Non-Crystalline Materials,* 2nd ed., Oxford: Clarendon (1979).

[24] S B Desu, *Phys. Status. Solidi.*, **141**, 119 (1994).

[25] K Venkata Saravanan, M Ghanashyam Krishna K C James Raju and A K Bhatnagar, *Proc. 50th Golden Jubilee DAE Solid-State Physics Symp.,* **50**, 441 (2006).

[26] E Burstein, *Phys. Rev.* B, **93**, 632 (1954).

[27] T S Moss, *Proc. Phys. Soc.* B, **67**, 775 (1954).

[28] A A Sirenko, C Bernhard, A Golnik, A M Clark, J Hao, W Si and X X Xi, *Nature*, **404**, 373 (2000).

Chapter V

Deposition of c-BST thin films and its structural, microstructural and optical properties

5.1 Introduction:

This chapter deals with the deposition as well as structural, microstructural and optical properties of crystalline BST5 (c-BST5) thin films. In contrast to the previous chapter, all BST5 films described in this chapter are deposited in situ at high temperatures. As mentioned in chapter 1, most of the studies on BST thin films for tunable microwave applications have been on single crystal substrates. In the previous chapter it was shown that crystallizing BST5 thin films on amorphous fused silica substrates is indeed possible. However, post deposition or ex situ annealing treatment failed to yield desired properties in terms of good surface morphology with suitable optical and electrical properties. The poor quality of ex situ crystallized BST5 film is mainly due to the difference in thermal expansion coefficient and the thermal shock encountered by the film and the substrate during the post deposition annealing process. As crystallization and densification takes place during the in situ growth process, BST5 films deposited this way are expected to give better optical and electrical properties.

5.2 Deposition of c-BST thin films:

BST5 thin films were deposited using the procedure mentioned in chapter 2. Two series of films were deposited as part of this study.

In order to investigate the effect of deposition temperature T_d, on the crystallinity, BST5 thin films were deposited at substrate temperatures from 400^{o}C to 800^{o}C in steps of 100^{o}C (*temperature series*) at a constant OMP of 50%. In the second case, deposition temperature was fixed at 800^{o}C and the OMP was varied from 0% to 100% in steps of 25% (*OMP series*) to determine the influence of OMP on the deposited BST5 thin films.

Initially, the sputtering chamber was evacuated to a base pressure of 2 $x10^{-6}$ Torr after loading the cleaned substrates on to the substrate holder placed inside the vacuum chamber. All the films were deposited at a fixed power density of 3.0 Wcm^{-2}. A working pressure of 20 mTorr was constantly maintained using a mixture of high pure (99.99%) argon and oxygen. The Ar:O_2 ratio i.e. OMP was varied from 0 to 100% in steps of 25% (*OMP series*) while maintaining the T_d at 800^{o}C. The target to substrate distance was fixed at 5 cms. To vary the degree of crystallinity, the deposition temperature (T_d) was varied from room temperature to 800^{o}C at intervals of 100^{o}C (*temperature series*) with a fixed OMP of 50%. It was observed that without any heating, the un-cooled substrate temperature increased to about 120-130^{o}C during the deposition, presumably due to ion bombardment. The thickness of thin films was around 500-600 nm. Prior to every deposition, the substrates were stabilized at the respective T_d for an hour and rate of increase in temperature was about 10^{o}C/min. After the deposition of BST5 films, the argon flow in to the chamber was cutoff and the film coated substrates were cooled down to ¼ T_d in oxygen atmosphere. The oxygen flow was cutoff when the temperature reached ¼ T_d. This procedure was adopted to ensure that the substrates and films do not undergo thermal shock during the ramp up and down process and ensure oxidation of the deposited films.

As mentioned in chapter 1, the main aim of this thesis is to deposit and characterize crystalline BST5 on amorphous fused silica substrates. Hence, the primary substrate used was fused silica. For comparison c-BST5 films were deposited on $LaAlO_3$ (LAO), c-plane Al_2O_3 (AlO) and MgO single crystal substrates. For electrical

characterization, where a MIM structure is required, BST5 films were deposited on Pt/Si substrates under identical conditions.

Following the deposition of BST5 thin films, a series of characterization techniques probing the structural, microstructural and optical properties of the films were performed. The stoichiometry of the films was established by Rutherford Backscattering Spectrometry (RBS) analysis as described in chapter 2. The crystal structure of c-BST5 films deposited on fused silica substrates as a function of deposition temperatures and OMP were characterized using X-ray diffraction (XRD) technique. Following the XRD measurements, Dynamic Force Microscope (DFM) was employed to measure the surface morphology of the films, which provided high resolution images. The root mean square roughness (rms roughness) was also determined using DFM.

Optical constants such as refractive index and optical band-gap of BST5 films deposited on fused silica substrates were determined from the spectral transmittance data obtained from UV-Vis-NIR spectrophotometer. A correlation between the structural, microstructural and optical properties of BST5 films is discussed.

5.3 Structural characterization - Temperature series:

In this section, the structural properties of c-BST5 thin films deposited on various substrates as a function of T_d is discussed.

5.3.1 Structural characterization of c-BST5 films deposited on fused silica substrates:

The crystal structure of BST5 thin films grown at different deposition temperatures, T_d on fused silica substrates were analyzed by XRD θ–2θ scans using Co Kα radiation (λ=1.7889Å) and are shown in figure 5.1. The onset of crystallization for the BST5 films deposited on fused silica substrates was found to be 600^{o}C. Cubic perovskite structure of polycrystalline BST5 films was observed for the films deposited at $T_d \geq$ 600^{o}C. Films deposited at 500^{o}C and below were found to be X-ray amorphous. The lattice constant calculated assuming a cubic crystal symmetry was about 3.954 ±0.01 Å for all the films deposited at various T_d. Crystallinity and crystallite size of the films were found to be strongly dependent on T_d. On comparing the intensity and the full width at half maximum (FWHM) of the major (110) peaks, it can be deduced that the crystallinity and crystallite size of the films increase with increase in T_d.

Another point derived from the XRD patterns in the present case is that there is little or no tendency of preferential orientation in BST5 films deposited on fused silica substrates. The crystallite size, *t*, as shown in figure 5.2 was estimated from the Full Width at Half Maximum (FWHM, β) of the XRD peak by Scherrer's formula,

$$t = \frac{0.9\lambda}{\beta \cos\theta} \qquad (5.1)$$

where, λ is the wavelength of the X-ray used and θ is the diffraction angle.

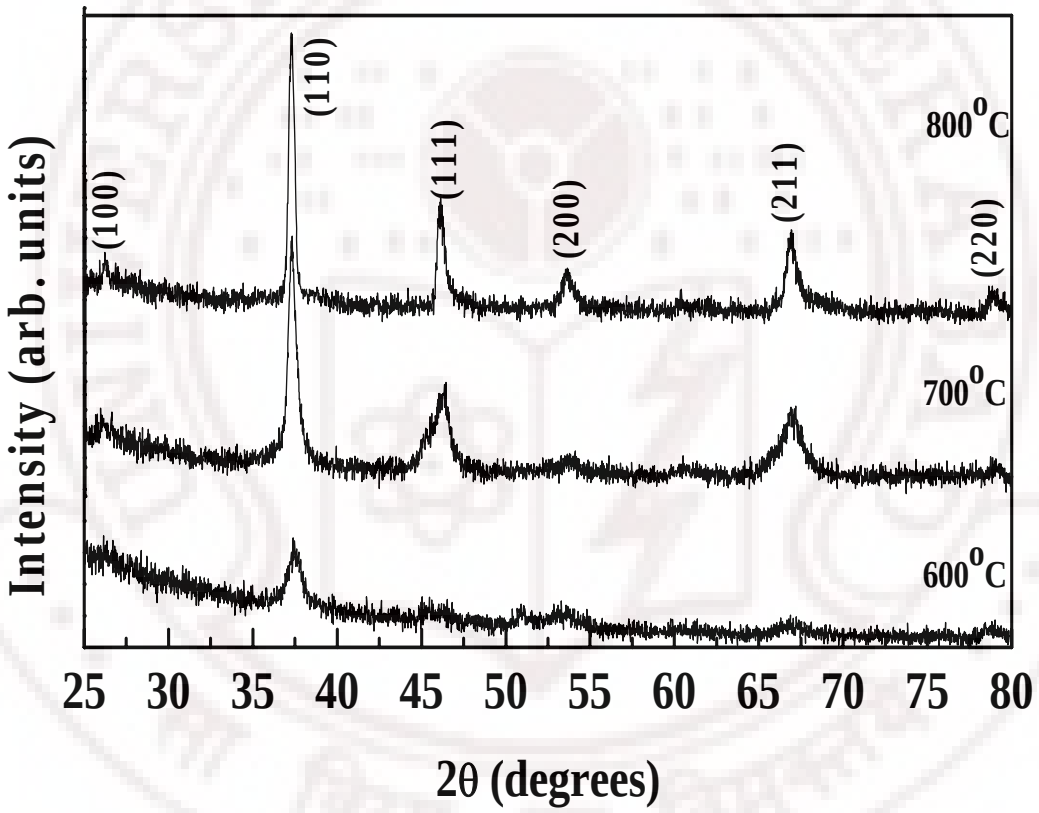

Figure 5.1: X-ray diffraction pattern of BST5 thin films deposited on fused silica substrates at different deposition temperatures, T_d.

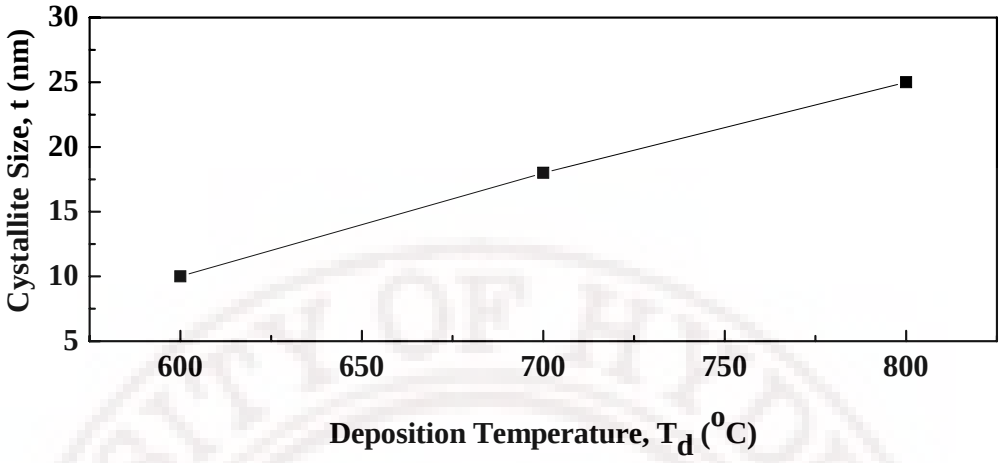

Figure 5.2: Graph showing the variation in crystallite size as a function of T_d.

The above figure 5.2 shows increase in crystallite size with increase in T_d. This variation can be attributed to the increase in grain growth due to sintering at higher substrate temperatures[1,2]. High quality films with good crystallinity were achieved on depositing BST5 at 800°C.

5.3.2 Structural characterization of c-BST5 films deposited on Pt/Si substrates:

Figure 5.3 shows the T_d dependent θ–2θ diffraction patterns of the BST5 films deposited on (111) oriented Pt/ Si substrates, analyzed by X-ray diffraction technique using Cu Kα radiation (λ=1.54056Å). The films deposited at 500^{o}C and below were x-ray amorphous and the onset of crystallization was found to be 600^{o}C. All the crystalline films show hetero-epitaxial growth along [111] direction. Apart from the orientation of the Pt underlayer, the orientation of the deposited films depends on the thin film processing conditions such as rate of deposition, working pressure during sputtering and T_d. Where, T_d not only facilitates crystallization of the film but also influences the orientation of the growing film. Improvement in the degree of crystallinity with increase in T_d is evident from figure 5.3.

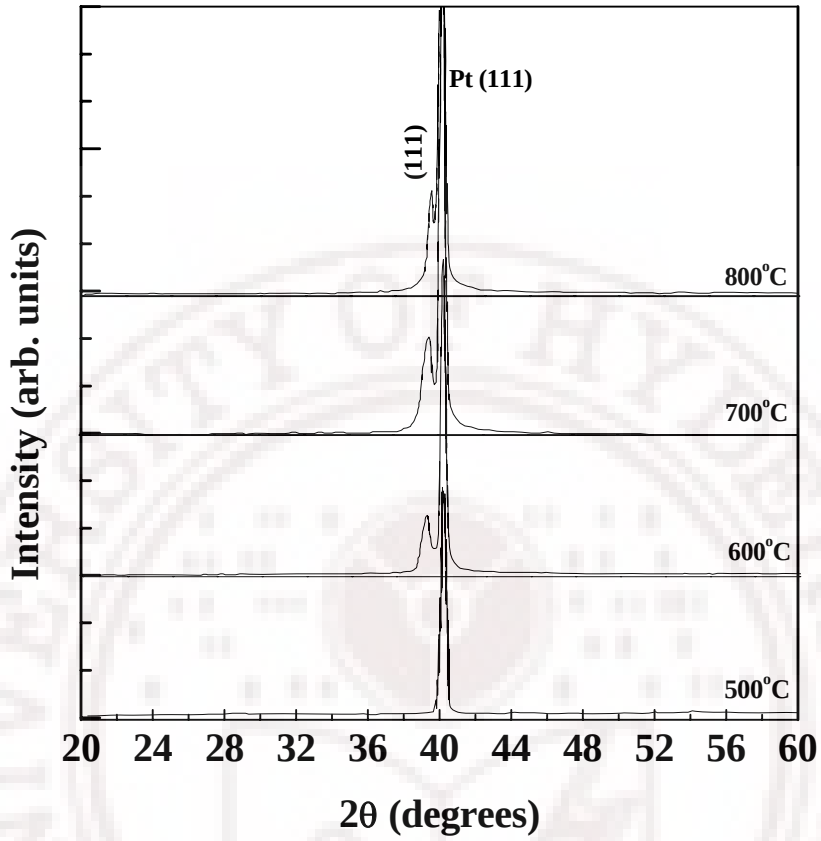

Figure 5.3: XRD pattern of BST5 deposited on a Pt/Si substrates at different temperatures showing (111) orientation

Apart from improvement in degree of crystallinity, a shift in the BST5 peak positions toward higher two-theta values can also be observed with increase in T_d indicating a decrease in the lattice parameters. The lattice constant calculated assuming cubic crystal symmetry of the BST5 films deposited at 600, 700 and 800°C are 3.991, 3.973 and 3.950 Å, respectively. The reported lattice constant of the BST5 bulk is 3.947 Å. The higher lattice constant for the films might be due to strain. The misfit strain u_m, was calculated using the formula[3,4],

$$u_m = \frac{a_s - a_f}{a_s} \qquad (5.2)$$

where, a_s is the substrate lattice parameter or that of the lower lying layer (Pt, 3.923 Å)[5] and a_f is the lattice parameter of the deposited film. Misfit strain is generally calculated for epitaxial films.

The misfit strain calculated for the films deposited at 600°C is -1.75%. The misfit strain reduces with increase in T_d to -1.27 % and -0.68% for the films deposited at 700°C and 800°C respectively.

The residual strain, u_b is given as,

$$u_b = \frac{d_b - d_f}{d_b} \qquad (5.3)$$

where, d_b is the inter-planar spacing of the bulk BST5 ($d_{b(111)}$=2.279 Å) and d_f is that of the film. The strain calculated with respect to the bulk for the films deposited at 600°C is -1.09%. The residual strain reduces with increase in T_d, to -0.62 % and -0.04% for the films deposited at 700°C and 800°C respectively. Thus, the films deposited at 800°C are strain relieved when compared to the films deposited at lower substrate temperatures. This could be explained by considering that, in physical vapor deposition technique such as sputtering, the surface mobility of the adsorbed particles varies with the surface temperature (or deposition temperature, T_d) and the films grow in such a way that the total energy i.e., surface energy of the films, film–substrate interface energy and the strain energy in the films is minimized[6,7]. At low T_d the adsorbed particles have low surface mobility and so the diffusion length becomes very small causing the vapor molecules to freeze on impact, resulting in a highly stressed film. As T_d increases the surface diffusion increases and so the atoms acquire sufficient energy to crystallize in such a way that the total energy is minimized. Thus, the films deposited at higher T_d are generally stress relieved.

5.3.3 Structural characterization of c-BST5 films deposited on single crystal substrates:

Figure 5.4 shows the X-ray diffraction pattern of BST5 films deposited at 50% OMP and 800°C on various single crystal substrates such as Magnesium oxide (MgO), c-plane sapphire (AlO) and Lanthanum Aluminate (LAO). The XRD pattern of BST5 film deposited on fused silica substrate is shown for comparison.

The Au peak in diffraction pattern of BST5 film deposited on c-plane sapphire originates from the device structure patterned on them.

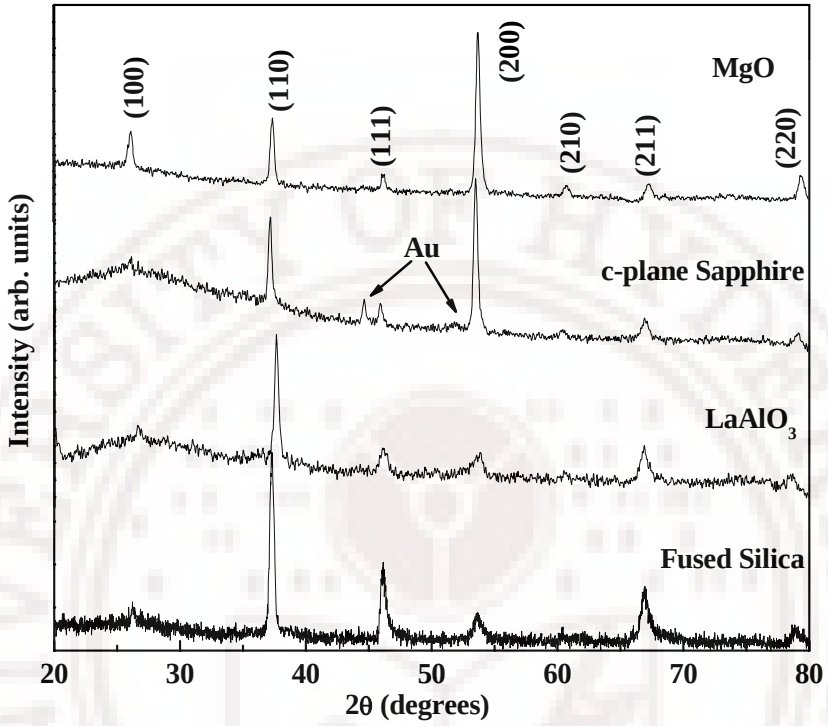

Figure 5.4: X-ray diffraction pattern of c-BST5 thin films deposited on single crystal substrates at 800^{o}C and 50 % OMP.

The diffraction pattern shows that BST5 films deposited on single crystal substrates have only pure perovskite phase. The BST5 films deposited on LAO do not show any sign of preferred orientation apart from the (110) prominent peak. The diffraction pattern is similar to that of BST5 films deposited on fused silica substrates. On the other hand, the BST5 films deposited on MgO and AlO show preferential orientation along (200). The orientation of the BST5 epilayer is considered to be associated with the surface free energy of the substrate used[8]. Even if there exists a large lattice mismatch, the [*200*] orientation is strongly developed at high T_d.

The inter-planar spacing, d_{hkl} of the BST5 film deposited on various single crystal substrates were calculated from the diffraction angle of the prominent peak. The inter-planar spacing of BST5 film deposited on LAO and fused silica substrates were calculated from the diffraction angle of the (110) peak where as the diffraction angle of

the (200) peak was used for determining the inter-planar spacing of BST5 films deposited on MgO and AlO substrates. The measured d_{110} values were 2.772 Å and 2.797 Å for BST5 films deposited on LAO and fused silica substrates respectively. The measured d_{200} values of BST5 films deposited on MgO and AlO were 1.979 Å and 1.983 Å respectively. For bulk BST5, the d_{110} value is 2.7918 Å and that of d_{200} is 1.973 Å[9]. The difference in inter-planar spacing could be due to residual strain developed in the film either due to lattice mismatch[10] or due to difference in thermal expansion coefficients[11]. The residual strain, u_b calculated using the formula as discussed in the previous section for the films deposited on various substrates are given in table 5.1.

Substrate material	**Residual strain u_b (%)**
MgO	-0.3
AlO	-0.5
LAO	0.7
Fused silica	-0.2

Table 5.1: Table showing the residual strain values of BST5 deposited on different substrates.

It could be inferred from the above table that the lattice constant of BST5 films deposited on LAO substrates are lower that the lattice constant of bulk BST5, inducing an in-plane compressive residual strain with respect to the bulk. On the other hand, BST5 film deposited on MgO and AlO substrates have a higher lattice constant than bulk BST5, inducing an in-plane tensile residual strain with respect to the bulk. A lowest residual strain value of -0.2% was obtained for the films deposed on fused silica substrates which are amorphous in nature. Unlike BST deposited on Pt/Si substrates, no noticeable variation in the strain value was observed for BST5 films deposited on fused silica substrates as a function of T_d. BST5 films were deposited on AlO substrates at 600, 700 and 800^{o}C, in order to study the influence of T_d on the strain in BST films deposited on single crystal substrates. The XRD pattern of BST5 films deposited on AlO substrates as a function of T_d is shown in figure 5.5.

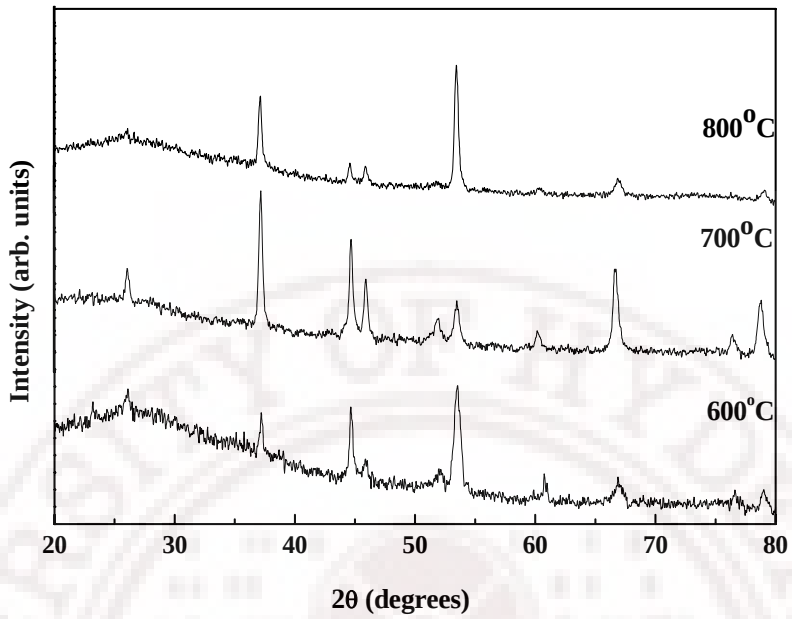

Figure 5.5: X-ray diffraction pattern of BST5 thin films deposited on c-plane sapphire substrates at different deposition temperatures, T_d.

No noticeable change in the value of strain was observed on BST5 films deposited as a function of T_d on AlO substrates. However, the peaks become intense and narrow with increase in T_d, which indicates that the crystallinity improves with increase in T_d. Interestingly, it was observed that the deposition temperature influences the direction of preferred orientation of BST5 films on AlO substrates. The films deposited at 600°C and 800°C had a preferred orientation along the [*200*] direction whereas the films deposited at 700°C were oriented along [*110*] direction.

The evolution of preferred orientation in polycrystalline thin films can be analyzed from the viewpoint of energy minimization. The total energy in any film deposited on a substrate is the sum of three components: (1) the surface energy of the film, (2) the film–substrate interface energy, and (3) the strain energy in the film [12,13]. Films grow in such a way that the total energy is minimized. In the case of polycrystalline films grown on single crystal substrates, interface energy minimization can lead to the dominance of epitaxial orientations. In most other cases, the film generally grows along the plane with the lowest surface energy parallel to the surface of the substrate, thus minimizing the surface free energy of the film[14].

In a simple metal system, a plane with the smallest surface energy is the one with the highest packing density, such as the [*111*] planes in face-centered metals. However, it is not easy to calculate the surface free energies of ceramic systems with unit cells containing metal cations and anions, the determination of the surface free energy must take into consideration the surface packing densities and the thermal energy rendered by the substrate to the approaching species. It is known that the surface mobility of the approaching species is proportional to deposition temperature.

During crystallization in ceramic thin films, the nuclei will be preferentially oriented parallel to the thermodynamically stable planes such as the (*110*) and (*111*) planes, due to their high packing densities in the ABO_3 perovskite structure[14]. In the present case, films deposited at 700^{o}C favor crystallization along the (*110*) and (*111*) which are thermodynamically stable.

The interface energy minimization is favored for the films deposited at 600^{o}C and 800^{o}C, which lead to (*200*) orientation.

5.4 Structural characterization of c-BST5 films deposited on fused silica substrates– OMP series:

Figure 5.6 shows the XRD patterns of BST5 thin films deposited at 800°C on fused silica substrates as a function of OMP of 0, 25, 50, 75 and 100%. All the BST5 films show cubic perovskite structure with no secondary phase formation. Films deposited at 50% OMP show good crystalline quality. The inter-planar spacing of (110) peak was obtained from the peak positions according to the following Bragg formula: $d_{110} = \lambda/2 \sin\theta$, where λ is 1.7889 Å, the wavelength of X-rays for Co Kα radiation and θ is the position of the (110) diffraction peak. The values are plotted in figure 5.7 as a function of OMP.

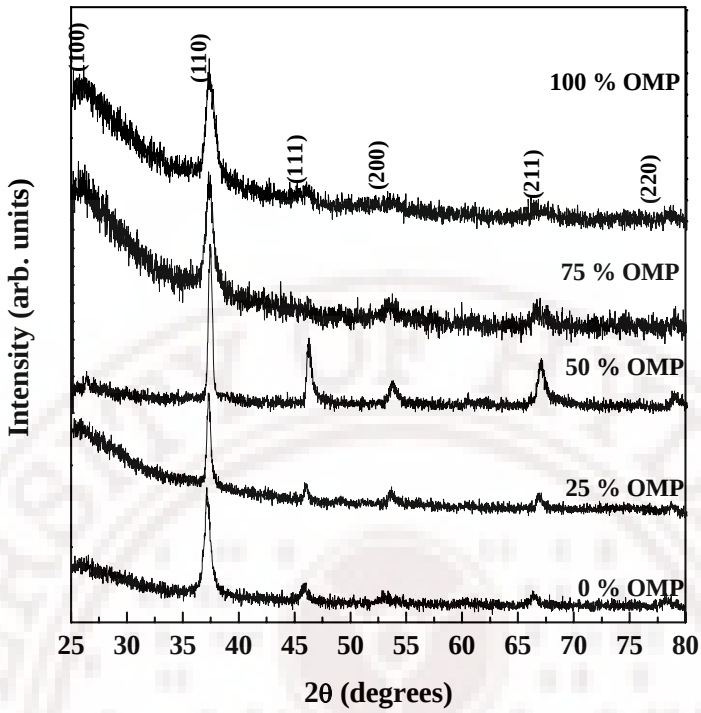

Figure 5.6: X-ray diffraction pattern of BST5 thin films deposited on fused silica substrates at different OMP.

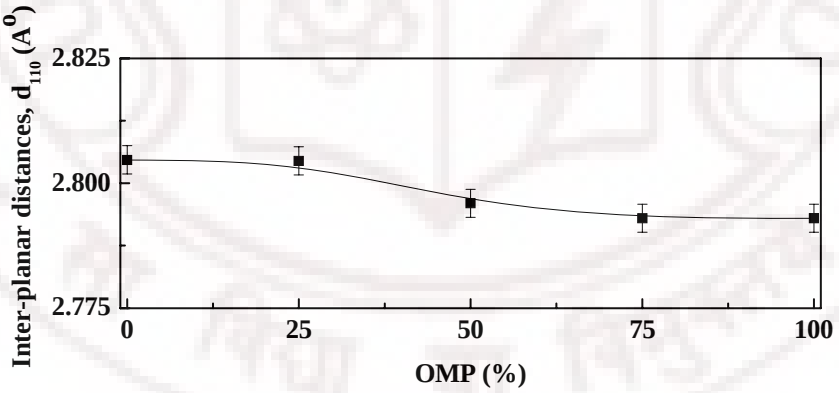

Figure 5.7: Variation in inter-planar spacing (d_{110}) in BST5 thin films deposited on fused silica substrates as function of OMP.

The slight increase in inter-planar distances at lower OMP is the result of lattice strain due to defects in the form of oxygen vacancies[15]. Oxygen vacancies affect the nearest neighbor distance by reducing the Coulomb attractive force between cations and anions, resulting in an increased lattice parameter[16]. The intensity of the diffraction peak

and crystallite size increases with increase in OMP from 0 to 50%, which indicates improved crystalline quality. Whereas, the films deposited at higher OMPs show deteriorating crystalline quality. The films deposited at 0% and 25% OMP have excess Ti as confirmed by RBS analysis. The excess Ti passivates the film's grain boundaries, which prohibits grain growth in BST5 films[17]. A possible explanation for the observed deteriorating crystalline quality for the films deposited at 75% and 100% OMP is the low rates of deposition. Films deposited at low rates have been shown to have smaller grains with low peak intensity than those deposited at higher rates[18]. However, the nucleation and growth kinetics for BST5 films deposited in pure oxygen atmosphere is not well understood and further studies have to be carried out to understand the sputtering process in pure oxygen atmosphere (high OMP).

The variation in crystallite size with OMP is shown in figure 5.8.

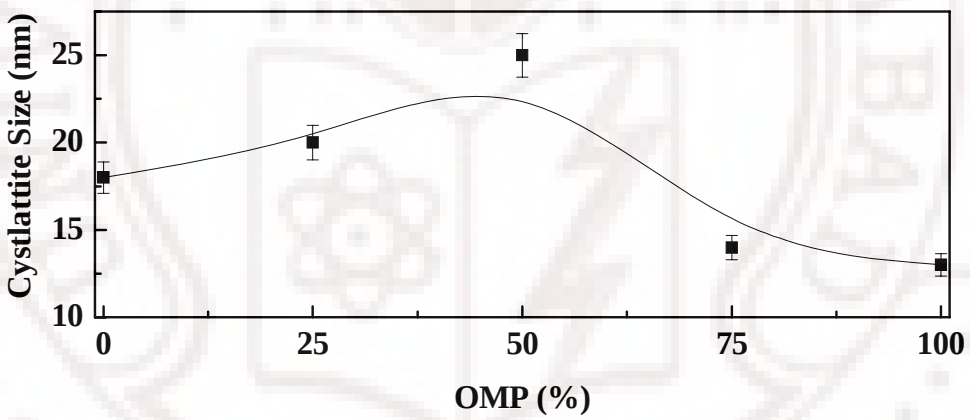

Figure 5.8: Graph showing the variation in crystallite size in BST5 thin films deposited on fused silica substrates as function of OMP.

5.5 Microstructural characterization – Temperature series:

In this section, the microstructural properties of c-BST5 thin films deposited on various substrates as a function of T_d has been discussed.

5.5.1 Microstructural characterization of c-BST5 films deposited on fused silica substrates:

We studied the surface morphology of the BST5 films using DFM. Figure 5.9 shows the two dimensional and corresponding three-dimensional DFM images of the

BST5 thin films deposited at different temperatures. The DFM micrographs indicate that the BST5 thin films are in general crack-free and relatively smooth. The evolution of the surface structures and grain growth are clearly visible through these images.

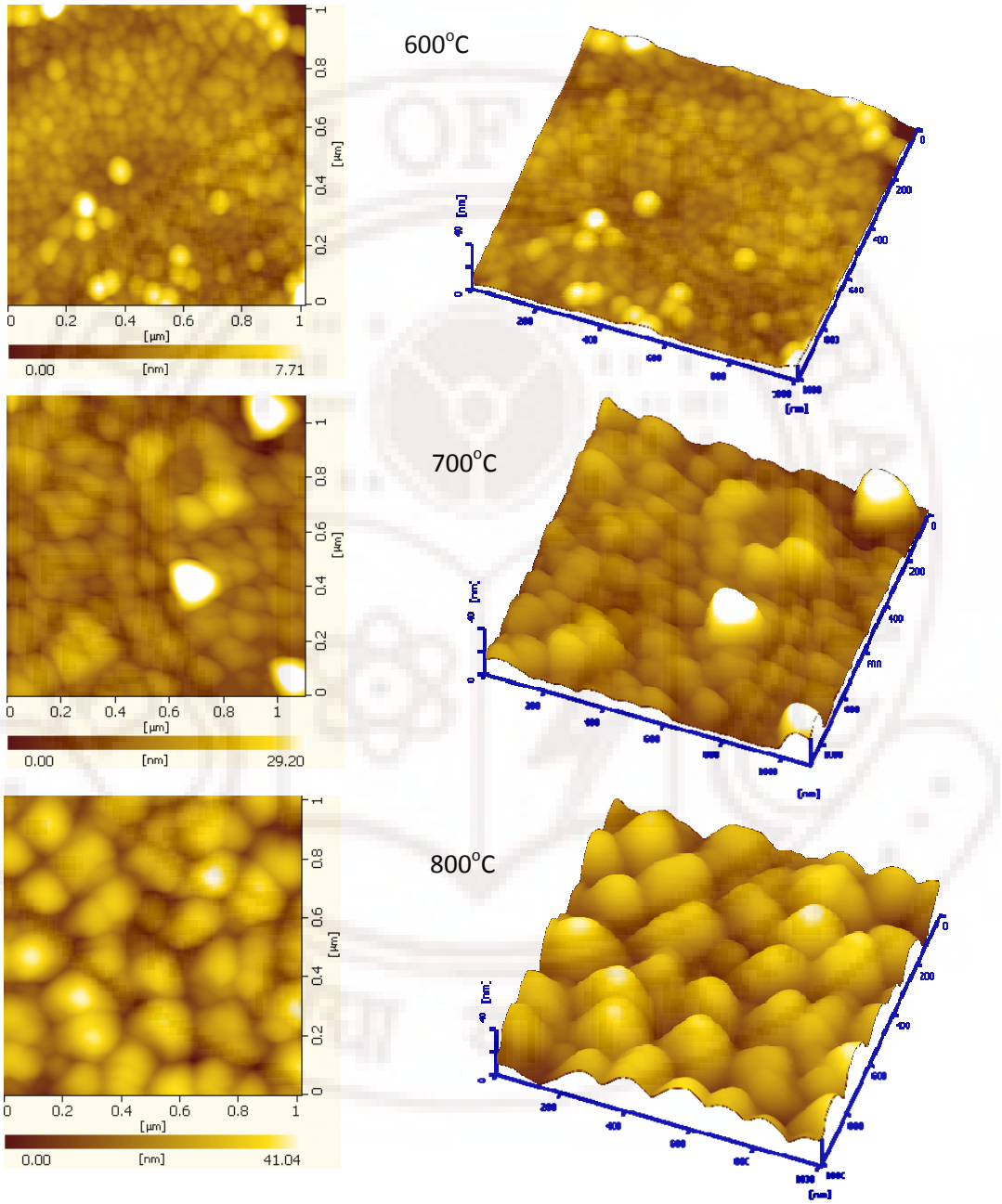

Figure 5.9: 1µm x 1 µm DFM images of BST5 films deposited at different temperatures on fused silica substrates.

It is noted that the increase in substrate temperature leads to increase in surface roughness in these thin films. As seen in figure 5.10, an increase in substrate temperature

from 600 to 800°C, the root-mean-square (rms) value of surface roughness of BST5 thin films increases from 3.17 to 7.52 nm. In addition, the crystallite size and hence the grain size of the films increases with increase in substrate temperature due to sintering[19,20].

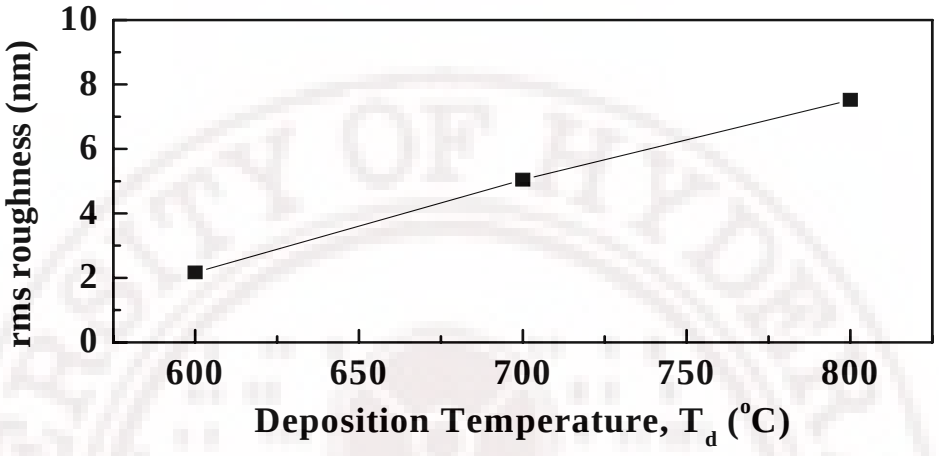

Figure 5.10: Graph showing the variation in rms roughness in BST5 thin films deposited on fused silica substrates as a function of T_d.

Although the surface roughness of BST5 films is found to increase with increase in substrate temperature, it is also accompanied by enhanced grain growth and improvement in crystallinity. These can influence the dielectric properties of BST5 films to a great extent[21,22]. This is confirmed by the dielectric property measurements discussed in chapter 6.

5.5.2 Microstructural characterization of c-BST5 films deposited on Pt/Si substrates:

The two dimensional and its corresponding three-dimensional, DFM image of BST5 films deposited on Pt/Si substrates at different T_d in figure 5.11 shows that the surfaces of the BST5 thin films are smooth. The grains are densely and regularly packed without cracks.

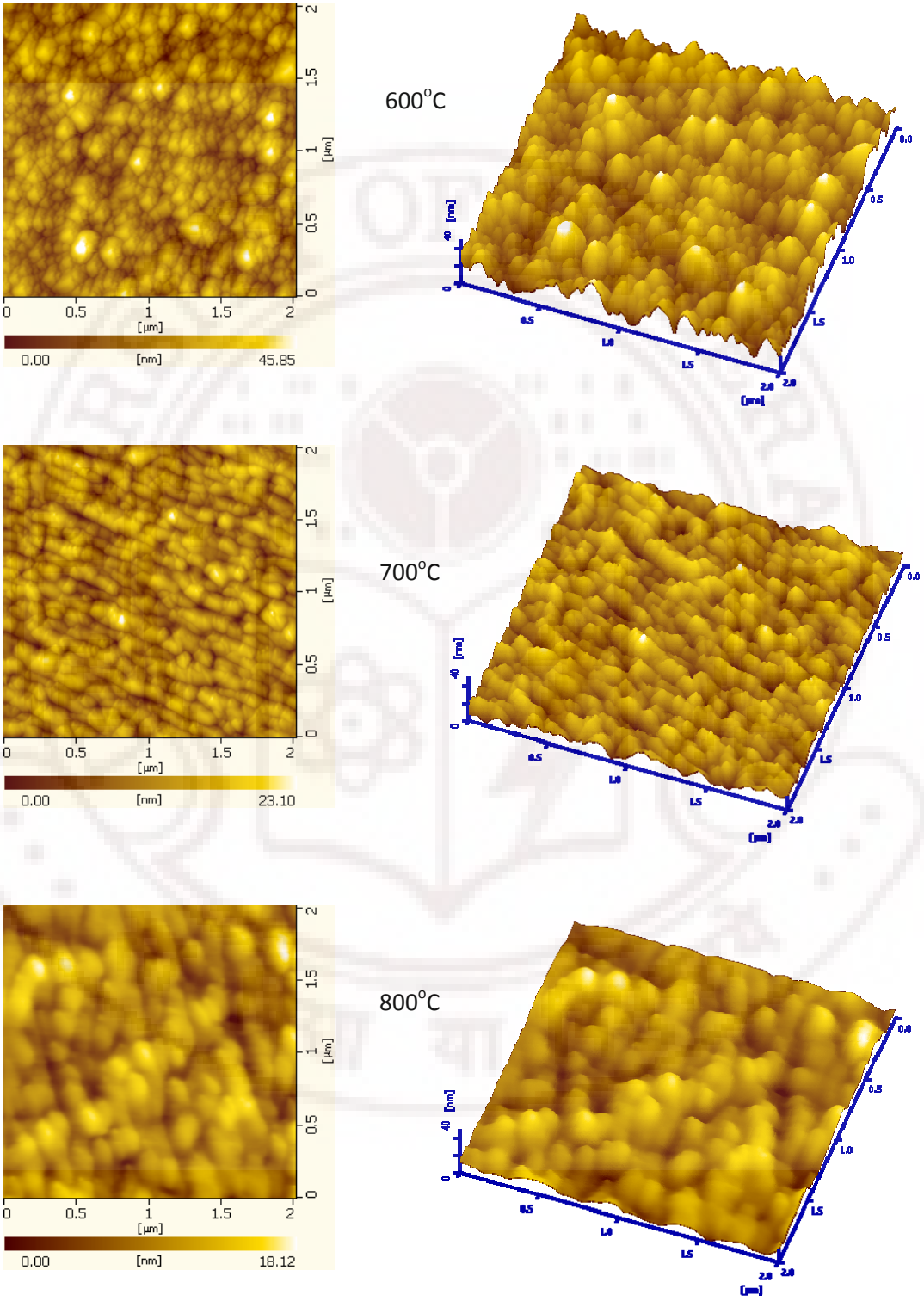

Figure 5.11: 2 µm x 2 µm DFM image of BST5 films deposited at different temperatures on Pt/Si substrates.

It is also observed that the films deposited at higher T_d have larger grains because of sintering. In figure 5.12, the closed circles represent the variation in rms roughness of BST5 films measured over a $2\mu m^2$ area. We see that the rms roughness decreases up to a T_d of 500^oC, peaks at 600^oC and decreases on further increase in T_d. The observed behavior of the films is in good agreement with that predicted by Yang et al.[23] i.e., increase in T_d generally reduces the roughness because thermal diffusion promotes surface reconstruction that flattens a rough surface and eliminates voided columnar structure.

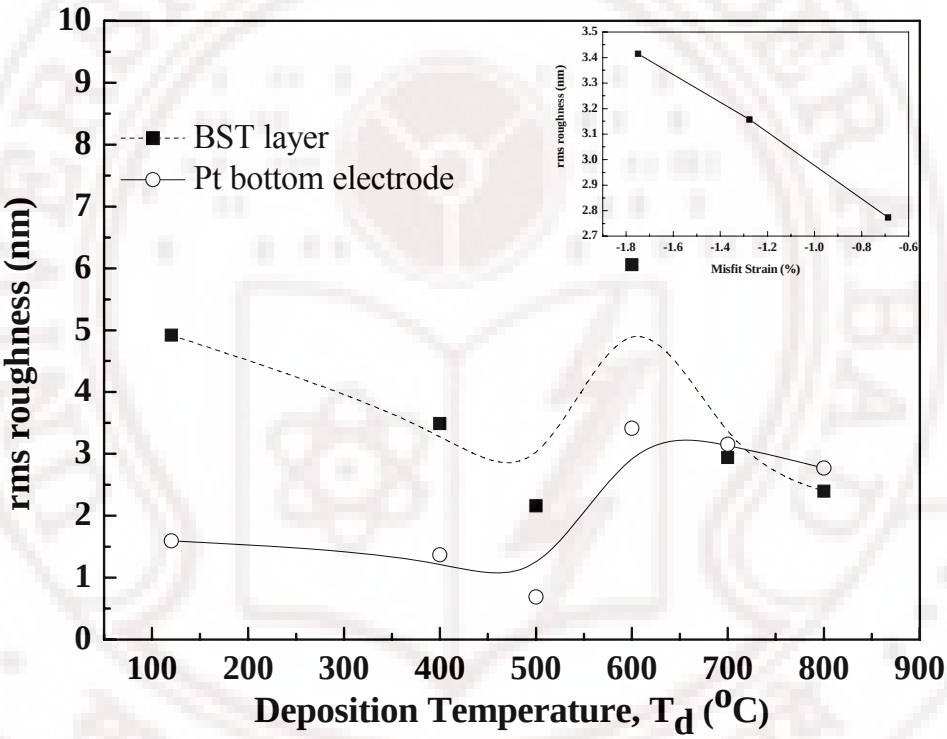

Figure 5.12: rms roughness of (▪) BST5 film and (o) Pt under-layer. The in set shows the dependence of rms roughness on the misfit strain of BST5 films.

It can be seen from the inset of figure 5.12 for crystalline films, that the magnitude of misfit strain has a good influence on the rms roughness of the films. We can see that the value of rms roughness decreases with decrease in misfit strain. So, by appropriately controlling the deposition parameters such as T_d, the magnitude of u_m can be controlled which in turn influences the surface morphology of the deposited films.

The effect of T_d on the surface morphology of the Pt layer was also investigated and is shown in figure 5.13. The open circles in figure 5.12 indicate the variation in rms roughness of Pt layer with T_d. In this case also, we find that the trend is almost similar to that of the rms roughness of BST5 layer. The films deposited at 700 and 800^{o}C show lower surface roughness than that of the Pt underlayer. This might be because T_d value of 700 and 800^{o}C corresponds to T_d/T_m value of 0.47 and 0.52 respectively (which is half the value of the melting temperature, T_m of both BST5 (Tm~ 2073K) and Pt (Tm~ 2045K)).

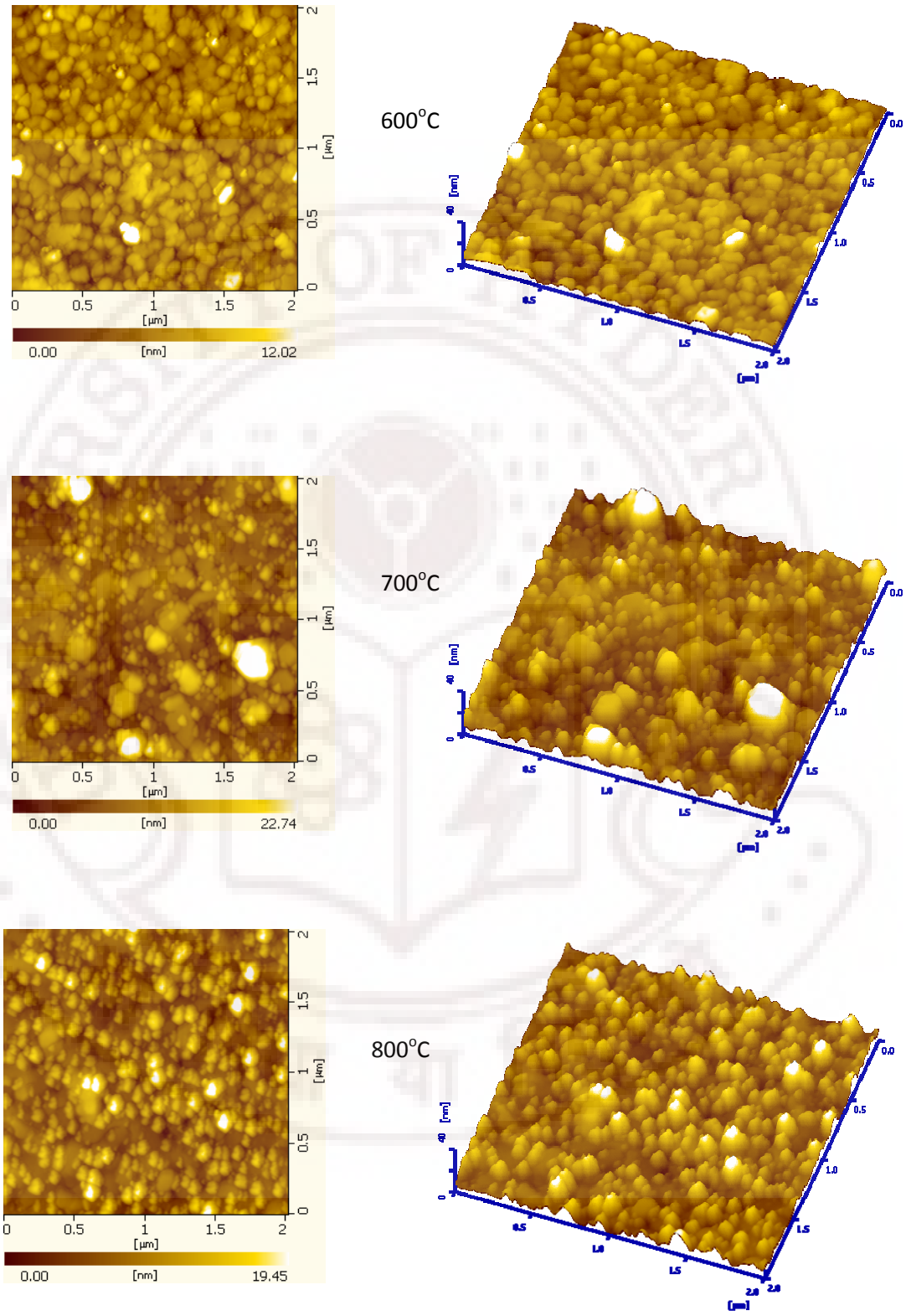

Figure 5.13: 2 µm x 2 µm DFM image of the Pt layer on Si substrates.

Thus the surface morphology of the BST5 layer is not only controlled by the processing conditions but also by the variation in morphology of the Pt underlayer. It can therefore be inferred that Pt acts as the seed layer, which influences the surface morphology of BST5 films deposited over it. The experimental evidence clearly suggests that the temperature at which the BST5 film is deposited can considerably change the surface morphology of the Pt layer and that these variations should be taken in to account while optimizing processing conditions for the BST overlayers.

5.5.3 Microstructural characterization of c-BST5 films deposited on single crystal substrates:

Figure 5.14 show the 1 μm×1 μm DFM micrographs of BST5 films deposited at 800^{o}C and 50 % OMP on single crystal substrates of AlO, MgO and LAO. It is obvious from the DFM images, that the surface morphology of BST5 thin films deposited on one type of substrate is different from that deposited on the other. In general, the crystal structure, lattice constant and thermal expansion coefficient of the substrate and the thin film as well as the processing conditions have a marked influence on the film nucleation and the relevant film structure.

In the present case, it is observed that the BST5 films deposited on MgO and AlO substrates, which indicated a preferred (200) orientation have very large grains with smaller sub-grains. Whereas BST5 films deposited on LAO substrates with no preferred orientation show a dense surface morphology with smaller grains. Therefore, surface morphology and roughness of BST5 thin films is influenced by the film texture/ orientation which results from the nature of the substrate used.

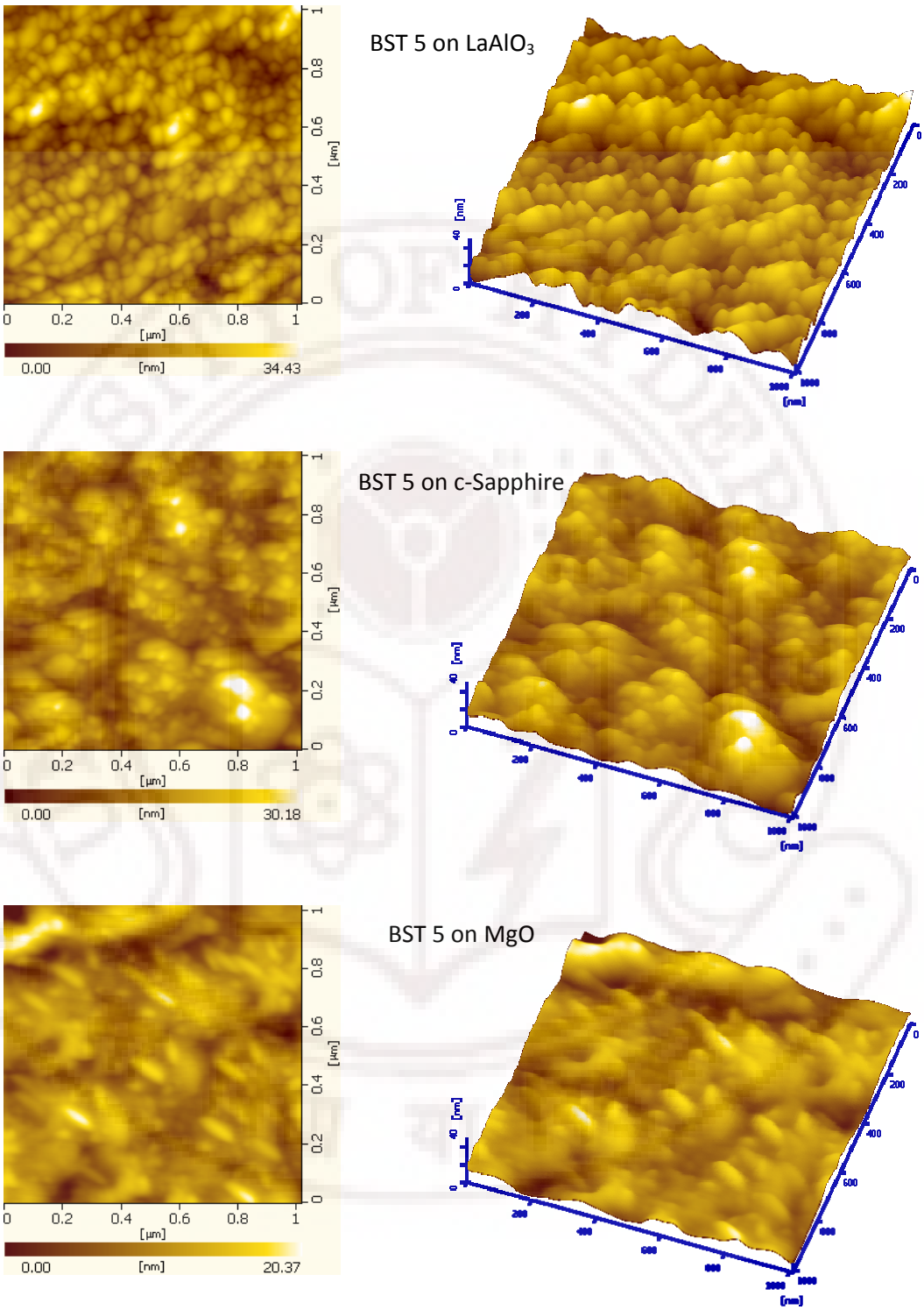

Figure 5.14: 1 µm x 1 µm DFM image of BST5 films deposited on various single crystal substrates.

It has been suggested that small grain size, which leads to larger grain boundary area and the associated interfacial capacitance is a major contributing factor to the lower value of dielectric permittivity observed in BST thin films relative to their bulk counterpart[24]. The dielectric properties of these films are discussed in chapter 6.

5.6 Microstructural characterization of c-BST5 films deposited on fused silica substrates– OMP series:

The microstructure of the BST5 films deposited on fused silica substrates as a function of OMP is shown in figure 5.15.

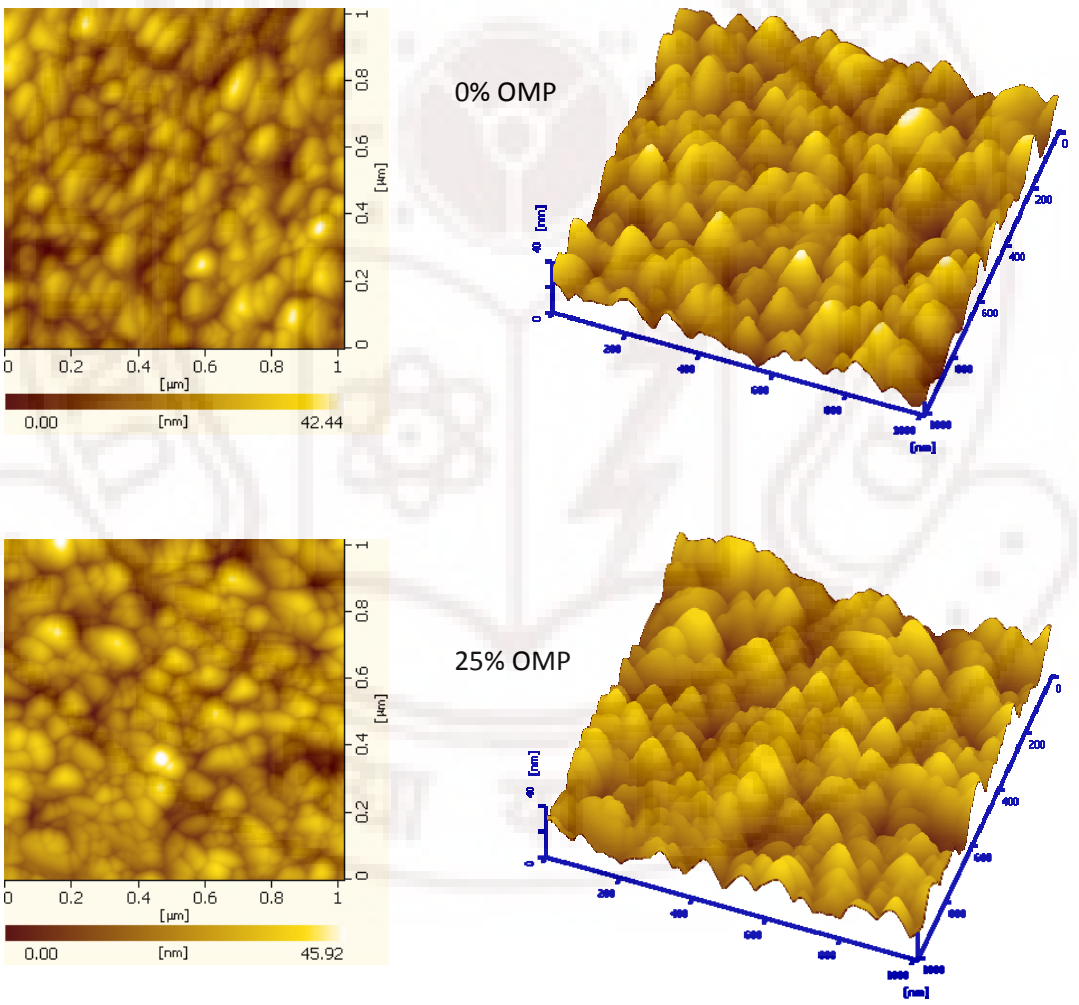

Figure 5.15: 1 µm x 1 µm DFM image of BST5 films deposited on fused silica substrates at different OMP.

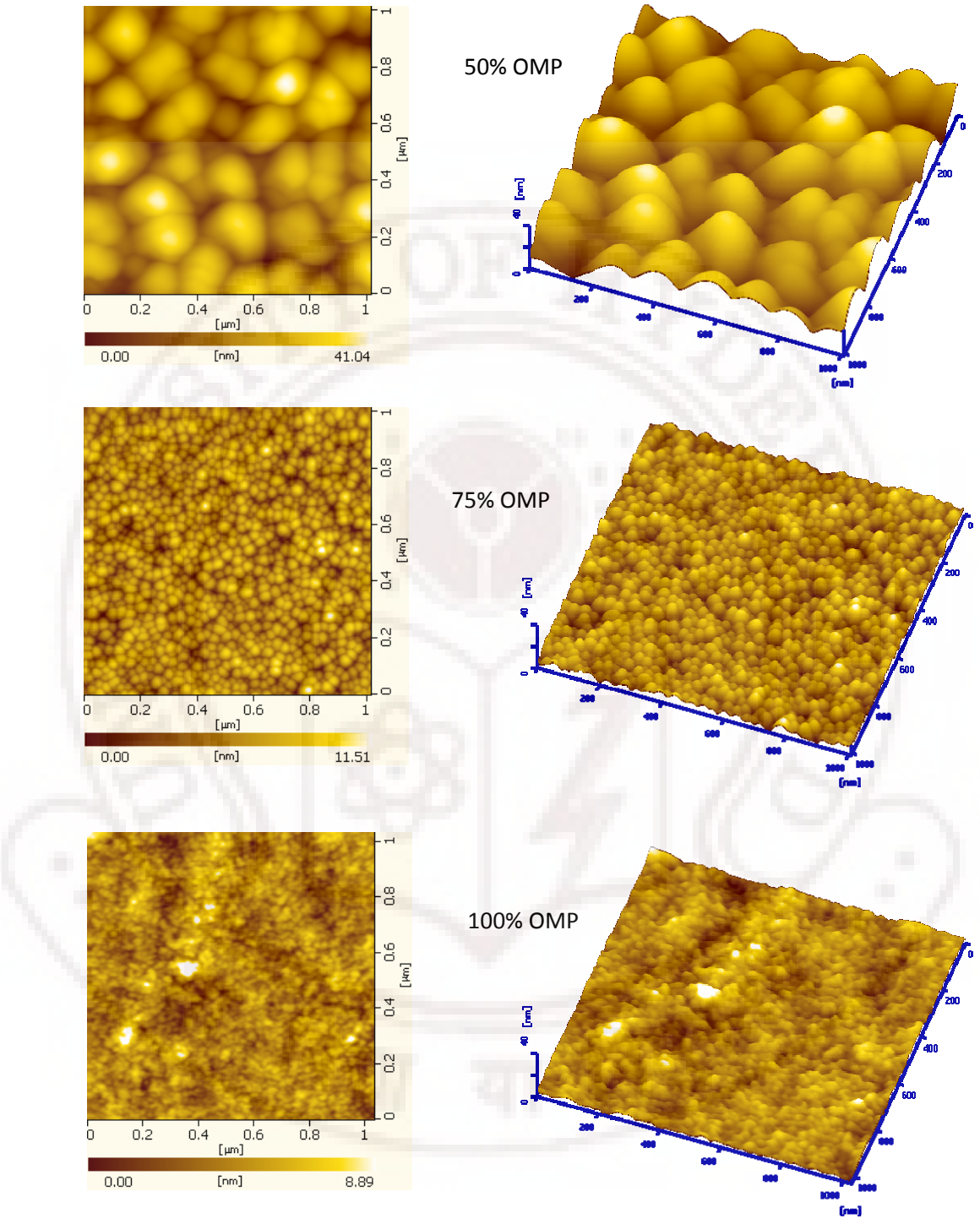

Figure 5.15: (continued) 1 µm x 1 µm DFM image of BST5 films deposited on fused silica substrates at different OMP.

It can be observed from figure 5.16 that the surface roughness increases marginally with increase in OMP up to 50% OMP. It is generally expected that films deposited with low OMP have a rough surface due to high rates of deposition. But in the present case, we found that films deposited in 100% Ar atmosphere have a smooth morphology when compared to the films deposited at 50% OMP. This is because, films deposited at low (0 and 25%) OMP have a Ti-rich phase, the excess Ti passivates the film's grain boundaries and hence the films deposited at low OMP have a smooth surface. On the other hand films deposited at high (75 and 100%) OMP have the lowest surface roughness as expected due to low rates of deposition. The results obtained here compliment the XRD observations.

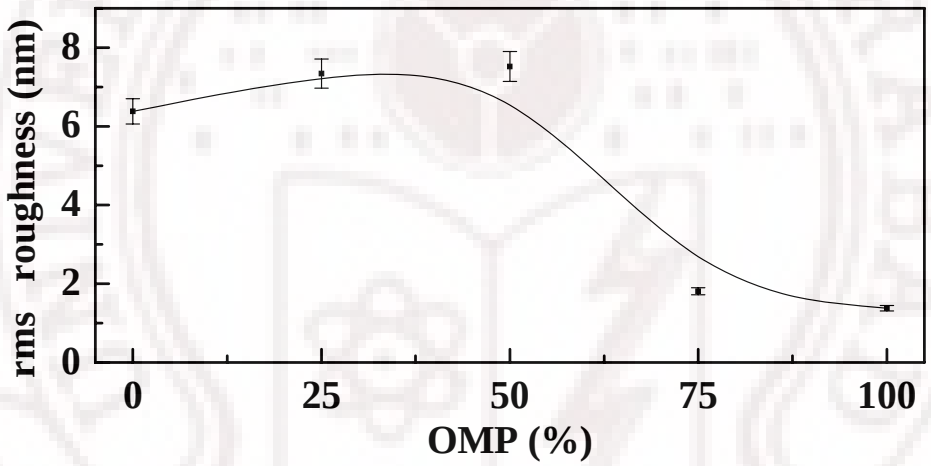

Figure 5.16: Graph showing the variation in rms roughness in BST5 thin films deposited on fused silica substrates as function of OMP.

5.7 Optical properties:

The optical constants of BST5 thin films are highly influenced by the structure, composition and fabrication techniques. A typical transmittance spectrum of c-BST5 film deposited on amorphous fused silica substrate is shown in figure 5.17 below.

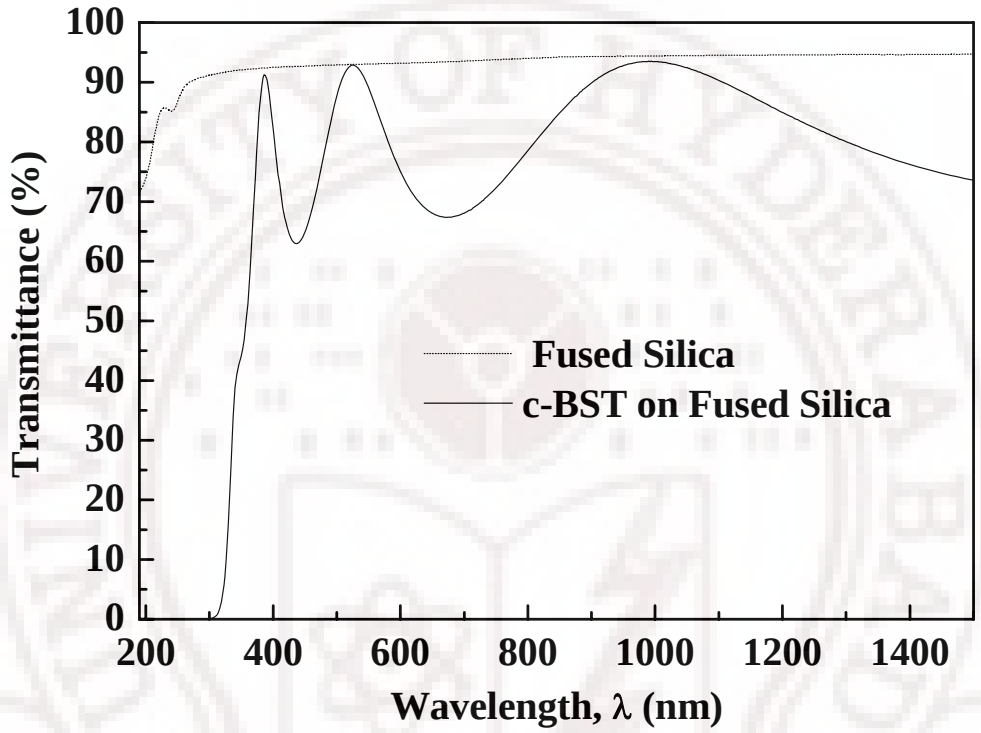

Figure 5.17: A typical spectral transmittance spectra of crystalline BST5 film deposited on fused silica substrates compared with that of the uncoated substrate.

As discussed in chapter 3, the spectrum can be divided into four regions: a transparent oscillating region, weak absorption, medium absorption and a region of strong absorption, where the transmittance decreases drastically.

The refractive index $n_f(\lambda)$ as a function of wavelength have been determined from the transmittance spectrum following the methods of Manifacier[25] and Swanepoel[26]. Here, λ indicates the wavelength. If two envelopes are drawn through the maxima $T_M(\lambda)$ and minima $T_m(\lambda)$ of the oscillating transmittance, the refractive index is given as:

$$n_f(\lambda) = [N + (N^2 - n_s(\lambda)^2)^{1/2}]^{1/2} \qquad (5.4)$$

where,

$$N = 2n_s(\lambda)\frac{T_M - T_m}{T_M T_m} + \frac{n_s(\lambda)^2 + 1}{2} \qquad (5.5)$$

and n_s is the refractive index of the thick bare fused silica substrate. The refractive index of the bare substrate is given by the famous expression,

$$n_s(\lambda) = \frac{1}{T_s(\lambda)} + \left(\frac{1}{T_s(\lambda)^2} - 1\right)^{1/2} \qquad (5.6)$$

where, $T_s(\lambda)$ is the transmission of the thick bare fused silica substrate as shown in figure 5.17. The calculated $n_s(\lambda)$ is shown in figure 5.18 along with the refractive index calculated for c-BST5 film deposited on fused silica substrate, for comparison.

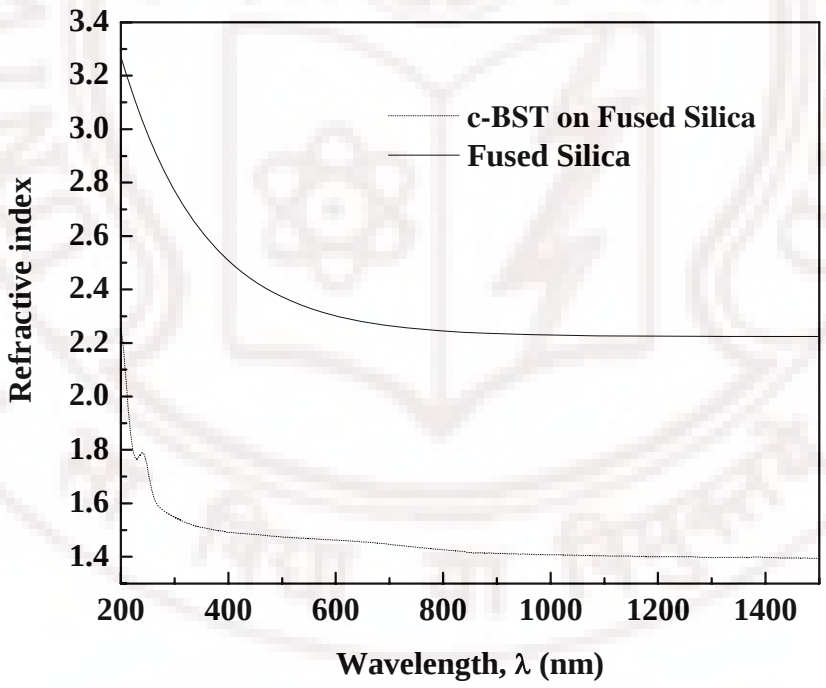

Figure 5.18: Graph showing the variation in refractive index as a function of wavelength for c-BST5 film and bare fused silica substrate.

5.7.1 Optical characterization of c-BST5 films deposited on fused silica substrates- Temperature series:

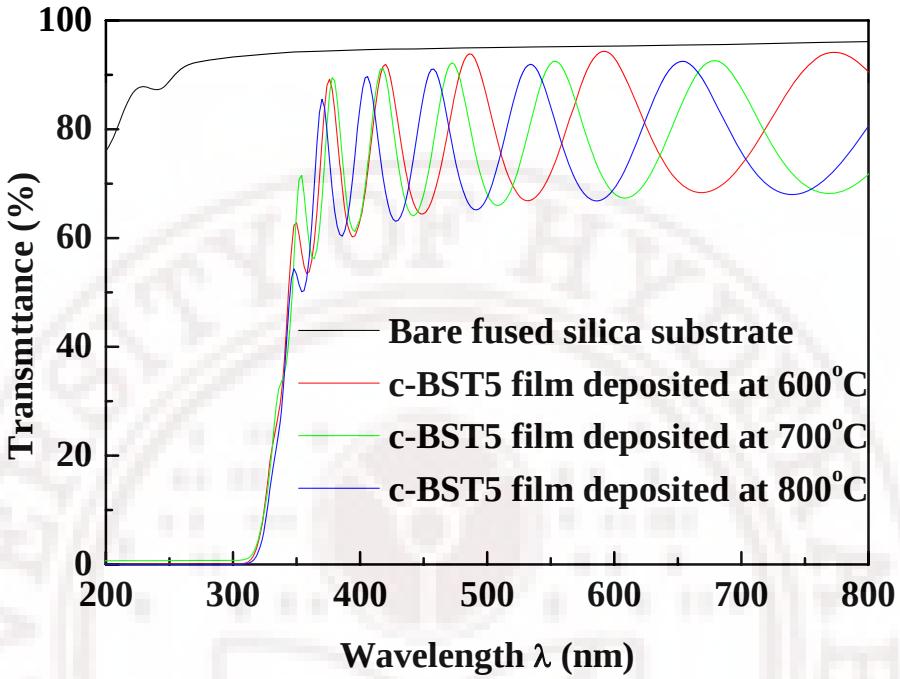

Figure 5.19: Spectral transmittance of c-BST5 films deposited on fused silica substrates at different T_d.

The spectral transmittance of c-BST5 films deposited at different temperatures is shown in figure 5.19. The transparency of the films exhibits a sharp decrease near the UV region. The films in general are highly transparent for wavelengths longer than 340 nm. The transmission drops rapidly at 340 nm, and the cutoff wavelength occurs at about 320 nm. This decrease is due to the fundamental absorption edge of the material at this wavelength. A close look at the transmittance spectra reveals that the c-BST5 films deposited at 600°C are comparatively more transparent than the films deposited at higher substrate temperatures. In other words, with increase in deposition temperature, the transmittivity decreases. This is attributed to increase in grain size and /or roughening[27]. This complements the DFM results, which show an increase in grain size and rms roughness with increase in T_d.

The variation in refractive index as a function of wavelength for the films grown at different deposition temperatures is shown in figure 5.20. The inset in figure 5.20

shows the value of refractive index at λ = 550nm as a function of deposition temperature. It is observed that the refractive index value increases with increase in T_d.

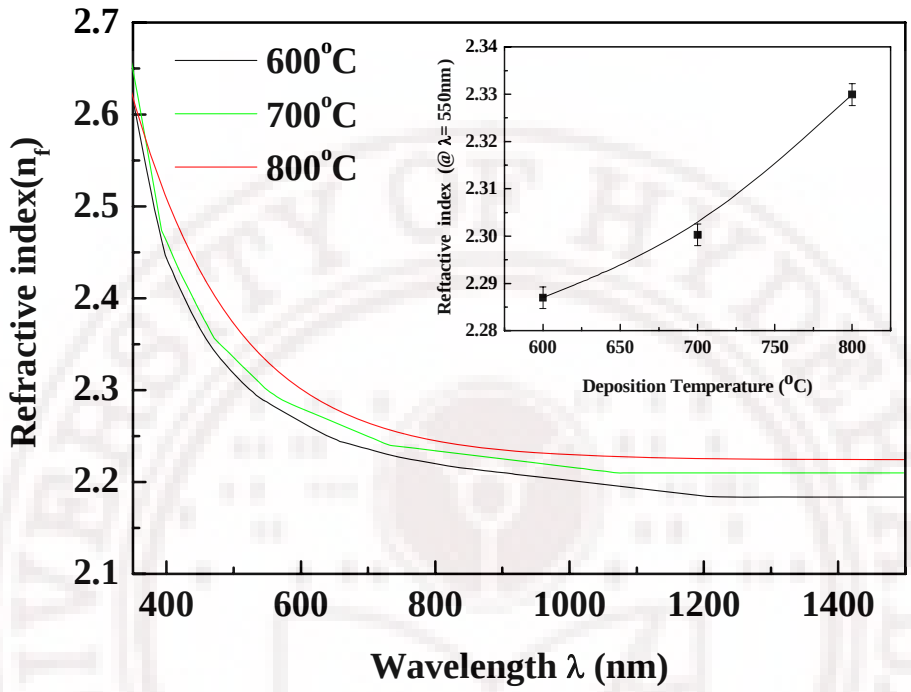

Figure 5.20: Variation in refractive index as a function of wavelength for BST5 films deposited on fused silica substrates. The inset shows the variation in refractive index (@ λ=550nm) for BST5 thin films as a function of T_d.

It is well known that the refractive index of a transparent thin film is directly proportional to its electronic polarization and the electronic polarization is in turn inversely proportional to the inter-atomic separation[28]. It can also be directly correlated to the film packing density, microstructure and crystallinity. Higher deposition temperature T_d increases the mobility of adsorbed atoms on the substrate surface, which leads to enhanced crystallinity and densification. The XRD studies showed that the films deposited at 800˚C had sharper and more intense peaks than the films deposited at 600 and 700˚C, suggesting better crystallinity in the films deposited at 800˚C.

The band-gap of the films deposited at different temperatures was determined using the Tauc plot as explained in chapter 3. An optical band-gap value to 3.7 ± 0.1eV was obtained for all the films.

5.7.2 Optical characterization of c-BST5 films deposited on fused silica substrates-OMP series:

The variation in refractive index as a function of wavelength for the c-BST5 films deposited on fused silica substrates is shown in figure 5.21. It is found that the index of refraction is strongly dependent on OMP.

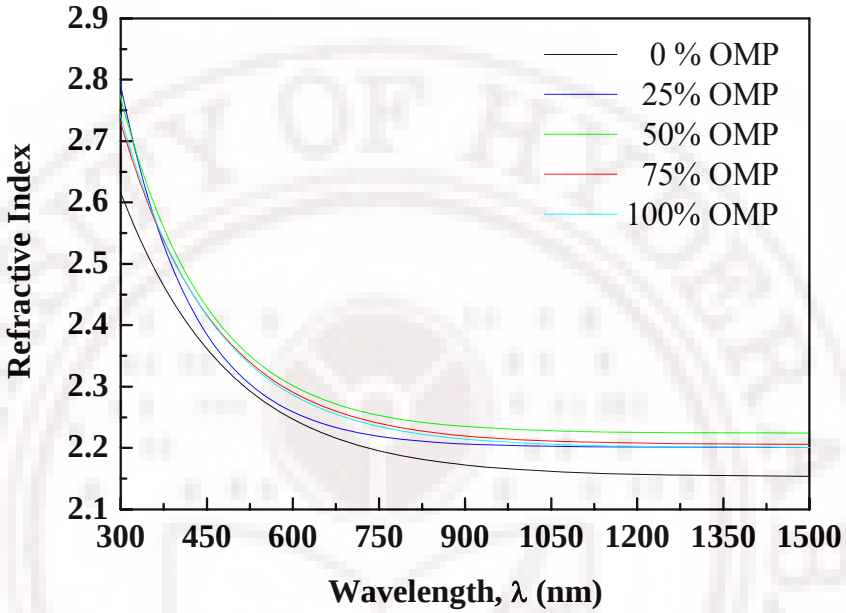

Figure 5.21: Dispersion in refractive index of c-BST5 thin films deposited at different OMP.

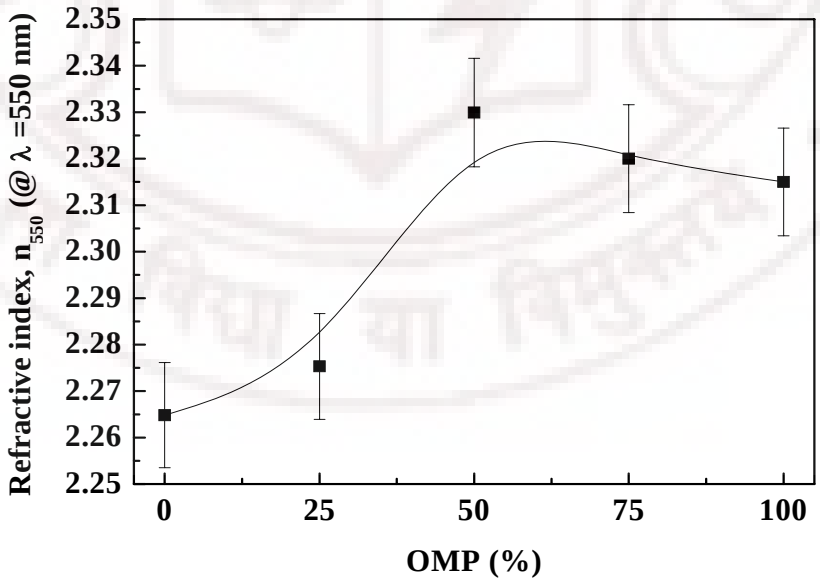

Figure 5.22: Graph showing the variation in refractive index as a function of OMP.

The refractive index measured at 550 nm as a function of OMP is shown in figure 5.22. Highest value of refractive index of about 2.33 was obtained for the films deposited at 50% OMP. Films deposited at 0 and 25 % OMP show lower value of refractive index and the films deposited at 75% and 100% OMP show refractive index values similar to the BST5 films deposited at 50% OMP within the error limits of the measurement technique.

The lower value of refractive index for the films deposited at 0 and 25% OMP might be attributed to the variation of the packing density, as shown in table 5.2. The refractive index data are indicative of the film packing density[29,30]. The relation between refractive index n_f and packing density P_d is given in chapter 4. The oxygen partial pressure (i.e., OMP) can influence the incorporation and stoichiometry of oxygen in the deposited films, which in turn can influence the packing density. Oxygen vacancies are easily formed when OMP is low, and adequate oxygen can eliminate oxygen vacancies[31] . The films deposited at 0 and 25% OMP have oxygen vacancies (as confirmed by RBS) and have low packing density which causes the decrease in refractive index. The films deposited at higher OMP have good oxygen stoichiometry and high packing density and so the refractive index value approaches the bulk value.

OMP (%)	Packing Density (%)
0	91
25	91
50	94
75	93
100	93

Table 5.2: Packing density of c-BST5 thin films deposited at different OMP.

The band-gap of c-BST5 is also found to be dependent on OMP, as seen in the transmission edge in figure 5.23.

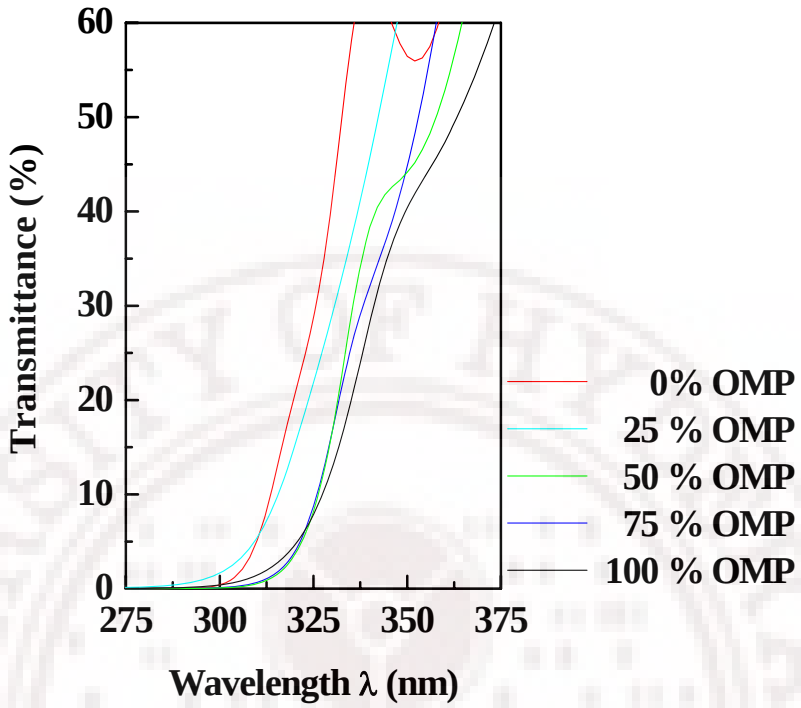

Figure 5.23: Graph showing the optical transmission edge of c-BST5 films deposited at different OMP.

The absorption at low wavelengths for BST5 films deposited on fused silica substrates is related to the fundamental absorption which refers to the band-to-band transition, i.e., to the excitation of an electron from the valence band to the conduction band. The energy gap, E_g, of BST5 can be obtained from the following equation[32]:

$$\alpha h\nu = \text{constant} \times \left(h\nu - E_g\right)^2 \qquad (5.7)$$

where, $h\nu$ is the photon energy. The absorption coefficient, α is given as[32]:

$$\alpha = \frac{\ln(1/T)}{d} \qquad (5.8)$$

in which T is the transmittance at a wavelength, λ and d is the film thickness. More details of this technique are provided in chapter 3.

The $(\alpha h\nu)^2$ vs. $h\nu$ plot for the c-BST5 films on fused silica substrates as represented by equation 5.7 shows good linearity above 3.7 eV. The representative plot of $(\alpha h\nu)^2$ *vs*. $h\nu$ is shown in figure 5.24 for c-BST5 films deposited at 0% and 100% OMP.

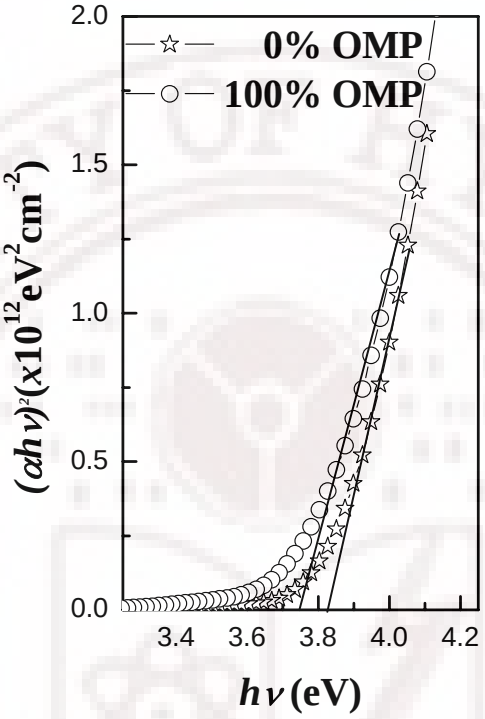

Figure 5.24: Plot of $(\alpha h\upsilon)^2$ versus $h\upsilon$ for the c-BST5 films deposited on fused silica substrates at 0 and 100% OMP.

The band-gap, E_g of c-BST5 films deposited as a function of OMP was determined by extrapolating the linear portion of the plot to $(\alpha h\nu)^2=0$, thus supporting the model of direct allowed electronic transition for deposited thin films. Electronic transition between the valence and conduction bands in the crystal starts at the absorption edge, which corresponds to the minimum energy difference E_g between the lowest energy state of the conduction band and the highest energy state of the valence band. The optical band-gap of the c-BST5 films as a function of OMP is shown in figure 5.25.

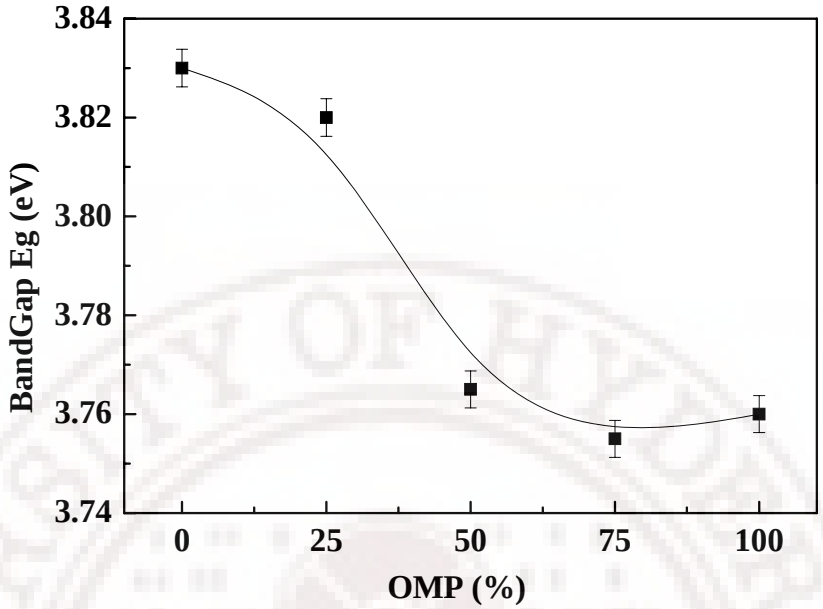

Figure 5.25: Graph showing the variation in optical band-gap as a function of OMP.

It is observed that the films deposited at 0 and 25% OMP have higher band-gap than those deposited at higher OMP. The band-gap of BST films depends on annealing / deposition temperature, crystallinity, grain size and defects. In the present case, the most probable reason for higher value of band-gap for the c-BST5 films deposited at lower OMPs are defects in the form of oxygen vacancies. It was confirmed from the RBS analysis that BST5 films deposited at low OMP have oxygen vacancies. The increase in E_g can be explained by the Burstein–Moss effect[33,34] as discussed in chapter 4.

5.8 Summary:

In summary, BST5 thin films were deposited *in situ* at elevated substrate temperatures. Two series of films were grown and they were (i) *OMP series* and (ii) *temperature series*. In the case of *OMP series*, BST5 thin films were deposited on fused silica substrates at fixed deposition temperature of 800^{o}C while varying the OMP from 0% to 100% in steps of 25%. In the case of *temperature series*, the OMP was fixed at 50% and the films were deposited on fused silica, Pt/Si, MgO, LAO and AlO substrates at different temperatures from 600^{o}C to 800^{o}C in steps of 100^{o}C. The XRD results on BST5 films deposited on fused silica substrates indicated an increase in degree of crystallinity with increase in substrate temperature without change in lattice parameter, while BST5 films deposited at 0% and 25% OMP showed an increase in lattice constant. The increase in lattice constant was attributed to strain due to defects in the form of oxygen vacancies. Films deposited on Pt/Si substrates show epitaxial growth along (*111*) plane whereas films deposited on MgO and AlO show polycrystalline behavior with preferred orientation along (*200*) direction. The misfit strain calculated for the BST5 films deposited at 600^{o}C on Pt/Si substrates was -1.75%. The misfit strain reduces with increase in deposition temperature to -1.27 % and -0.68% for the films deposited at 700^{o}C and 800^{o}C respectively.

In the case of BST5 films deposited on fused silica substrates, the surface roughness of the films increased from 2.17 to 7.52 nm with increase in deposition temperature from 600 to 800^{o}C while the rms roughness showed decreasing trend for the films deposited above 50% OMP. The decrease in rms roughness is attributed to lower rates of deposition. The optical band gap was 3.7 eV±0.1 eV for all the BST5 films, irrespective of their deposition temperature while refractive index increased from 2.28 to 2.33 with increase in deposition temperature from 600 to 800^{o}C. The increase in refractive index is attributed to increase in packing density due to sintering. The band gap of the films deposited at low (0 and 25%) OMP show higher values than that deposited at OMPs ≥ 50%. The higher value of E_g can be explained using the Burstein–Moss effect.

References:

[1] B. Su, T. W. Button, T. Price, D. Iddles and D. Cannell, *J. Mater. Sci.*, **43**, 847 (2008).

[2] B. Su, J. E. Holmes, B. L. Cheng and T. W. Button, *J. Electroceram*., **9**, 111(2002).

[3] Z.-G. Ban and S. P. Alpay, *J. Appl. Phys*., **91**, 9288 (2002).

[4] Z.-G. Ban and S. P. Alpay, *J. Appl. Phys*., **93**, 504 (2003).

[5] JCPDS card No. 04-0802 for Pt (a=3.923 Å).

[6] T.J. Zhang, S.Z. Li, and B.S. Zhang, *Key Eng. Mater*., **336**, 79 (2007).

[7] D. Y. Wang, C. L. Mak, K. H. Wong, H. L. W. Chan and C. L. Choy, *Ceram. Int*., **30**, 1745 (2004).

[8] W.J. Lee, I.K. Park, G.E. Jang, H.G. Kim, *Jpn. J. Appl. Phys*., **34**, 196 (1995).

[9] JCPDS card No. 39-1395 for bulk $Ba_{0.5}Sr_{0.5}TiO_3$.

[10] L. Goux, M. Gervais, F. Gervais, C. Champeaux and A. Catherinot, *Int. J. Inorg. Mater*., **3**, 839 (2001).

[11] M. B. Okatan, M. W. Cole and S. P. Alpay, *J. Appl. Phys*., **104**, 104107 (2008).

[12] S.Z. Li, Y.Q. Yang, W.H. Huang, T.J. Zhang and S.B. Wang, *Eur. Phys. J. Appl. Phys*., **42**, 95 (2008).

[13] X. H. Zhu, H. L. Chan, C. L. Choy and K. H. Wong, *Appl. Phys. A.*,**80**, 591 (2005).

[14] Zhang Bai-Shun, Guo Tao, Zhang Tian-jin, Wang Jin-zhao and Quaz Zu-Ci, *Trans. Nonferrous Met. Soc*.,**16**, s126 (2006).

[15] J. Xu, W. Menesklou and E. Ivers-Tiffee, *J. Eur. Ceram. Soc*.,**24**, 1735 (2004).

[16] L.A. Knauss, J. M. Pond, J. S. Horwitz, D. B. Chrisey, C. H. Mueller and R. Treece, *Appl. Phys. Lett.*, **69**, 25 (1996).

[17] S. Stemmer, S. K. Streiffer, N. D. Browning, and A. I. Kingon, *Appl. Phys. Lett*., **74**, 2432 (1999).

[18] Ru-Bing Zhang, Chun-Sheng Yang and Gui-Pu Ding, *Mater. Lett*., **59**, 1741 (2005).

[19] Manoj Kumar, Somnath C. Roy, M. C. Bhatnagar, Seema Agarwal and G. L. Sharma, *Ferroelectrics*, **329**, 33 (2005).

[20] C. Carter, S. Horwitz, B. Chrisey, M. Pond and W. Kirchoefer, *Mat. Res. Soc. Symp. Proc*., **493**, 347 (1998).

[21] Su-Jae Lee, Seung Eun Moon, Min-Hwan Kwak, Han-Cheol Ryu, Young-Tae Kim and Kwang-Yong Kang, *Jpn. J. Appl. Phys*., **43**, 6750 (2004).

[22] M. C. Chiu, H. C. Yao and C. J. Huang, *J. Appl. Phys*., **102**, 014110 (2007).

[23] Y. G. Yang, X. W. Zhou, R. A. Johnson and H. N. G. Wadley, *Acta. Mater*., **49**, 3321 (2001).

[24] T. Shaw, Z. Suo, M. Huang, E. Liniger, R. Laibowitz and J. Baniecki, *Appl. Phys. Lett*., **75**, 2129 (1999).

[25] J.C. Manifacier, J. Gasiot and J.P. Fillard, *J. Phys. E, Sci. Instrum*., **9**, 1002 (1976).

[26] R. Swanepoel, *J. Phys. E, Sci. Instrum*., **16**, 1214 (1983).

[27] N. W. Jang, S. B. Mah, D. S. Paik, H. W. Choi and Y. C. Park, *Mater. Res. Bull*., **34**, 1463 (1999).

[28] P. Li, J. F. McDonald and T. M. Lu, *J. Appl. Phys*., **71**, 5596 (1992).

[29] H. J. Cho and C. K. Hwangbo, *Appl. Opt*., **35**, 5545 (1996).

[30] W. Heitmann, *Thin Solid Films*, **5**, 61 (1970).

[31] Y.A. Zhao, Y.J. Wang, H. Gong, J.D. Shao and Z.X. Fan, *Appl. Surf. Sci*., **210**, 353 (2003).

[32] S. R. Elliott, *Physics of amorphous materials*, Wiley, New York (1990).

[33] E. Burstein, *Phys. Rev.* B, **93**, 632 (1954).

[34] T. S. Moss, *Proc. Phys. Soc.* B, **67**, 775 (1954).

Chapter VI

Frequency dependent dielectric properties and tunability of c-BST thin films at low and microwave frequencies

6.1 Introduction:

In the previous chapter the methodology for depositing crystalline BST5 (c-BST5) films on amorphous fused silica substrates has been shown. The films deposited in situ at high temperatures yielded high-quality films with good structural, microstructural and optical properties. The required characteristics of BST5 thin films for frequency agile applications; are high dielectric constant (dispersion free), low dielectric loss, high tunability (at the frequency of interest) and low cost of production on inexpensive substrates.

For successfully implementing these films in frequency-agile devices, its dielectric and tunable characteristics at low and microwave range of frequencies are to be studied. However, there is no single technique which can be used to characterize the dielectric properties of thin films from kHz to GHz frequency range. One has to use a number of techniques to cover this wide frequency range.

In this chapter, we discuss the low and microwave frequency dielectric and tunable properties of BST5 thin films grown on different substrates. The Metal-Insulator-Metal (MIM) capacitor structures were used to characterize the frequency and voltage dependent dielectric properties of these BST5 thin films at low frequencies. For the measurements of dielectric constant and loss tangent at a spot frequency of 10GHz, split post dielectric resonator (SPDR) based techniques were used. Calibration comparison technique was used for determining the broad band microwave dielectric and tunable properties of c-BST5 thin films grown on various substrates.

The results of this investigation yields a deeper understanding of the dielectric properties of c-BST5 thin films both from the fundamental research point of view and on device development aspects.

6.2 Low frequency dielectric properties of BST thin films:

The MIM structures were used for determining the relative dielectric constant and loss tangent of c-BST5 thin films deposited on platinum coated silicon substrates. The capacitance was measured as a function of frequency from 100Hz to 100 kHz using a Fluke PM6304 RLC meter and the value of relative dielectric constant was derived using the formula:

$$\varepsilon` = \frac{Cd}{\varepsilon_0 A} \qquad (6.1)$$

where C is the capacitance (in farads), ε_0 the permittivity of free space (8.85×10^{-12} F/m), A the capacitor area (in m^2) and d the BST5 film thickness (in m).

The value of relative dielectric constant (ε`) and loss tangent (tanδ) of BST5 films deposited at various temperatures are given in figure 6.1.

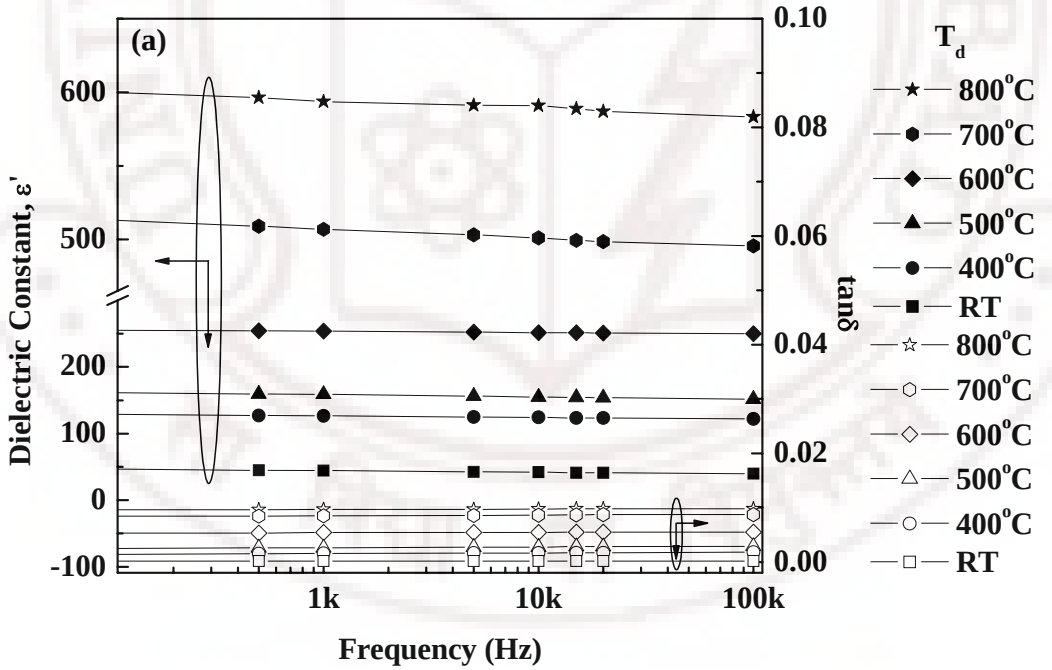

Figure 6.1: Dielectric constant and loss tangent of BST5 films measured as a function of frequency using MIM capacitor structure

It could be observed that all the BST5 films deposited at various T_d do not show any significant dispersion in relative dielectric constant (in the measured frequency range)

indicating excellent film homogeneity and the absence of internal interfacial barriers[1]. Similar observations have been reported by Yan et al.[2] and Adikary et al.[3]

The variation of relative dielectric constant and loss tangent (measured at 100 KHz) of the films deposited at different T_d in figure 6.2 shows that BST5 films deposited at room temperature had the lowest dielectric constant and loss values of ~46 and ~0.001 respectively. Though the films deposited at 400°C and 500°C were x-ray amorphous, the measured dielectric constant was 122 and 151 respectively. These films also had low dielectric loss values of 0.002 and 0.003.

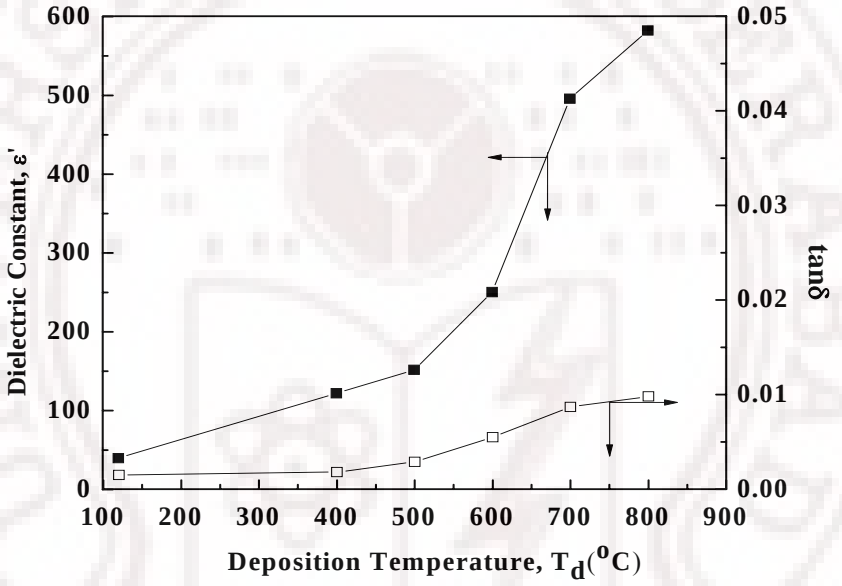

Figure 6.2: Dielectric constant and loss tangent of BST5 films measured at 100 KHz, plotted as a function of deposition temperature, T_d.

It is seen that the dielectric constant increases with increase in T_d, due to improved crystallinity (figure 5.3), grain growth (figure 5.11) and reduction in the magnitude of misfit strain (figure 5.12), which is in good qualitative agreement with that predicted by Ban and Alpay[4,5]. On the other hand improvement in grain size and crystallinity is known to increases the dielectric constant[6] and the same conclusion is demonstrated in figure 6.2. Similar behavior has been reported by Adikary et al.[3] on $(Ba_{0.65}, Sr_{0.35})TiO_3$ films deposited by RF-sputtering. The BST5 thin films deposited at higher temperatures, such as 700 and 800°C, have higher values of dielectric constant, while their dielectric losses are also much higher than that of the films deposited at lower T_d. The room temperature

relative dielectric constant and dielectric loss are 583 and 0.01 for the BST5 deposited at 800^{o}C. In general, the dielectric loss originates from two competing mechanisms. They are resistive loss and relaxation loss. The energy is consumed by mobile charges present in the film in the former case and in the later case, the energy is dissipated due to the relaxation of the dipoles. If the loss in BST5 thin films can be reduced while maintaining a large dielectric tunability, then the devices utilizing these films would have a much more attractive performance. In the present case, as the deposition temperature increases, the dielectric constant as well as the dielectric loss also increases. This could be due to the increase in grain size with increase in T_d which in turn results in reduction in the number of grain boundaries. Reduction in the number of grain boundaries increases conductivity and hence the films deposited at 800^{o}C have higher loss tangent due to contributions from resistive loss.

6.3 Effect of deposition temperature on the microwave dielectric properties of BST5 thin films deposited on fused silica substrates:

The dielectric properties of BST5 thin films at microwave frequencies are found to be strongly influenced by the deposition temperature[7,8]. In order to study the influence of deposition temperature, the samples were deposited at different substrate temperatures from 400°C to 800°C. The measurement of permittivity and loss tangent of these thin films was carried out at an X-band spot frequency of 10GHz using split post dielectric resonator technique. The details about the measurement technique are given in chapter 3. The measured dielectric constant (ε_r) and loss tangent (tanδ) of the BST5 thin films are shown in figure 6.3. It is observed that the dielectric constant of BST5 films deposited on fused silica increases with increase in substrate temperature. The increase is attributed to increase in packing density, crystallinity and grain size in the film deposited at high substrate temperatures. BST5 films deposited at room temperature had a dielectric constant of 50, which increased to 150 for the films deposited at 500^{o}C. These films were x-ray amorphous as mentioned earlier. A huge increase in dielectric constant is observed for the films deposited at $T_d \geq 600^{o}$C. This increase is attributed to crystallization of BST5 films. As observed in the case of BST5 deposited on Pt/Si substrates, the films deposited at 800^{o}C have the highest dielectric loss. This is attributed to contribution from the resistive loss originating from increased conductivity due to reduction in grain boundary area.

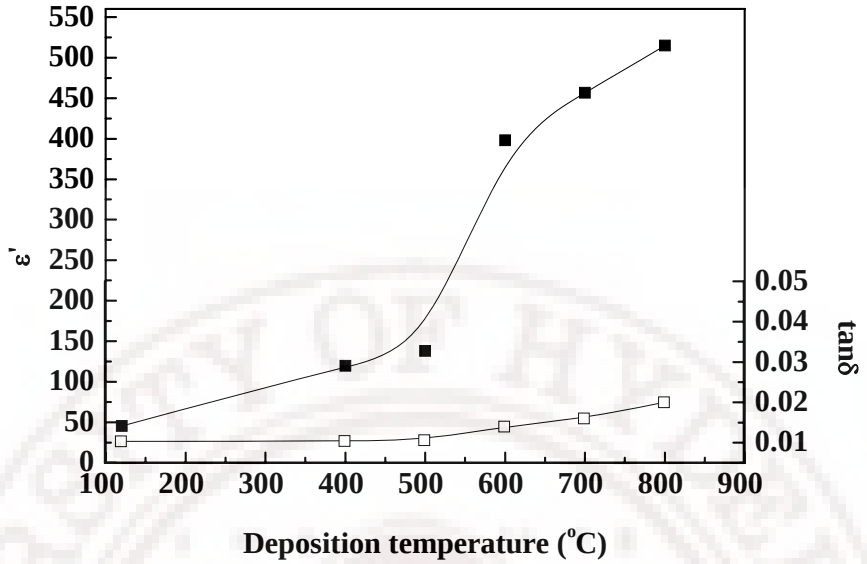

Figure 6.3: Dielectric constant and loss tangent measured at 10GHz for BST5 films deposited on fused silica substrates, plotted as a function of deposition temperature, T_d.

6.4 Effect of OMP on the microwave dielectric properties of BST5 thin films deposited on fused silica substrates:

The variation in microwave dielectric constant and loss tangent of BST5 films deposited at 800°C at various OMP is shown in figure 6.4.

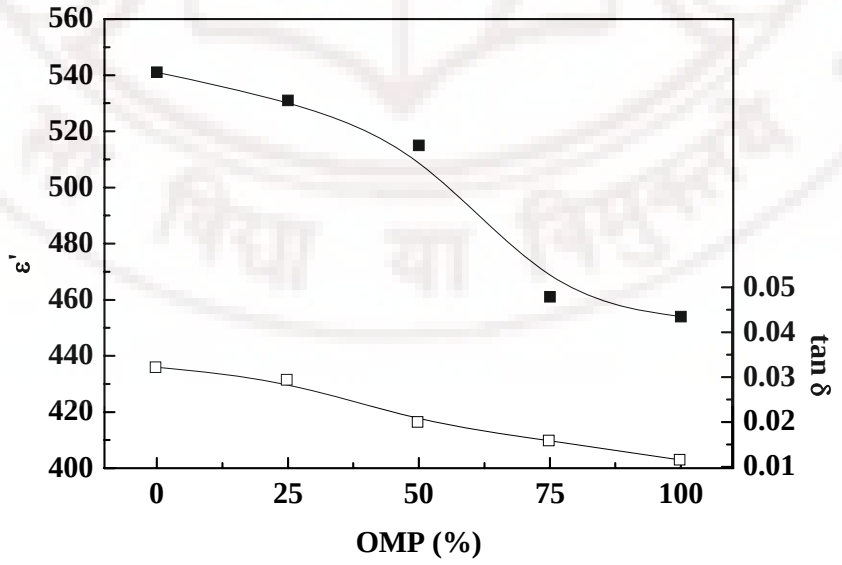

Figure 6.4: Dielectric constant and loss tangent of BST5 films deposited at 800°C at different OMP. Frequency of measurement: 10 GHz.

Though the films deposited at higher OMP have sufficient oxygen incorporation, they show a low value of dielectric constant. In this case the lower value of dielectric constant might be due to,

1. Lower film density and
2. Lower crystallinity due to lower rates of deposition (as seen in chapter 5).

The higher value of loss in the films deposited at lower OMP could be attributed to the presence of oxygen vacancies and excess Ti. A little excess-Ti along the grain boundaries are found to be favorable, as it passivates the grain boundaries thereby decreasing the loss[9].

On the other hand, higher concentration of Ti along the grain boundaries leads to scattering loss at the grain boundaries. The excess Ti can also diffuse in to the grain. In the present case, the RBS results indicated that the BST5 films deposited at low (0 and 25%) OMP show excess Ti, but these films also show oxygen deficiency. The XPS results indicate that the oxidation state of Ti is 4+ for all the films deposited at different OMP. Hence, the contribution for higher loss in the BST5 films from excess-Ti cannot be the only reason for higher loss, but must be a combination of excess-Ti and oxygen deficiency.

6.5 Broadband microwave dielectric properties of c-BST5 thin films deposited on different substrates:

The effect of substrate on the structure and dielectric properties of oxide thin films has attracted a lot of attention in recent years[10]. In particular, ferroelectric thin films exhibit different dielectric and ferroelectric behavior when grown on different substrates. Substrates can modify the physical properties of thin films via the strains induced by lattice misfit or by differences in thermal expansion between the film and the substrate[11, 12, 13, 14]. As a result, the properties of the thin films can be markedly different from the intrinsic properties of the corresponding unstrained bulk materials. Although such strain sometimes leads to degraded film properties, if judicious use is made of substrates and growth parameters, strain offers the opportunity to enhance particular properties of a chosen material in the thin film form, and this is called “strain engineering”[15]. Strain engineering is a hot topic in state-of-the-art thin film studies, since strain is an effective way to adjust the in-plane dielectric constant of the BST thin films deposited on different

substrates. Apart from the above strain induced effects, films grown epitaxially/ preferentially oriented have shown better properties than the polycrystalline films[16,17,18].

We have observed in chapter 5, that the films deposited on MgO and AlO show polycrystalline behavior with preferential orientation along the (200) direction, while BST5 films on LAO and fused silica substrates show polycrystalline structure with no preferential orientation. BST5 films grown on LAO substrates show in-plane residual strain of 0.7% whereas, BST5 films grown on AlO, MgO and fused silica substrates show an in-plane residual strain of -0.5%, -0.3% and -0.2% respectively.

The broad band microwave dielectric properties of c-BST5 thin films deposited on amorphous fused silica substrate as well as on various single crystal substrates were characterized by calibration comparison technique using coplanar waveguide (CPW) test structures. In the coplanar geometry the field is parallel to the plane (in-plane) of the film and hence we measure the in-plane dielectric response in CPW test structures. The CPW test structures were fabricated on bare substrates as well as on c-BST5 thin films. The test structures were characterized by determining the attenuation and phase constant with and without BST5 thin films. The broadband microwave dielectric properties of c-BST5 films deposited on various single crystal substrates are shown in figure 6.5.

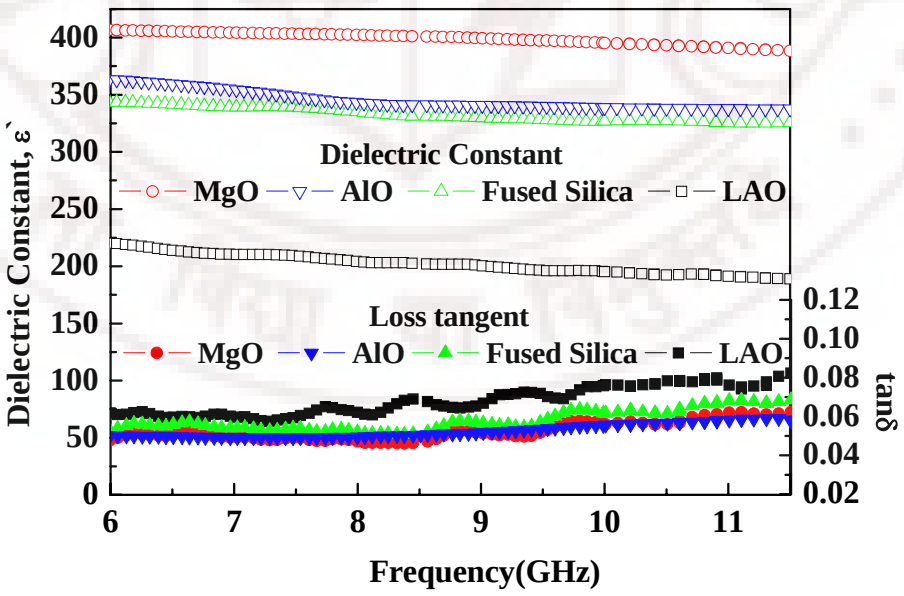

Figure 6.5: Broadband microwave dielectric properties of c-BST5 thin films deposited on various single crystal substrates.

The c-BST5 thin films grown on MgO substrates have the highest in-plane dielectric constant of about 395 (@10GHz) while the films grown on LAO substrates have the lowest in-plane dielectric constant of about 195 (@10GHz). The in-plane dielectric constant of c-BST5 thin films deposited on AlO and fused silica substrates are 338 and 327 (@10GHz) respectively.

The high value of dielectric constant in the films deposited on MgO and AlO can be attributed to their (200) preferential orientation and in-plane tensile strain. It is well known that, an increase in the lattice parameter along a direction increases the ionic displacement along the same direction, which promotes the polarization of electric dipoles resulting in an increase in the net polarization. This increase in net polarization leads to an increase in dielectric constant[19]. In the present case, c-BST5 films deposited on MgO, AlO and fused silica substrates show increase in in-plane lattice parameter leading to higher in-plane dielectric constant. Films deposited on LAO substrates show a compressed lattice along the probing direction hence shows lower value of in-plane dielectric constant.

Apart from the parameters discussed above, the microstructure of the films also plays a crucial role in determining the dielectric properties. From the DFM images it is clear that the microstructure of BST5 grown on different substrates is considerably different from one another. It has been reported that the films with smaller grains will have lower dielectric constant than the films with larger grains[20,21]. In short, the dielectric properties of a thin film grown on a substrate depends on many factors such as lattice mismatch, thermal mismatch, defects, non-stoichiometry, lattice parameter of the films, microstructure etc. All these parameters are interrelated to each other and hence reaching an exact correlation between them is difficult. But it can be stated in general that the strain can modulate the dielectric properties of the thin films to a great extent.

6.6 Broadband microwave dielectric properties of c-BST5 thin films deposited at different deposition temperatures on c-plane sapphire substrates:

The broadband microwave dielectric properties of c-BST5 thin films grown at different temperatures on c- plane sapphire substrates are shown in figure 6.6. It shows that the dielectric constant and loss tangent of the films increases with the increase in deposition temperature.

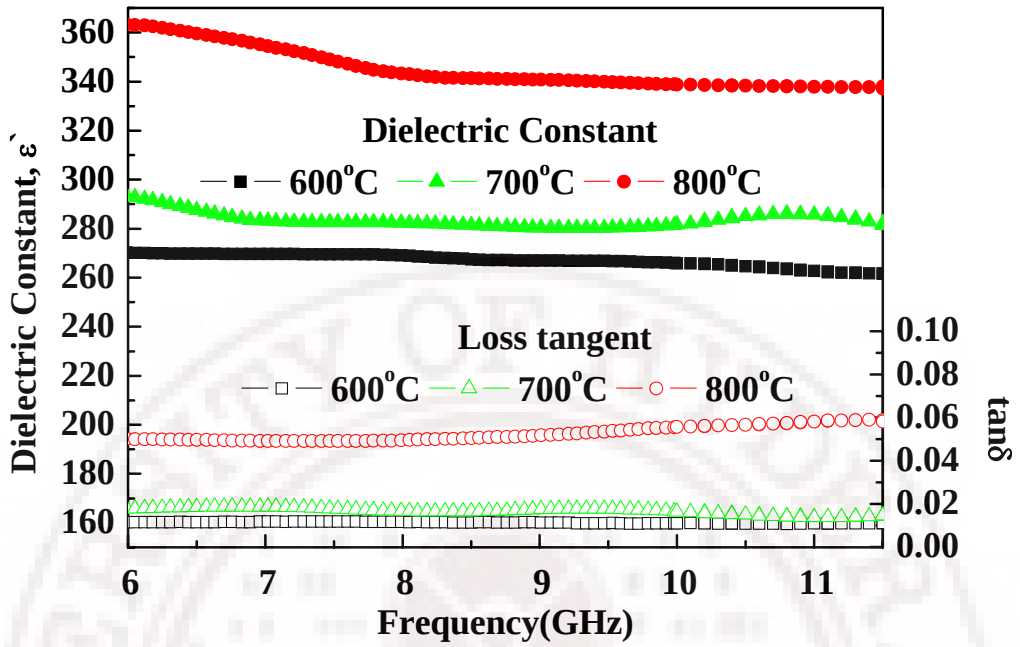

Figure 6.6: Broad band microwave dielectric properties of c-BST5 thin films deposited on c-plane sapphire substrates at different temperatures.

The measured dielectric constants for the films deposited at 600°C were 265 at 10 GHz while it was 338 for the films deposited at 800°C. These observed variations can be attributed to the change in structure and microstructures. Porosity, which is a consequence of microstructural evolution, has a major role in controlling the dielectric properties in the thin films. It is known that relative permittivity decreases with the increasing porosity. Thus, controlling porosity can yield a spectrum of dielectric constants from a single material.[22] Degradation of dielectric constant due to the porous microstructure has been reported in thin films by Brassard et al.[23] and Hiroya et. al.[24] In the present case the low value of dielectric constant for the films deposited at low deposition temperature can be attributed to its low crystallinity, as seen in section 5.3.3. As the deposition temperature increases the degree of crystallinity increases and the films become dense which in turn results in high dielectric constant.

6.7 Voltage dependent dielectric properties of c-BST5 thin films at low frequency:

Low- frequency tunability experiments were performed on all the BST5 thin film capacitors which were deposited at different T_d. Figure 6.7 shows the variation in

dielectric constant (closed circles) of all the films and tan δ(open circles) of the films deposited at 600, 700 and 800°C as a function of applied field. No splitting in the capacitance curves for increasing or decreasing bias voltage was observed in any of the films, indicating that these films are not ferroelectric and do not have mobile ions.

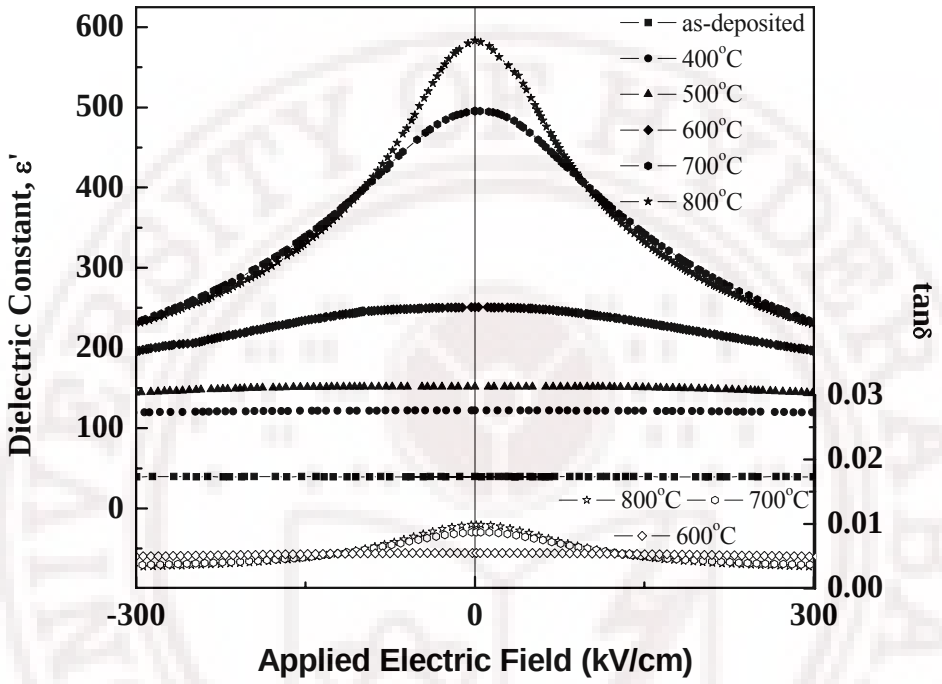

Figure 6.7: Field dependence of permittivity of the BST5 thin films deposited at different temperatures measured at 100kHz and room temperature.

The dielectric tunability of all the films deposited at different T_d as a function of applied electric field is shown in figure 6.8, where tunability is defined as[25,26],

$$Tunability \quad (\%) = \frac{\varepsilon_{max} - \varepsilon_{min}}{\varepsilon_{max}} x100 \qquad (6.2)$$

were, ε_{max} is the maximum dielectric constant, generally obtained at zero applied bias, and ε_{min} is the minimum dielectric constant measured when the bias filed is applied to the thin film. It is clearly seen that the tunability increases with increasing T_d and applied electric field.

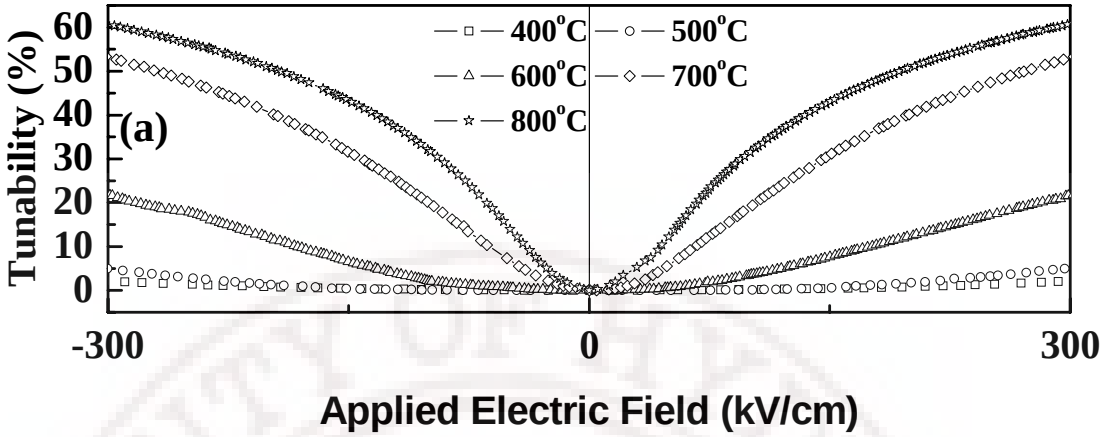

Figure 6.8: Field dependant tunability of the BST5 thin films deposited at different temperatures, measured at 100 kHz and room temperature.

The figure 6.8 indicates that the films deposited at 400°C and 500°C which were x-ray amorphous show poor (less than 5% at 300kV/cm) tunability. The films deposited at 600°C showed a tunability of about 22 % at 300kV/cm. Tunability increased on increase in T_d (700°C) to 54% and increased further for the films deposited at 800°C. As seen in figure 6.9, maximum tunability of about 62% (at 300kV/cm) was observed for the BST5 films deposited at 800°C.

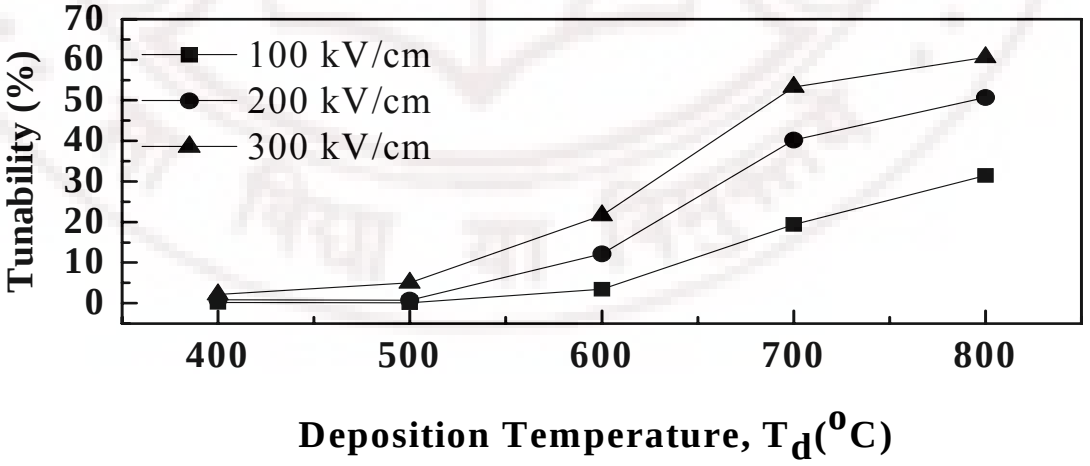

Figure 6.9: Tunability as a function of applied dc bias for the BST5 thin films deposited at different temperatures, measured at 100 kHz and room temperature.

Based on the Landau–Devonshire phenomenological model, Ban and Alpay carried out a theoretical analysis to develop a misfit strain temperature phase diagram of $Ba_{0.5}Sr_{0.5}TiO_3$, $Ba_{0.6}S_{r0.4}TiO_3$ and $Ba_{0.7}Sr_{0.3}TiO_3$ thin films. The phase diagram was constructed by considering a single-domain (001) BST film epitaxially grown on a (001) cubic substrate. The substrates under consideration were Si, MgO, $LaAlO_3$, and $SrTiO_3$. It was shown that the type of strain induced on BST films deposited on $LaAlO_3$, and $SrTiO_3$ were compressive in nature and that for BST films deposited on MgO and Si were tensile. The model predicted that the dielectric constant and tunability increases as the misfit strain decreases.

It is also known that the tunability is closely related to the soft phonon mode, which originates from the vibration of Ti and O ions in oxygen octahedra with opposite directions in ABO_3 perovskite lattice. If an external force acts up on the system in such a way that the ionic displacement is constrained then the soft phonon frequency and the dielectric constant changes significantly[27]. In the present case, the misfit strain acts as the external force that constrains the ionic displacement in BST5 films. It was observed that the magnitude of misfit strain is highest for the film deposited at 600^{o}C which reduces with increase in T_d. Thus, high tunability is achieved for the films with lowest strain (i.e., the films deposited at 800^{o}C) and as the strain increases the tunability decreases.

From the device point of view, low tanδ and high dielectric tunability are required. This is referred to as figure of merit (FOM), given as,

$$FOM = \frac{\varepsilon_{max} - \varepsilon_{min}}{\varepsilon_{max}} \mathrm{X} \frac{1}{\tan \delta} \qquad (6.3)$$

FOM is commonly used to evaluate the material properties for tunable devices[28].

Figure 6.10, shows the FOM as a function of T_d measured at 100, 200 and 300kV/cm.

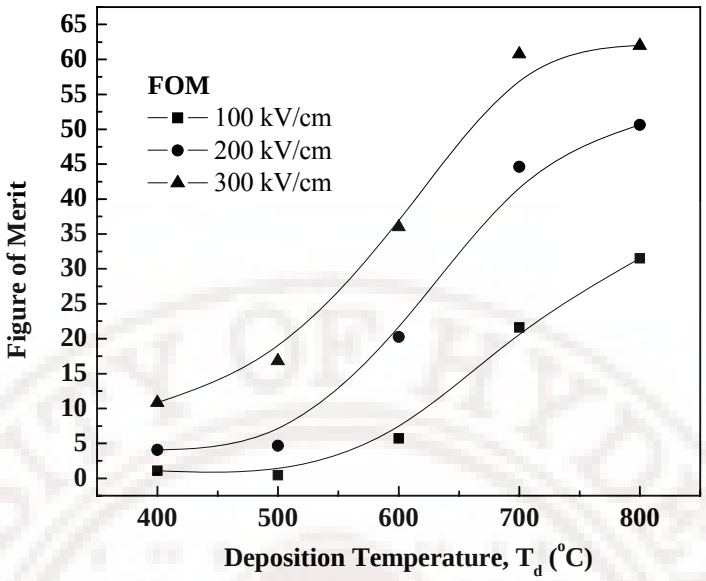

Figure 6.10: Figure of merit (FOM) as a function of applied dc bias for the BST5 thin films deposited at different temperatures, measured at 100 kHz and room temperature.

The best FOM of 62 (@300kV/cm) was obtained for the films deposited at 800°C in spite of the tan δ value being about 0.01. The dependence of FOM of BST films on deposition temperature instigates from parameters such as, tunability, tan δ, nature of crystallinity, grain size, strain and surface roughness. The XRD results show that the onset of crystallization is above 500°C. The films deposited at 600°C and above show (111) texture. It is also observed that the tunability increases with increase in T_d. The films deposited at 800°C have the highest FOM of 62 because of large tunability (~62%) originating from the larger dielectric constant value, (111) textured growth, low misfit strain and a very smooth surface morphology (rms roughness = 2.39 nm). Due to similar reasons the films deposited at 700°C also has a similar FOM of about 61. The films deposited at 600°C were crystalline and showed (111) texture with a dielectric constant of 250. However, the tunability and FOM were found to be low i.e., 21% and 39 respectively. The low value of FOM is due to low magnitude of tunability with a tan δ value of 0.006, high misfit strain and high value of surface roughness (3.4 nm). The lower FOM for the films deposited at 400°C and 500°C is because of low value dielectric constant and tunability arising due to poor crystallinity of these films. The value of

tunability and FOM obtained in the present study is comparable with the values reported for BST thin films deposited on Pt/Si substrates. The comparison is given in table 6.1.

	Frequency of Measurement	Tunability (%)	FOM	Applied field strength (kV/cm)
Borderon et. al.[29]	10kHz	29.4	1.6	2
Chen et. al.[30]	100kHz	36.6	19.4	300
Yu et. al.[31]	100kHz	43.1	27.6	200
Nayak et. al.[6]	100kHz	52	17.3	200
Tang et. al.[32]	1MHz	63	42	250
Present study	100kHz	61	61	300

Table 6.1: The values of tunability and FOM of BST thin films: a comparison.

It is evident from our study that the tunability is profoundly affected by the strain in the films as well as the rms roughness. This is in addition to the well documented effects of crystallographic texture. The present study quantifies these effects as well as the fact that roughness and strain can be correlated. A significant finding of the current study is that the surface morphology of the Pt underlayers exhibits a drastic variation under the influence of the processing parameters. These morphological variations also contribute to the morphology of the BST overlayers and hence their dielectric behavior. Thus, it is important that processing conditions are suitable not only for the growth of optimal BST layers but also are detrimental to the already grown Pt under layers.

6.8 Voltage dependent dielectric properties of c-BST5 thin films at the microwave range:

It has been mentioned earlier that the frequency agility in the tunable microwave devices is achieved through the non linear dielectric response of ferroelectric thin films to an applied dc electric field. In this section the voltage dependant microwave dielectric properties of BST5 thin films grown on different substrates are discussed.

The frequency and voltage dependent dielectric properties of c-BST5 thin films deposited on different substrates are shown in figures 6.11 to 6.14.

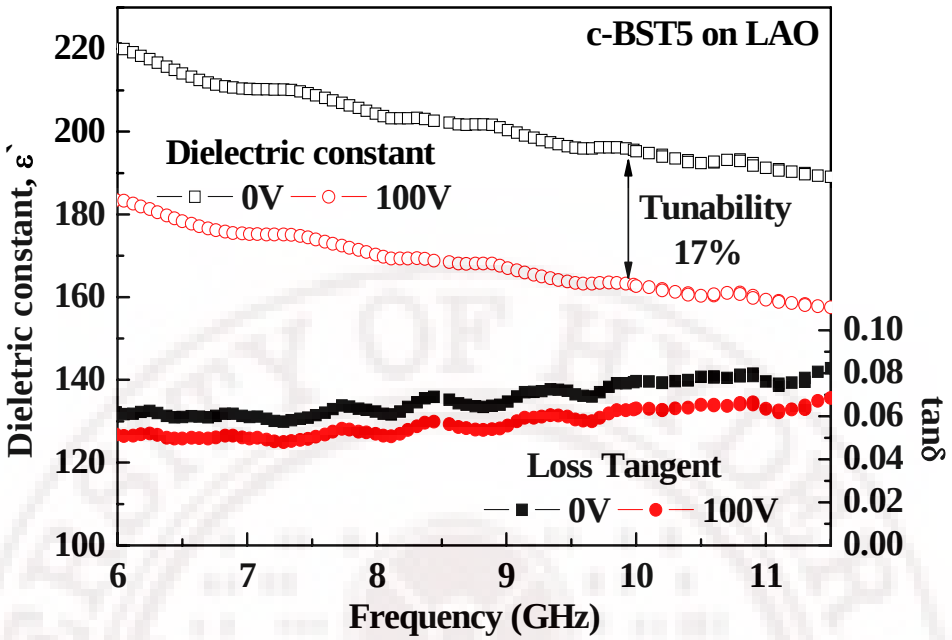

Figure 6.11: Voltage dependent broadband microwave dielectric constant of c-BST5 thin films deposited on $LaAlO_3$ substrate.

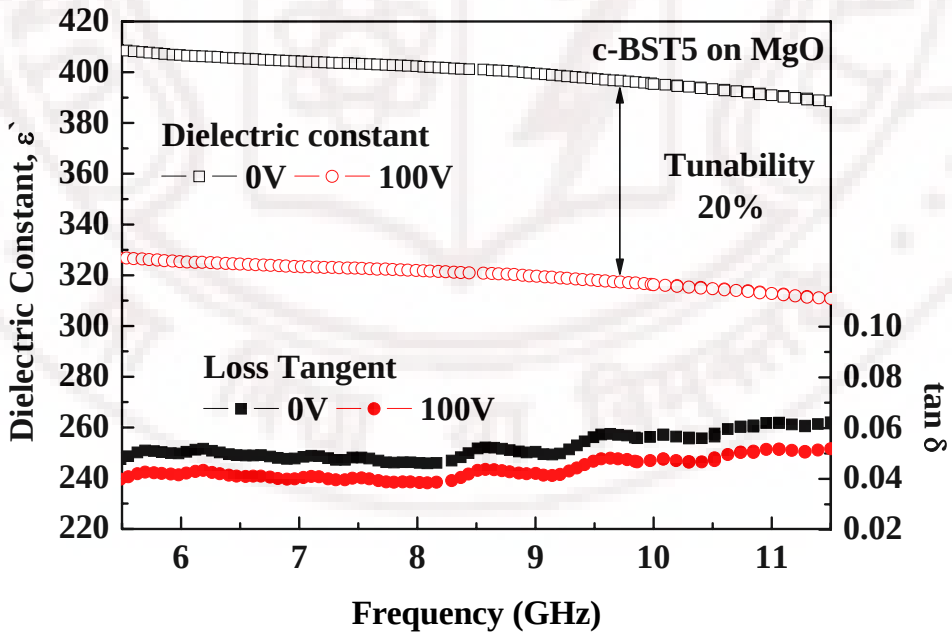

Figure 6.12: Voltage dependent broadband microwave dielectric constant of c-BST5 thin films deposited on MgO substrate.

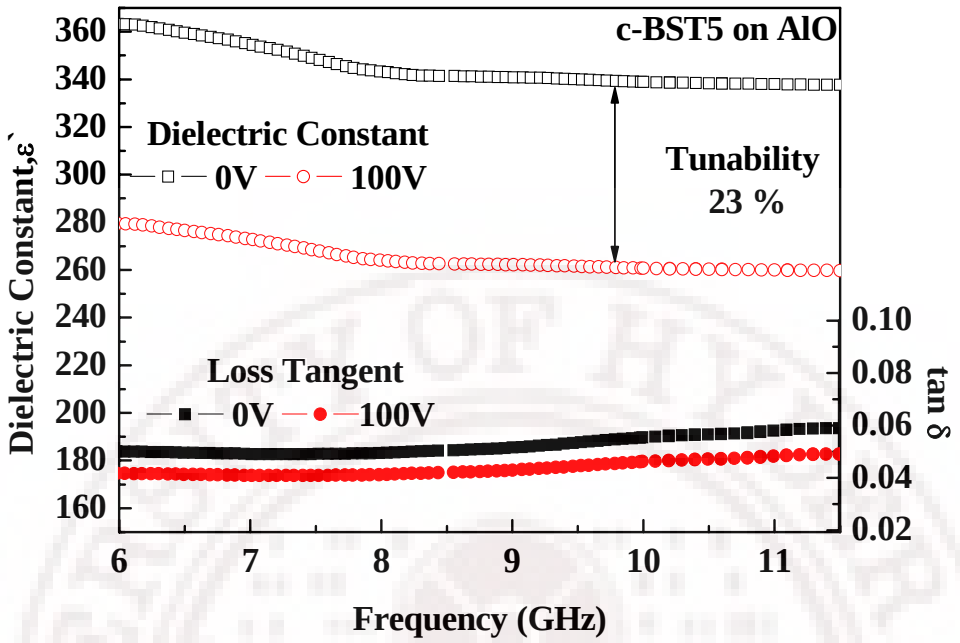

Figure 6.13: Voltage dependent broadband microwave dielectric constant of c-BST5 thin films deposited on c- plane sapphire substrate.

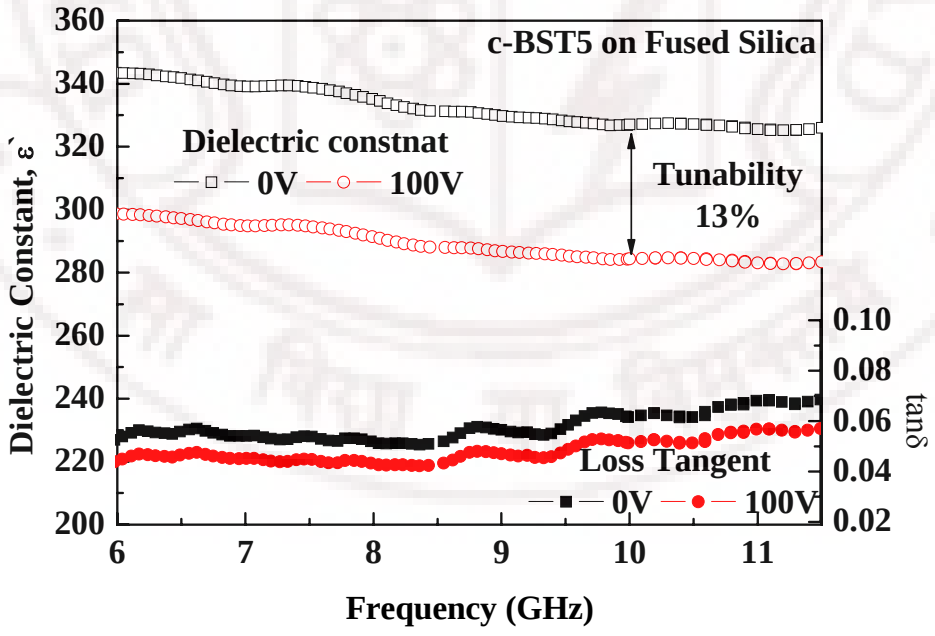

Figure 6.14: Voltage dependent broadband microwave dielectric constant of c-BST5 thin films deposited on fused silica substrate.

The figures 6.11 to 6.14 show that the voltage dependant dielectric properties (tunability) of c-BST5 films are different on different substrates. For example, the calculated dielectric permittivity for c-BST5 thin films grown on sapphire is 338(at $0V_{dc}$) and its tuning is 23% with $100V_{dc}$, i.e., [338 ($0V_{dc}$) – 260(100 V_{dc})/ (338 (0 V_{dc})] at 10 GHz. It is noted that the magnitude of the measured tunability of these films is less compared to the reported values of tunability. This is because of the maximum applied bias voltage of 100V across the ground and central conductor of the CPW lines correspond to an applied bias field of about 10 kV/cm. Due to limitations in the bias tees, tunability measurements at higher bias voltages were not possible. Very recently Varanasi et al[33] reported a dielectric tunability of about 76% @ 20 GHz for an applied electric field of about 400kV/ cm, which is much higher than the electric field strength used in the present study.

The dielectric tunability, loss tangent (at $0V_{dc}$) and Figure of Merit (FOM) at 10 GHz for an applied dc field of 10kV/cm of c-BST5 films deposited on different substrates are shown in table 6.2.

c-BST5 film deposited on	**Tunability (%, at 10GHz)**	**Loss Tangent (at $0V_{dc}$)**	**FOM**
$LaAlO_3$ (LAO)	17	0.076	2.2
MgO	20	0.056	3.5
c-plane sapphire (AlO)	23	0.055	4.2
Fused Silica	13	0.061	2.1

Table 6.2: Dielectric tunability, loss tangent and Figure of Merit (FOM) of c-BST5 film deposited on different substrates.

The low value of FOM is due to measurements being done at low applied bias fields as mentioned earlier. On comparing the tunability of c-BST5 films deposited on various substrates, it is found that a maximum tunability of 23% (at 10 kV/cm, 10 GHz) was obtained on AlO substrates. The difference in tunability is attributed to the in-plane strain in the films rendered by the substrate used. The variation in tunability with strain is shown in figure 6.15.

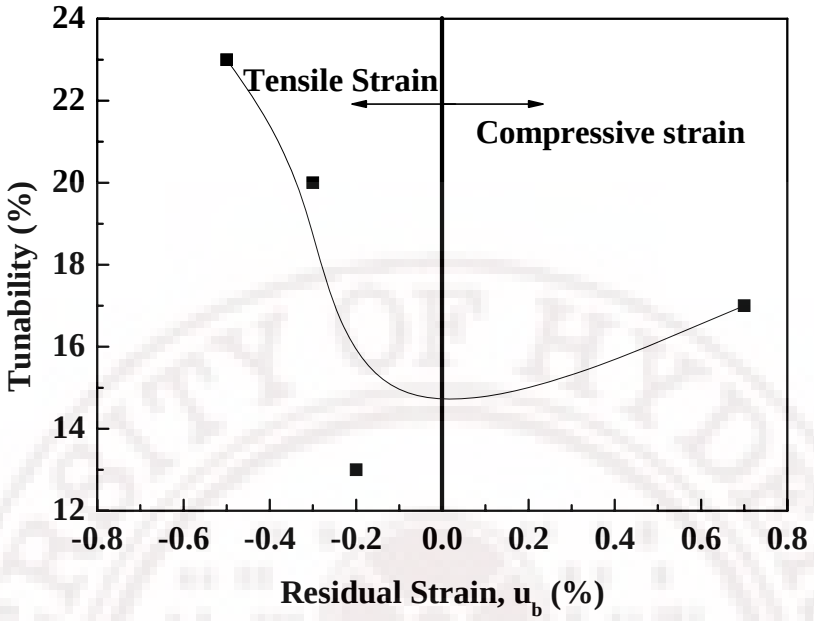

Figure 6.15: Graph showing the variation in tunability as a function of residual strain.

The above figure indicates that the tunability in c-BST5 films is highly influenced by the residual strain in the films. Strain in thin films is fundamentally significant because it affects the soft phonon mode, which is closely related to the field dependent dielectric properties of ferroelectric materials. Stress induced hardening of the soft mode in STO thin films has been confirmed experimentally by far-infrared ellipsometry and low-frequency dielectric measurements[34]. A small, uniform tensile stress in STO thin films grown on closely matched substrates can shift its phase transition temperature to room temperature[35]. A theoretical analysis of the thermodynamic potential for epitaxial single-domain thin films of $BaTiO_3$ and $PbTiO_3$ by Pertsev et. al.[36] showed that a misfit strain between a thin film and substrate can modify the phase diagram significantly. The biaxial epitaxy-induced internal stresses enable phase transformations to unusual ferroelectric phases that are not possible in single crystals and bulk ceramics. It is shown that by adjusting strain via substrate selection and film thickness, a high dielectric response can be obtained, especially in the vicinity of structural instabilities. It is known that the tunability and loss tangent values in BST is high near the phase transition temperature, T_c

and starts decreasing away from T_c. Hence, in the present case, the variation in tunability in c-BST5 thin films on different substrates can be due to strain induced effects[4, 5].

A significant result in this work is that c-BST5 films on fused silica substrates not only showed high dielectric constant but also exhibited tunability of about 13 % (at 10 GHz, 10kV/cm). The low value of tunability might be due to low residual strain of ~ -0.2% when deposited on amorphous fused silica substrates. The tunability of c-BST5 films deposited on fused silica can further be improved by appropriately engineering the strain IN the films.

6.9 Summary:

In summary, the dielectric properties of c-BST5 thin films grown on various substrates at low frequency as well as at microwave frequencies have been studied. The Metal- Insulator- Metal (MIM) capacitor structures were used to characterize the frequency and voltage dependent dielectric properties BST5 thin films at low frequencies. For the measurements of dielectric constant and loss tangent at a spot of 10GHz, A Split Post Dielectric Resonator (SPDR) based techniques was used. Calibration comparison technique was used for the determining the broad band microwave dielectric and tunable properties of c-BST5 thin films.

The c-BST5 thin films deposited at higher temperatures, such as 700 and 800^{o}C, had higher values of dielectric constant, while their dielectric losses were also much higher than that of the films deposited at lower T_d. The room temperature relative dielectric constant and dielectric loss measured at 100 kHz was 583 and 0.01 for the BST5 deposited at 800^{o}C. These films showed a maximum dielectric tunability and FOM of 62% and 62 for an applied dc field of 300kV/cm.

The c-BST5 films deposited on AlO, MgO and fused silica substrates show high in-plane dielectric constant of 338, 395 and 327 respectively when compared to c-BST5 films deposited on LAO substrates with a dielectric constant of 195. The high in-plane dielectric constant on AlO, MgO and fused silica substrates is attributed to their in-plane tensile residual strain.

Voltage dependant dielectric properties of c-BST5 films deposited on various substrates show that the residual strain highly influences tunability. A highest tunability of 23% was obtained for the films deposited on AlO substrates. c-BST films deposited on AlO substrates showed an in-plane residual strain of -0.5%. An important finding of this work is that c-BST5 films on fused silica substrates exhibit high tunable dielectric constant. These films showed a tunability of about 13 % (@ 10 GHz, 10kV/cm).

The next chapter deals with the dependence of physical properties such as spectral transmittance, refractive index, optical band gap and dielectric characteristics on the processing parameters like deposition/post-deposition annealing temperature. The optimal combination of substrate temperature and OMP for achieving device quality films has been discussed.

References:

[1] S. B. Krupanidi and C. J. Peng, *Thin Solid Films*, **305**, 144 (1997).

[2] F. Yan, P. Bao, Z.G. Zhang, J.S. Zhu, Y.N. Wang, H.L.W. Chan and C.L. Choy, *Thin Solid Films*, **375**, 184 (2000).

[3] S. U. Adikary and H. L. W. Chan, *Thin Solid Films*, **424**, 70 (2003).

[4] Z.-G. Ban and S. P. Alpay, *J. Appl. Phys*., **91**, 9288 (2002).

[5] Z.-G. Ban and S. P. Alpay, *J. Appl. Phys*., **93**, 504 (2003).

[6] M. Nayak, and T. Y. Tseng, *Thin Solid Films*, **408**, 194 (2002).

[7] Wontae Chang, Charles M. Gilmore, Won-Jeong Kim, Jeffrey M. Pond, Steven W. Kirchoefer, Syed B. Qadri, Douglas B. Chirsey, and James S. Horwitz*, J. Appl. Phys*., **87**, 3044 (2000).

[8] Robert Schafranek, Andre Giere, Adam G. Balogh, Thorsten Enz, Yuliang Zheng, Patrick Scheele, Rolf Jakoby and Andreas Klein, *J. Eur. Ceram. Soc*., **29**, 1433 (2009).

[9] S. Stemmer, S. K. Streiffer, N. D. Browning, and A. I. Kingon, *Appl. Phys. Lett*., **74**, 2432 (1999).

[10] T. R. Taylor, P. J. Hansen, B. Acikel, N. Pervez, R. A. York, S. K. Streiffer and J. S. Specka, *Appl. Phys. Lett*., **80**, 1978 (2002).

[11] J. S. Speck and W. Pompe, *J. Appl. Phys*., **76**, 466 (1994).

[12] J. S. Speck, A. Seifert, W. Pompe, and R. Ramesh, *J. Appl. Phys*., **76**, 477 (1996).

[13] W. Pompe, X. Gong, Z. Suo, and J. S. Speck, *J. Appl. Phys*. **74**, 6012 (1993).

[14] A. E. Romanov, W. Pompe, and J. S. Speck, *J. Appl. Phys*. **79**, 4037 (1996).

[15] K.J. Choi, M. Biegalski, Y.L. Li, A. Sharan, J. Schubert, R. Uecker, P. Reiche, Y.B. Chen, X.Q. Pan, V. Gopalan, L.Q. Chen, D.G. Schlom and C.B. Eom, *Science*, **306**, 1005 (2004).

[16] P. Padmini, T. R. Taylor, M. J. Lefevre, A. S. Nagra, R. A. York and J. S. Speck, *App. Phys. Lett*., **75**, 3186 (1999).

[17] D. Y. Kim, S. E. Moon, E. K. Kim, S. J. Lee, J. J. Choi, and H. E. Kim, *Appl. Phys. Lett*., **82**, 1455 (2003).

[18] D. Y. Wang, C. L. Mak, K. H. Wong, H. L. W. Chan, and C. L. Choy, *Ceram. Int*., **30**, 1745 (2004).

[19] C-J. Peng and S.B. Krupanidhi, *J. Mater. Res*., **10**, 3 (1995).

[20] Hongyan Miao, Yaohui Zhou, Guoqiang Tan and Min Dong, *J. of Electroceram*., **21**, 553 (2008).

[21] Jae-Ho Jeon, Yoo-Dong Hahn and Hai-Doo Kim, *J. Eur. Ceram. Soc*., **21**, 1653 (2001).

[22] X. Gong, W Han She, Eric E. Hoppenjans, Z. N. Wing, R. G. Geyer, J. W. Halloran and W. J. Chappell, *IEEE Trans. Micro. Theo.Tech*., **53**, 3638 (2005).

[23] D. Brassard and M. A. Elkhakni, *J.Appl.Phys*., **98**, 054912 (2005).

[24] Hiroya Kitahata, Kiyoharu Tadanaga, Tsutomu Minami, Norifumi Fujimura and Taichiro Ito, *J.Am.Ceram.Soc*., **81**, 1357 (1998)

[25] Q. X. Jia, J. R. Groves, P. Arendt, Y. Fan, A. T. Findikoglu, S. R. Foltyn, H. Jiang and F. A. Miranda, *Appl. Phys. Lett*., **74**, 1564 (1999).

[26] F. Paul, A. Giere, W. Menesklou, J. R. Binder, P. Scheele, R. Jakoby, and J. Haußelt, *Int. J. Mat. Res*., **99**, 1119 (2008).

[27] Tatsuo Schimizu, *Solid State Commun*., **102**, 523 (1997).

[28] H.C. Li, W.D. Si, A.D. West, and X.X. Xi, *Appl. Phys. Lett*., **73**, 190 (1998).

[29] C. Borderon, D. Averty, R. eveno and H. W. Gundel, *Ferroelectrics*, 362:1–7, 2008

[30] Hongwei Chen, Chuanren Yang, Bo Wang, Hong Ji and Jihua Zhang, *J. Appl. Phys*., **105**, 034112 (2009).

[31] Huichun Yu, Min Li, Chun Hui, Ailan Xu and Wenwen Shao, *Thin Solid Films*, **493**, 20 (2005).

[32] X. G. Tang, D. Y. Wang, J. Wang and H. L. W. Chan, *Integ. Ferroelectrics*, **77**, 151 (2005).

[33] C. V. Varanasi, K. D. Leedy, D. H. Tomich and G. Subramanayam, *Thin Solid Films*, **517**, 2878 (2009).

[34] A. Sirenko, C. Bernhard, A. Golnik, A. M. Clark, J. Hao, W. Si and X. X. Xi, *Nature,* **404**, 373 (2000).

[35] J. H. Haenl, *Nature*, **430**, 758 (2004).

[36] N. A. Pertsev ,A. G. Zembilgotov and A. K. Tagantsev, *Phys. Rev. Lett*., **80** 1988 (1998)

Chapter VII

Process parameter-physical property correlation and device realization

7.1 Introduction:

In chapter 4, 5 and 6 the structural, microstructural, optical and dielectric properties of a-BST5 and c-BST5 thin films were discussed. The c-BST5 films were obtained by (a) ex situ annealing a-BST5 thin films at high temperatures and (b) by depositing BST5 films in situ at elevated temperatures. In this chapter a comparison between in situ and ex situ annealing on the properties of BST5 have been discussed. The variation in the properties of BST5 films as it transforms from an amorphous to crystalline phase has also been discussed.

Finally, a set of optimized sputtering conditions are identified and varactors of interdigitated and parallel plate electrode configurations were fabricated for device realization.

7.2 Effect of annealing/deposition temperature:

Thin films of BST5 were deposited on amorphous fused silica substrates by RF magnetron sputtering. To achieve crystallinity on these amorphous substrates,

(a) BST5 films were annealed *ex situ* at different temperatures and

(b) BST5 films were deposited *in situ* at elevated temperatures.

In the case of *ex situ* annealed BST5 films, the onset of crystallinity was about 700°C, where as for the films deposited *in situ*, it is 600°C. The variation in crystallite size is shown in figure 7.1.

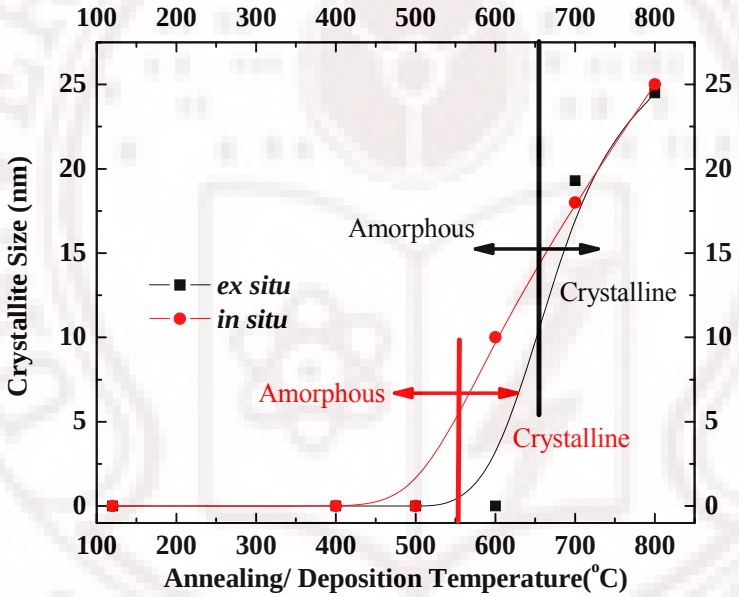

Figure 7.1: Variation in crystallite size with annealing/deposition temperature for *ex situ* annealed films and films *in situ* deposited at elevated temperatures.

The crystallite size in the case of *in situ* and *ex situ* crystallized films were similar, but the graph clearly shows that the films deposited *in situ,* crystallized at lower temperatures when compared to *ex situ* annealed films. The lattice constant of c-BST5 films was 3.95Å in both (*in situ* and *ex situ*) the cases and no variation was found with temperature, of deposition/annealing.

The spectral transmittance of room temperature deposited a-BST5, *ex situ* annealed c-BST5 and *in situ* annealed c-BST5 films are shown in figure 7.2.

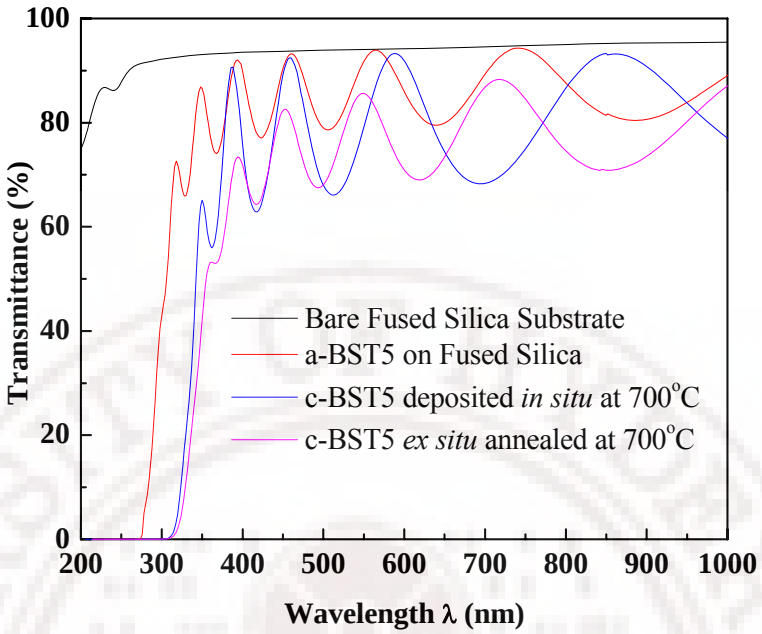

Figure 7.2: Optical transmittance spectra of BST5 thin films.

The above graph indicates that the optical transmittance of RT deposited a-BST5 is higher than that for the c-BST5 film realized by annealing *ex situ* at 700°C. The spectral transmittance in the region above the band gap is similar for the a-BST5 and c-BST5 films deposited *in situ* at 700°C (blue curve). However, the height of the fringes in the latter case is much greater, indicating increase in refractive index (as discussed later). Between the *ex situ* annealed films and the films deposited at elevated temperatures *in situ*, significantly, there is a large difference in the spectral transmittance as well as the height of fringes. Since both height of fringes (refractive index) and absolute transmittance (absorption) are changing, the most likely reason for this is the loss of oxygen during post deposition annealing of the films. However, optical losses due to scattering can be neglected. This is evident from figure 7.3, where the rms roughness is plotted as a function of temperature. Evidently, independent of whether the films are heat treated during deposition (*in situ*) or subjected to post deposition annealing (*ex situ*), the roughness values are similar. Hence, optical losses due to scattering from grain boundaries can be neglected for a comparison.

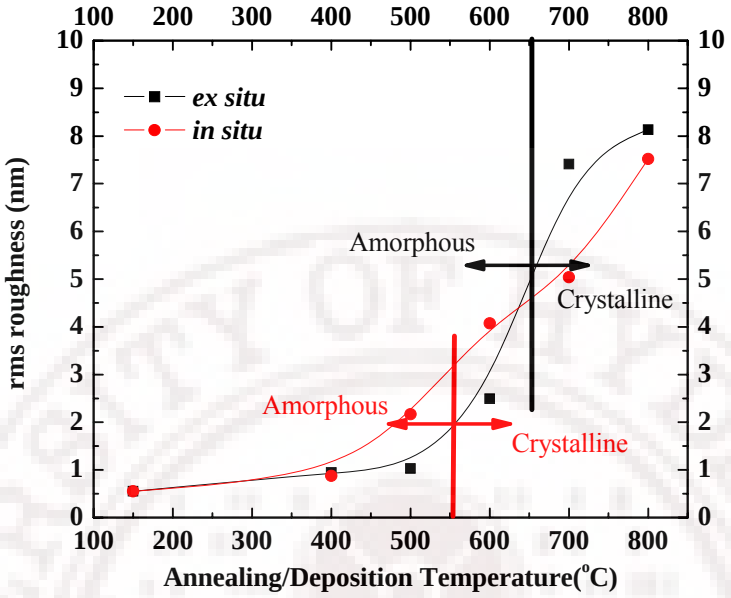

Figure 7.3: Variation in rms roughness with annealing/deposition temperature for *ex situ* annealed films and films *in situ* deposited at elevated temperatures.

The variation in refractive index of *in situ* and *ex situ* annealed BST5 films is shown in figure 7.4 as a function of annealing/ deposition temperature.

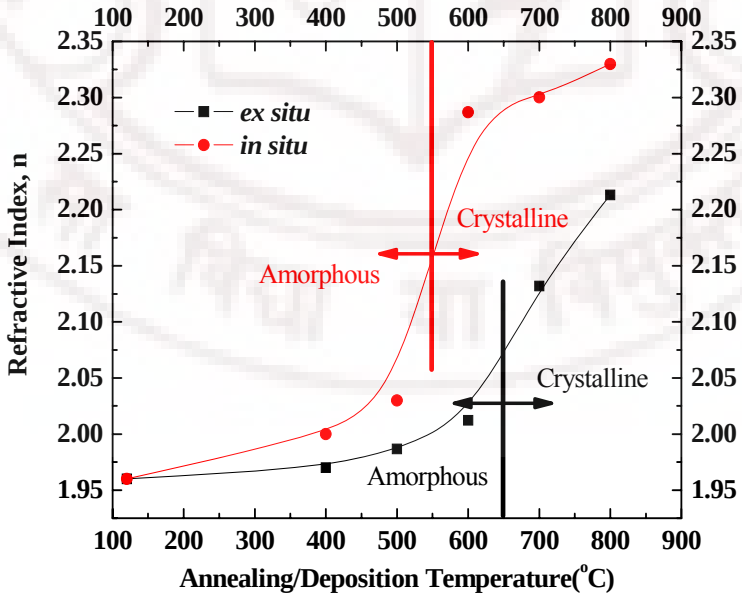

Figure 7.4: Variation in refractive index with annealing/deposition temperature for *ex situ* annealed films and films *in situ* deposited at elevated temperatures.

It is observed that the room temperature deposited a-BST5 films show low value of refractive index when compared to that of c-BST5 films. The low value of refractive index for a-BST5 films could be due to the absence of long range ordering. The *in situ* annealed films show higher value of refractive index when compared to *ex situ* annealed films. This difference in refractive index could be due to difference in packing density, as the *in situ* annealed c-BST5 films are more densely packed than the *ex situ* annealed films. With increase in annealing/deposition temperature, the value of refractive index increases as seen in figure 7.4. The increase in refractive index is due to the reduction in porosity as a result of viscous sintering while annealing/depositing at higher temperatures. The refractive index of the films is proportional to electronic polarization and is thus inversely related to inter-atomic spacing. Therefore, increasing annealing/ deposition temperature results in a reduction of inter-atomic spacing (in agreement with the X-ray diffraction) and porosity, which leads to the densification of the films and an enhancement of refractive index.

On the other hand, within the amorphous phase of BST5 films we see a significant increase in refractive index value above 500^{o}C in the case of *in situ* and above 600^{o}C for *ex situ* annealed films respectively. Usually an increase in the index of refraction is attributed to either densification or crystallization. Since crystallization was observed above 600^{o}C in the case of *in situ* and above 700^{o}C for *ex situ* annealed films respectively, the prominent difference in the index of refraction below these temperatures cannot be explained as resulting from crystallization. Thus, the change in the index of refraction is believed to correlate with the increase in film density.

It is also suggested that, at temperatures just below the crystallization temperature, the atoms in the amorphous matrix gain enough thermal energy to form local crystalline order in the amorphous matrix with a higher atomic packing density in the temperature range where complete crystallization did not occur.

The optical band gap calculated using the Tauc relation for *in situ* and *ex situ* annealed films are shown in figure 7.5.

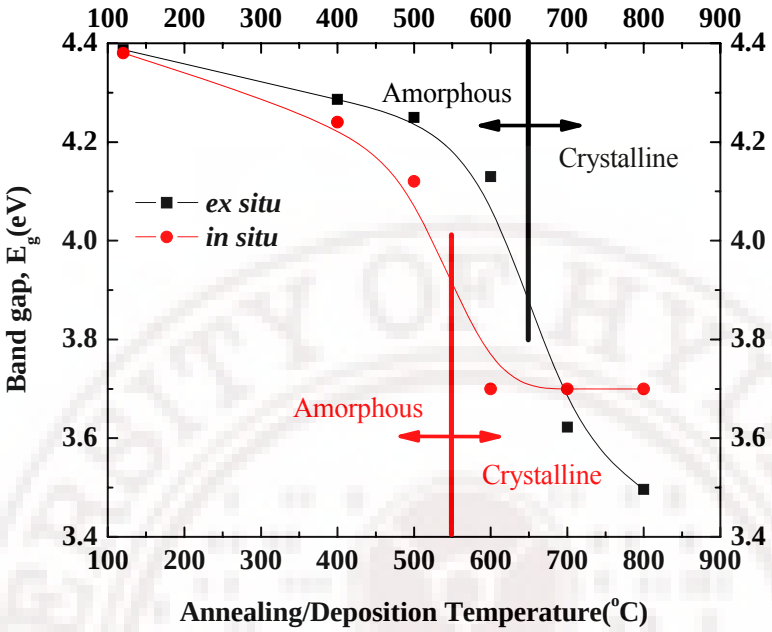

Figure 7.5: Variation in band gap with annealing/deposition temperature for *ex situ* annealed films and films *in situ* deposited at elevated temperatures.

The as-deposited a-BST5 films have a band edge, E_g, value of about 4.4 eV. On increasing the annealing/deposition temperature, the E_g value decreases marginally. The BST5 films remain X-ray amorphous as confirmed by XRD. But, for temperature greater than 600°C for *in situ* and 700°C for *ex situ* annealing respectively, there is a sudden decrease in the value of E_g. The possible reason for higher value of band gap in the amorphous BST5 is the existence of density of states within the gap, as explained by Davis and Mott[1], causing the formation of a fundamental absorption edge due to the band tailing rather than an optical band gap. In the crystalline state the states within the gap disappear and the optical band gap then becomes equal to that of the single crystal value which is the difference between the top of the valence band and the bottom of the conduction band. Although the band gap energy is a constant for a material in the bulk form it is known to vary in thin films.

Figure 7.6 shows the microwave dielectric constant and loss tangent of BST5 films annealed/deposited at different temperatures.

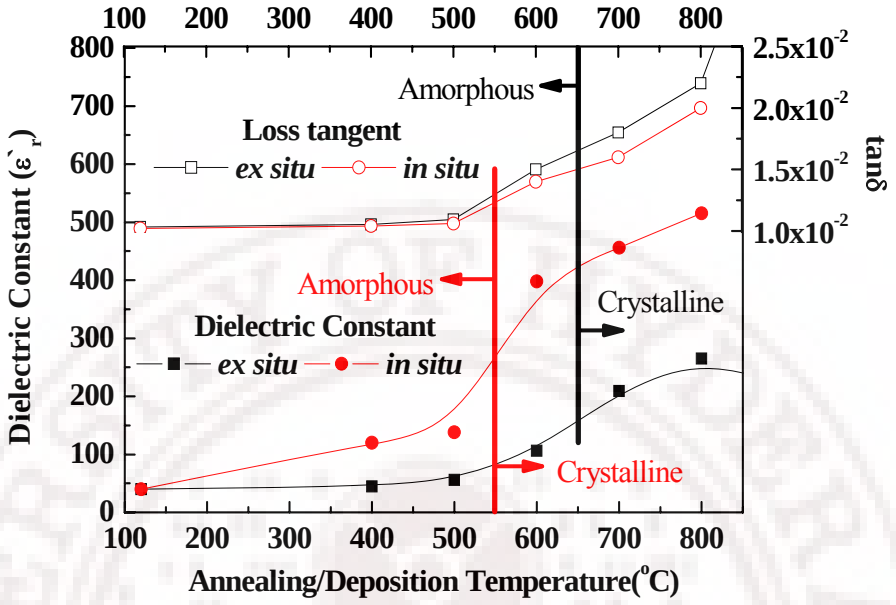

Figure 7.6: Variation in dielectric constant and loss tangent with annealing/deposition temperature for *ex situ* annealed films and films *in situ* deposited at elevated temperatures.

The dielectric constant shows a significant change with annealing temperature. A prominent increase in dielectric constant is observed as the films crystallize.

To understand the variation in the dielectric constant we tried to estimate the dielectric properties of the BST5 thin films from their chemical compositions. The molecular polarizability, α, which contains both ionic and electronic components is directly connected to the crystal chemistry. It can be calculated from the real part of the relative permittivity ε' and the molar volume V_m (in Å^3) using the Clausius–Mossotti (C–M) relation given as[2],

$$\alpha = \frac{V_m(\varepsilon' - 1)}{b(\varepsilon' + 2)} \qquad (7.1)$$

where b is assumed to be $4\pi/3$ for a cubic material. Application of this relation to the oxide materials has been extensively discussed by Shannon et. al.[3] There are considerable variations for this theory in the cases of ferroelectrics and piezo-electric materials and for materials with larger ionic or electronic conductivity.

From the C–M relation above, we can derive an expression for the relative permittivity in terms of molecular polarizability and molar volume,

$$\varepsilon' = \frac{1 + 2b\alpha/V_m}{1 - b\alpha/V_m} \qquad (7.2)$$

From the above expression, it can be seen that ε' increases with the increase in α and increases rapidly when α approaches V_m/b. Thus a crystalline film will have a higher dielectric constant when compared with the amorphous film of the same composition. Based on the above arguments we can account for the variation in the dielectric properties of BST thin films as a function of the annealing temperature. The total dielectric polarizability of BST5 can be calculated in terms of the ionic polarizabilities of the constituent atoms according to Shannon's theory[4]. The ionic polarizabilities of Ba^{2+}, Sr^{2+}, Ti^{4+} and O^{2-} are 6.40, 4.25, 2.94 and 2.0, respectively[5]. The molecular polarizability of BST5 adds upto 14.265 (the molecular polarizability of any material is independent of frequency up to the optical frequency region and after which it relaxes out and the reported lattice parameter of the BST5 is 3.947Å[6]. Based on these quantities, the calculated dielectric permittivity of $Ba_{0.5}Sr_{0.5}TiO_3$ is 102.4. On comparing this value with the measured dielectric permittivity of the BST5 thin films, assuming this as the maximum possible value of the dielectric permittivity for a dense (i.e. without any porosity) BST5, under the rigid lattice model of C–M (i.e. excluding the phonon contribution to the dielectric constant), we can see that the crystalline thin films have dielectric constant values higher than the calculated value while the amorphous films exhibit lower values compared with the calculated value.

The lower value of dielectric constant exhibited by amorphous films compared to the calculated value can be attributed either to the change in polarizability or to the changes in the cell volume. The ionic polarizabilities of the constituent atoms in BST5 thin films will be the same in the amorphous and the crystalline states. Hence the total molecular polarizability will remain the same. So the deviation from C–M theory is because of the possible increase in the molar volume V_m due to the amorphous nature of the film[7]. As the annealing/deposition temperature increases, the inter-atomic distance decreases. This can be seen from the increase in the refractive index in figure 7.4.

The onset of crystallization is accompanied by a sudden increase in the dielectric constant. It could be attributed to the additional polarizability originating from the lattice

modes which are intrinsic to a crystalline material[7]. This will add to the total polarizability of the films.

The dielectric loss tangent of the *in situ* and *ex situ* annealed BST5 thin films are also shown in figure 7.6. It is observed that the amorphous thin films have a lower dielectric loss when compared with that of the crystalline thin films. This is because amorphous BST thin films have low intrinsic losses due to the absence of lattice modes. As the films crystallize, it generates a lattice potential which will allow the phonon–phonon interactions opening up many loss mechanisms. The Transverse Optic (TO) modes of the perovskites are known to offer large dielectric loss values and the probing microwave field will couple to this phonon mode increasing the dielectric loss of crystalline films[8].

There are two possible interpretations for the increase in dielectric constant in the amorphous phase with annealing/deposition temperature. The formation of the local ordering in the amorphous matrix usually increases the dielectric constant of the film. However this simple model cannot explain such a large dielectric constant change, since the observed increase in the dielectric constant is about 100%. A more reasonable interpretation is the densification of the amorphous component, and the possible densification induced atomic bonding change. That is, the densification itself can increase the dielectric constant by increasing the atomic polarization per unit volume. Although there has been no direct experiment showing a densification induced atomic bonding change, it was reported that for $BaTiO_3$ thin films, as the structure changes from amorphous to crystalline, the interatomic distance decreases and the electron charge transfer between Ti and O increases, which is evidenced by the fact that the amorphous and crystalline $BaTiO_3$ films displayed different optical absorption edges[9]. It is speculated that the annealing induced densification causes an average inter-atomic distance reduction, which consequently increases the electron transfer between Ti and O. This increased electron transfer might then enhance the Ti-O dipole in the films. These enhanced Ti-O dipoles could manifest themselves as an increase in the total polarization in unit volume, and consequently, an increase in the dielectric constant.

7.2.1 A comparison of *in situ* deposition at higher temperatures and *ex situ* annealing:

In physical vapor deposition process, as the film grows, it develops a structure or morphology, which includes both topography (surface morphology and roughness) and crystallography. The crystallography of the film may range from amorphous to polycrystalline to epitaxy.

Depending upon the deposition conditions of thin films on a foreign substrate, the initial nucleation and growth stages are strongly influenced by the free energy, γ of the substrate. Here, we need to consider the γ of both the substrate free surface, γ_s, and of the substrate-film- interface, γ_i, relative to that of the film free surface, γ_f. All the three γ values will generally depend on crystallographic orientation, passivation, and sometimes other factors also[10]. Assume that there is enough surface diffusion so that the depositing material can rearrange itself to minimize γ, that is, assume that the nucleation is not kinetically limited and can approach equilibrium. For this, we must have the diffusion length, Λ to be much greater than the hoping distance of the atoms, a, i.e., $\Lambda >> a$. In the opposite case, i.e., when $\Lambda < a$, the atoms stick where it lands, and the growth behavior is "quenched".

The condition, $\Lambda >> a$ is achieved only in the case of films deposited *in situ* at elevated temperatures and for the films deposited at room temperature, the growth behavior is quenched where the approaching atoms on the substrate surface freeze at the place of impact, resulting in a porous, amorphous microstructure. When these films are subjected to *ex situ* annealing treatments, the randomly ordered atoms try to order themselves in such a way that the free energy is minimized. But once deposited, the degree of freedom available to the atoms in rearranging spatially at annealing stage could be quite limited as they need to overcome many potential barriers.

As, *ex situ* annealing is a dynamic process, the control over the parameters that influence the physical properties of the material is very limited.

The results presented in this section clearly demonstrate that films deposited at elevated temperatures *in situ* provide greater control over the growth of crystalline BST5 films and therefore its properties. Hence, by appropriately maneuvering the processing parameters during deposition, device quality BST5 films with good structural,

microstructural, optical and dielectric properties can be achieved. This is demonstrated in the next section where the performance of devices fabricated using BST5 films grown at optimized parameters are discussed.

7.3 Realization of tunable varactors:

Ferroelectric varactors are important for frequency agile phase shifters, filters and tunable impedance matching networks[11,12]. As mentioned in chapter 1, interdigitated electrodes and parallel-plate electrodes are two different types of electrode configurations[13,14,15] that are being used not only for measuring the dielectric properties of thin films but also as a circuit element in frequency agile devices and circuits.

In the present work, c-BST5 films were deposited under a set of optimized conditions as shown in table 7.1 below,

Parameter	Value
Power density (W/cm^2)	3.0 W/cm^2
Substrate to target distance (cms)	5 cms
Working pressure (mTorr)	20 mTorr
Oxygen mixing percentage, OMP (%)	50 %
Substrate Temperature (^{o}C)	800^{o}C
Substrate Type	Fused silica and Pt/Si.
Post-deposition annealing treatment	None

Table 7.1: Set of optimized parameters from this study used for depositing c-BST5 thin films for the realization of tunable varactors.

Varactors with both interdigitated and parallel plate electrode configurations were fabricated for device realization. For the interdigitated configuration, c-BST5 films were deposited on amorphous fused silica substrates and for the parallel plate configuration, c-BST5 films were deposited on Pt/Si substrates. The top electrodes in both the cases were patterned by a single step photolithography process using a contact mask. The setup used to characterize the dielectric and tunable properties of these device structures at microwave range of frequencies consisted of an Agilent 8722ES Vector Network

Analyzer (VNA), a Xantrex XT-200-0.25 voltage source, a RF probe with 250 μm pitch with Ground- Signal- Ground (GSG) configuration (GGB Industries) mounted on the *XYZ* stage of a probe station (LMS 2709, J microtechnology) and bias tee for adding dc bias on the RF probes.

In this section we describe the realization and characterization of parallel plate and interdigitated varactors using c-BST5 thin films.

7.3.1 Parallel plate varactor realization:

For realization of varactors in the parallel plate electrode configuration a Circular Patch Capacitor (CPC) technique was used. The cross section of the electrode layout of the test structures used is shown in Figure 7.7. It consists of a 450 nm thick BST5 thin film on top of a 200 nm thick Pt buried layer. The top electrode consists of 400 nm silver capped by 100 nm og gold film. Circular patches with different inner diameters ranging from 80 μm to 120 μm and a concentric ground plane with a constant diameter of 300μm were photo-lithographically defined without damaging the BST thin films.

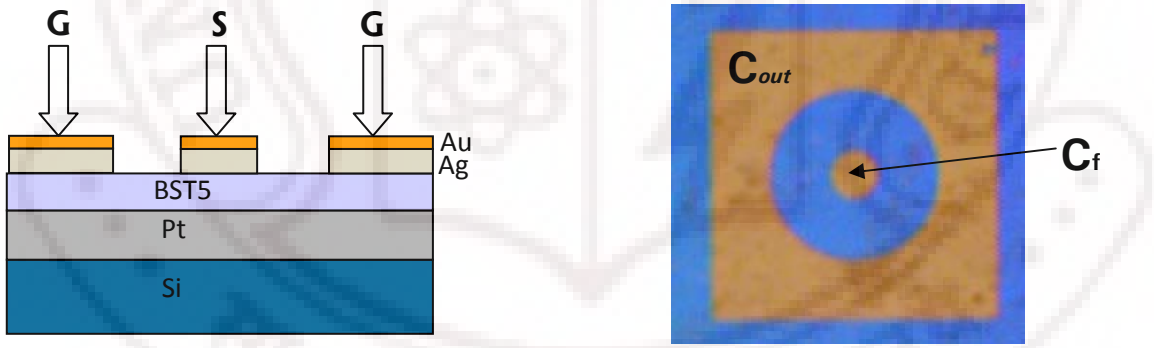

Figure 7.7: (a) Cross section and (b) Microphotograph of the tunable capacitor fabricated using BST thin films

The total capacitance measured between the center patch and the surrounding concentric electrode is:

$$C = (C_f C_{out}) / (C_f + C_{out}) \qquad (7.3)$$

where, C_f is the capacitance between the center patch and the bottom plate and C_{out} is the capacitance between the top outer electrode and the bottom plate. Typically $C_{out} >> C_f$ because the area of the outer patch is much greater than the inner circle and hence the

total capacitance in the CPC structure is dominated by capacitance C_f when the small capacitance C_f is in series with large capacitance C_{out}, as shown in the figure 7.7b. Hence, the top outer electrode provides an effective microwave connection to the bottom plate ($C \approx C_f$)[16].

All microwave measurements were carried out at room temperature using the VNA and GSG probes. The standard one port open-short-load calibration procedure was used to measure the S_{11} parameters of the test structures between the central and outer patch. The measured reflection coefficient S_{11} is converted into impedance for the test structure Z_T using[17],

$$Z_T = Z_0 \frac{1+S_{11}}{1-S_{11}} = R + jX \qquad (7.4)$$

Here, Z_0 =50 Ohm. The capacitance and loss tangent of the capacitor can be derived from the complex impedance using the following relations:

$$C = -\frac{1}{\omega X} \qquad \tan\delta = -\frac{R}{X} \qquad (7.5)$$

The relative permittivity of the materials can be calculated using the simple parallel plate capacitor model.

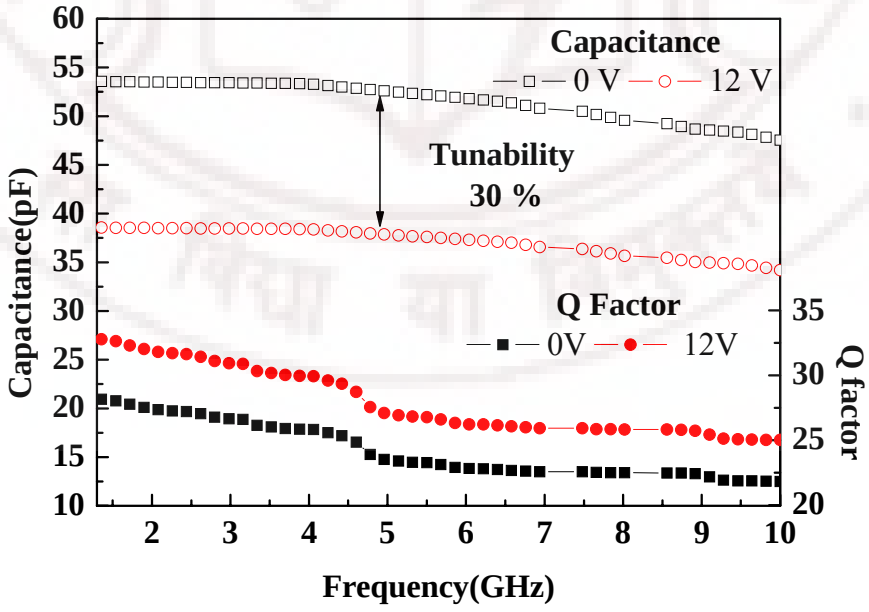

Figure 7.8: Capacitance and Q factor as a function of frequency in CPC structure, measured at different dc voltages.

Figure 7.8 shows the capacitance and Q value of c-BST5 films with the CPC structure, as a function of frequency from 1 GHz to 10 GHz with and without dc bias. The tunability of the parallel plate varactor was about 30% at 5 GHz under 12V dc bias. This value of dielectric tunability is comparable with the values of 40% at 20V, 29% at 12V and 30% at 12V reported earlier[18,19,20] for BST thin films using CPC structures.

7.3.2 Interdigitated varactor realization:

For the interdigitated varactor realization the c-BST5 thin films were deposited directly on fused silica substrate and the interdigitated electrodes were patterned on top of the c-BST5 thin films. A schematic diagram of the interdigitated varactor is shown in figure 7.9a. The fabricated interdigitated varactor on c-BST5 films is shown in figure 7.9b. The width (W) of the fingers was 5 μm, gap (G) between the fingers was 3 μm, length (L) of the fingers was 100 μm and number of finger pairs was 3. The top electrode was patterned using a single step photolithographic and lift-off process.

These varactors were designed in such a way that it can be probed using 150 μm ground-signal-ground (GSG) probes.

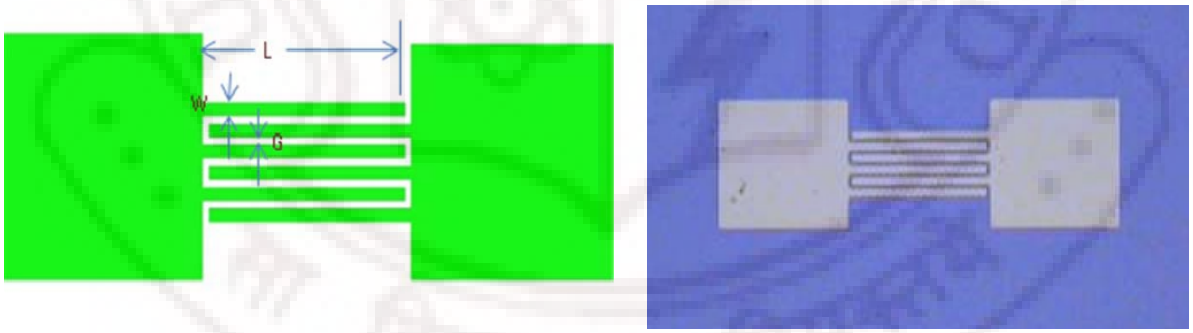

Figure 7.9: (a) Schematic diagram of the simulated and (b) fabricated interdigitated varactor.

The fabricated interdigitated varactors were probed using GSG probes (housed in J microtechnology make probe station) and a VNA. The TRL (Through-Reflect-Line) calibration was performed using a standard calibration substrate (CS-5 of GGB Industries) to adopt the CPW probes in the measurement setup for minimizing the experimental errors. The measured S-parameters were used to calculate the capacitance, C using the formulae[21,22],

$$Y_{11} = Y_0\left(\frac{1-S_{11}}{1+S_{11}}\right) \qquad (7.6)$$

$$C = \frac{-1}{2\pi f.\,\mathrm{Im}\left(\frac{1}{Y_{11}}\right)} \qquad (7.7)$$

where, Y_0 is the reference admittance and S_{11} is the reflection coefficient.

Figure 7.10 displays the capacitance and quality factor of the c-BST5 film with the interdigitated varactor structure as a function of frequency up to 5GHz with and without dc bias.

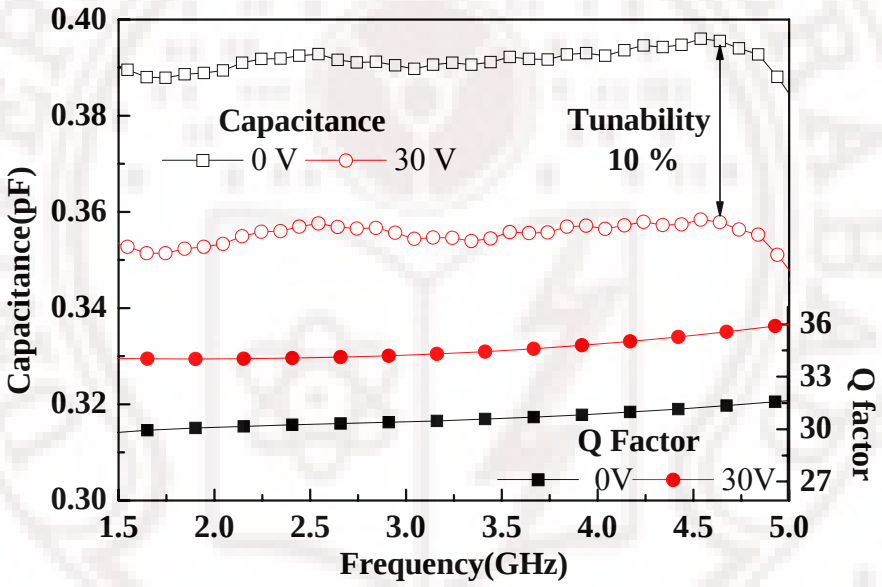

Figure 7.10: Capacitance and Quality factor as a function of frequency for c-BST5 based interdigitated varactor under 0 and 30 V dc bias.

The obtained capacitance of c-BST5 at 5 GHz is 0.4pF at zero dc bias, which reduces to 0.37 pF with application of a dc bias of 30V. A dielectric tunability of about 10% was obtained for c-BST5 films in interdigitated varactor configuration. Since the in-plane tunability of the BST film is sensitive to the width of gap in the interdigitated structure and the type of substrate used, it is therefore difficult to compare our present results with other studies [23,24].

The parameters and results obtained for the c-BST5 film based parallel plate and interdigitated varactors are presented in Table 7.2.

	Parallel-plate varactor	**Interdigitated varactor**
Frequency (GHz)	5	5
Substrate Used	Pt/Si	Fused silica
Top-bottom electrodes	(Au/Ag)-Pt	(Au/Ag)
Thickness of BST5 film (nm)	450	450
Number of gaps	--	5
Length of fingers (μm)	--	100
Width (W) and gap (G) of fingers (μm)	--	5 (W) and 3 (G)
Area of capacitance (mm^2)	0.04π	--
Capacitance *C* (pF)	52	0.4
Applied dc voltage (V)	12	30
Tunability	30	10
Q factor (0V)	23	32

Table 7.2: Parameters and results of parallel-plate and interdigitated varactors.

It could be noted that the tunability in the CPC structure is considerably larger than that in the interdigitated structure even under lower applied dc field. That is, the in-plane tunability was found to be much lower than the out-of-plane tunability. Cole *et al.*[25] addressed this issue that the CPC varactor offers high tunability compared to the interdigitated structure since the electric fields in CPC are well confined within the film, as compared to the IDC structure where only a portion of the electric field is confined within the film. Also, the field strength seen by the film in the CPC geometry is much higher than that in the IDC geometry.

References:

[1] E. A. Davis, N. F. Mott*, Phil. Mag.*, **22**, 903 (1970).

[2] Yidong Xia, Cong Cai, Xiaoyuan Zhi, Bai Pan, Di Wu, Xiangkang Meng and Zhiguo Liu, *Appl. Phys. Lett*., **88**, 182909 (2006).

[3] M. A. Subramanian and R. D. Shannon, *Mater. Res. Bull.*, **24**, 1477 (1989).

[4] R. D. Shannon and G. R. Rossman, *Am. Mineral*., **77**, 94 (1992).

[5] R. D. Shannon, *J. Appl. Phys.*, **73**, 348 (1993).

[6] JCPDS card No. 39-1395 for bulk $Ba_{0.5}Sr_{0.5}TiO_3$ (a=3.94710 Å)

[7] R. D. Shannon, *Chemistry of Electronic Materials* ed P K Davies and R S Roth, **804**, 457 (1991).

[8] D. A. Tenne, A. Soukiassian,X. X. Xi, H. Choosuwan, R. Guo and A. S. Bhalla, *Phys. Rev. B*, **70**, 174302 (2004).

[9] A. Onton and V. Marrello, *AIP Conf. Proc. No. 3*, edited by G. Lucovsky and F. L. Gallener, American Institute of Physics, New York (1976).

[10] Kai-Ming Ching, Wei-Der Chang and Tsung-Shune Chin, *Appl. Surf. Sci*., **92**, 471 (1996).

[11] S. S. Gevorgian and E. L. Kollberg, *IEEE Trans. Microwave Theory Tech*., **49**, 2117 (2001).

[12] M. W. Cole, P. C. Joshi and M. H. Ervin, *J. Appl. Phys*., **89**, 6336 (2001).

[13] Y.-K. Yoon, D. Kim, M. G. Allen, J. S. Kenney and A. T. Hunt, *IEEE Trans. Microw. Theory Tech.,* **51**, (2003) 2568.

[14] J. Nath, D. Ghosh, J.-P. Maria, A. I. Kingon, W. Fathelbab, P. D. Franzon and M. B. Steer, *IEEE Trans. Microw. Theory Tech.*, **53**, 2707 (2005).

[15] Xiao-Yu Zhang, Peng Wang, Su Sheng, Feng Xu and C. K. Ong, *J. Appl. Phys*., **104**, 124110 (2008).

[16] K.Khamchane, A.Vorobiev,T.Claeson and S.Gevorgian, *J. Appl. Phys*., **99**, 034103 (2006).

[17] S.Sheng, P.Wang, X.Y. Zhang and C.K.Ong, *J. phys.D:Appl.phys.*, **42**, 015501 (2009).

[18] A. Vorobiev, P. Rundqvist, K. Khamchane and S. Gevorgian, *J. Appl. Phys*., **96**, 4642 (2004).

[19] A. Mahmud, T. S. Kalkur, A. Jamil and N. Cramer, *IEEE Microw. Wirel. Compon. Lett.*, **16**, 261 (2006).

[20] Xiao-Yu Zhang, Peng Wang, Su Sheng, Feng Xu and C. K. Ong, *J. Appl.Phys*., **104**, 124110 (2008).

[21] Young Chul Lee, Young Pyo Hong, Duk Man Kim and Kyung Hyun Ko, *Proceedings of the 36th European Microwave Conference*, 1347 (2006).

[22] G. Lakshmi Narayana Rao, K. Venkata Saravanan and K.C. James Raju, *Proceedings of the 10th TENCON-2008 IEEE Region 10 Conference*, 1 (2008).

[23] L. M. B. Alldredge, W. Chang, S. B. Qadri, S. W. Kirchoefer and J. M. Pond, *Appl. Phys. Lett*., **90**, 212901 (2007).

[24] H. S. Kim, T. S. Hyun, H. G. Kim, I. D. Kim, T. S. Yun and J. C. Lee, *Appl. Phys. Lett*., **89**, 052902 (2006).

[25] M. W. Cole, C. V. Weiss, E. Ngo, S. Hirsch, L. A. Coryell and S. P. Alpay, *Appl. Phys. Lett*., **92**, 182906 (2008).

Chapter VIII

Conclusions and outlook for future work

Conclusions:

The research presented in this dissertation is centered around the structural, microstructural, optical and microwave dielectric properties of Barium Strontium Titanate {BST, $(Ba_x,Sr_{1-x})TiO_3$} thin films with Ba:Sr ratio of 50:50 [$(Ba_{0.5}, Sr_{0.5})TiO3$, BST5]. One of the core aims of this dissertation is deposition of crystalline BST5 thin films on amorphous fused silica substrates and demonstration of voltage tunable dielectric properties at low and high frequencies for frequency agile applications. RF magnetron sputtering was chosen as the technique for depositing these thin films. The salient conclusions of the thesis are given below.

Target fabrication:

Fabrication of stoichiometric sputtering targets of BST5 using conventional solid-state reaction method with a relative density of 96% with good surface finish, suitable for sputtering after sintering the green pellets at 1400^oC for 2 hours, has been demonstrated.

Compositional analysis:

The rate of sputtering and stoichiometry of the deposited films were determined by Rutherford Back Scattering Spectroscopy and it was found that the rate of sputtering decreases with increase in OMP in the sputter atmosphere. The decrease in rate of sputtering is due to lower molecular weight of oxygen when compared to that of atomic Argon (Ar). The effect of OMP on Ba/Sr ratio was found to be marginal. The films deposited at 0 and 25% OMP were oxygen deficient and had excess Ti. A close replication of the target stoichiometry was achieved for films sputter deposited at 50% OMP.

The XPS results clearly indicated the presence of oxygen vacancies in the films deposited at 0 and 25% OMP, complementing the RBS results. The oxygen vacancy chemisorbs moisture, forming metal hydroxides on the surface of the film. An increase in OMP shows decrease in oxygen defect density.

Deposition of a-BST5 thin films:

Amorphous-BST5 (a-BST5) films were deposited on water cooled substrates at different OMP and their structural, microstructural, optical and electrical properties were studied. The a-BST5 films have band-gap, refractive index and dielectric constant values comparable to most of the technologically important oxides. These films show zero tunability, but have excellent dielectric strength. Hence a-BST5 films can be considered for applications which require moderate dielectric constant (~30) with high power handing capabilities. The low loss tangent in a-BST5 is an additional advantage.

Effect of annealing process:

Two different *ex situ* (post-deposition) annealing approaches were used in order to crystallize a-BST5 films. In the first approach, all the BST5 films deposited as a function of OMP at RT were crystallized by cold inserting a-BST5 films at 900^{o}C for 1 min.

In the second approach, the a-BST5 films deposited at 50% OMP were *ex situ* annealed from 400^{o}C to 800^{o}C in intervals of 100^{o}C.

***Ex situ* annealing:**

Ex situ annealing approach yielded crystalline BST5 (c-BST5) films with good structural, optical and microwave dielectric properties on fused silica substrates. BST5 films *ex situ* annealed above 800^{o}C lost oxygen, which resulted in an increase in optical band-gap, E_g. The increase in E_g was explained using the Burstein-Moss (B-M) Effect. The onset of crystallinity was found to be 700^{o}C. One of the significant observations in the current work is the effect of amorphous to crystalline transition on structural, microstructural and optical properties of BST5 thin films. The BST thin films in the amorphous phase have higher absorption edge, lower refractive index and lower dielectric constant when compared to their crystalline counterpart. The transition from amorphous to crystalline phase is accompanied by an increase in refractive index, decrease in optical band gap and increase in dielectric constant and loss tangent. The surface of a-BST5 film was smooth when compared to that of c-BST5.

***In situ* deposited:**

The XRD results of c-BST5 films deposited *in situ* at elevated substrate temperatures on fused silica substrates indicated an increase in degree of crystallinity with increase in substrate temperature without change in lattice parameter, while BST5 films deposited at 0% and 25% OMP showed an increase in lattice constant due to defects in the form of oxygen vacancies. The onset of crystallization was found to be 600^{o}C. Films deposited on Pt/Si substrates show epitaxial growth along (*111*) plane whereas films deposited on MgO and AlO show polycrystalline behavior with preferred orientation along (*200*) direction.

It is clear from our experiments that the temperature at which the BST5 film is deposited can considerably change the surface morphology of the Pt layer, which in turn influences the morphology of the BST5 over layer and that these variations in the Pt layer has to be taken in to account while optimizing processing conditions for the BST over layer.

In the case of BST5 films deposited on fused silica substrates, the surface roughness of the films increased with increase in deposition temperature from 600 to 800^{o}C while the rms roughness showed decreasing trend for the films deposited above 50% OMP. The decrease in rms roughness is attributed to lower rates of deposition. The optical band gap was 3.7 eV±0.1 eV for all the BST5 films, irrespective of their deposition temperature while refractive index increased from 2.28 to 2.33 with increase in deposition temperature from 600 to 800^{o}C due to increase in packing density brought about by sintering.

***In situ* Vs *ex situ* annealing treatment:**

The results presented in this dissertation clearly demonstrate that films deposited at elevated temperatures *in situ* provide greater control over the growth of crystalline BST5 films and therefore its properties. Hence, by appropriately maneuvering the processing parameters during deposition, device quality BST5 films with good structural, microstructural, optical and dielectric properties can be achieved.

The onset of crystallization was 600^{o}C in the case of BST5 films deposited *in situ*

at elevated substrate temperatures, which was 100^{o}C less than that of the *ex situ* annealed films.

Though both the *ex situ* annealing approaches gave crystalline BST5 films, no good MIM structures were realized on Pt/Si substrates due to high thermal shock received through the annealing process. The difference in thermal expansion coefficient of Pt and Si resulted in hillock formation on Pt layer, which in turn significantly deteriorated the surface morphology of the c-BST5 layer. This lead to electrically shorted MIM structures. No such problem was encountered in the *in situ* case.

Frequency dependent dielectric properties:

Conventional photolithography process and metal lift-off technique were employed to make Co-Planar Waveguide (CPW), Circular Patch Capacitor (CPC) and Inter Digitated Capacitor (IDC) structures directly onto the films' surface for measuring their broadband microwave dielectric properties. The metallic electrodes i.e., bi-layers of Ag (500nm) and Au (50 nm, as capping layer), deposited for this purpose had sharp edges and very good adhesion, withstanding many of the on-wafer probe tests. The feature sizes realized as part of this work range from 120 μm, down to 3 μm.

Low-frequency dielectric properties of c-BST5 thin films:

The c-BST5 thin films deposited at higher temperatures, such as 700 and 800^{o}C, had higher values of dielectric constant, while their dielectric losses were also much higher than that of the films deposited at lower T_d. The room temperature relative dielectric constant and dielectric loss measured at 100 kHz was 583 and 0.01 for the BST5 deposited at 800^{o}C. These films showed a maximum dielectric tunability and FOM of 62% and 62 for an applied dc field of 300kV/cm. The value of tunability obtained (at low frequency) in the present study is comparable to the reported values.

High-frequency dielectric properties of c-BST5 thin films:

The c-BST5 films deposited on AlO, MgO and fused silica substrates show high in-plane dielectric constant of 338, 395 and 327 respectively when compared to c-BST5 films deposited on LAO substrates with a dielectric constant of 195. The high in-plane dielectric constant on AlO, MgO and fused silica substrates is attributed to their in-plane tensile residual strain.

Voltage dependant dielectric properties of c-BST5 films deposited on various substrates show that the residual strain highly influences tunability. A highest tunability of 23% was obtained for the films deposited on AlO substrates for an applied field of 10kV/cm. c-BST5 films deposited on AlO substrates showed an in-plane residual strain of -0.5%. However, the tunability values reported in the present study cannot be compared with that in the literature because the dc field used in this study is very low (of the order10kV/cm). Due to limitations in the bias tees, tunability measurements at higher bias voltages weren't possible.

Dielectric tunability of BST5 on fused silica substrates:

An important finding of this work is that c-BST5 films on fused silica substrates exhibit high and tunable dielectric constant. These films showed a tunability of about 13 % (@ 10 GHz, 10kV/cm). This value of tunability on fused silica can further be improved by appropriately engineering the strain in the films.

Realization of tunable varactors:

Two types of varactors were realized as part of this work. Varactors with CPC structures on Pt/Si substrates yielded a tunability of 30% whereas varactors with IDC structure on fused silica substrates yielded a tunability of 10%.

Outlook for future work:

There are many issues that still need to be resolved and could form part of future work:

Thin film processing:

Studies on the properties of BST thin films deposited at 100% Oxygen are non-existing. In this dissertation some preliminary work has been carried out in this direction on BST5 films but more detailed work is necessary to have a complete understanding of the process.

Device realization and integration with Silicon technology:

Varactors based on BST have the potential for it to be used in various RF and MW circuits. It is still an emerging technology and optimization in the processing can help

create better BST varactor. One aspect which needs sure attention is improving the conductor loss for better device performance. For minimizing metallization losses, at least 3 skin depths of metal layer are required. Efforts should be directed towards optimization including improved lithographic tools and metallization process.

Another area which can be looked into is the integration of BST based tunable circuits on Si substrates wherein mass production process can be easily realized through large size availability of Si wafer and the widespread industrial use of Si-based processing technology. Through the present work it has been shown that crystalline BST5 with tunable dielectric permittivity can be realized on amorphous SiO_2. The tunability in BST5 can be improved by introducing suitable oxide buffer layer between the BST film and the SiO_2/Si substrate. Materials suitable to serve as buffer layers include TiO_2, MgO, $LaAlO_3$, CeO_2, $MgAl_2O_4$, $Bi_2Zn_{2/3}Nb_{4/3}O_7$ and $Bi_{1.5}Zn_{1.0}Nd_{1.8}O_7$. Very thin (thickness less than 50nm) amorphous BST seed layer can also be used to control the orientation and strain in the BST5 films to obtain improved tunability.

Other aspects of BST thin film property:

The ferroelectric and dielectric properties of BST5 films have been well studied and reported in literature, but the nonlinear optical properties of BST5 thin films are less studied till now. Knowledge of their optical (linear and nonlinear) response is also quite important for practical device applications, which would be beneficial in the integration of optoelectronics with microwave electronics in the future. The linear response such as the refractive index and band-gap of BST5 films were studied as part of this work and the nonlinear optical measurements are to be carried out using a single beam Z-scan technique.

Residual stress within these materials is known to have a drastic effect on there structural, microstructural, electrical and dielectric properties. This is of particular importance in thin film materials, where the residual stress can be several orders of magnitude higher than that in bulk materials. Nano-indentation technique can be employed to calculate the residual stress in the films. The calculated values can be validated using HRXRD based calculations.

List of Publications

Refereed Journals:

1. K Venkata Saravanan, K Sudheendran, K.C. James Raju, M. Ghanashyam Krishna and Anil K Bhatnagar, "*Effect of process parameters and post deposition annealing on the optical, structural and microwave dielectric properties of RF magnetron sputtered ($Ba_{0.5}$,$Sr_{0.5}$)TiO_3 thin films*". Vacuum, Volume 81, Page 307-316, 2006.

2. K. Venkata Saravanan, K.Sudheendran, M Ghanashyam Krishna and K.C.James Raju, *"Broadband microwave dielectric properties of BST thin films on quartz substrates"*, Ferroelectrics, Volume 356, Page156-163, 2007).

3. *K. Venkata Saravanan, M. Ghanashyam Krishna, K.C.James Raju and Anil K Bhatnagar, "*Preparation of Barium Strontium Titanate using a Modified Polymeric Precursor method"* Journal of Materials Science, Volume 42, Page 1149-1155, 2007.

4. *K. Venkata Saravanan, K.Sudheendran, M Ghanashyam Krishna and K.C.James Raju, *"Structural, optical and microwave characteristics of sol-gel derived Barium Strontium Titanate thin films"*, Materials Chemistry and Physics, Volume105, Page 426-432, 2007.

5. K. Venkata Saravanan, K.Sudheendran, M Ghanashyam Krishna and K.C.James Raju, "*Effect of the amorphous – crystalline transition in $Ba_{0.5}Sr_{0.5}TiO_3$ thin films on optical and microwave dielectric properties*" Journal of Physics D: Applied Physics, Volume 42, No. 045401.

6. K. Venkata Saravanan, M Ghanashyam Krishna and K.C.James Raju, *"Effect of misfit strain and rms roughness on the tunable dielectric behavior of $Ba_{0.5}Sr_{0.5}$ TiO_3 thin films"*(Under Review, Journal of Applied Physics)

*** Not a part of the present thesis**

Conference Presentations:

1. K. Venkata Saravanan, M. Ghanashyam Krishna, K.C.James Raju and Anil K Bhatnagar, *"Structural, Optical and Electrical Characteristics of Barium Strontium Titanate Thin Films"*, poster presented at 16th Annual General Meeting of MRSI (Materials Research Society of India) February 10th –12th 2005, National Chemical Laboratoty (NCL), Pune, India.

2. K.Sudheendran, K. Venkata Saravanan, K.C.James Raju, M.Ghanashyam Krishna and Anil K Bhatnagar, "Microwave Behavior of Compositionally Modulated Barium Titanate based Thin Films for Rf-MEMS Applications", Proceedings of ISSS 2005 International Conference on Smart Materials, Structures and Systems, Vol.2, Pages SC-85 – SC-91 July 28-30 2005, Indian Institute of Science, Bangalore, India.

3. K.Sudheendran, K.Venkatasaravanan, K.C.James Raju, M.Ghanashyam Krishna and Anil K Bhatnagar, *"On wafer characterization of BST thin films for RF MEMS"*, Proceedings of the International conference on MEMS and nanotechnology, December 20-22, 2005, Indian institute of technology, Kharagpur, India.

4. K.Sudheendran, K, Venkata Saravanan, D Pamu, M Ghanashyam Krishna and K.C.James Raju, *"Size dependence of the microwave dielectric properties of oxide thin films"*, presented in Nano2006 Aug 21-25, 2006, IISc Bangalore.

5. K. Venkata Saravanan, K.Sudheendran, M Ghanashyam Krishna and K.C.James Raju *"Broadband microwave dielectric properties of BST thin films on quartz substrates"* presented in the 5th Asian Meeting on Ferroelectrics (AMF-5), september3-7, Tokyo, Japan.

6. K.Sudheendran, K. Venkata Saravanan, M Ghanashyam Krishna and K.C.James Raju, *"Characterization techniques for thin film ferroelectrics in the microwave range"*, Proceedings of national seminar on advances in electroceramics, page 343,Pune, may 5-6 ,2006.

7. K.Sudheendran, K. Venkata Saravanan, M Ghanashyam Krishna and K.C.James Raju, *"Measurement of microwave dielectric properties of BST thin films on low-K substrates for tunable microwave devices"*, Proceedings of the National conference on ferroits (NCF-2006) CVR College, Hyderabad India.

8. K. Venkata Saravanan, K.Sudheendran,M Ghanashyam Krishna and K.C.James Raju, *"Correlation between the optical, structural and microwave dielectric properties of RF magnetron sputtered ($Ba_{0.5}$,$Sr_{0.5}$)TiO_3 thin films"*, Proceedings of the National conference on ferroics (NCF-2006) CVR college,Hyderabad India

9. K.Sudheendran, K, Venkata Saravanan, M Ghanashyam Krishna and K.C.James Raju *"Microwave characterization of ferroelectric thin films using CPW based transmission lines and the extraction of the conductor losses"I*, Jaipur.

10. K. Venkata Saravanan, V. Sivasubramanian, M. Ghanashyam Krishna and K.C.James Raju, *"Phonon modes in $Ba_{0.5}Sr_{0.5}TiO_3$ thin films: A study using Raman spectroscopy"*, Proceedings of the DAE Solid State Physics Symposium, Volume 51, Page 565, 2006.

11. K Sudheendran, K. Venkata Saravanan, M Ghanashyam Krishna and K.C.James Raju, *"Broadband characterization techniques for dielectric and metallic thin films at microwave frequencies"* presented at International symposium on Microwaves, Bangalore, December 2006.

12. K.Sudheendran, D pamu, K Venkata Saravanan, M Ghanashyam Krishna and K.C James Raju, *"Broadband Microwave characterization of Nano Crystalline TiO_2 and BST thin films"*, presented in NSFD 2006 at IIT Kharagpur in December 2006.

13. K. Venkata Saravanan, M. Ghanashyam Krishna, and K. C. James Raju, "Effect of substrate on the crystallographic and morphological texture of $Ba_{0.5}Sr_{0.5}TiO_3$ thin films", Proceedings of the DAE Solid State Physics Symposium Vol. 52, page 681-682**,** December 2007.

14. K. Venkata Saravanan, M. Ghanashyam Krishna, and K. C. James Raju, "Influence of *ex situ* annealing on the structural, microstructural and optical properties of BST thin films", presented in National Conference on Physics of Materials (NCPM-2008), March 19-20, 2008, Pondicherry University, Pondicherry.

15. K. Venkata Saravanan, K.Sudheendran, M Ghanashyam Krishna and K.C.James Raju, "Impedance spectroscopy of crystallinity dependent dielectric properties of Barium Strontium Titanate thin films" presented in NSFD 15 at Thapar University, Patiala in November 2008.

16. G. Lakshmi Narayana Rao, K. Venkata Saravanan and K. C. James Raju, "Characterization of $Ba_{0.5}Sr_{0.5}TiO_3$ Thin Films Using Interdigitated Capacitor Structures", presented in NSFD-15 at Thapar University, Patiala, November December 2008

17. G. Lakshmi Narayana Rao, K. Venkata Saravanan and K.C. James Raju, "Planar interdigitated capacitors on single crystal substrates for MIC and MMIC technology" to be presented at DAE Solid State Physics Symposium**,** December 2008

18. G. Lakshmi Narayana Rao, K. Venkata Saravanan and K.C. James Raju "Ferroelectric Thin Film Based Tunable Devices for Software Defined Radio" presented at TENCON 2008 at University of Hyderabad